SYNTHESIS AND KINETICS OF FORMATION OF CERIA AND CERIA BASED MATERIALS *via* THERMAL DECOMPOSITION OF OXALATES

Thesis submitted to
the University of Calicut in partial fulfillment of
the requirements for the award of the degree of

DOCTOR OF PHILOSOPHY IN CHEMISTRY

by

NUSRATH. K

DEPARTMENT OF CHEMISTRY
UNIVERSITY OF CALICUT
KERALA- 673 635
JULY- 2018

CERTIFICATE

This is to certify that the dissertation, entitled **"SYNTHESIS AND KINETICS OF FORMATION OF CERIA AND CERIA BASED MATERIALS *via* THERMAL DECOMPOSITION OF OXALATES"** submitted to the University of Calicut, in partial fulfillment of the requirements for the award of the **Degree of Doctor of Philosophy in Chemistry** is a bonafide record of research work done by **Ms. NUSRATH. K,** during the period **2013-2018** in the Department of Chemistry at University of Calicut, under my supervision and guidance. The contents of the thesis have been checked for plagiarism using the software 'Urkund' and similarity index falls under permissible limit. I further certify that the thesis or part has not previously formed the basis for the award of any Degree / Diploma / Associate ship / Fellowship or other similar title to any candidate of any University.

University of Calicut

Dr. K. Muraleedharan
Professor
Department of Chemistry
University of Calicut

CERTIFICATE

This is to certify that the dissertation, entitled **"SYNTHESIS AND KINETICS OF FORMATION OF CERIA AND CERIA BASED MATERIALS *via* THERMAL DECOMPOSITION OF OXALATES"** submitted to the University of Calicut, in partial fulfillment of the requirements for the award of the **Degree of Doctor of Philosophy in Chemistry** is a bonafide record of research work done by **Ms. NUSRATH. K,** during the period **2013-2018** in the Department of Chemistry at University of Calicut, under my supervision and guidance. The contents of the thesis have been checked for plagiarism using the software 'Urkund' and similarity index falls under permissible limit. I further certify that the thesis or part has not previously formed the basis for the award of any Degree / Diploma / Associate ship / Fellowship or other similar title to any candidate of any University. I also hereby certify that the corrections/suggestions from the adjudicators have been incorporated in the revised thesis. Content of the CD submitted and the hardcopy of the thesis is one and the same.

University of Calicut

Dr. K. Muraleedharan
Professor
Department of Chemistry
University of Calicut

DECLARATION

I, **NUSRATH. K**, hereby declare that the thesis, entitled **"SYNTHESIS AND KINETICS OF FORMATION OF CERIA AND CERIA BASED MATERIALS *via* THERMAL DECOMPOSITION OF OXALATES"**, submitted to the University of Calicut, is a bonafide record of research work done by me during the period **2013-2018** under the supervision and guidance of **Dr. K. Muraleedharan**, Professor, Department of Chemistry, University of Calicut and the same has not formed the basis for the award of any Degree / Diploma /Associate ship / Fellowship or other similar title to any candidate of any University**.**

University of Calicut **NUSRATH. K**

ACKNOWLEDGEMENT

*It gives me immense pleasure to acknowledge my sincere gratitude for my supervising teacher **Dr. K. Muraleedharan**, Professor, Department of Chemistry, University of Calicut, Kerala, for his guidance, valuable suggestions, motivation, and constant inspiration which greatly helped me in completing this work successfully.*

*With deep sense of gratitude, I copiously thank **Dr. P. Raveendran**, Head of the Department of Chemistry, former Heads **Dr. V.M. Abdul Mujeeb** and **Dr. K. Muraleedharan** (and also the supervising teacher) for providing me adequate facilities to carry out this research work.*

I would like to express my gratitude to the authorities of the Department of Physics, University of Calicut, National Institute of Technology, Calicut, Central Sophisticated Instrumentation Facility (CSIF), University of Calicut, Department of nano Science and Technology, University of Calicut and STIC, CUSAT, Cochin, for carrying out the XRD, FE-SEM, PL and SEM analysis which facilitated in completing my research work in time. I also remember the facilities arranged by Amala Cancer Research Centre, Trissur for conducting the cytotoxicity studies and by Sree Chitra Tirunal Institute for Medical Sciences and Technology, Trivandrum for the micro Raman analysis of the samples.

For the financial support, I thank University Grants Commision(UGC), New Delhi, India. I was receiving Junior Research

Fellowship for two years and Senior Research Fellowship for rest of the time during my Ph. D. tenure.

I wish to express my heartfelt thanks to our research group members for giving their valuable suggestions. I also extend my sincere gratitude to all research scholars, all other faculty members and non-teaching staffs of the Department of Chemistry, University of Calicut for their help, cooperation and support.

Finally, there is no word to express my gratitude for the solemn prayers and dedicated support of my family.

Above all, I am proud of the God Almighty and His showers of blessings for completing this research work successfully.

University of Calicut ***Nusrath. K***

The thesis is dedicated to

Tittu, Riya, Riyaumma and to my parents

GLOSSARY OF TERMS

Tc	-	Transition temperature
DTA	-	Differential thermal analysis
TG	-	Thermogravimetry
DSC	-	Differential scanning calorimetry
KAS	-	Kissinger- Akahira- Sunnose
FWO	-	Flynn-Wall-Ozawa
DFT	-	Density functional theory
VASP	-	Vienna *ab initio* simulation package
DOS	-	Density of states
KKR	-	Korringa-Kohn-Rostoker
LDA	-	Local density approximation
GGA	-	Generalized gradient approximation
U	-	Hubbard correction
TWC	-	Three way catalyst
DTG	-	Derivative thermogravimetry
CTAB	-	Cetyl trimethyl ammonium bromide
PEG	-	Poly ethylene glycol
FT-IR	-	Fourier transform infrared
UV	-	Ultra violet
XRD	-	X-ray diffraction
SEM	-	Scanning electron microscope
TEM	-	Transmission electron microscope

HRTEM	-	High resolution transmission electron microscope
SAED	-	Selected area electron diffraction
FE-SEM	-	Field emission scanning electron microscope
EDS	-	Energy dispersive spectra
PL	-	Photo luminescence
PBS	-	Phosphate buffered saline
CC_1	-	100 m/m (%) cerium oxalate
CC_2	-	90 m/m (%) cerium oxalate
CC_3	-	70 m/m (%) cerium oxalate
CC_4	-	33.33 m/m (%) cerium oxalate
CC_5	-	100 m/m (%) calcium oxalate
nm	-	nanometer
μm	-	micrometer
Ea	-	Activation energy
A	-	Arrhenius pre exponential factor
R	-	Universal gas constant
c	-	Contribution
K	-	Kelvin
Eg	-	Optical band gap
eV	-	Electron volt
Ce-Ox	-	Cerium oxalate decahydrate
A_0	-	Ce-Ox

A_1	-	Ce-Ox + Fe_3O_4 (2/5/10 m/m (%))
A_2	-	Ce-Ox + Co_3O_4 (2/5/10 m/m (%))
A_3	-	Ce-Ox + NiO (2/5/10 m/m (%))
A_4	-	Ce-Ox + $CoFe_2O_4$ (2/5/10 m/m (%))
A_5	-	Ce-Ox + $NiFe_2O_4$ (2/5/10 m/m (%))
COX	-	Cerium oxalate decahydrate
Nps	-	Nanoparticles
ROS	-	Reactive oxygen species
c_1	-	Undoped cerium oxalate
c_2	-	2 % copper doped cerium oxalate
c_3	-	10% copper doped cerium oxalate
c_4	-	20 % copper doped cerium oxalate
c_5	-	30% copper doped cerium oxalate
s_1	-	Ceria prepared from c_1
s_2	-	Ceria prepared from c_2
s_3	-	Ceria prepared from c_3
s_4	-	Ceria prepared from c_4
s_5	-	Ceria prepared from c_5
CT	-	Charge transfer
IC_{50}	-	Half maximal inhibitory concentration
H_1	-	Cerium oxalate prepared *via* simple precipitation using PEG-800 as surfactant

H_2	-	Cerium oxalate prepared *via* hydrothermal method using PEG-800 as surfactant
H_3	-	Cerium oxalate prepared *via* simple precipitation using CTAB as surfactant
H_4	-	Cerium oxalate prepared *via* hydrothermal method using CTAB as surfactant
P_1	-	ceria synthesized from H_1
P_2	-	ceria synthesized from H_2
P_3	-	ceria synthesized from H_3
P_4	-	ceria synthesized from H_4
PBE	-	Perdew, Burke and Ernzerhof
TDOS	-	Total density of states

CONTENTS

PREFACE

Cerium oxalate is a pharmacologically important compound. It is an antiemetic drug, used for treating motion sickness, side effects of opioid analgesics, general anesthetics, antipsychotic medication and chemotherapy against cancer. In material synthesis field, it is an important precursor to synthesize ceria nano/micro structures. The thesis encompassed with elucidation of kinetics of thermal decomposition of cerium oxalate decahydrate up to the formation of ceria micro/nanostructures, significant influence of various additives such as CaC_2O_4, semiconducting nano metal oxides of Fe, Co and Ni, ferrites of Fe and Co, various reactant molar concentrations of Cu^{2+} - dopant and effect of surface morphology and synthetic route of oxalate precursors on the kinetics and thermal decomposition behaviors were established. An important application drawn for the doped and surface modified ceria exposed enhanced anticancerous properties against Dalton's Lymphoma ascite cells. DFT studies for the band structure and density of states of single unit cell ceria and copper doped ceria were also incorporated. The thesis is divided into *9 chapters*.

Chapter 1 deals with general introduction emphasizing important applications of ceria and ceria based nano materials, methods to study solid state decomposition kinetics, theories (*in brief*) of band structure and density of states and density functional theory (DFT). Recent studies regarding the thermal decomposition kinetics, the applications of ceria and ceria based materials in the medicinal field and in the field of theoretical investigations are also included in this chapter. Materials

and various experimental techniques used for the investigations are briefly discussed in *Chapter 2*. *Chapter 3* related with investigation regarding the kinetics of the thermal dehydration of solid state reaction between cerium oxalate micro rods and calcium oxalate, which was studied using non-isothermal TG/DTA technique. The effect of calcium oxalate in varying compositions upon the kinetics of dehydration of cerium oxalate decahydrate was discussed. As the extension of the above mentioned work, the kinetic and mechanistic features of the synthesis of micro structural rods of CeO_2 *via* the oxidative thermal decomposition of cerium oxalate in air and the effect of dry mixing of 10 mass % calcium oxalate with cerium oxalate upon the reaction pathway and mechanism were incorporated in *chapter 4*. *Chapter 5* provides the significant effects of semiconducting nano metal oxides of Fe, Co and Ni and ferrites of Co and Ni on the thermal events and thermal decomposition kinetics of cerium oxalate decahydrate up to the production of ceria material. The synthesis of cerium oxalate discs/flowers and the establishment of Ea for producing ceria (discs/flower) and various copper ceria solid solutions were discussed in *Chapter 6*. Photo physical properties and cytotoxic studies of synthesized solid solutions were also drawn in this chapter. As the last section of the kinetic study of decomposition, effect of synthetic route (simple precipitation and hydrothermal) and surface characteristics of the oxalate precursors (nano *flower petals*, *plates*, *discs/ flower* and *array of nano hexagonal* Ce-Ox) on the kinetic behavior of formation of ceria nano structures were elucidated in *Chapter 7.* Optical and luminescent properties and cytotoxicity studies for the synthesized ceria nano structures were also described in this

chapter. On moving into the last section of the thesis (*Chapter 8*), the computation of electronic structure (DOS and band structure) of bulk ceria (1×1×1) and copper doped ceria were performed by the plane wave based DFT method using *VASP 5.4.1* version. Besides, the charge density distribution of ceria and copper introduced ceria in different crystallographic directions were also brought with this chapter. The thesis concludes with a summary of results (*Chapter 9*) obtained in the present work and brief mention on the future prospects.

NUSRATH. K “SYNTHESIS AND KINETICS OF FORMATION OF CERIA AND CERIA BASED MATERIALS via THERMAL DECOMPOSITION OF OXALATES”. THESIS. DEPARTMENT OF CHEMISTRY, UNIVERSITY OF CALICUT, 2018.

1.1. General Introduction

Solid state materials have pivotal role in the progress of human kind since the ancient time. Usage of solid state materials starts from the Stone Age. In that period man used sharp stone as weapons. But in the next era, metals are the most profounded material. Properties of naturally available materials were known by trial and. error method. Solid state chemistry deals with synthesis, structure characterization and applications of materials. The back bone of new technological development is the solid state chemistry. Solid state materials include metals, semiconductors, high Tc super conductors, polymers, magnetic materials, hydrogen storage materials, etc.

Evolution of nanomaterial became one of the revolutionary aspects in the modern science and technology. Because of the extremely complicated nature and exhibiting wide variety in their composition and structural characteristics, knowledge of solid state reactions have always been a most intriguing task[1]. Studies regarding the factors which influencing the solid state reactions are of both fundamental and practical importance. Hence, the control of the reaction rate is an important objective. Certain solid state reactions need higher reactivity (in case of solid propellants and catalysts) whereas other required lower reaction rate as in the case of oxidation and corrosion of metals. Therefore it is essential to have knowledge of the basic mechanism of reaction of solids, so as to control the reaction rate in specified situation.

Solid state studies have three aspects; *the phenomenological*, *the thermodynamic* and *the kinetic*. The phenomenological study is associated with qualitative and semi qualitative observation of the phenomena occurring during the reaction. The thermodynamic aspects include initial, final and equilibrium states of the system and to the stimulating force behind the transformation. The rates of transformation of the reactant to product are reflected in the kinetic aspects. This can be done at controlled set of conditions while the mechanism describes the complete set of reaction stages leading to the products.

In solution state, kinetic aspects of the reaction are expressed in terms of concentration of the reactant and product. Reaction rate in solid state are diffusion controlled. Rules regulating the kinetics of solid state reactions are different from those of reaction between liquids. Factors such as morphology, geometry of the reaction interface, diffusion of the reaction species, possibleness of the nucleation and anisotropy of the crystallites affect the rate of the reaction[2]. Solid state reaction most often proceeds through the following four elementary steps:

1. Sorption phenomena (adsorption and desorption)

2. Reaction on the atomic scale (homogeneous or interphase reactions)

3. Nucleation of a new phase (in the bulk or at the surface of the reacting solid)

4. Transport phenomena (diffusion and migration)

Solid state reactions can be classified as follows:

(a) Solid-solid reaction

(b) Solid-liquid reaction

(c) Solid-gas reaction

(d) Reactions of single solid (*e.g.*, solid state decomposition)

Among these, we are concerned only with solid state decomposition reaction.

1.1.1. Solid state reaction kinetics

Chemical kinetics provides mathematical models for explaining and forecasting the transformation rate of a chemical system. The fundamental concept of chemical kinetics is based on the law of mass action established by Cato M. Guldberg (1836-1902) and Peter Waage (1833-1900) in the latter half of nineteenth century, where equilibrium constant were derived in terms of kinetic data and rate equations. Solid state kinetics or heterogeneous kinetics is the challenging areas of research since the past years. Many methods are available for studying solid state kinetics. The first work in the solid state kinetics was done by Kujirai and Akahira in 1925[3] on the effect of temperature on the degradation of fibrous industrial materials. There have been established a number of methods for studying the solid state kinetics using data obtained from thermogravimetry (TG), differential thermal analysis (DTA) and differential scanning calorimetry (DSC) in

addition to variety of other methods. Solid state kinetics can be studied *via* either *isothermal* or *non-isothermal* experimental condition. Among these, non-isothermal method is more preferred over isothermal because all interesting information can be obtained from a single experimental run[4–6]. The mathematical method chosen for predicting kinetics may be model fitting, single heating rate or isoconversional methods. Among these methods, model fitting method is most popular[7]. Isoconversional methods are model free methods, which allow the prediction of kinetic parameters without evaluating the reaction model and pre-exponential factor. Besides, these methods allow the activation energy to be determined as a function of the extent of conversion[7]. In this method, the kinetic analysis is carried out over a set of kinetic runs at a fixed value of conversion function. The reaction rate is predicted as a function of temperature only.

1.1.1.1. Model fitting method

Using model fitting method, mechanism of the solid state reaction can be predicted. For this purpose usually Coats Redfern method[8] is used.

$$\int_0^{\alpha} \frac{d(\alpha)}{f(\alpha)} = g(\alpha) = \int_0^{T} \frac{A}{\beta} e^{-Ea/RT}\, dT \qquad (1)$$

where $g(\alpha)$ represents the reaction model, which describe specific solid state reaction mechanism. The plots of ln [g (α)/T^2] *vs* 1/T were drawn for each model by the linear regression method. The model giving the *best fit i.e.*, maximum correlation coefficient (*approximately to unity*) is taken as the best model describing the mechanism of the reaction.

From the plot, *Ea* and *A* can be calculated from slope and intercept respectively.

The mechanism of solid state reaction are generally occurs with reorganization of chemical bonds and molecular changes which causes for the transformation of reactant to products. The rate of the formation of solid state reaction products at the reaction interface is largely dependent on the effective surface area and surface concentration of reactants and intermediates.

1.1.1.2. Isoconversional methods

These methods can be used to calculate kinetic parameters such as *Ea* and *A*. This method doesn't need the knowledge of particular reaction model describing the solid state reaction. In the model free method, rate of reaction at a constant conversion is supposed to be a function of temperature only. The commonly used isoconversional methods are KAS[9], Kissinger[10], FWO[11,12], Friedman[13,14] and iterative isoconversional method[15, 16].

1.1.1.2.1. Kissinger-Akahira-Sunose (KAS)

The equation corresponding to KAS method is:

$$l\,\mathrm{n}\left[\beta/T^2\right] = \ln\left[AR/Eg(\alpha)\right] - E\,/\,RT \qquad (2)$$

Apparent activation energy *Ea* can be calculated from the slope of the linear representation of ln β/T^2 vs. $1/T$ with a given value of α.

The value of pre-exponential factor A can be obtained from the intercept if the form of integral reaction model $g(\alpha)$ is known.

1.1.1.2.2. Flynn-Wall-Ozawa (FWO)

The equation based on FWO method is:

$$\ln \beta = \ln \left[{AE}/{Rg(\alpha)} \right] - 5.331 - 1.052 \, {E}/{RT} \tag{3}$$

Using linear representation of ln β *vs. 1/T*, *Ea* and *A* can be obtained from the slope and intercept respectively

1.1.1.2.3. Kissinger method

The Kissinger method, which was utilized to determine the apparent activation energy for the overall reaction from the DSC curves or DTG curves recorded at different β.

$$\ln\left(\frac{\beta}{T_P^{\,2}}\right) = \ln\left[-\frac{f(\alpha_p)}{d\alpha}\frac{AR}{Ea}\right] - \frac{Ea}{RT_P} \tag{4}$$

Where, T_p is the peak maximum temperature characteristics for the overall reaction. The Kissinger plots *ln* (β/T_p^2) versus T_p^{-1}. From the values of slope and intercept, *Ea* and *A* respectively can be determined.

1.1.1.2.4. Friedman method

For the estimation of *Ea* and *A*, *Friedman* plot was used.

$$\ln\left(\frac{d\alpha}{dt}\right) = \ln\left[\frac{A}{f(\alpha)}\right] - \frac{Ea}{RT} \tag{5}$$

In this method, ln(dα/dt) is plotted against 1/T. From the values of slope and intercept, *Ea* and *A* can be calculated.

1.1.1.2.5. Iterative isoconversional method

To calculate the approximate value of activation energy *Ea* approaching to the exact value can be determined by the iterative procedure[15-17]. It is based on the following equation:

$$\ln {}^{\beta}\!/_{h(x)T^2} = \ln {}^{AR}\!/_{g(\alpha)Ea} - {}^{Ea}\!/_{RT} \tag{6}$$

where $h(x)$ can be expressed by the fourth Senum and Yang approximation formulae[18]:

$$h(x) = \frac{x^4+18x^3+88x^2+96x}{x^4+20x^3+120x^2+240x+120} \tag{7}$$

where $x = Ea/RT$

Zhipeng *et al*[19] performed the following procedure for the calculation of *Ea* by the iterative method: (i) assume $h(x) = 1$ to calculate the initial value of the activation energy Ea_1. The conventional isoconversional method stops the calculation of *Ea* at this

step. (ii) Using the value of Ea_1, a new value of Ea_2 can be calculated from the plot of ln $[\beta/h(x)\ T^2]$ *vs.1/T* (iii) Replace Ea_1 with Ea_2 and repeat step (ii). When Ea_i-$Ea_{(i-1)} < 0.01$ KJmol^{-1}, the value of Ea_i is considered to be the exact value of activation energy. The estimation of activation energy doesn't require the knowledge of reaction model, $g(\alpha)$. Therefore this method is model independent.

1.1.2. Solid state kinetics of multistage reactions

The main cause of multistage reactions is physico-geometrical constraints which may occur due to the changes in reaction conditions as the reaction advances[20]. Koga *et al*[21] stated that complex reaction proceeds in a combination of multistep behavior controlled by physico-geometrical features of solid state reactions and successive chemical reaction schemes. During the early stage of reaction, a smooth surface product layer is generated between the reactant and reaction interface. Upon thermal decomposition, this surface product layer come into action *i.e.*, it will impede the diffusional removal of gaseous molecules. This causes to increase the internal pressure of the reactant leading to change in the reaction condition at the reaction interface. Presence of cracks and holes on the surface of the product played as diffusion channel for the removal of gaseous products. Due to the experimental inconvenience of separately tracking the component process, deconvolution of overall kinetic information into reaction component is the only possible method for interpreting the reaction scheme of successive processes[22, 23]. Hence kinetic analysis of the decomposition process was performed using the kinetic deconvolution method[24].

In this method, a formal kinetic analysis was performed by assuming a single step reaction for the overall reaction using the fundamental kinetic equation[25].

$$\frac{d\alpha}{dt} = Ae^{-Ea/RT} f(\alpha) \tag{8}$$

where t is time, T the temperature, R the ideal gas constant, A the apparent Arrhenius pre-exponential factor, Ea the apparent activation energy and $f(\alpha)$ the apparent kinetic model function used to describe the physico-geometrical reaction mechanism as a function of the fractional reaction, α. Based on Eq. (14), plots of ln (dα/dt) *vs*T^{-1}at different α for the series of kinetic data recorded under linear non-isothermal condition. After the kinetic characterization of independent reaction processes, the overall process is studied by the cumulative equation.

$$\frac{d\alpha}{dt} = \sum_{i=1}^{n} c_i A_i \exp\left(\frac{-E_{a,i}}{RT}\right) f_i(\alpha_i) \tag{9}$$

With $\sum_{i=1}^{n} c_i = 1$ and $\sum_{i=1}^{n} c_i \alpha_i = \alpha$

where n and c are the number of component step and contribution ratio of each reaction step to the overall process while A, Ea and $f(\alpha)$ are Arrhenius parameter, activation energy and kinetic model function in different forms respectively.

The present investigations covers the area of solid state reaction kinetics of coordination compounds of oxalate ligand formed with rare earth metal Ce, up to the formation of nano/micro ceria under the atmosphere of air as well as N_2. Reaction kinetics was performed through the detailed kinetic strategy of deconvolution procedure.

1.1.3. Oxalate as the ligand

Oxalate, $C_2O_4^{2-}$ is the *dianion*, is an excellent bidentate ligand for metal ions forming 5-memebered MO_2C_2 ring. X-ray crystallographic studies revealed that the anion adopted either a planar conformation with D_{2h} molecular symmetry or approximate D_{2d} symmetry where O-C-C-O dihedrals approach 90º. Most often, D_{2h} symmetry of the free oxalate dianion is selected for the allocation of IR absorption spectra of a number of metal-oxalate compounds[26, 27]. The conformation adopted by the oxalate anion depends on the size of metal to which it is confined as well as the extent to which hydrogen atom bonded in the crystal.

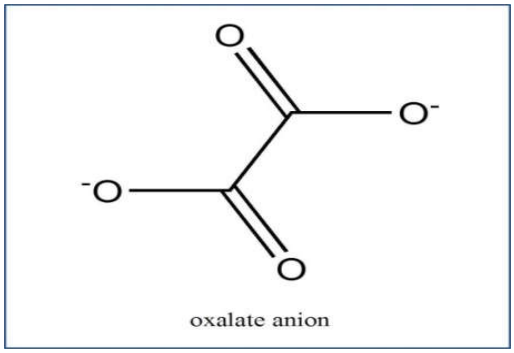

Fig. 1 The structure of free oxalate *dianion*

1.1.4. Cerium oxalate decahydrate

Rare earth metal Ce forms insoluble precipitate with oxalic acid or oxalate salt. It has the general formula $Ce_2(C_2O_4)_3.10H_2O$. The crystal structure of cerium oxalate decahydrate like all other lanthanide oxalates was proposed to have monoclinic structure with space group of $P2_{1/C}$. The proposed structure consists of 2D network with edge sharing of 1:5:3 co-ordinations polyhedral identical to the (020) set of planes. Each Ce atom is surrounded by three chelating oxalate ligands and three aqua ligands. The remaining seven lattice water molecules are spreaded over the intervening space. Fig. 2 represents schematic representation of cerium oxalate decahydrate.

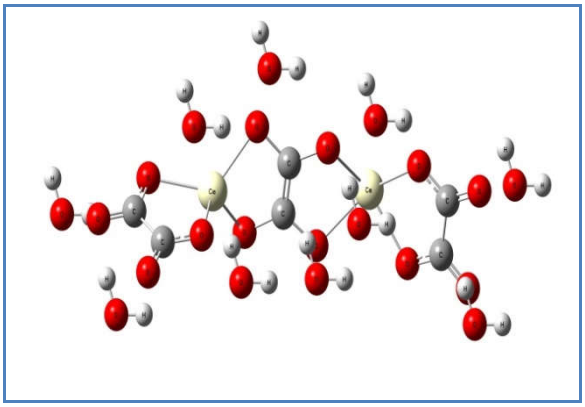

Fig. 2 Schematic representation of cerium oxalate decahydrate

Cerium or cerous oxalate is a white crystalline solid. It is an *antiemetic drug* used for vomiting and nausea. Usually antiemetic are effective for treating motion sickness and side effects of opioid analgesics, general anesthetics, antipsychotic medication and chemotherapy against cancer. Cerium oxalate can be utilized safely for

the severe cases of gastroenteritis and morning sickness of pregnant women. Fig. 3 shows the schematic representation of anhydrous cerium oxalate.

In material synthesis field, cerium oxalate is an important material because it can generate most promising biomaterial ceria *via* thermal decomposition method. In order to modify the properties of ceria for suitable applications, control over the parameters of oxalate precursor is essential.

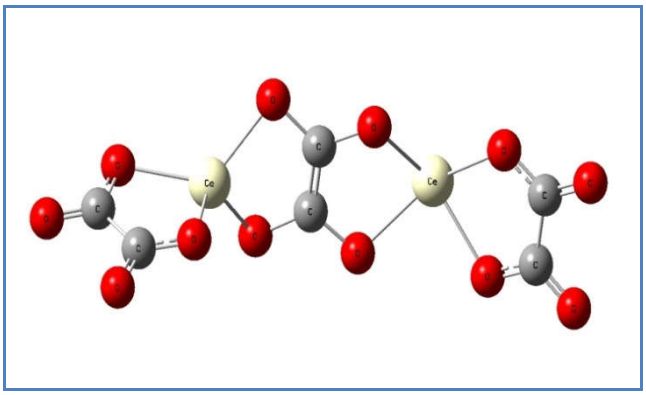

Fig. 3 Schematic representation of cerium oxalate

Nano ceria can be prepared through a variety of methods such as hydrothermal, solvothermal[28,29], sol-gel[30], micro emulsion[31], thermal decomposition[32], etc. CeO_2 nano particle were prepared by rapid thermal decomposition by microwave heating of cerium oxalate and concluded that shape of resultant specimen depends on the precursor material shape[33]. Using thermal decomposition method, particle size and shape can be effectively controlled. It can produce highly homogeneous nano particle[34–36]. It requires shorter preparation time and fewer impurities in the final product. Hydrothermal and

solvothermal synthesis have found the limitations of temperature. Even though combustion synthesis is a good method with regard to time, it is difficult to control size and shape of the particles formed. Fig. 4 represents schematic illustrations of cubic structure of ceria.

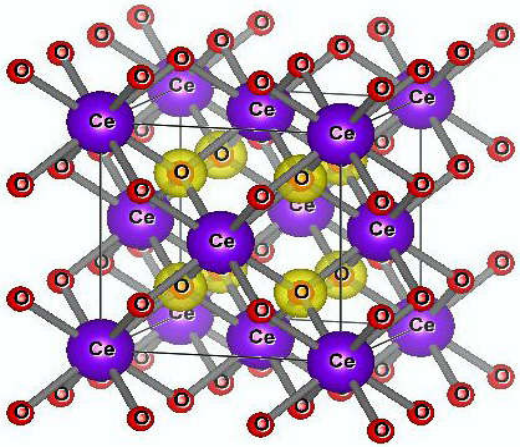

Fig. 4 Schematic representation of CeO_2 crystal

Because of the reduction property of oxalate *dianion*, thermal decomposition process of metal oxalates is relatively complicated. It involves the cleavage of C-C bond, since the products are CO and CO_2 which consists of one carbon atom each. In most of the time, the C-C bond breaking is the rate determining step[37]. During this process, the transfer of an electron from $C_2O_4^{2-}$ to the cation occurs, which is assumed to be the first stage of decomposition, leading to the breakage of C-C bond[38]. Both external and internal factors affect the solid state reaction. Internal factors include lattice spacing, symmetry, surface area and lattice defects (interstitial, vacancies, impurities, electrons, holes and dislocations). External factors such as applied voltage, pressure, temperature, pretreatment and irradiation affect the solid state

thermal decomposition reaction. Pretreatments of the sample by mechanical grinding, doping, irradiation, etc., can affect the rate as well as temperature of decomposition of oxalates. The solid state material can be bombarded with neutrons, protons or other particles, or pre-treatment with X- ray, UV ray or γ irradiation. Most often this can generate electronic or atomic imperfections, cause to the shortening of the induction period and to an increase in the rate constant of thermal decomposition[1]. Literature survey reported that most of the studies regarding pre-irradiation of the sample with γ-ray enhanced the decomposition reaction by decreasing the activation energy and the effect was increased with amount of irradiation[39, 40–42]. In certain cases, treatment itself bring both dehydration and decomposition of the materials[38,43,44]. Nature of the dopants greatly affects the decomposition temperature as well as rate[45,46]. The lattice structure of the solid has predominant role in the kinetics of solid state reaction than that from liquid or gaseous state chemical reaction.

In solid state science, the information regarding the kinetic parameters such as activation energy and decomposition temperature are important factor for determining the reaction mechanism. The basic fact underlying the distinct features of a material is the reaction mechanism associated with the preparation. Moreover, there are many practical applications based on the reaction rate and temperature dependence. The industry needs the measurement of kinetic parameters, which will become more helpful for proper installation and programming condition, otherwise the manufacture of materials would become uneconomic. Therefore, using thermo analytical experiments

and accurate mathematical treatment of the data hopes the establishment of kinetic characteristics essential for the industrial thermal processes.

1.1.5. Applications of ceria and ceria based nano materials

Potential performances of rare earth oxide ceria have great work of art. It constitutes as the most promising biomaterial. Ceria constitutes as the one of the major components of TWCs for the removal of toxic automobile exhaust gases[47–49], humidity sensors[50], oxygen sensors and oxygen permeation membrane systems[51]. On reducing the size of CeO_2 to nanometers, it possesses highly interesting properties because it allows the modification of surface area to volume ratio. Ceria performs as excellent UV absorbents and filters[52]. It can be utilized as the good absorbent for the removal of fluoride ion and arsenic[53] based compounds. It have substantial role in the dispersed fields such as catalysis, sensors, solid electrolytes and polishing powders[32]. Due to the presence of O-H group on the surface of ceria, it becomes more reactive as an adsorbent for the removal of pollutants from water even at higher temperatures[54]. Manifestation of oxygen vacancies have predominant role for performing ceria as an eventual material. Because of its oxygen storage capacity, it is utilized as solid electrolyte in solid oxide fuel cell[53]. It can inactivate some of the most toxic ROS such as super oxide radical, hydrogen peroxide and nitrosyl radical[55]. Researchers proposed that nano ceria act as radical scavenger of H_2O_2 in normal tissues but as a producer of H_2O_2 in cancer environment[56]. These properties of ceria largely depend on its particle shape, size, surface chemistry, surface additives and ligand that

involves in redox reaction[57–59]. Anti –invasive behavior of nanoceria was observed in human melanoma cells, whereas antitumor and anti-antigenic effects were studied *in vivo* tumor model[60].

Doping of ceria with rare earth elements (Gd, Nd, La and Th) enhanced the oxygen ion conductivity and the mechanical properties[61]. Other important characteristics of ceria include oxygen ion conductivity and oxygen storage capacity. The oxygen storage capacity of ceria increases on doping with metallic cations (*e.g.*, Ca^{2+}, Ba^{2+}, Pb^{2+}, etc.)[62]. The role of Cu^{2+} in the ceria lattice on the oxidation of CO over CuO/CeO_2 catalyst was discussed[63]. Both redox couple Ce^{4+}/Ce^{3+} and Cu^{2+}/Cu^{1+} is involved in the reaction. Hence ceria can provide lattice oxygen for copper, thus increasing the oxidative properties of the binary system. Besides, it was reported that insertion of Co/Mn oxides in to the copper- ceria crystal lattice made substantially distinguishable behavior to the surfaces, which are coated on fiber glass system[64]. Due to the existence of synergetic effect in the three components Co-Cu-Ce-O/FG system, it attributed its higher catalytic activity but the same is absent in the Mn-Cu-Ce-O/FG system. Moreover, the membrane – deposited active layer of $CuO\text{-}CeO_2$/SG exposed higher catalytic activity for CO conversion[65].

Additionally it is worth to note that properties of ceria are monitored by structural and morphological parameters[66–69]. Different morphologies of ceria are synthesized and studied, which involves nano rods, nano cube, octahedron or polyhedron, etc[70]. It was investigated that CeO_2 nanorods selectively exhibits higher activity for CO oxidation and NO reduction[71,72], whereas nanocubes show superior

properties in soot combustion[73], hydrogen oxidation[74]and preferential oxidation of CO[75]. For water gas shift reaction processes, gold supported ceria nano rod performed as best catalyst than ceria, while Cu-based ceria polyhedral Nps[76]contributed best structural support[77,78]. But due to the existence of large proportion of reactive planes on the surface of ceria nanowire, made it as potential redox catalyst for CO oxidation. *3D* flower like ceria has owned enhanced catalytic activity towards the oxidation of CO for the removal of As (V) and Cr (VI). Presence of large surface area and channels in the 3D flower ceria can provide better interaction between gas molecules and catalytic support[79].

The revolutionary upright of 'nanotechnology' brought progressive research challenges in the medical field designed for improving therapeutic strategies against various diseases threatening to our life. It improved the pharmacodynamics and pharmacokinetic properties of conventional chemotherapeutic agent and enhanced their efficacy with less toxicity[80]. Among nano metal oxides, rare earth oxide ceria possess excellent antioxidant and anti-inflammatory properties. This happens because of its triggering nature of Ce^{3+} and Ce^{4+} oxidation state depending on the environment[81,82]. The nature of oxygen storage capacity of it increases the antioxidant behavior. It performs as anticancerous drug for various cancer cell lines in different manner because it can reduce the oxidative stress induced by the generation of reactive oxygen species. Ceria can directly accept hydrogenated radicals from the blood stream and thus preventing the cell damage caused by the oxidative stress. Doping of the parent matrix with elements which can emits radiation by itself upon excitation in the

UV-visible region of the spectrum[50]. Nano medicine with modified structure can kill tumor cell by increasing ROS level in tumor cells or by directing the nucleus or organ cells[83]. Among *p*- block elements, Si and first transition series metal oxides such as Cu, Fe aroused the induced oxidative stress and cytotoxicity in airway epithelial cells. It was aroused that besides the surface and core oxide composition, size of nanoparticle has key role on imparting its effect on certain diseases[84]. The present work includes synthesis of different series of Cu-Ce-O solid solutions from the oxalate precursor and correlation of cytotoxic effects of mixed oxides towards Dalton's Lymphoma ascites cells. The findings of this analysis were discussed in detail in *Chapter 6*. PEGlycated ceria nanoparticle expressed enhanced radioprotection on human liver cell under γ-irradiation[85]. Up to now, any investigations related with the influence of different shapes of ceria nano particle upon its anticancerous properties still not exist. The detailed discussion regarding this kind of cytotoxic behavior is involved in *Chapter 7*. Fig. 5 represents the schematic representation of normal cell and cancer cells.

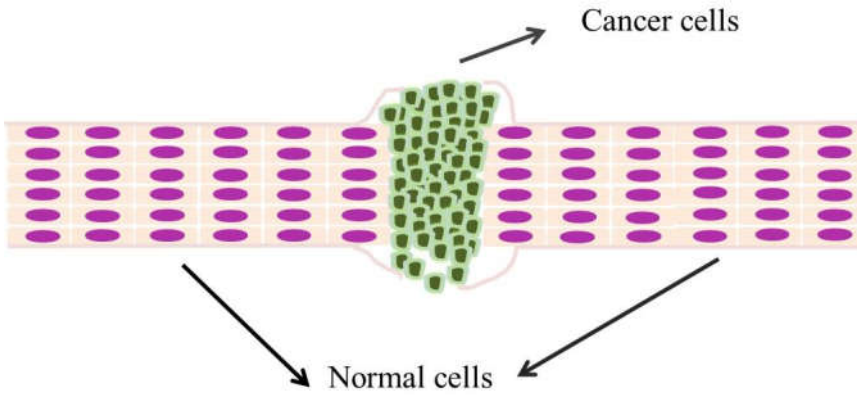

Fig. 5 Schematic illustration of normal and cancer cells

1.1.6. Computational study

Computational aspects of electronic structure of ceria and ceria based materials were studied by *ab initio* quantum mechanical Density functional theory (DFT) package of Venna *ab initio* simulation Package (VASP 5.4.1). Band structure, density of states (DOS) and charge density distribution of ceria and copper doped ceria were compared.

1.1.6.1. Band structure and density of states

The band structure of a solid means the range of energies that an electron associated within the solid and range of energies that are not associated with an electron. A solid consists of large number of atoms. The atomic orbitals overlap with each other to form molecular orbitals with different energies. Since the solid consists of large number of atoms ($N \sim 10^{22}$), there are very large number of orbitals and hence they are much closely spaced in energy (of the order of 10^{-22}eV). The closely space energy levels are considered as continuum, an energy band. In the formation of bands, most often valence electrons are treated. The width of the band depends on the extent of overlapping. Bands at higher energy are associated wider energies due to more overlap, but bands of core electrons are narrow due to the reduced level of overlap from the adjacent atomic orbital. Therefore, the band gaps generated by core electrons are large. In solids, the isolated atomic and molecular energy levels are broadening into bands of allowed energy state, which are separated by a forbidden energy gap. The qualitative description of an electronic conduction can be

predicted for materials with band gaps. For metals the forbidden energy band gap is negligible, while for semiconductors, the band gap is small (< 3eV) and for insulators have wide band gap (> 3eV). The determination of band gap of semiconductor materials is helpful to control its application in various fields. Another important thing associated with the determination of band gap is what is the Fermi energy of the semiconducting materials? Fermi energy is the energy of the highest occupied electronic state. Depending upon the nature of impurities present in the lattices, the value of Fermi energy state varies. For a typical solid, for each centimeter cube, about 10^{23} valence electrons contribute towards bonding. Hence the calculation of electronic structure of a solid must be a complex many-body problem, *i.e.*, exact wave function and energy of each electron would depend on those of each other. Plane wave DFT can be utilized to characterize electronic structure calculation of extended system. The estimation of band structure method could help to understand total energy of all possible structure of the crystal, Fermi energy, density of states, optical properties, electron transport, bulk modulus, wave function of the electron and elastic properties. On limiting the movement of electron into fewer dimensions, the density of the states is modified near the band gap. In order to understand this electronic density near the band edge, we need to calculate DOS of the structure. The method of DFT can find solution to this problem.

DFT calculation for electronic structure of a semiconducting material is performed using Blochl tetrahedron method for interpolation in k-space. This theorem states that the wave functions of

the one electron Hamiltonian can be chosen to have the form of a plane wave times a function with the periodicity of the lattice.

Solid state materials are crystalline with periodic lattice. The ground state electronic structure of a solid is periodic in nature because of the same charge distribution in each unit cell. Therefore the potential V(r) is also periodic with V(r+R) = V(r), where R is a vector joining the same point in two different unit cell[86]. The complete calculation of band structure of a solid indeed takes this periodic lattice, making use of symmetry operations forming space groups. The execution of Schrödinger equation for the crystal lattice results the wave function, known as Bloch waves.

$$\psi_{n\vec{k}}(\vec{r}) = e^{i\vec{k}.r} u_{n\vec{k}}(\vec{r}) \qquad (10)$$

Where *n* is the band index which simply numbers the energy bands, $\vec{k}$ is the wave vector which is related to the direction of motion of the electron in the crystal. The wave vector takes any value in the Brillouin zone corresponding to the crystal lattice of solid. The particular high symmetry points or direction in the Brillouin zone is labeled as Γ, Λ Δ, Σ, etc. The energy of the electron changes with change in $\vec{k}$.

1.1.6.2. Theory of band structure in crystal

Periodic lattice of a crystal structure can be identified by Bravais lattice, which in turn can be determined by reciprocal lattice. The reciprocal lattice encloses the periodicity in a set of three reciprocal

lattice vectors $(\vec{b_1}, \vec{b_2}, \vec{b_3})$. The periodic potential V(r) which exhibits same periodicity as the direct lattice can be represented as a Fourier series, whose only abiding components are those correlated with reciprocal lattice. So it can be represented as:

$$V(\vec{r}) = \sum_k V_k e^{i\vec{k}\cdot\vec{r}} \tag{11}$$

where $\vec{k} = m_1\vec{b_1} + m_2\vec{b_2} + m_3\vec{b_3}$ with m_1, m_2 and m_3 being integers.

Using this theory one can be able to predict the band structure of a solid material by executing several *ab initio* methods. Some of the theories to predict the band structures of crystalline materials are discussed in brief. This includes Kronig- Penney model[86], nearly free electron model[86], tight-binding methods[87], Korringa-Kohn-Rostoker (KKR) method[86] and DFT methods.

1.1.6.2.1. Nearly free electron model

The major assumptions of this approximation are similar to the free electron model. In this approximation, metal crystal consists of positively charged metal ion, whose valence electrons are free to move around the metal ions in such a way that they constitute an electron gas. Further, the electron-electron repulsion is ignored and the potential field inside the crystal is aroused due to the positive ions are completely homogeneous in nature. This theory assumes that the potential in the periodic lattice in many ways exhibits small perturbance to that seen from the electron in free space. Based on this, the band structure is calculated by considering crystal potential even

though slight difference is exists from the constant free space potential. This model works particularly for metallic materials, where the distance between the adjacent atoms are small. Therefore the overlap of atomic orbitals and potentials on the adjacent atoms are relatively large.

1.1.6.2.2. Kronig-Penney model

This model assumes that an electron in a ID- periodic potential. Periodic potential is considered as a periodic square waves. Using Schrödinger equation, the number of possible states that can be occupied by electrons can be determined. The major advantage of this theory is that the energy eigen values and eigen functions can be analyzed. Possible values of dispersion relations (*E vs k*) and electronic density of states can be determined.

1.1.6.2.3. Korringa-Kohn-Rostoker (KKR) method

Here atoms are considered as the non-overlapping spheres (*Muffin tin*). Inside the sphere, the potential experienced by the electron is spherically symmetric about the given nucleus. The remaining interstitial regions are associated with screening potential which is approximated as constant. The potential continuum of atom centered spheres and interstitial regions are implemented using this theory.

1.1.6.2.4. Tight binding methods

This method is opposite to the nearly free electron model. In this approximation, electrons in the periodic lattice behave in same fashion

as the assembly of constituent atoms. This model yields solution to the time independent single electron Schrödinger equation. Based on this method, excellent description of the energy spectrum for bound states up to rather small interval separations can be performed. This model work best for seeking of low lying energy levels, and less accurate for the higher level excited state properties[88].

1.1.6.2.5. Density Functional Theory

Nowadays, for the prediction of electronic structure of crystalline materials, the most useful tool is DFT[89]. It is not a model but a theory considering ground state electronic density of states. It is a microscopic first-principle theory of condensed matter physics for the solution of electron-electron many body problems. DFT calculations for the extended systems are performed based on the introduction of exchange correlation term in the functional of electronic density. The detailed description of the theory is given in section 1.1.6.4.

1.1.6.3. Density of states

Density of states describes the available occupied energy levels per unit energy range in each zone. It can be determined by dividing the volume of sphere having definite radius by the volume of a single state. Therefore, the number of available quantum state having energy levels between E and E+dE can be determined as follows:

$$\frac{dN}{dE} = 8\Pi m \frac{(2mE)^{1/2}}{h^3} V \qquad (12)$$

Where the quantity dN/dE is called the density of states

Metals are materials with non-zero DOS at the Fermi level. DOS can be separated into two regions: valence band and conduction band. Valence band is the collection of all occupied energy state, while the conduction band consists of unoccupied energy state. The band gap is the region where no DOS can be found. The slope of the DOS changes discontinuously in a number of places. These are known as van Hove singularities[89].

From the last fifteen years, the revolutionary aspects of computational simulations are based on the use of first principle approach for exploring the properties of condensed matters. Using this approach many of the properties of the material can be explored by solving the Schrodinger equation for the electrons of the atom, molecule, and assemblies of atoms in solids or liquids. The combination of molecular dynamics and electronic structure methods called *ab initio* molecular dynamics which can predict approximate solutions for the problems of many electron systems.

1.1.6.4. Density Functional Theory

DFT is the most powerful *ab initio* tool for the theoretical characterization of material properties in the condensed system than other methods. The principle behind it is based on the calculation of energy of the system from the electron density rather than wave functions[90]. This method is computationally less expensive giving most accurate results. The ancestors to DFT was Thomas-Fermi model, elaborated by Thomas and Fermi[91]. Hohenberg-Kohn (HK) introduced a DFT having firm theoretical foothold. This theory rests on two

fundamental physical laws without using free parameters. The first theorem states that "the ground state energy from a Schrödinger equation is a unique functional of the electron density". This theorem demonstrates the existence of one-to-one mapping between the ground state wave function and electron density. Second theorem established that ground state electron density which minimizes the energy of the overall functional is the true electron density with respect to the full solution of Schrödinger equation[89]. But the main drawback of this theory was it ignores the exchange correlation functional. So the accuracy of the solution of Schrödinger equation can be improved by applying parameters suited with experiment[92].

The main goal of DFT is to substitute many-body electronic wave functions with the electronic density as a principal part. The idea underlying approximate solution for a problem is based on the selection of suitable potential to the level of appropriate approximation chosen for solving Schrödinger equation. Hence Hohenberg-Kohn-Sham DFT using pseudo potential *i.e.*, Local Density Approximation (LDA) and Generalized Gradient Approximation (GGA) has been the most powerful electronic structure calculation for the condensed matters[89].

In the many-electron systems, there exist strong interaction between electron and nuclei. Hence the all electron calculation involving core electrons make large computational burden. Most of the physical and chemical properties of solid materials are described in terms of distribution of valence electrons. The core electrons are participated negligibly in chemical bonding. Besides, their overlapping

with core electrons of neighboring atoms is imperceptible. Hence the environments of core electrons are not changes with changing the chemical environ ments of atoms. This implies the advantages of “frozen-core approximation”. Core electrons are treated as “frozen”. This led to the consideration of calculation of less electrons and Eigen states of Kohn-Sham equation. So the total energy scale is largely reduced when the core electrons are neglected from the calculation, which in turn helps to make the calculation of difference in energy between atomic wave functions much more stable. The substitution of ionic core potential by pseudo potential leads to the nod less valence wave functions. So the pseudo potential approach with Kohn-Sham DFT is more economic method. In fact, pseudo potential is substituted with electron density which from a chosen set of core electrons with smoothed density is used to match various properties of the true iron core. As a result, the properties of the core electrons are fixed in this approximation model in all consequent calculations. The major pseudo potential approximations are LDA and GGA. LDA is the simplest approximation which uses only local density to describe the approximate exchange-correlation functional. It is based upon exact exchange energy for a uniform electron gas. The results obtained using LDA with DFT doesn’t give exact solution to the Schrödinger equation because of the incorporation of true-exchange correlation functional. GGA assumes a gradient in charge density. This approximation is more physically significant than LDA. Majority of the problems of the isolated molecules are defined by using GGA. But it doesn’t applicable for the delocalized electrons in the uniform electron gas. Presently there are large varieties of GGA functional to give information about

gradient of electron density. Majorly used functional for solid state calculations are Perdew-Wang (PW91) and Perdew-Bruke-Ernzerhof (PBE) functionals[89].

1.1.6.4.1. Kohn-Sham Equations

The most powerful electronic structure theories like Kohn-Sham DFT using pseudo potential *i.e.*, LDA and GGA have been implemented for the intractable many body problems of interacting electrons in a static external potential for the purpose of reducing to a problem of non-interacting electrons system[93]. Conceptually, pseudo potential includes the external potential and the effects of Coulomb interactions between the electrons, *e.g.*, the exchange and correlation interactions. Kohn-Sham equations have the form of Eq.13. The solution of this equation is for single electron wave function. The most common approach for the purpose of extended system is the expansion of single –particle Eigen states of the Kohn-Sham equation into a set of basis functions. The Schrödinger equation is utilized for the generation of expansion co-efficient, which then solved by various well established numerical methods.

$$\left[\frac{\hbar^2}{2m}\nabla^2 + V(r) + V_H(r) + V_{XC}(r)\right]\psi_i(r) = \varepsilon_i\psi_i(r) \qquad (13)$$

We consider extended periodic system with atoms at positions R+τ, where R represents a Bravais lattice vector locating a unit cell of the crystal and τ represents a basis vector giving the positions within the unit cell. The energy operator, Hamiltonian for the energy of the system is given by

$$\hat{H} = -\sum_{i=1}^{N} \frac{1}{2m} \nabla_i^2 + \sum_{i=1}^{N} V_{ion}(r_{i)} + \frac{1}{2} \sum_{i \neq j} v(r_i - r_j) + V_{I-I} \tag{14}$$

$$v(r) = \frac{e^2}{|r|} \tag{15}$$

where N= number of electrons at positions r_i with Coulomb potential as in Eq. 15

Static potential of the ion is formulated as

$$V_{ion}(r) = \sum_{m,s} V_{ion}^{(s)}(r - R_m - \tau_s) \tag{16}$$

and ion-ion repulsion is given by

$$V_{I-I} = \frac{1}{2} \sum_{mm'ss'} \frac{Z_s Z_{s'} e^2}{|R_m + \tau_s - R_{m'} - \tau_{s'}|} \tag{17}$$

Here, $\hbar = 1$, $2m = 1$, $e^2 = 2$ are Rydberg units, distance and energies are measured in Bohr and Rydberg units respectively. First three terms of Eq.13 is taken as the electron energy operator H_{el}

The ground state electronic energy E^{el} of the system can be represented as

$$E^{el} = T_0[n] + \int V_{ion}(r) n(r) dr + E_h[n] + E_{xc}[n] \tag{18}$$

where $T_0[n]$ represent kinetic energy, $E_h[n]$ stands for Hartee-Fock energy or classical interaction energy and E_{xc} is the exchange correlation energy of function n having density n(r).

Hence, Hartee-Fock energy can be described as

$$E_h[n] = \frac{1}{2}\int\int n(r)v(r-r')n(r')drdr' \tag{19}$$

Considering the number-conserving variations of the true ground state electron density $n_0(r)$, ground state electronic energy E^{el} is minimized.

$$\delta\left\{E^{el}[n] - \mu\int n(r)dr = 0\right\} \tag{20}$$

where, μ is the chemical potential of the electronic system.

Kohn-Sham potential of the many body problems is obtained by the self -consistent calculation of the following equations

$$\hat{H}\psi_i(r) = \left\{-\frac{1}{2m}\nabla^2 + V_{eff}(r;n)\right\}\psi_i(r) = E_i\psi_i(r) \tag{21}$$

where electron density

$$n(r) = \sum_{i=1}^{N} |\psi_i(r)|^2 \tag{22}$$

and $V_{eff}(r; n) = V_{ion}(r)+V_h(r; n)+V_{xc}(r; n)$ (23)

ψ_i is the ortho normal eigen functions and E_i is the Eigen value of the operator $\hat{H}$

Hartee and exchange correlation potential functions[94] are given as:

$$V_h(r;n) = \int v(r-r')n(r')dr' \tag{24}$$

$$V_{xc}(r;n) = \frac{\delta E_{xc}[n]}{\delta n(r)} \tag{25}$$

The exchange correlation functional is given by the sum of a correlation functional and exchange functional[93]. The assumption of LDA includes that exchange correlation energy of an electron at every point in space is equal to the exchange correlation energy per electron of a uniform electron gas. For the weakly correlated materials (semiconductors and simple metals) LDA gives most accurate result, while for studying bulk properties (elastic properties, bulk modulus etc.), GGA functional is more suitable. GGA[95] assumes a gradient in the charge density. The gradient correction to the exchange correlation functional results in the formation of spin densities and their gradients in the function. Hence GGA can modify the quality of the LDA results.

1.1.6.5. Pseudo potential plane wave approach

Nowadays, pseudo potential plane wave approach became the bench mark model of the DFT method for calculating the ground state electronic properties of the extended system. The advantage of plane wave approach is that it leads to very efficient numerical calculation of Kohn-Sham equation[96]. For the extended system, the employment of pseudo potentials are carried out by using relatively small set of plane waves. Plane waves are exact Eigen functions of the homogeneous electron gas. They are ortho normal and energy independent. Plane wave are not biased to any particular atom. In solving equation, plane wave basis set with certain cut off wave vector is used. The size of

basis set is fixed by the convergence calculation controlled by a single parameter. Besides, it can be verified by simply increasing the length of the cut off vector. In the plane wave based calculations, the coulomb potential of the electron-nucleus interaction in the core region are substituted with pseudo potentials. The introduction of pseudo potentials replaces the true valence wave functions, the so-called pseudo wave functions correctly match with exact true valence wave functions outside the ionic core region. It considers Hartee potentials and the total charge density of the system[96].

1.2. Review of the work

Thermal decomposition studies were started by the thinking of Wendlandt *et al*[97](1958). The thermal decomposition behavior of scandium, yttrium, lanthanum, cerium (III), neodymium, samarium, europium, gadolinium, holmium and erbium were carried out on thermo balance. Based on the thermal decomposition data, authors classified rare earth metal oxalates as three groups. First group containing La, Pr and Nd oxalates, second group involves: oxalates of Sm, Eu and Gd and third groups: Y, Ho and Er. First group oxalates undergoes decomposition without the formation of hydrates. Formation of oxides occurs at higher temperature than other two groups. Second group passes through the hydrates as intermediate. Temperature corresponding to the formation of oxide is lower than the first group. Third group oxalates go through the stable hydrate intermediate. Oxalates of Ce decompose at lower temperature than other rare earth oxalates. Wendlandt *et al*[98](1959) carried out the investigation regarding the thermal decomposition of heavier rare earth metal

oxalates of terbium, dysprosium, thulium, ytterbium and lutetium in a thermo balance. It was found that oxalates began to response to temperature from 45 to 60ºC. Thermal reaction passed through several intermediate formation and decomposition, and finally forms the oxide in the temperature range of 715 to 745ºC.

From the reports of Wendlandt *et al*[98] and Srivastava *et al*[99] (1960), it was found that thermal dehydration of cerous oxalate occurred at 50-220ºC, and the decomposition was completed at 360ºC. The small weight loss was observed at above 360ºC could be due to the occurrence of decomposition of small amount of carbonates which aroused from the decomposition of oxalates. Padmanabhan *et al*[100] (1960) reported the formation of a dihydrate. It was reported that the temperature range of loss of water from the lanthanum oxalate varies between 55ºC and 370ºC. The thermal decomposition reaction of Lanthanum oxalate (La-Ox) starts at 400ºC, and then at 550-750 ºC, a stage corresponding to the formation of oxy carbonate intermediate is reached. The final stage of decomposition was occurred from 740ºC and the weight loss became constant at 840ºC corresponding to the formation of La_2O_3. Subba Rao *et* al[101](1965) brought out the mechanism of thermal decomposition of oxalates of La, Ce, Nd and Pr *via* TG from the temperature 30-1100ºC both in air and CO_2 atmosphere. It was disclosed that under CO_2 atmosphere, the delayed nucleation and slow growth rate was became the reason for the delayed nature of the reaction. It was suggested by the authors that cerous oxalate starts dehydration above 150ºC and continue the reaction at about 275ºC, where the decomposition of oxalates starts to occur. At

about 375ºC, sharp weight loss (51.2%) was observed and then weight loss (52.5%) was remained constant at 550 ºC. It was discussed by the authors that even though the mechanism of decomposition was similar in the CO_2 atmosphere, the reaction followed with slowest steps. In CO_2 atmosphere, the decomposition was started at 325 ºC. Sharp break in the weight loss at 450ºC was corresponds to the formation of intermediate $Ce_2O_3.CO_2$, but this formation of intermediate is relatively less stable to be resolvable in the atmosphere of air. In the CO_2 condition, after 650ºC onwards, the weight loss remains constant. Along with cerous oxalate, Subba Rao *et al*[101] also carried out the establishment of thermal decomposition mechanism of oxalates of La, Pr and Nd both in the atmosphere of air and CO_2. It was concluded that lanthanum oxalate takes the removal of water in the range of 100-300ºC without any indication of intermediate hydrate. Thermal decomposition of praseodymium oxalate undergoes with similar fashion to the La-Ox in air. It follows through the formation of oxy carbonate intermediate and finally the formation of Pr_6O_{11} in the temperature range of 550-650ºC. Moreover, these authors also discussed the thermal decomposition behavior of Neodymium oxalate. The dehydration was occurred rapidly in the temperature range of 100-350ºC. The decomposition stage corresponding to the formation of Nd_2O_3 occurs in the temperature range 700-740ºC. Hence the authors concluded that except cerous oxalate, oxalate of Pr, La and Neodymium undergoes thermal decomposition reaction through the formation of oxy carbonate intermediate ($M_2O_3.CO_2$). The decomposition of the concerned oxalates was found to be delayed and sluggish in CO_2 atmosphere.

Agarwala *et al*[102](1961) brought out the investigation regarding the kinetics of decomposition of yttrium, cerous and zirconium oxalates *via* thermo gravimetrically and differential thermo gravimetry. Moosath *et al* [103](1963) described thermal decomposition behavior of oxalates of La, Pr and Nd on a Stanton thermo balance, and shown that these form a group based on their concerned process. These oxalates, before giving the final oxide product, yield basic carbonates, which are stable. The decomposition starts after the completion of dehydration rapidly, indicating the unstable nature of anhydrous oxalate. These authors studied about thermal decomposition behavior of oxalates of Sm, Eu, Gd, Tb and Dy and disclosed that no weight level corresponding to the hydrated intermediate was observed in the thermo gravimetric analysis. They also discussed that basic carbonate intermediate did not formed before the formation of oxide at higher temperature 690-720ºC[104]. Thermal behavior of heavier rare earth oxalates of Ho, Er, Tm, Yb, Lu, and Y were studied on a Stanton thermo balance and posted that dehydration of oxalates at lower temperature occurs through the formation of stable dihydrate in the temperature range of 230-330ºC. Also they confirmed that these oxalates decomposed to form the final product oxide (680-700ºC) without any stable intermediate[105]. Group IV oxalates (Ce, Th) upon thermal decomposition shows anomalous behavior with respect to each other, but exhibited major difference from the decomposition behavior of other oxalates[106]. De Almeida *et al*[107](2012) postulated new insights regarding the thermal decomposition behavior of cerium oxalate under inert and oxidizing atmosphere. It was viewed as a resemblance to the thoughts of Subba Rao *et al*[101], regardless of the atmosphere,

dehydration occurs at about 170ºC without any intermediate hydrate, but thermal decomposition behavior is entirely different in both air and argon atmosphere. Under air, the decomposition takes place in one step between the temperature 270 and 450ºC, releasing CO_2, whereas in argon, the decomposition occurs in two step between the temperature 350 and 800ºC with the release of CO and CO_2. Gabal *et al*[32] (2012) synthesized CeO_2 nano powder *via* thermal decomposition of cerium oxalate. Thermal decomposition behavior was studied through DTA-DTG-TG measurements in air. They observed majorly two weight loss steps in the temperature region of 60-160 and 270-350ºC. The first weight loss step with a broad endothermic DTA peak is associated with loss of 10 water molecules of $Ce_2(C_2O_4)_3.10H_2O$, forming anhydrous oxalate. Literatures in 1960's reported that anhydrous oxalate is very unstable and hence it undergoes rapid decomposition. On contrary to this, Gabal *et al*[32] disclosed that anhydrous cerium oxalate is stable up to 270ºC, which undergoes exothermic decomposition at 350ºC to form ceria nanoparticle. They calculated kinetic parameters for each thermal decomposition stage of precursor oxalate.

Up to now, there are few reports regarding thermal decomposition of mixed rare earth metal oxalates. Thermal decomposition of cerium oxalate and mixed cerium–gadolinium oxalate was studied. The corresponding mixed oxide $(CeO_2)_{0.9}(Gd_2O_3)_{0.1}$ is prepared by calcination[108]. Ubaldini *et al*[109] investigated the thermal properties of mixed cerium–gadolinium oxalate and found that their dehydration stages are similar to that of

gadolinium oxalate. Effect of additives to the precursor salt significantly governs the rate of decomposition. Selection of additives which cause to decrease the *Ea* and increase the rate of process and its separation from the product is most considered. Furuichi *et al*[110] studied the effect of transition metal oxide α-Fe_2O_3 additive on the thermal decomposition of salts of halogen oxoacids, oxalates, azide, permanganate and oxides by gas-flow type DTA and X-ray diffraction pattern. It was shown that α-Fe_2O_3 exhibited remarkable catalytic effect on the decomposition of halogen oxoacids, but it didn't show any effect on other salts. The effect of ferro spinel additive Cd_{1-x} Co_x Fe_2O_4 (x = 0.0, 0.5 and 1.0) on kinetics and mechanism of thermal decomposition of lithium oxalate was studied[111]. It was found that with increasing the concentration of cobalt, the rate of thermal decomposition was enhanced with x in the order 0.0 < 0.5 < 1.0. John *et al*[112] explored the effect of semi conducting metal oxides CuO and TiO_2 on the thermal decomposition of sodium oxalate. It was suggested that regardless of n-type or p-type oxide, both CuO and TiO_2 enhanced the rate of thermal decomposition at lower concentration (1 wt %), whereas suppressed the rate at higher concentration because of the adsorption of CO, one of the byproduct. The effect of additives CuO, MnO_2 and TiO_2 on thermal decomposition kinetics of KIO_4 to KIO_3 was investigated[113]. These oxides showed remarkably little effect on the rate of decomposition except with concentration of oxides 10 wt%, when observed small decrease of rate.

The multistep mass loss behaviors of solids are controlled by physico-geometrical constraints which may occur due to the changes in

reaction conditions as the reaction advances[114]. In thermally stimulated processes, surface product layer is formed in the early stages of the reaction. The occurrence of geometrical restrictions between the surface product layer and the inward advancement of the reaction interface generated at the boundary between surface product layer and internal reactant[24]. There are numerous works regarding the establishment of kinetic parameters of partially overlapped thermal decomposition processes. Koga *et al*[115] investigated the kinetic parameters responsible for the thermal degradation of ploy (L-lactic acid) *via* multistep kinetic approach. Using the similar methodology, kinetics of formation of Ag from Ag_2CO_3 was carried out[22].

Even though large numbers of investigations regarding the multistep kinetic behavior of solid state materials are established, solid state decomposition kinetics of hydrated cerium oxalate through multistep kinetic approach were not evaluated. So the authors interested to find out the effect of cationic dopant, nano semiconducting metal oxides, ferrites and oxalates upon the thermal behavior as well as its kinetics for the formation of ceria nanoparticles.

Potential growth of the ceria nano particle due to the unique physical and chemical properties, they possessed wide variety of applications in material science fields including catalysis, sensors, control of pollutants, etc. The emergence of the nano particles became great hazards to human health. This became reason for the researchers to rethink about the unknown biological effects underlying the nanoparticles.

Chen *et al*[116] (2008) made comparative study on the cytotoxicity of metal oxide nano particles of Fe_2O_3, CuO and ZnO and their metal ion counter parts (Fe^{3+}, Cu^{2+} and Zn^{2+}) towards human SH-SY5Y neuroblastoma and H4 neuroglioma cells. For the purpose, they taken the test samples of concentration range of range of 0.01–100 mM for 48h, under the cell culture conditions: 95% O_2, 5% CO_2, 85% humidity, 37ºC. Based on the cell viability test of nanoparticles and their metal ion counter parts, the most striking results were obtained for CuO. Significant cell death was observed for both H4 and SH-SY5Y cell lines. While the toxic effects of Fe_2O_3 and ZnO were found to be marginal. Based on the evidence of their data, they argued the complex nature of neurotoxic response and hence they justified further through *in vivo* studies.

Wang et al[117](2011) investigated the mechanism of *in vitro* cytotoxicity of metal oxide nano particles (ZnO, TiO_2, CuO and Co_3O_4) using catfish primary hepatocytes and human HepG2 cells. It was proved that CuO and ZnO exhibited significant toxicity in both HepG2 cells and catfish primary hepatocytes. The evidences verified that HepG2 cells are more sensitive than catfish primary hepatocytes towards the toxicity imposed by metal oxide nanoparticle. The authors arranged the tested metal oxides in the increasing order of their toxicity as follows: $TiO_2 < Co_3O_4 < ZnO < CuO$. They reached into the conclusion giving mechanism for the toxicity imposed by nano particle in such a way that both ROS mediated cell death and damages to cell and mitochondrial membranes accounts for it.

Wang *et al*[83](2013) explored the possibility of cuprous oxide

nano particle for curing of melanoma and metastatic lung tumor based on B16-F10 mouse melanoma cells through both *in vitro* and *in vivo* models. The analysis was interpreted as cuprous oxide nano particle significantly reduced the growth of melanoma cell, inhibited the metastasis of B16-F10 cells and enhanced the survival rate of tumor bearing mice. As the nanoparticles are cleared from the organs rapidly, it causes to little systemic toxicity. Activity of cuprous oxide nano particle begins through the mitochondrion- mediated apoptosis pathways, it results in the release of cytochrome C from the mitochondrion and activated caspase-3 and caspase-9 after the nano particle entered the cells.

Ivask *et al*[118](2015) searched the cytotoxicity of nano particles of oxides of Al, Mg, Si, Mn, Cu, Fe, Ti, Co, W, Sb and Zn) towards three cell lines such as human alveolar epithelial cells A549, human epithelial colorectal cells Caco2 and murine fibroblast cell line Balb/c 3T3. For three cell lines, both nano particle and metal ion counterpart contribute comparative toxicity. Based on the analysis, the authors discussed that six metal oxides (oxides of Fe, Al, Mg, Si, Ti and W) did not show any toxic effect below100 μgmL^{-1}). For five metal oxides, the averaged 24h IC_{50} value was found for three cell lines were 16.4 (Cu), 22.4 (Zn), 57.3 (Sb), 132.3 (Mn) and 129 μgmL^{-1} (Co). The authors argued that oxides of Cu, Zn and Sb exposed the toxicity by releasing metal ions; whereas ROS mediated cytotoxicity was performed by oxides of Mn and Co.

Titma *et al*[119](2016) studied the *in vitro* cytotoxicity exhibited by antimony, copper, cobalt, manganese, titanium and zinc oxide nano

particle towards the alveolar and intestinal epithelial barrier cells. Here they executed time dependent toxicity of Nps (24h & 9 days incubation). The short term monitoring of incubation of Caco2 & A549 cells with 100 μgmL^{-1} of Nps, Sb_2O_3, Mn_3O_4 and TiO_2 Nps didn't show any toxic effect, but Co_3O_4 and ZnO shown moderate effect, while, CuO Nps exhibited toxicity below 100 μgmL^{-1}. Upon long term monitoring, both Mn_3O_4 and Sb_2O_3 displayed remarkably enhanced toxicity. Authors rechecked the analysis with trans-epithelial electrical resistance (TEER) measurements and concluded that Caco2 cells were more sensitive towards the toxic effects of Nps. This assay resulted that more toxic effect was by Sb_2O_3 Nps.

Rajiv *et al*[120](2016) made comparative assay on the cytotoxicity and genotoxicity of Co (II)&(III) oxides, Fe(III) oxides, silicon dioxide and aluminum oxide Nps towards the human lymphocytes via *in vitro* model. Short term exposure of human lymphocytes cell lines with Nps shows that Co_3O_4 Nps exhibited decrease in cell viability and increase in cell membrane damage. The reason for toxicity was ascribed due to the oxidative stress induced by ROS, lipid peroxidation, depletion of catalase, reduced glutathione and super oxide dismutase. In the concerned work, Al_2O_3 exposed least DNA damage. The difference in the antioxidant properties showed DNA damage and chromosomal aberrance in human lymphocytes.

Asati *et al*[59](2010) investigated that cerium oxide nano particle has acquired great potential of antioxidant nature and radio protective agents in cancer therapy. They prepared various polymer coated ceria nanoparticle for the surface functionalization. They engineered

different surface charges (positive, negative and neutral) on the polymer coated ceria nano particle and their internalization and toxicity towards normal cells and cancer cell lines. Nano ceria carrying positive or neutral charge get into the most of the cell lines, but nano ceria with negative charge on the surface internalizes mostly in cancer cells. Depending upon the surface charge of nano ceria, it enters into different cell compartments. Depending upon the internalization and subcellular localization of ceria nano particle, it affects the nature of cytotoxicity of ceria nano particle. Significant toxicity is observed when nano ceria enters into lysosome of the cancer cells, but for the entrance to cytoplasm, no significant toxicity was observed.

Xue *et al*[121](2011) established radical scavenging properties of ceria by the *in vitro* simple photometric system. In the concerned reaction, when methyl violet treated with hydroxyl radical, its absorbance change. But in the presence of ceria, it protects methyl violet from the attack of OH radical by scavenging the radical by ceria. Hence radical scavenging ability of ceria is directly evidenced through the absorbance change.

Marzi *et al*[122](2013) proposed that cytotoxicity and genotoxicity of ceria nano particle towards different cell lines. They reached into the conclusion by executing long term and short term exposure *in vitro* assay towards A549, CaCo2 and HepG2 cell lines. Both cytotoxicity and genotoxicity assay was performed over a concentration range of 0.5 to 5000μgmL^{-1}. But it was found that no toxicity was observed by short term exposure, while long term exposure exhibited significant toxicity towards all the cancer cells. The

result also confirmed that the capacity of ceria nanoparticle to withstand the attack of oxidant like H_2O_2.

Clark *et al*[123](2013) explored H_2O_2 mediated apoptosis of Ti-doped CeO_2 in tumor bearing cells. This catalase like activity of Nps was dependent on the specific cellular environment. The authors described that the study would become the preliminary step for the clinical studies and for the generation of new nanoparticle therapy.

Gao *et al*[124](2014) reviewed on the novel therapeutic agent ceria Nps in cancer treatment. Based on the research data, authors argued that ceria Nps are able to show toxicity towards cancer cells, to inhibit invasion, and make sensitive the cancer cells to radiation therapy and chemotherapy. It exposes minimal toxicity to normal cells and protects cells from the generation of reactive oxygen species like OH radical. Since its affinity for scavenging hydroxyl radical, it protects the cells from the oxidative stress induced by the generation of ROS. It was shown that nano medicinal level of ceria was increased due to its dual capability as oxidant in cancer cell and antioxidant in normal cell. Hence it would become a substitute for reducing the harmful effect of the radiation therapy.

Kargar *et al*[125](2015) synthesized ceria Nps using bio based material such as egg white. *In vitro* cytotoxic studies of the synthesized nanoparticle towards the human periodontal fibroblasts cells exhibited concentration dependent toxicity with non-toxic effect up to the concentration range of $800\mu gmL^{-1}$.

Diaconeasa *et al*[126](2015) put forwarded that as ceria attained

radical scavenging properties, it find applications in the drug delivery or chemo therapy agents. Cytotoxicity and cellular uptake of nano ceria were tested on cultured human lung cancer cells. MTT assay resulted the cell viability test, exposed the toxicity expressed by the ceria nanoparticle. The results are dose dependent and exposure time decreased cell viability.

Gagnon *et al*[127](2015) reviewed on protective effect and toxicity of ceria. In the concerned area, reviewers' attention goes into that the protective effect of ceria aroused due to its inherent oxygen storage capacity. Hence it is able to uptake and release oxygen reversibly. This was the main cause of its entry to the biomedical applications. They suggested that toxicity of ceria Nps depends on synthesis condition, physical and chemical properties, surface properties, cell type, exposition method and various other features associated with it.

Nelson *et al*[128](2016) made another review regarding the antioxidant behavior of cerium oxide Nps in biology and medicine. This review entitled on mechanism for antioxidant behavior, radical scavenging process, designing and method of preparation of radical scavenging ceria Nps, illustration of antioxidant capacity of ceria from *in vitro* and *in vivo* models, regeneration and therapeutic applications and for the treatment of photoreceptor degeneration. Based on their review, they ensured that ceria nano particles have capabilities to become a substitute for the therapeutic agents for treating oxidative-stress and nitrosative-stress related diseases and disorders.

Joydeep *et al*[129](2017) performed nano ceria mediated drug delivery of doxorubicin. This was carried out *via* the apoptosis of ovarian cancer cell. *In vitro* analysis of DOX/CeO_2 proved higher cell proliferation inhibition and apoptosis compared with free DOX. They brought out the mechanism as that negatively charged ceria nanoparticle can couple with positively charged doxorubicin through the electrostatic interaction under the physiological condition resulting in the formation of doxorubicin-loaded nano ceria (DOX/CeO_2). This complex can behave as a superior drug for the cancer cell than free DOX taking the advantage of higher cellular uptake and fast release from the organ.

Khan *et al*[130](2017) made an evaluation regarding the *in vitro* cytotoxicity, biocompatibility and change in the expression of apoptosis regulatory protein induced by ceria nano crystals. Based on the Western blot assay, it was confirmed that ceria nano crystals directed to HT29 cancer cell lines varied the expression level of anti-apoptotic proteins Bcl2 and BclxL, whereas increased the expression level of Bax, PARP, and cytochrome c proteins. Specific ratios of Bax/Bcl2 protein are caused for cell death, which decides the death or life of particular cells with respect to an apoptosis stimulus. But higher ratios of Bax/Bcl2 robustly expressed inhibition of cellular resistance to apoptotic stimuli.

Up to now, large number of research regarding the cytotoxicity of ceria nanoparticles is performed. The main cause of its mechanism not yet understood. But the major reason for exhibiting the toxicity was argued that radical scavenging ability and antioxidant behavior. It can

reduce oxidative stress induced by the generation of ROS. Because of the inherited ability of oxygen storage capacity, it can uptake and release oxygen reversibly. Ceria act as oxidant for cancer cells whereas antioxidant for normal cell. Cytotoxicity of ceria nanoparticle depends on the synthesis condition, size and shape, surface charge, cell type, etc. In the present condition, we enquired how the presence of Cu^{2+} in the lattice of nano plates of ceria affected the cytotoxicity towards DLA (Dalton's Lymphoma Ascites cell) *in vitro*. We have prepared a series of oxides of Ce:Cu in different molar ratios *via* thermal decomposition of its oxalate.

Nolan *et al*[131](2005) studied the DFT calculations of bulk ceria and low index surfaces (111), (110) and (100). They contributed that the stabilities of the surfaces follows the order (111) > (110) > (100), whereas the surface relaxation pursued the inverse order. They analyzed the electronic properties of bulk and surfaces by means of charge, charge density and electronic density of states. They reminded that some partial ionic character in pure ceria along with covalent character. This confirmed that the Ce 4*f* states are above the Fermi level. On analyzing bulk and surface charge distribution, there appeared only small difference in the surface atoms when compared to bulk. DOS calculation of both shows major difference in the O *2p* and Ce *5d* states. They also contributed that DFT approach can't predict accurately the delocalization of electrons in Ce^{3+}, partially reduced ceria because of the strong correlational effect of Ce *4f* states. But the accurate prediction of electronic structure can be made within the

DFT+U formalism. They also found that the contribution of localization of Ce *4f* correctly predicted the defect surfaces.

Castleton *et al*[132](2007) made an examination on real space and electronic structure of oxygen vacancies in ceria with DFT+U approach using exchange correlational GGA and LDA. They performed several quantification schemes and found that the localization of the charge starts to be occurring at U ~ 3eV. The degree of localization of charge was reached to maximum at U ~ 6eV for LDA+U approach and U~5.5eV for GGA+U approach. They found that for higher U value the localization of charge is decreased since the transfer of charge to the nearest neighbors. Maximum localization of about 80-90% of the Ce *4f* charge was located on the two nearest neighboring Ce ions. They rechecked the properties of defect free ceria utilizing LDA+U with U = 3 – 4eV. But the agreement of theoretical prediction of band structure with experiments was observed at U = 7 – 8eV. The best description of electronic localization with GGA functional was found to be with correlation term U = 5eV.

Loschen *et al*[133](2008) performed plane wave DFT to investigate electronic structure of a series of CeO_2 Nps. They found that the strong correlation effect of 4*f* electron of Ce occurs due to the reduction of Ce^{4+} to Ce^{3+}. In order to account the correct structure of ceria nanoparticle, DFT method choosing exchange correlation functional GGA or LDA was not sufficient. Hence they introduced Coulomb repulsion term U (Hubbard effective term) was introduced with DFT. Thus, they described that DFT+U approach is more efficient method for studying electronic structure of molecules, clusters and

extended solids. The most stable cluster species is cuboctahedral $Ce_{13}O_{26}$. Based on the DFT+U method, it can be predictable that highly co-ordinated ceria have more number of Ce^{4+} state, while low co-ordinated ceria possessed largely the reduce state Ce^{3+}.

Zhang *et al*[134](2008) carried out a systematic study on the adsorption of Au atoms on the various ceria surfaces. They show the crucial importance of Ce *4f* states in the adsorption of Au atoms on the stoichiometric and reduced ceria surfaces. In the stoichiometric case (Ce^{4+}), Ce *4f* states (non-bonding) occupy above the Fermi level, whereas in the reduced (Ce^{3+}) case, the partially occupied 4*f* state due to the removal of oxygen atoms lye just below the Fermi level. While adsorption of Au on the stoichiometric ceria surfaces, 4*f* states act as electron acceptor causing to the stabilization of adsorbed Au atoms on the surfaces. Reduced ceria surface with partially occupied 4*f* sates behave as electron donor so as to stabilize adsorbed Au atoms. In the stoichiometric surfaces, the most preferred adsorption site for Au is on the bridge like site where two where Au directly binds with two oxygen atoms *via* O *2p- d* (Au) mixing. In the reduced surface with oxygen vacancies, the suitable site for adsorption is near vacancy position. They found that the binding energy for adsorption of Au is higher at stoichiometric surfaces than in the Ce vacancy site.

Branda *et al*[135](2010) investigated the interaction of Cu, Ag and Au atoms on the regular ceria surface (111) within the frame work of DFT+U using the exchange correlational LDA and GGA and compared the results with periodic surface slab model. The interaction of Cu and Ag based on all methods gave same qualitative description

of the stable active site with same order of stability and oxidized character of Cu and Ag on the surface of ceria. In the case of Au, the interactions are method dependent and due to the presence of nearly degeneracy between the solutions between cationic and neutral Au.

Tang *et al*[136](2012) made comparative studies on the adsorption behavior of Cu, Ag and Au atoms on the technologically important catalytic surfaces of ceria within the frame work of DFT+U. They generated a set of model configurations by placing metal atoms on the three surface sites, *viz*, on top of an O, an O bridge site and a Ce bridge site. Before doing optimization, small distortions in the selected Ce-O distance were imposed in order to explore the energies associated with reduction of Ce^{4+} to Ce^{3+} during the adsorption of metal. Further the charge redistribution of adsorbed ceria surface was confirmed by spin density isosurfces and site projected DOS. They reached into the conclusion that while adsorption, Cu and Au atoms are oxidized to $Cu^{2+}$and Au^{2+}. They pointed out that adsorption energies for O bridge site was higher at where the 2 Ce^{3+} are nearest neighbors exist, while for Ce bridge site, adsorption energies was higher for 3 Ce^{3+} nearest neighbors. They also found that CeO_2 exposed with (110) crystal plane exhibits higher adsorption energies than (111) crystal plane of ceria.

Jalborg *et al*[137](2014) calculated the electronic structure of super cells of $CeO_{2-\delta}$ within the frame work of DFT+GGA. The equilibrium properties such as lattice constants, bulk moduli and magnetic moments of super cells are well characterized with exchange correlational GGA. Electronic excitations are simulated by robust-total energy calculation for constrained states with atomic core holes or

valence holes. Non-magnetic insulator pristine ceria become magnetic when it is reduced by removing oxygen atoms. They put forwarded that in the ground state oxygen deficient ceria, the partially occupied 4*f* states lye near the Fermi level. The presence of 4*f* electrons have predominant role in realizing catalytic properties of ceria and related materials.

Kehoe *et al*[138](2011) examined the effect of divalent dopants on the reducibility and oxygen storage capacity of ceria using DFT. For this purpose, they utilized the range of divalent dopants and characterized their effects. Based on their investigations they proposed the blueprints for the choice of dopants to enhance the reducibility and oxygen storage capacity of an oxide catalyst. They generalized the selection of effective dopants by incorporating the following ideas that: (a) the ionic radius of the dopant ion should be small enough to adopt the alternative positions in the lattice, (b) the coordination of the dopant ion in the respective binary oxide should be lower than that of the host ion in order to create under coordinated or weakly bound oxygen ion, (c) in the case of transition metals, the effect of driving force of altered crystal field splitting, which can lead to alternate coordination.

Lu *et al*[139](2011) studied the effect of copper dopant into the ceria lattice and (111) surface of ceria utilizing *ab initio* quantum mechanical spin polarized density functional theory. They investigated the formation of oxygen vacancies and found that first oxygen vacancy is formed spontaneously while second is created easily in the doped system. Regardless of the number of oxygen vacancies in the lattice,

Cu is in +2 oxidation state and four coordinated in a close to planar structure. The formation energies for the oxygen vacancies are depend on charge compensation, structural relaxations and available Cu-O states. Formation energies for both first and second vacancies are smaller than that required for pure ceria (3.28eV). For the creation of first vacancy in the bulk-doped ceria, much larger decrease in energy (2.98eV) was found. This energy was attributed with 53% due to electronic effects and 47% due to large structural relaxation of doped system. For the creation of second oxygen vacancy, the energy needed was 0.89eV. This was attributed with 100% electronic effects.

Szabova *et al*[140](2013) studied the effect of Cu on stoichiometric and partially reduced ceria. It was observed that Cu adsorption on stoichiometric surface caused to the reduction, but on partially reduced surface it can regenerate partially oxidizing character of the ceria.

Vanpoucke *et al*[141](2014) studied the modification of the properties of ceria *via* aliovalent dopants Mg, V, Co, Cu, Zn, Nb, Ba, La, Sm, Gd, Yb and Bi to form fluorite type $Ce_{1-x}M_xO_{2-y}$ (where $0.00 \leq x \leq 0.25$) theoretically by means of DFT+U formalism. Lattice parameter, dopant radii, bulk moduli and thermal expansion co-efficient were calculated. The relative stability and oxygen vacancies of the solid solution were investigated. It was shown that the presence of oxygen vacancies in the doped system increased the lattice parameter whereas decreased the bulk moduli. They proposed that the defect formation energies are correlated with crystal and covalent radii of the dopant atoms. The introduction of aliovalent dopant exhibited

inverse relationship between change in thermal expansion coefficient and in bulk modulus. Different dopants impose differently in the ceria lattice. But the presence of oxygen vacancies in the doped system has much influence in the thermal expansion coefficient and bulk modulus. They proposed that bulk doping unfavorable with elements Cu, Co and Zn whereas favorable with La, Gd and Sm.

Again Vanpoucke *et al*[142](2014) studied the effect of group IV (a & b) elements (C, Si, Ge, Sn, Pb, Ti, Zr and Hf) as dopants to the ceria lattice within the frame work of DFT+U. They calculated the concentration dependent formation energies for the $Ce_{1-x}Z_xO_2$ where $0 \leq x \leq 0.2$. Based on their investigations, they proposed that a roughly decreasing formation energies with ionic radius. They compared the effect of IV a & b elements on the properties of ceria, and found that group IV elements are better suitable for surface modification, while group IV b elements for bulk properties. The influence of dopants on the mechanical properties such as thermal expansion co-efficient and bulk modulus were discussed. It was shown that group IV a elements causes to increase thermal expansion co-efficient, while IV b elements made a small decrease in thermal expansion co-efficient. The inverse relationship of bulk modulus and thermal expansion co-efficient are maintained. Their results of analysis revealed that not only valence shell electrons but also filled orbitals can bring the modifications to ceria.

Musa Alaydrus *et al*[143](2016) investigated the atomic and electronic properties of Ln-doped CeO_2 (Ln = La, Pr, Nd, Pm, Sm, Eu and Gd] and pointed out that the contribution of 4f electrons to the

cation-anion interaction. They contributed to the literature that effect of dopants on the stable configuration and energies of oxygen ion migration in the doped CeO_2. In order to compensate the localization effects of 4f electrons of all Ln dopants, strong correlation term Hubbard U correction were treated within the DFT+GGA frame work. This study revealed that the variable occupancy of 4f states was found to be important for early Ln elements to produce covalent interactions since those contain number of empty 4f orbitals. The covalent character of 4*f* electrons are generated by the delocalization due the hybridization of O 2p states. The presence of covalent interactions in Ln doped ceria essentially affects its oxygen vacancy formation and migration.

Chagas *et al*[144](2016) performed both experimental and theoretical investigations on the effect of doping concentration of Ni and Cu to the ceria lattice. From the experimental point of view, it was noticed that Ni forms solid solution through isomorphic substitution of Ce sites, this was retained around concentration of 9-10% and above this limit it reached into saturation and hence the extra Ni atoms doesn't affect the crystal structure of ceria. This was due to the formation of NiO phases as surface domain. The introduction of small percentage of Cu to the solid solution of $NiCeO_\delta$ neither disturbed the bulk structure of solid solution. This confirms the formation segregated phases of CuO domains. Theoretically these were proven by calculating the formation energies of solid solution. It was analysed that small addition of Ni can easily generate the solid solution, while arising the concentration above 6.25–9.37 Ni% increased the formation

energy. The same effect was also observed in the doping of larger percentage of Cu to the Ni-Ce solid solution. Moreover, the strong contraction of lattice parameter was observed with larger concentration above 6.25–9.37 %.

1.3. Aim and scope of the work

The present investigation aims at synthesis, characterization of ceria and ceria based nano materials *via* multistage thermal decomposition strategy and allows the evaluation of kinetic characteristics of the thermal events responsible for the process. The need and significance of various additives such as oxalate, oxide and dopant in various concentrations on thermal decomposition behavior and kinetics of hydrated cerium oxalate are forecasted. No work on alterations in thermal decomposition behaviors of cerium oxalate caused by the surface morphology of oxalate precursor has been reported so far. This study covers how the anticancerous properties of nano ceria are effectuated with surface morphology and copper dopant concentrations. The derivation of electronic structure of ceria and ceria based materials still exist with experimental limitations. So, the theoretical studies by the use of plane wave density functional theory with proper exchange correlation functional are an upcoming domain.

1.4. References

1. Hannay NB. *Treatise in Solid State Chemistry – Change of States, Vol. 4, Plenum Press, New York.*; 1976.

2. Ropp RC. *Solid State Chemistry, Elsevier, Amsterdam,.*; 2003.

3. Kujirai T, Akahira T. Effect of temperature on the deterioration of fibrous insulating materials. *Sci Pap Inst Phys Chem Res*. 1925;2:223-252.

4. Tang TB, Chaudhri MM. Analysis of isothermal kinetic data from solid-state reactions. *J Therm Anal*. 1979;17:359-370.

5. Tang TB, Chaudhri MM. Analysis of dynamic kinetic data from solid-state reactions. *J Therm Anal*. 1980;18:247-261.

6. Sestak J, Satava V, Wendlandt WW. The study of heterogeneous processes by thermal analysis. *Thermochim Acta*. 1973;7:333.

7. Khawam A, Flanagan DR. Complementary use of model-free and modelistic methods in the analysis of solid-state kinetics. *J Phys Chem B*. 2005;109:10073-10080.

8. Coats AW, Redfern JP. Kinetic parameters from thermogravimetric data. *Nature*. 1964;201:68-69.

9. Sbirazzuoli N, Girault Y, Elégant L. Simulations for evaluation of kinetic methods in differential scanning calorimetry. Part 3 — peak maximum evolution methods and isoconversional methods. *Thermochim Acta.* 1997;293:25-37.

10. Kissinger HE. Reaction kinetics in differential thermal analysis. *Anal Chem*. 1957;29:1702−1706.

11. Ozawa T. A new method of analyzing thermo gravimetric data. *Bull Chem Soc Jpn*. 1965;38:1881-1882.

12. Flynn JH, Wall LA. Direct method for the determination of activation energy from thermo gravimetric data. *Polym Lett*. 1966;4:323-328.

13. Ozawa T. Applicability of Friedman plot. *J Therm Anal*. 1986;31:547–551.

14. Gotor FJ, Criado JM, Malek J, Koga N. Kinetic analysis of solid-state reactions: the universality of master plots for analyzing isothermal and

non-isothermal experiments. *J Phys Chem A*. 2000;104:10777–10782.

15. Liqing L, Donghua C. Application of iso-temperature method of multiple rate to kinetic analysis: Dehydration for calcium oxalate monohydrate. *J Therm Anal Calorim*. 2004;78(1):283-293.

16. Budrugeac P. An iterative model-free method to determine the activation energy of non-isothermal heterogeneous processes. *Thermochim Acta*. 2010;511:8-16.

17. Chunxiu G, Yufang S, Donghua C. Comparative method to evaluate reliable kinetic triplets of thermal decomposition reactions. *J Therm Anal Calorim*. 2004;76:203-216.

18. Pérez-Maqueda LA, Criado JM. Accuracy of Senum and Yang's approximations to the Arrhenius integral. *J Therm Anal Calorim*. 2000;60:909-915.

19. Zhipeng C, Qian C, Sen L, et al. Application of isoconversional calculation procedure to non-isothermal kinetic study: III. thermal decomposition of ammonium cobalt phosphate hydrate. *Thermochim Acta*. 2012;543:205-210.

20. Wada T, Nakano M, Koga N. Multistep kinetic behavior of the thermal decomposition of granular sodium percarbonate : hindrance effect of the outer surface layer. 2015;2:0-11.

21. Nakano M, Wada T, Koga N. Exothermic behavior of thermal decomposition of sodium percarbonate : kinetic deconvolution of successive endothermic and exothermic processes. *J Phys Chem A*. 2015;119:9761-9769.

22. Yoshikawa M, Yamada S, Koga N. Phenomenological interpretation of the multistep thermal decomposition of silver carbonate to form silver metal. *J Phys Chem C*. 2014;118:8059-8070.

23. Koga N, Goshi Y, Yamada S, Pe´rez-Maqueda LA. Kinetic approach to partially overlapped thermal decomposition processes; co-precipitated zinc carbonates. *J Therm Anal Calorim*. 2013;111:1463-1474.

24. Nusrath K, Muraleedharan K. Effect of Ca(II) on the multistep kinetic behavior of thermally induced oxidative decomposition of cerium(III) oxalate to CeO_2(IV). *J Anal Appl Pyrol*. 2016;120:379-388.

25. Koga N. Ozawa ' s kinetic method for analyzing thermoanalytical

curves. *J Therm Anal Calorimrm*. 2013;113:1527-1541.

26. Shippey TA. Vibrational studies of anhydrous lithium, sodium and potassium oxalates. *J Mol Struct*. 1980;67:223-233.

27. Shippey TA. Vibrational studies of calcium oxalate monohydrate (whewellite) and an anhydrous phase of calcium oxalate. *J Mol Struct*. 1980;63:157-166.

28. Wright CS, Fisher C, Thompsett D, Walton RI. Hydrothermal synthesis of a cerium (IV) pyrochlore with low-temperature redox properties. *Angew Chem Int Ed*. 2006;45:2442–2446.

29. Corradi AB, Bondioli FB, Ferrari AM, Manfredini T. Synthesis and characterization of nano sized ceria powders by microwave-hydrothermal method. *Mater Res Bull*. 2006;41:38-44.

30. Christel LR, Jeffrey WL, Erik ML, et al. Sol−gel-derived ceria nano architectures: synthesis, characterization, and electrical properties. *Chem Mater*. 2006;18:50-58.

31. Ali B, IZ M, Julian E, Lata P. Microemulsion-based synthesis of CeO_2 powders with high surface area and high-temperature stabilities. *Langmuir*. 2004;20:11223-11233.

32. Gabal MA, Elroby SAK, Obaid AY. Synthesis and characterization of nano-sized ceria powder via oxalate decomposition route. *Powder Technol*. 2012;229:112-118.

33. Miyazaki H, Kato JI, Sakamoto N, Wakiya N, Ota T, Suzuki H. Synthesis of CeO_2 nanoparticles by rapid thermal decomposition using microwave heating. *Adv Appl Ceram*. 2010;109:123-127.

34. Payakgul W, Mekasuwandumrong O, Pavarajarn V, Praserthdam P. Effects of reaction medium on the synthesis of TiO_2 nanocrystals by thermal decomposition of titanium (IV) n-butoxide. *Ceram Int*. 2005;31:391-397.

35. Sungmin C, Eunseuk P, Minsu K, Jongsoo J. Photocatalytic degradation of methylene blue with TiO_2 nanoparticles prepared by a thermal decomposition process. *Powder Technol*. 2010;201:171-176.

36. Jitlada K, Wansiri P, Kosin P, Piyasan P, Alisa SV, Varong P. Activity of nanosized titania synthesized from thermal decomposition of titanium(IV) n-butoxide for the photocatalytic degradation of diuron. *Sci Technol Adv Mater*. 2005;6:290-295.

37. L'vov BV. Kinetics and mechanism of thermal decomposition of nickel, manganese, silver, mercury and lead oxalates. *Thermochim Acta*. 2000;364:99 −109.

38. Dollimore D, Griffiths DL, Nicholson D. The thermal decomposition of oxalates. Part II. thermogravimetric analysis of various oxalates in air and in nitrogen. *J Chem Soc*. 1963;26:17-23.

39. Bose S, Sahu K, Bhatta D. Effect of gamma-irradiation on the thermal decomposition of barium oxalate hemihydrate. *J Radioanal Nucl Chem*. 1994;181:441-446.

40. Alshehri SM, Monshi MAS, El-Salam NMA, Mahfouz RM. Kinetics of the thermal decomposition of γ-irradiated cobaltous acetate. *Thermochim Acta*. 2000;363:61-70.

41. James C, Samuel J. The effect of gamma-irradiation on the thermal decomposition of anhydrous cadmium nitrate. *J Radioanal Nucl Chem*. 2003;258:665-668.

42. Nair SMK, Malayil KK. The thermal decomposition of γ-irradiated lead nitrate by dynamic thermogravimetry. *Thermochim Acta*. 1988;127:275-283.

43. Dollimore D. The thermal decomposition of oxalates. a review. *Thermochim Acta*. 1987;117:331-363.

44. Rossberg M, Khairetdinov EF, Linke E, Boldyrev VV. Effect of mechanical pretreatment on thermal decomposition of silver oxalate under nonisothermal conditions. *J Solid State Chem*. 1982;41:266-271.

45. Gusev EA, Dalidovich SV, Shandakov VA, Vecher A. Thermal decomposition of copper(II), nickel(II), cobalt(II) and iron(II) oxalates in self-generated atmospheres. *Thermochim Acta*. 1985;89:391-394.

46. Freeberg FE, Hartman KO, Hisatsune IC, Schempf JM. The kinetics of calcium oxalate pyrolysis. *J Phys Chem*. 1967;71:397– 402.

47. Sun C, Li H, Zhang H, Wang Z, Chen L. Controlled synthesis of CeO_2 nanorods by a solvothermal method. *Nanotechnology*. 2005;16:1454-1463.

48. Trovarelli A. Catalytic properties of ceria and CeO_2-containing materials. *Catal Rev Sci Eng*. 1996;38:439-520.

49. Laha SC, Ryoo R. Synthesis of thermally stable mesoporous cerium oxide with nanocrystalline frameworks using mesoporous silica templates. *Chem Commun*. 2003:2138-2139.

50. Khadse VR, Sharada T, Patil KR, Pradip P. Humidity-sensing studies of cerium oxide nanoparticles synthesized by non-isothermal precipitation. *Sens Actuators B Chem*. 2014;203:229-238.

51. Larachi F, Pierre J, Adnot A, Bernis A. Ce 3d XPS study of composite $Ce_xMn_{1-x}O_{2-y}$ wet oxidation catalyst. *Appl Surf Sci*. 2002;195:236-250.

52. Hu C, Zhang Z, Liu H, Gao P, Wang ZL. Direct synthesis and structure characterization of ultrafine CeO_2 nanoparticles. *Nanotechnology*. 2006;17:5983-5987.

53. Dong-En Z, Xiao-Jun Z, Xiao-Min N, Ji-Mei ZH-G, Hua-Gui Z. Fabrication of novel threefold shape CeO_2 dendrites: optical and electrochemical properties. *Chem Phys Lett*. 2006;430:326–329.

54. Pavel J, Tomas HK, Martin K, Jakub E, Martin S. Thermal treatment of cerium oxide and its properties: adsorption ability versus degradation efficiency. *Adv Mater Sci Eng*. 2014;2014:1-12.

55. Zholobak NM, Ivanov VK, Shcherbakov AB, et al. UV-shielding property, photocatalytic activity and photocytotoxicity of ceria colloid solutions. *J Photochem Photobiol B Biol*. 2011;102:32-38.

56. Wason MS, Colon J, Das S, Seal S, Turkson J, Zhao J BC. Sensitization of pancreatic cancer cells to radiation by cerium oxide nanoparticle-induced ROS production . *Nanomedicine*. 2013;9:558-569.

57. Grulke E, Kenneth R, Matthew B, Xing H, Alastair C, Sudipta S. Nanoceria: factors affecting its pro- and anti-oxidant properties. *Environ Sci Nano*. 2014;1:429-444.

58. Kumar A, Das S, Munusamy P, et al. Behavior of nanoceria in biologically-relevant environments. *Env Sci Nano*. 2014;1:516-532.

59. Asati A, Santra S, Kaittanis C, Perez JM. Surface-charge-dependent cell localization and cytotoxicity of cerium oxide nanoparticles. *ACS Nano*. 2010;4:5321-5331.

60. Alili L et al. Downregulation of tumor growth and invasion by redox-active nanoparticles. *Antioxid Redox Signal*. 2013;19:765-778.

61. Kenji H, Kazutoshi S, Hiroshi O, Soichiro S, Yoshihiro H. Synthesis and sintering of rare-earth-doped ceria powder by the oxalate co-precipitation method. *J Mater Res*. 1999;14:957-967.

62. Zhang Y, Andersson S, Muhammed M. Nanophase catalytic oxides : I. synthesis of doped cerium oxides as oxygen storage promoters. *Appl Catal B Environ*. 1995;6:325-337.

63. Moreno M, Bergamini L, Baronetti GT, Laborde MA, Marino FJ. Mechanism of CO oxidation over CuO/CeO_2 catalysts. *Int J Hydrog Energ*. 2010;35:5918-5924.

64. Desyatykh IV, Vedyagin AA, Mishakov IV, Shubin YV. CO oxidation over fiberglasses with doped Cu-Ce-O catalytic layer prepared by surface combustion synthesis. *Appl Surf Sci*. 2015;349:21-26.

65. Desyatykh IV, Vedyagin AA, Kotolevich YS, Tsyrul'nikov PG. Preparation of $CuO\text{-}CeO_2$ catalysts deposited on glass cloth by surface self-propagating thermal synthesis. *Combust Explos Shock Waves*. 2011;47:677-682.

66. Qiu N, Zhang J, Wu Z, Hu T, Liu P. Tuning ceria nanocrystals morphology and structure by copper doping. *Cryst Growth Des*. 2012;12:629-634.

67. Sun Y, Xia Y. Shape-controlled synthesis of gold and silver nanoparticles. *Science* 2002;298:2176-2179.

68. Lin G, Yun LJ, Huibin X, Paul S, Ziyu W. Regularly shaped, single-crystalline ZnO nanorods with wurtzite structure. *J Am Chem Soc*. 2002;124:14864-14865.

69. Fei Y, Jingjing W, Wei L, Jinxin G, Yanzhao Y. Copper doped ceria nanospheres: surface defects promoted catalytic activity and a versatile approach. *J Mater Chem A*. 2014;2:5662-5667.

70. Ren Z, Peng F, Li J, Liang X, Chen B. Morphology-dependent properties of Cu/CeO_2 catalysts for the water-gas shift reaction. *Catalysts*. 2017;7:48.

71. Huang XS, Sun H, Wang LC, Liu YM, Fan KN, Cao Y. Morphology effects of nanoscale ceria on the activity of Au/CeO_2 catalysts for low-temperature CO oxidation. *Appl Catal B Environ*. 2009;90:224-232.

72. Tana WS, Zhang M, Juan L, Li H, Li Y, Shen W. Morphology-

dependent redox and catalytic properties of CeO_2 nanostructures: nanowires, nanorods and nanoparticles. *Catal Today*. 2009;148:179-183.

73. Aneggi E, Wiater D, De Leitenburg C, Llorca J, Trovarelli A. Shape-dependent activity of ceria in soot combustion. *ACS Catal*. 2014;4:172-181.

74. Désaunay T, Bonura G, Chiodo V, et al. Surface-dependent oxidation of H_2 on CeO_2 surfaces. *J Catal*. 2013;297:193-201.

75. Gamarra D, López Cámara A, Monte M, et al. Preferential oxidation of CO in excess H_2 over CuO/CeO_2 catalysts: Characterization and performance as a function of the exposed face present in the CeO_2 support. *Catal Today*. 2014;229:104-113.

76. Si R, Flytzani-Stephanopoulos M. Shape and crystal-plane effects of nanoscale ceria on the activity of $Au-CeO_2$ catalysts for the water-gas shift reaction. *Angew Chemie - Int Ed*. 2008;47:2884-2887.

77. Yao SY, Xu WQ, Johnston-Peck AC, et al. Morphological effects of the nanostructured ceria support on the activity and stability of CuO/CeO_2 catalysts for the water-gas shift reaction. *Phys Chem Chem Phys*. 2014;16:17183-17195.

78. Komateedi NR, Pankaj B, Thrimurthulu G, Benjaram MR. Supported copper-ceria catalysts for low temperature CO oxidation. *Catal Commun*. 2010;11:863-866.

79. Wei L, Lijun F, Cong Z, et al. A facile hydrothermal synthesis of 3D flowerlike CeO_2 via a cerium oxalate precursor. *J Mater Chem A*. 2013;1:6942-6948.

80. Wicki A, Witzigmann D, Balasubramanian VHJ. Nano medicine in cancer therapy: challenges, opportunities, and clinical applications. *J Control Release*. 2015;200:138-157.

81. Hochella MF Jr, Lower SK, Maurice PA, et al. Nano minerals, mineral nanoparticles, and earth systems. *Science.* 2008;319:1631-1635.

82. Carl W, Soumen D, Sudipta S, et al. Catalytic properties and biomedical applications of cerium oxide nanoparticles. *Environ Sci Nano*. 2015;2:33-53.

83. Wang Y, Yang F, Zhang H-X, et al. Cuprous oxide nanoparticles

inhibit the growth and metastasis of melanoma by targeting mitochondria. *Cell Death Dis*. 2013;4:e783.

84. Wongrakpanich A, Mudunkotuwa IA, Geary SM, Morris AS, et al. Size-dependent cytotoxicity of copper oxide nanoparticles in lung epithelial cells. *Environ Sci Nano*. 2016;3:365-374.

85. Li H, Yan ZY, Liu C, et al. PEGylated ceria nanoparticles used for radioprotection on human liver cells under γ-ray irradiation. *Free Radic Biol Med*. 2015;87:26-35.

86. Kittel C. *Introduction to Solid State Physics, 8th Edition, Berkeley*.; 1996.

87. Atkins P, Friedman R. *Molecular Quantum Mechanics, 4th Edition, Oxford University Press*.; 2005.

88. Cramer CJ. *Essentials of Computational Chemistry: Theories and Models, 2nd Edition, John Wiley & Sons, Ltd, England*.; 2004.

89. Sholl DS, Steckel JA. *Density Functional Theory; a Practical Introduction, John Wiley & Sons, Inc., Canada*.; 2009.

90. David CY. *Computational Chemistry: A Practical Guide for Applying Techniques to Real-World Problems, John Wiley & Sons, Inc, New York*.; 2001.

91. Thomas LH. *The Calculation of Atomic Fields. Mathematical Proceedings of the Cambridge Philosophical Society*.; 1927.

92. Errol GL. *Computational Chemistry: Introduction to the Theory and Applications of Molecular and Quantum Mechanics*. 2nd editio. Springer Dordrecht Heidelberg London New York; 2011.

93. Kohn W, Sham LJ. Self-consistent equations including exchange and correlation effects. *Phys Rev*. 1965;140:1133-1138.

94. Karin E, Oliver T, Holger O, Marco H, Reinhart A. Auxiliary basis sets to approximate Coulomb potentials. *Chem Phys Lett*. 1995;240:283-289.

95. Xiang W, Shan Q, Ziyu W. Generalized gradient approximation calculations of the pressure-induced phase transition of $YAlO_3$ perovskite. *J Phys Condens Matter*. 2006;18:3907-3916.

96. Bernd M. The pseudopotential plane wave approach. *Comput*

Nanosci. 2006;31:71-83.

97. Wendlandt WW. Thermal decomposition of scandium, yttrium and rare earth metal oxalates. *Anal Chem*. 1958;30:58-61.

98. Wendlandt WW. Thermal decomposition of rare earth metal oxalates. *Anal Chem*. 1959;31:408-410.

99. Srivastava OK, Murthy ARV. Thermogravimetric behaviour of lanthanum, thorium and cerium oxalates in an atmosphere of carbon dioxide. *Curr Sci*. 1960;29:470-471.

100. Padmanabhan VM, Sariya SC, Sundaram AK. Thermal decomposition of some oxalates. *J Inorg Nucl Chem*. 1960;12:356-359.

101. Subba Rao VV, Rao RVG, Biswas AB. Thermogravimetric analysis of La, Ce, Pr and Nd oxalates in air and in carbon dioxide atmosphere. *J Inorg Nucl Chem*. 1965;27:2525-2531.

102. Agarwala KP, Naik MC. Kinetics of decomposition of yttrium, cerous and zirconyl oxalates. *Anal Chim Acta*. 1961;24:128-133.

103. Moosath SS, Abraham John, Swaminathan TV. Thermal decomposition of rare earth metal oxalates. I. oxalates of lanthanum, praseodymium and neodymium. *J Inorg Gen Chem*. 1963;324:90-95.

104. Moosath SS, Abraham J, Swaminathan TV. Thermal decomposition of rare earth metal oxalates. II. oxalates of samarium, europium, gadolynium, terbium and dysprosium. *J Inorg Gen Chem*. 1963;324:96-98.

105. Moosath SS, Abraham J, Swaminathan TV. Thermal decomposition of rare earth metal oxalates. III. oxalates of holmium, erbium, thulium, ytterbium, lutetium and yttrium. *J Inorg Gen Chem*. 1963;324:99-102.

106. Moosath SS, Abraham J, Swaminathan TV. Thermal decomposition of rare earth metal oxalates. IV. oxalates of cerium and thorium. *J Inorg Gen Chem*. 1963;324:103-105.

107. Almeida L De, Grandjean S, Vigier N, Patisson F. New insights on the thermal decomposition of lanthanide(III) and actinide(III) oxalates : from neodymium and cerium to plutonium. *Eur J Inorg Chem*. 2012;31:4986-4999.

108. Overs A, Riess I. Properties of solid electrolyte gadolinia-doped ceria prepared by thermal decomposition of mixed ceriumgadolinium

oxalate. *J Am Ceram Soc*. 1982;65:606-609.

109. Ubaldini A, Artini C, Costa GA, Carnasciali MM, Masini R. Thermal decomposition of mixed Ce and Gd oxalates and thermal properties of mixed Ce and Gd oxides. *J Therm Anal Calorim*. 2006;84:207-211.

110. Furuichi R, Ishii T, Yamanaka Z, Shimokawabe M. Effect of α-Fe_2O_3additive on the thermal decomposition of salts of halogen oxoacids, oxalates, azide, permanganate, and oxides. *Thermochim Acta*. 1981;51:245-267.

111. Girgis MM, El-Awad AM. Kinetics and mechanism of thermal decomposition of lithium oxalate catalysed by $Cd_{1-x}Co_xFe_2O_4$(x = 0.0, 0.5 and 1.0) ferrospinel additives. *Thermochim Acta*. 1993;214:291-303.

112. Jose John M, Muraleedharan K, Kannan MP, Ganga Devi T. Effect of semiconducting metal oxide additives on the kinetics of thermal decomposition of sodium oxalate under isothermal conditions. *Thermochim Acta*. 2012;534:71-76.

113. Muraleedharan K, Kannan MP, Gangadevi T. Effect of metal oxide additives on the thermal decomposition kinetics of potassium metaperiodate. *J Therm Anal Calorim*. 2010;100:177-181.

114. Wada T, Nakano M, Koga N. Multistep kinetic behavior of the thermal decomposition of granular sodium percarbonate : hindrance effect of the outer surface layer. *J Phys Chem A*. 2015;2:9749-9760.

115. Yoshikawa M, Goshi Y, Yamada S, Koga N. Multistep kinetic behavior in the thermal degradation of poly (L‐lactic acid): a physico-geometrical kinetic interpretation. *J Phys Chem B*. 2014;118:11397-11405.

116. Chen J, Zhu J, Cho HH, et al. Differential cytotoxicity of metal oxide nanoparticles. *J Exp Nanosci*. 2008;3:321-328.

117. Wang Y, Aker WG, Hwang H, Yedjou CG, Tchounwou PB. A study of the mechanism of in vitro cytotoxicity of metal oxide nanoparticles using catfish primary hepatocytes and human HepG2 cells. *Sci Total Env*. 2011;409:4753-4762.

118. Ivask A, Titma T, Visnapuu K, et al. Toxicity of 11 metal oxide nanoparticles to three mammalian cell types in vitro. *Curr Top Med Chem*. 2015;15:1914-1929.

119. Titma T, Shimmo R, Siigur J, Kahru A. Toxicity of antimony, copper, cobalt, manganese, titanium and zinc oxide nanoparticles for the alveolar and intestinal epithelial barrier cells in vitro. *Cytotechnology*. 2016;68:2363-2377.

120. Rajiv S, Jerobin J, Saranya V, et al. Comparative cytotoxicity and genotoxicity of cobalt(II, III) oxide, iron(III) oxide, silicon dioxide, and aluminum oxide nanoparticles on human lymphocytes in vitro. *Hum Exp Toxicol*. 2016;35:170-183.

121. Xue Y, Luan Q, Yang D, Yao X, Zhou K. Direct evidence for hydroxyl radical scavenging activity of cerium oxide nanoparticles. *J Phys Chem C*. 2011;115:4433-4438.

122. Marzi L, Joaquin De L, Ramos D, et al. Cytotoxicity and genotoxicity of ceria nanoparticles on different cell lines in vitro. *Int J Mol Sci*. 2013;14:3065-3077.

123. Clark A, Zhu A, Petty HR. Titanium-doped cerium oxide nanoparticles protect cells from hydrogen peroxide-induced apoptosis. *J Nanopart Res*. 2013;15:2126.

124. Gao Y, Chen K, Ma J, Gao F. Cerium oxide nanoparticles in cancer. *Onco Targets Ther*. 2014;7:835-840.

125. Kargar H, Ghazavi H, Darroudi M. Size-controlled and bio-directed synthesis of ceria nanopowders and their in vitro cytotoxicity effects. *Ceram Int*. 2015;41:4123-4128.

126. Leopold L, Mesaros A, Pop O. Cerium oxide nanoparticles and its cytotoxicity human lung cancer cells. *Rom Biotechnol Lett*. 2015;20:10679-10687.

127. Gagnon J, Fromm KM. Toxicity and protective effects of cerium oxide nanoparticles (nanoceria) depending on their preparation method, particle size, cell type and exposure route. *Eur J Inorgnic Chem*. 2015;27:4510-4517.

128. Nelson BC, Johnson ME, Walker ML, Riley KR, Sims CM. Antioxidant cerium oxide nanoparticles in biology and medicine. *Antioxidants*. 2016;5:1-21.

129. Das J, Choi Y, Han JW, Musa A, Reza T, Kim J. Nanoceria-mediated delivery of doxorubicin enhances the anti- tumour efficiency in ovarian cancer cells via apoptosis. *Sci Rep*. 2017;9513:1-12.

130. Khan S, Ansari AA, Rolfo C, Coelho A, Al-khayal K, Ahmad R. Evaluation of in vitro cytotoxicity, biocompatibility, and changes in the expression of apoptosis regulatory proteins induced by cerium oxide nanocrystals. *Sci Technol Adv Mater*. 2017;6996:1-10.

131. Nolan M, Sayle DC, Watson GW. Density functional theory studies of the structure and electronic structure of pure and defective low index surfaces of ceria. *Surf Sci*. 2005;576:217-229.

132. Castleton CW, Kullgren J, Hermansson K. Tuning LDA+U for electron localization and structure at oxygen vacancies in ceria. *J Chem Phys*. 2007;127:244704-244711.

133. Loschen C, Migani A, Bromley ST, Neyman KM. Density functional studies of model cerium oxide nanoparticles. *Phys Chem Chem Phys*. 2008;10:5730-5738.

134. Zhang C, Michaelides A, King DA, Jenkins SJ. Structure of gold atoms on stoichiometric and defective ceria surfaces. *J Chem Physic*. 2008;129:194708-8.

135. Branda MM, Hernández NC, Sanz JF, Illas F. Density functional theory study of the interaction of Cu, Ag, and Au atoms with the regular CeO_2 (111) surface. *J Phys Chem C*. 2010;114:1934-1941.

136. Lixia C, Yuanhao T, Zhang H, et al. First-principles investigation of transition metal atom M (M = Cu, Ag, Au) adsorption on CeO_2 (110). *Phys Chem Chem Phys*. 2012;14:1923-1933.

137. Jarlborg T, Barbiellini B, Lane C, et al. Electronic structure and excitations in oxygen deficient $CeO_{2-\delta}$ from DFT calculations. *Phys Rev B*. 2014;89:165101-1-165101-165107.

138. Kehoe AB, Scanlon DO, Watson GW. Role of lattice distortions in the oxygen storage capacity of divalently doped CeO_2. *Chem Mater*. 2011;23:4464-4468.

139. Lu Z, Yang Z, He B, Castleton C, Hermansson K. Cu-doped ceria: oxygen vacancy formation made easy. *Chem Phys Lett*. 2011;510:60-66.

140. Szabová L, Skála T, Matolínová I, Fabris S, Farnesi Camellone M, Matolín V. Copper-ceria interaction: a combined photoemission and DFT study. *Appl Surf Sci*. 2013;267:12-16.

141. Vanpoucke DEP, Bultinck P, Cottenier S, Van Speybroeck V, Van

Driessche I. Aliovalent doping of CeO_2 : DFT study of oxidation state and vacancy effects. *J Mater Chem A*. 2014;2:13723-13737.

142. Vanpoucke DEP, Cottenier S, Van Speybroeck V, Van Driessche I, Bultinck P. Tetravalent doping of CeO_2: the impact of valence electron character on group IV dopant influence. *J Am Ceram Soc*. 2014;97:258-266.

143. Alaydrus M, Sakaue M, Kasai H. A DFT+U study on the contribution of 4f electrons to oxygen vacancy formation and migration in Ln-doped CeO_2. *Phys Chem Chem Phys*. 2016;18:12938-12946.

144. Eugenio FS, Carlos AC, Robinson LM, Mariana MVMS, Ricardo BA, Martin S. Combined DFT and experimental study of the dispersion and interaction of copper species in Ni-CeO_2 nanosized solid solutions. *RSC Adv*. 2016;6:5057-5067.

NUSRATH. K “SYNTHESIS AND KINETICS OF FORMATION OF CERIA AND CERIA BASED MATERIALS via THERMAL DECOMPOSITION OF OXALATES”. THESIS. DEPARTMENT OF CHEMISTRY, UNIVERSITY OF CALICUT, 2018.

2.1. Materials

All the chemicals used were of analytical reagent grade and used without any further purification. Chemicals used for the synthesis of materials are following:

Chapters 3 &4

Cerium oxalate decahydrate *(99.9%, Indian Rare Earth Products Ltd, Cochin)*

$CaCO_3$ *(Sigma-Aldrich)*

1MHCl

NH_4OH *(Merck, India)*

$(NH_4)_2C_2O_4$.

Chapter 5

$Ce_2(C_2O_4)_3.10H_2O$ (99.9%, Indian Rare Earth Products Ltd, Cochin),

$FeSO_4(NH_4)_2SO_4.6H_2O$

$Co(NO_3)_2.6H_2O$ *(Merck, India)*

$NiCl_2.4H_2O$

$Na_2C_2O_4$ (*Sigma Aldrich*)

Chapter 6

$Ce(NO_3)_3.6H_2O$ *Himedia*

$Cu(NO_3)_2.3H_2O$ (*Merck*, *India*)

$Na_2C_2O_4$ (*Sigma Aldrich*)

CTAB (*Merck, India*)

Chapter 7

$Ce\ (NO_3)_3.6H_2O$ (*Himedia*)

$Na_2C_2O_4$ (*Sigma Aldrich*)

CTAB (*Merck, India*)

PEG-800 (*Merck, India*)

Materials are prepared following the procedures as prescribed *in each chapter*.

2.2. Characterization techniques

2.2.1. FT-IR

Using Jasco FT-IR-4100 instrument, FT-IR spectrum of the samples in KBr pellet was recorded[1] in the wave number region of 450-4000cm^{-1} [2].

2.2.2. UV-Visible spectroscopy

UV–Vis reflectance which was measured using UV–Vis diffuse reflectance spectrum (Model: Jasco V-550 spectrophotometer)[2].

2.2.3. XRD

Powder X-ray diffraction (XRD) pattern of the samples were recorded using a diffractometer (Miniflex 600, Model: Rigaku D/Max) with Cu-Kα (1.5418 Å) radiation (40kV, 15mA) with a scan rate of 2θ min^{-1} [2].

2.2.4. Optical Microscopy

The appearance of the samples was observed using an optical microscope (Axio-Lab A1 attached with AxioCam ER C5S, Lens; Carl Zeiss-micro image, GmbH Analyzer)[2].

2.2.5. SEM

The scanning electron microscopic (SEM) analyses of all the samples studied were performed using a Jeol Jsm-6390 LV. The instrument offers a resolution of 3nm ACC V3.0 KV, WD8m and magnification of 5× to 300,000. The imaging techniques employed was secondary electrons (SE)[1] and back scattered electrons (BSE)[2,3].

2.2.6. TEM

The morphology and topographical studies of the oxide samples were brought with TEM (Jeol, JEM 2100) with an

accelerating voltage of 200kV. Electronic and crystalline properties are well characterized by using HRTEM and SAED pattern.

2.2.7. FE-SEM

FE-SEM image of the samples were taken with Carl Zeiss (Model: Gemini 300).

2.2.8. EDS

Energy dispersive spectra (EDS, Ametek, Z2 analyser) were used for identifying elemental composition involved in the oxides.

2.2.9. PL Spectra

Photo luminescent properties are well characterized by using a Perkin Elmer LS 55 fluorescence spectrometer at room temperature.

2.2.10. Micro Raman spectra

Micro Raman spectra of the samples were collected using confocal Raman microscope (WITec GmbH, alpha 300A) with the excitation of 532nm laser (Nd: YAG dye laser, 40mW).

2.3. Thermal analysis

Analyzed by DSC (TA instruments, Model: Q20) and TGA (Perkin Elmer Thermal Analyzer, Model: STA 8000). The operational characteristics of thermal analysis systems are as follows: atmosphere: flowing N_2 at a flow rate of 50mLmin^{-1}, sample mass: 6 mg and sample pan: aluminium.

Simultaneous TG-DTA were made on Perkin Elmer Thermal Analyser (Model: Diamond TG/DTA) at four different heating rates, *viz*. 5, 10, 15 and 20 K min^{-1}. The operational characteristics of the thermal analysis system are as follows: atmosphere: flowing air, at a flow rate of 100 mL min^{-1}; sample mass: 10 mg; and sample pan: Platinum. Repetition of the works were made under similar conditions and found that the data converged with each other, indicating acceptable reproducibility[2,1].

2.4. Kinetic Analysis

Analysis was performed by taking TG/DTA/DSC at different heating rate. Mathematical calculations were done and converted to α-T data. Now, in the entire thesis regards the formation of ceria nano structures, its mixed oxides and doped oxides from the corresponding oxalates through the multi stage thermal decomposition strategy. The physico-geometrical kinetic behavior of the reaction was investigated by performing kinetic deconvolution procedure[4-6]. The procedure for this kinetic deconvolution is described in the chapters. Linear non-isothermal techniques in the flowing atmosphere of air/ N_2 were used with TGA/DSC/DTA instrument. The decomposing kinetics of each kinetically resolved stage of oxalate samples were studied either treating each stage within the conversion function, α between 0 to 1 or considering α of the overall decomposition from the room temperature to specified temperature within 0 to 1.

2.5. Cytotoxicity Assay

In vitro cytotoxicity for short term was studied for ceria, copper doped samples surface modified ceria with using Dalton's Lymphoma ascite cells. For this purpose, tumor bearing cells of mice were sucked from the peritoneal cavity and these cells were washed with PBS. Cytotoxicity assay was determined by trypan blue exclusion method[7–9]. For the various test samples of concentrations10, 20, 50, 100 and 200μgmL^{-1}, viable cell suspension (1×10^{6} cells in 0.1mL) was added [9]. Finally the volume was made up to 1ml using PBS. This mixture was then incubated at 310K for 3h. Moreover the cell suspension was mixed with 0.1mL of 1% trypan blue dye and kept for 2-3 minutes[9]. These analysis mixtures were then loaded on haemocytometer. Diazodye, trypan blue is negatively charged, it does not interact with cell membrane unless the cell membranes are damaged. Moreover, this dye stained selectively the damaged cells with blue color while excluding the undamaged cells. The numbers of stained and unstained cells were counted individually[7, 10–12].

% cytotoxicity = (No. of dead cells) *100 / (No. live cells+ No. dead cells)[12]

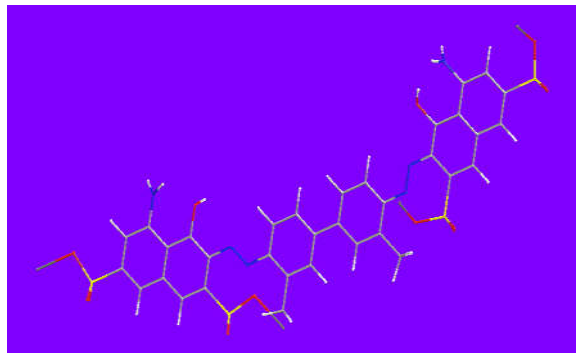

Fig. 1 3D chemical structure of trypan blue

2.6. Softwares used

- *Peak fit 4.12*
- *VESTA (Visualization for Electronic and Structural Analysis)4.4.0*
- *p4vasp*

2.7. References

1. Muraleedharan K, Kripa S. DSC kinetics of the thermal decomposition of copper(II) oxalate by isoconversional and maximum rate (peak) methods. *J Therm Anal Calorim*. 2014;115:1969-1978.
2. Nusrath K, Muraleedharan K. Effect of Ca(II) on the multistep kinetic behavior of thermally induced oxidative decomposition of cerium(III) oxalate to CeO_2(IV). *J Anal Appl Pyrol*. 2016;120:379-388.
3. Nusrath K, Muraleedharan K. Effect of Ca(II) additive on the thermal dehydration kinetics of cerium oxalate rods. *J Therm Anal Calorim*. 2017;128:541-52.
4. Kitabayashi S, Koga N. Physico-geometrical mechanism and overall kinetics of thermally induced oxidative decomposition of tin(II) oxalate in air: formation process of micro structural tin(IV)oxide. *J Phys Chem C*. 2014;118:17847−17861.
5. Yoshikawa M, Yamada S, Koga N. Phenomenological interpretation of the multistep thermal decomposition of silver carbonate to form silver metal. *J Phys Chem C*. 2014;118:8059-8070.
6. Wada T, Nakano M, Koga N. Multistep kinetic behavior of the thermal decomposition of granular sodium percarbonate : hindrance effect of the outer surface layer. *J Phys Chem A*. 2015;2:9749-9760.
7. Lonza, Products and services, Bio-research, Cell-culture products, Reagents C culture reagents. Trypan blue 0.04 solution.
8. National institute of environmental health sciences. Cell viability testing with Trypan blue exclusion method. :1-2.
9. Aiswarya G, Venkatta Ramana K. Evaluation of in vitro cytotoxic activity of different extracts of Acslepias curassavica leaf. *World J Pharm Sci*. 2016;4:287-289.
10. Bioresearch. Protocol for performing a Trypan blue viability test: technical reference guide. 2012:1-2.
11. Alessandra P, Luca M, Grazia G, et al. Ceria nanoparticles for the treatment of Parkinson-like diseases induced by chronic manganese intoxication. *RSC Adv*. 2015;5:20432-20439.
12. Ravi kkumar VR, Gopal V, Ravichandaran N, Brindha P, Sudha T. In-vitro anti-inflammatory and anti-cancer activity of extracts of stem bark of Zanthoxylum tetraspermum Wight & Arn. *Int J Adv Res Biol Sci*. 2015;2:48-53.

NUSRATH. K “SYNTHESIS AND KINETICS OF FORMATION OF CERIA AND CERIA BASED MATERIALS via THERMAL DECOMPOSITION OF OXALATES”. THESIS. DEPARTMENT OF CHEMISTRY, UNIVERSITY OF CALICUT, 2018.

3.1. Introduction

Studies on the solid state reaction kinetics of metal oxalates from experimental thermo analytical (TA) data are the subject of many researchers[1–5]. There is large number of reports regarding the kinetics of dehydration of inorganic solids[5-6]. Studies on the thermal dehydration kinetics of potassium titanium oxalate, $K_2TiO(C_2O_4)_2.2H_2O$ by using thermogravimetry (TG), differential thermal analysis (DTA) and differential scanning calorimetry (DSC) have been reported and disclosed that dehydration reaction occurs in a single step through a practically irreversible process and the kinetic parameters were estimated using isoconversional methods[5]. Muraleedharan *et al*[7] investigated the kinetic behavior of thermal dehydration and degradation kinetics of chitosan Schiff bases of o-, m- and p- nitro benzaldehyde and explored that thermal stability of Schiff bases follows in the order o- < m- < p-. Honcova *et al*[8] studied the kinetics of dehydration calcium oxalate trihydrate using DSC method and found that dehydration proceeds in two stages where 2 molecule of water is dehydrated in first step and finally 1 molecule of water in second step. Chambre' *et al*[9]studied the non-isothermal dehydration kinetics of ion exchange resins with acrylic-divinyl benzene matrix and observed that the dehydration step corresponds to the elimination of osmotic water and hydrogen bounded water with carboxylic group. Galina *et al*[6] reported the enthalpy of dissolution and thermal dehydration process of calcium oxalate hydrates. They calculated enthalpy contribution of water in calcium oxalate hydrates from determined values of dissolution and dehydration enthalpy. Jankovic *et al*[10] investigated the

dehydration process of equilibrium swollen poly (acrylic acid) under isothermal condition in the temperature range of 306-361K. They calculated kinetic parameters using *initial rate* and *stationary point* methods of Johnson-Mehl- Avrami.

Rare earth element, cerium exerts diverse biological effects mainly due to their resemblance with calcium. This enables the element to replace calcium in biomolecules without necessarily substituting for it functionally. Historically, cerium oxalate was used as a prophylactic against vomiting due to its anti-emetic effect[11]. It has wide application in medicinal field due to its pharmacological properties and therapeutic effect[12]. Cerium oxalate has much importance due to their technological importance, for instance, as a precursor of nano ceria[13]. By the thermal decomposition method, particle morphology, crystalline phase and surface chemistry of thermally decomposed particles can be controlled by regulating the precursor composition, reaction temperature, pressure, solvent property and aging time[14-15]. Doping of ceria with Ca, make it as the most effective electrolyte material for low temperature solid electrolyte fuel cell[16, 17]. Due to the twittering ($Ce^{4+} \rightarrow Ce^{3+}$) nature, it has better redox property[13]. Solids prepared by co-precipitation of ceria with those of sodium, lithium, cesium or calcium, consist of a single phase with at least some incorporation of the guest ion in the ceria lattice[18]. Co-precipitation of calcium and cerium results in the formation of homogeneous mixed oxides of cerium and calcium. Surface properties depend on the calcium content of mixed oxide[18]. Thermal stability and

water content are important characteristics when they are used as a catalyst in organic, anhydrous or aqueous media.

There are few reports regarding thermal decomposition of rare earth metal oxalates. Thermal decomposition of cerium oxalate and mixed cerium–gadolinium oxalate were studied. The corresponding mixed oxide $(CeO_2)_{0.9}(Gd_2O_3)_{0.1}$ is prepared by calcination[19]. Ubaldini *et al*[20]investigated thermal properties of mixed cerium-gadolinium oxalate and found that their dehydration stages are similar to that of gadolinium oxalate. But the studies on the thermal decomposition of alkaline earth metal, Ca(II) mixed cerium oxalate rods are not reported yet. Both Ce(III) and Ca(II) have approximately same atomic radius. Cerium oxalate decahydrate undergoes thermal decomposition mainly through two stages. First stage corresponds to dehydration and second stage corresponds to decomposition to ceria[17]. Estimation of kinetic parameters of dehydration process has much importance because it can predict safe storage and service life of high energy materials. Hence, the derivation of kinetics of a solid state reaction has significant role such as assessing the stability and reactivity of materials, evaluating the effectiveness of energetic materials involved in safety assessment, and controlling the material synthesis process.

Thermal dehydration processes of many of the inorganic solids are predominantly regulated by geometrical constraints in the relation between the surface product layer produced during the preliminary stage of the reaction and the inward advancement of the reaction interface generated at the boundary between surface product layer and internal reactant[21,22]. As the reaction progresses, the role of surface

product layer came into act. Depending on the reaction condition, the nature of surface product layer is varied[23]. On account of the generation of self-generated reaction condition at the reaction interface, its changes would reflect in partially overlapping multi step reaction features. In a typical reaction process, each constituent chemical reaction provides different thermal effects for the overall reaction (exothermic or endothermic). Thermal decomposition reaction proceeded in multistep behaviors are controlled by physico-geometrical features of solid-state reactions and successive chemical reaction schemes[23]. For estimating kinetic solution of complex reaction, kinetic deconvolution method is practically useful[24].

The present work focused on studying the kinetics of thermal dehydration of incorporated water from cerium oxalate and its mixed oxalates with calcium oxalate in varying compositions such as 10, 30, 66.67, and 100 mass (%). For characterizing the partially overlapped independent process, kinetic deconvolution method is employed. For estimating kinetic parameters, isoconversional methods such as Kissinger – Akahira- Sunose (KAS), Flyn – Wall-Ozawa (FWO) and iterative isoconversional procedure were used.

3.2. Method of preparation

3.2.1. Preparation of calcium oxalate dihydrates

Calcium chloride is prepared from $CaCO_3$ and 1M HCl. Calcium oxalate is precipitated using ammonium oxalate as precipitating agent. The precipitate is collected, washed with ethanol and water repeatedly and dried in an air oven at 60^oC.

3.2.2. Preparation of physical mixture of cerium and calcium oxalates

The particle size of oxalates of cerium and calcium were fixed in the range 95-105μm. Different compositions; 100m/m(%) cerium oxalate (CC_1), 90 m/m(%) cerium oxalate (CC_2), 70m/m(%) cerium oxalate (CC_3), 33.33m/m(%) cerium oxalate (CC_4) and 100m/m(%) calcium oxalate (CC_5), were prepared each by thorough mechanical mixing in an agate mortar.

3.3. Characterization

For the characterization of dehydrated sample, FT-IR, XRD, SEM and DTA technique were used. Kinetic analysis of thermal dehydration of different compositions of physical mixture of cerium oxalate and calcium oxalate were executed using simultaneous TG-DTA technique at four different heating rates, *viz*. 5, 10, 15 and 20 K min^{-1}.

3.4. Results and discussion

Fig. 1 represents FT-IR spectra of the samples. Fig. 1a represents FT-IR spectrum of CC_1. The broad band observed at 3023-3666 cm^{-1} corresponds to water molecules which are removed only at higher temperature[25]. Fig. 1b-e represents respectively the FT-IR spectra of the samples CC_2, CC_3, CC_4, and CC_5. The strong peak observed at 1633.9 and 1622.45 cm^{-1} are attributed to combined effect of asymmetric stretching and bending of water molecules[26]. The strong peak observed at 1318 and 1317.01 cm^{-1} in Fig. 1 corresponds to

asymmetric stretching of CO_2 molecule associated with oxalate ligand group[26, 27]. The band observed at 523.8 and 514.4 cm^{-1}correspond to the M-O stretching frequency[25, 28].

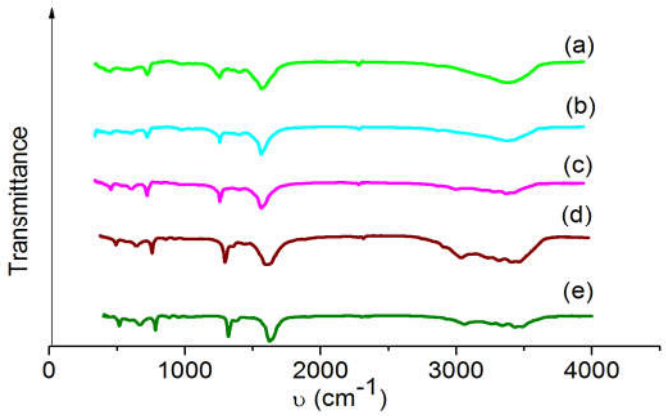

Fig. 1 FT-IR spectra of the samples: CC_1 (a), CC_2 (b), CC_3 (c), CC_4 (d), and CC_5 (e).

Fig. 2 shows the XRD patterns of the samples at 2θ values ranging from 20-70°. The reflections from the sample indicate that cerium oxalate CC_1 (Fig. 2a) crystallizes in the monoclinic system (JCPDS. No. 20-0268). Figs. 2b-d represents respectively the XRD patterns of the samples CC_2, CC_3 and CC_4. Fig. 2e represents the XRD pattern of calcium oxalate CC_5 (JCPDS. ASTM File No. 15-762). From the XRD patterns, it was shown that the peak intensity and crystalline nature enhances with mixing of calcium oxalate. The sample CC_1 (Fig. 2a) shows major peak at 20.44, 28.24, 42.70 and 46.40°, while CC_2 (Fig. 2b) at 20.26, 26.37, 29.52, 31.95 and 43.83° majorly. The XRD patterns of the samples CC_2, CC_3, CC_4 and CC_5 has similarity in the diffracting angle but shows difference in peak intensity due to the variation of mass percentage of the additive calcium oxalate. This

reveals identical crystalline structure for these samples. The Scherrer equation can be used to calculate the average crystallite size of cerium oxalate, calcium oxalate and Ca(II) mixed cerium oxalate from the maxima of peak and found that all of them have size in nanometer region. Table 1 shows the average crystallite size of the samples and found that CC_2 shows lower crystallite size than others.

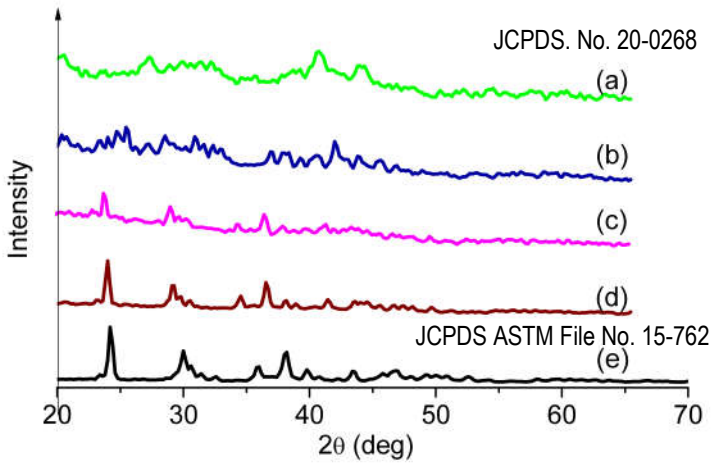

Fig. 2 XRD patterns of the samples. CC_1 (a), CC_2 (b), CC_3 (c), CC_4 (d) and CC_5 (e).

Table 1 Average crystallite size of the samples

Sample	Average crystallite size (nm)
CC_1	56.7
CC_2	10.4
CC_3	19.2
CC_4	50.2
CC_5	33.0

Fig. 3 represents the SEM images of samples of pure and Ca(II) mixed cerium oxalate. The morphological studies revealed that pure cerium oxalate CC_1 (Fig. 3a) possessed rod like morphology with edge length of the rod in micrometer range (1.71-2.01μm). Therefore, cerium oxalate nano particles are aggregated to form microstructural rods and formed secondary particles along with aggregated particles. The addition of calcium oxalate to cerium oxalate in varying compositions causes to destruct the rod morphology of cerium oxalate as shown in Fig. 3b-d. Rod like morphology of cerium oxalate disappeared with increasing the mass percentage of calcium oxalate. In mixed cerium oxalate, the rods are covered with small particles of calcium oxalate. Hence strain is experienced on the surface of the rods which results in the breakdown of the rods into small pieces. Significant boundaries between the rods are accompanied by holes. These are possibly served as diffusion channels for the removal of H_2O vapors. Fig. 3e represents the SEM image of calcium oxalate crystals dehydrated at 623K. Some deformations present on the surface of crystals can act as path for the removal of incorporated water molecules.

Fig. 4A shows the TG curves of decomposition of pure and mixed cerium oxalates CC_1 (Fig. 4A: a), CC_2 (Fig. 4A: b), CC_3 (Fig. 4A: c), CC_4 (Fig. 4A: d) and CC_5 (Fig. 4A: e) obtained at $10Kmin^{-1}$. Fig. 4B represents DTA curves for thermal decomposition of pure and mixed cerium oxalates CC_1 (Fig. 4B: a), CC_2 (Fig. 4B: b), CC_3 (Fig. 4B: c), CC_4 (Fig. 4B: d) and CC_5 (Fig. 4B: e) obtained at $10Kmin^{-1}$. The first stage in all the TG and DTA curves correspond to

dehydration reaction, second and third stage for decomposition reaction. The dehydrated sample is stable up to 300^{o}C.

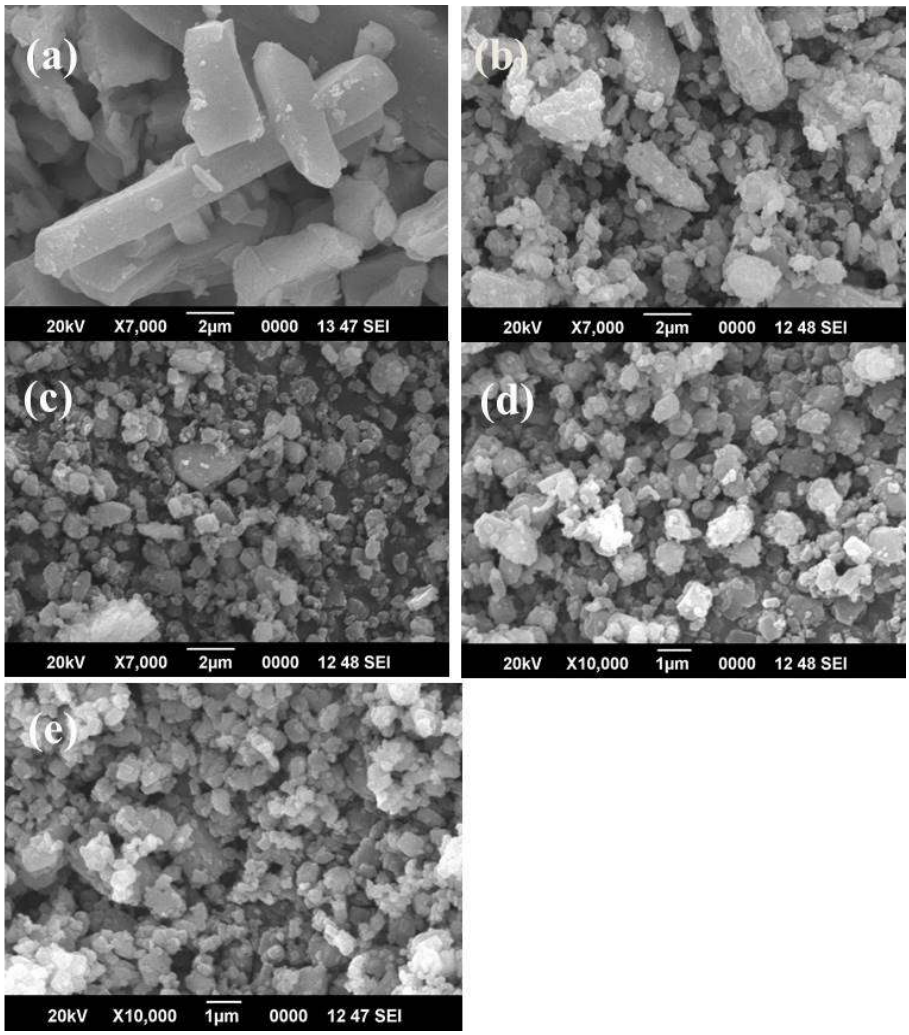

Fig. 3 SEM images of CC_1 (a), CC_2 (b), CC_3 (c), CC_4 (d) and CC_5 (e).

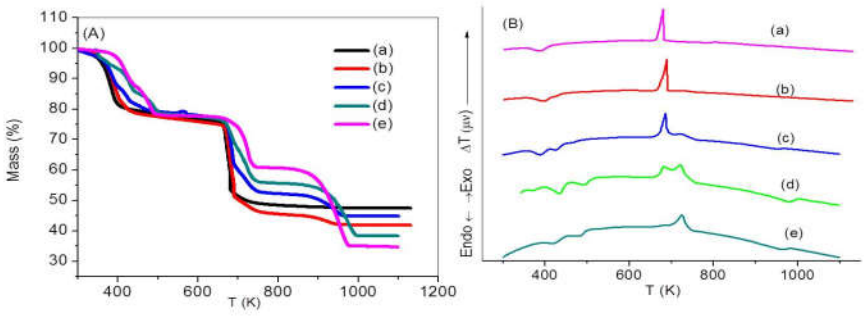

Fig. 4A TG curves for CC_1 (a), CC_2 (b), CC_3 (c), CC_4 (d) and CC_5 (e) at 10Kmin^{-1}. **B**; DTA curve for CC_1 (a), CC_2 (b), CC_3 (c), CC_4 (d) and CC_5 (e) at 10Kmin^{-1}.

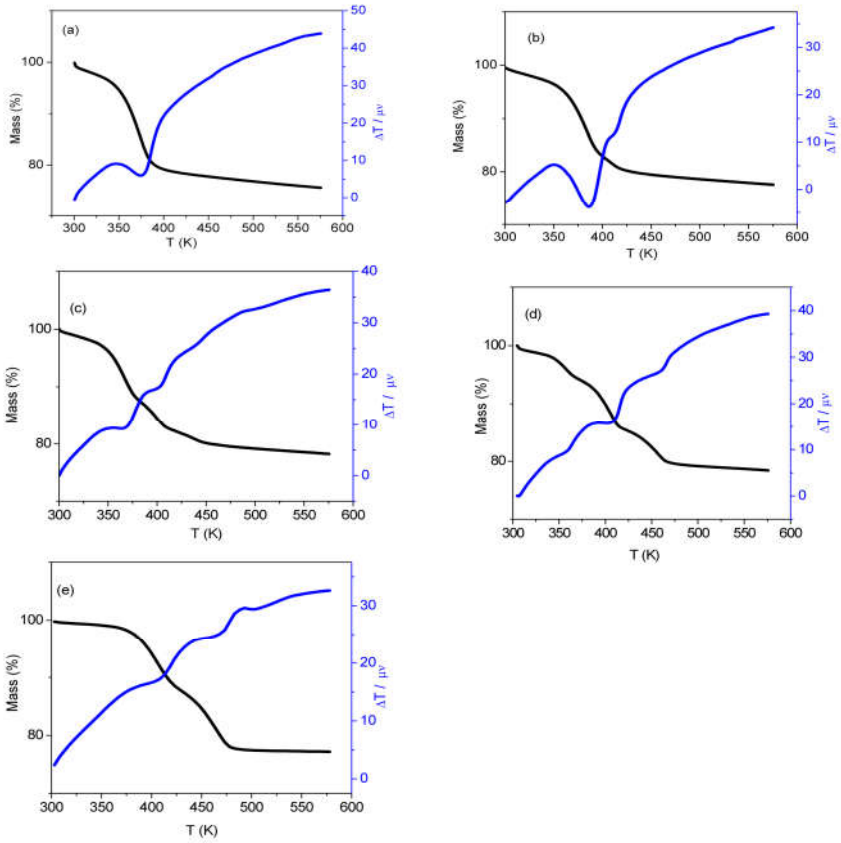

Fig. 5 TG-DTA curves of thermal dehydration stage for CC_1 (a), CC_2 (b), CC_3 (c), CC_4 (d) and CC_5 (e) at 5Kmin^{-1}.

Figs. 5a-e represent TG-DTA curves for the dehydration of the sample CC_1 (Fig. 5a), CC_2 (Fig. 5b), CC_3 (Fig. 5c), CC_4 (Fig. 5d) and CC_5 (Fig. 5e) obtained at a heating rate of $5Kmin^{-1}$. The experimental mass loss for dehydration reaction was found to be 19.92% for pure cerium oxalate which are in good agreement with theoretical mass loss (21%). This revealed that 10 molecule of water is incorporated with cerium oxalate. Dehydration occurs from 60-150°C. The experimental mass loss for the dehydration stage for calcium oxalate was found to be 22.08% which was found to be in good agreement with theoretical mass loss 21.94%. This confirms that 2 molecule of water is attached with calcium oxalate. TG and DTA curves shows two partially overlapping reaction steps of dehydration reaction for pure oxalates (CC_1 and CC_5) whereas three steps for mixed oxalates. These partially overlapped dehydration reactions arise due to the changes in self-generated reaction condition as the reaction progresses. With the introduction of calcium oxalate to cerium oxalate, dehydration reaction is shifted to higher temperature region.

The reaction scheme for the decomposition reaction is as follows[26]

$$Ce_2(C_2O_4)_3.10\,H_2O \xrightarrow{\Delta T} Ce_2(C_2O_4)_3.3H_2O + 7H_2O^{26} \quad (1)$$

$$Ce_2(C_2O_4)_3.3H_2O \rightarrow Ce_2(C_2O_4)_3 + 3H_2O \quad (2)$$

$$Ce_2(C_2O_4)_3.10\,H_2O + CaC_2O_4.2H_2O \xrightarrow{\Delta T} Ce_2(C_2O_4)_3.nH_2O + CaC_2O_4 + (12-n)\,H_2O \quad (3)$$

$$CaC_2O_4.2H_2O \rightarrow CaC_2O_4.\,H_2O + H_2O \quad (4)$$

$$CaC_2O_4.\,H_2O \rightarrow CaC_2O_4 + H_2O \quad (5)$$

3.4.1. Kinetic behavior

Thermal decomposition processes of the partially overlapped reactions are kinetically analyzed using the deconvolution method. Performance of the kinetic deconvolution was evaluated based on an accumulative kinetic equation for the independent processes overlapped partially in views of the peak deconvolution and kinetic evaluation[24].

Before conducting a detailed kinetic characterization of each mass loss step of the reaction, a formal kinetic analysis was performed by assuming a single step reaction for the overall reaction using the fundamental kinetic equation[29].

$$\frac{d\alpha}{dt} = A \exp\left(-\frac{Ea}{RT}\right) f(\alpha) \tag{6}$$

where t is time, T the temperature, R the ideal gas constant, A the apparent Arrhenius pre-exponential factor, Ea the apparent activation energy and $f(\alpha)$ the apparent kinetic model function used to describe the physico-geometrical reaction mechanism as a function of the fractional reaction, α. No practical method was available to determine Ea experimentally. Therefore attempt was made to estimate apparent values of Ea were calculated roughly for the overall reaction by KAS[30], FWO[31, 32] and iterative isoconversional procedure[33,34].

The equation corresponding to KAS method is:

$$\ln\left[\beta / T^2\right] = \ln\left[AR / Eg(\alpha)\right] - E / RT \tag{7}$$

Apparent activation energy *Ea* can be calculated from the slope of the linear representation of ln β/T^2 vs. $1/T$ with a given value of α. The value of pre-exponential factor *A* can be obtained from the intercept if the form of integral reaction model $g(\alpha)$ is known.

The equation based on FWO method is:

$$\ln \beta = \ln\left[AE/Rg(\alpha) \right] - 5.331 - 1.052\, E/RT \tag{8}$$

Using linear representation of ln β *vs*. $1/T$, *Ea* and *A* can be obtained from the slope and intercept respectively.

3.4.2. Calculation of the values of *Ea* by iterative isoconversional procedure

To calculate the approximate value of activation energy *Ea* approaching to the exact value can be determined by the iterative procedure[33–35] . It is based on the following equation

$$\ln \beta/h(x)T^2 = \ln AR/g(\alpha)Ea - Ea/RT \tag{9}$$

where $h(x)$ can be expressed by the fourth Senum and Yang approximation formulae[36]:

$$h(x) = \frac{x^4+18x^3+88x^2+96x}{x^4+20x^3+120x^2+240x+120} \tag{10}$$

where $x = Ea/RT$

Zhipeng *et al*[33] performed the following procedure for the calculation of *Ea* by the iterative method: (i) assume $h(x) = 1$ to calculate the

initial value of the activation energy Ea_1. The conventional isoconversional method stops the calculation of Ea at this step. (ii) Using the value of Ea_1, a new value of Ea_2 can be calculated from the plot of ln $[\beta/h(x)\ T^2]$ *vs.*$1/T$ (iii) Replace Ea_1 with Ea_2 and repeat step (ii). When Ea_i-$Ea_{(i-1)} < 0.01$ kJmol^{-1}, the value of Ea_i is considered to be the exact value of activation energy.

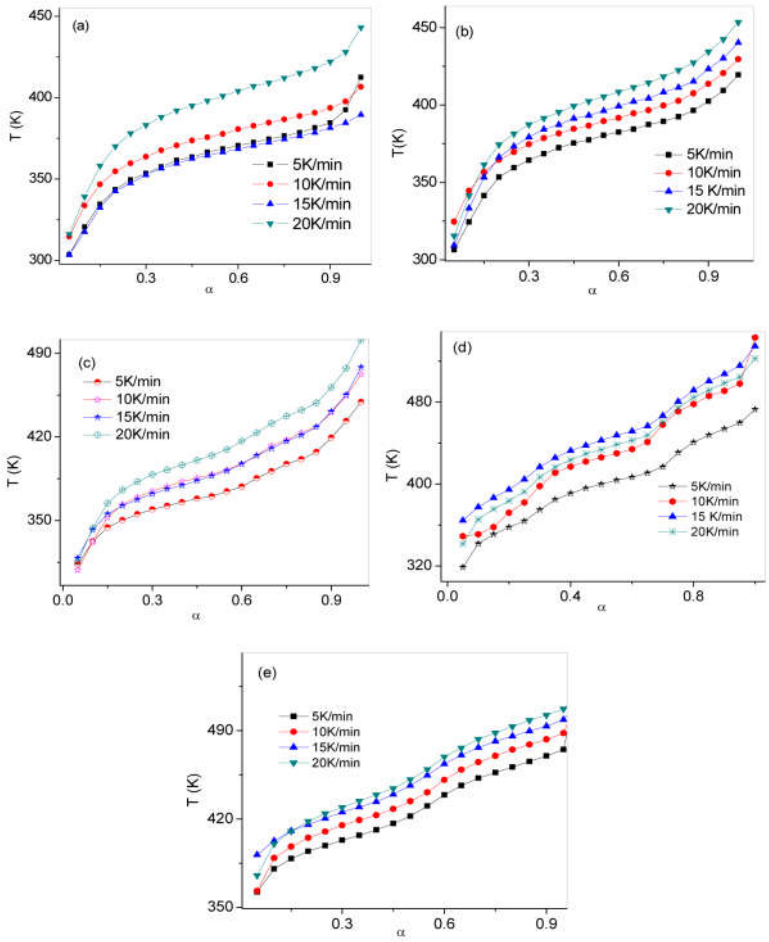

Fig. 6 α –T curves for thermal dehydration of CC_1 (a), CC_2 (b), CC_3 (c), CC_4 (d) and CC_5 (e) at heating rate of 5, 10, 15 and 20Kmin^{-1}.

The α –T curves (Fig. 6) shows multistep dehydration reaction of both pure and mixed cerium oxalate. The same curve for CC_1 (Fig. 6a) shows two steps. The α –T curves for CC_2 (Fig. 6b), CC_3 (Fig. 6c) and CC_4 (Fig. 6d) show three steps while CC_5 (Fig. 6e) shows two steps.

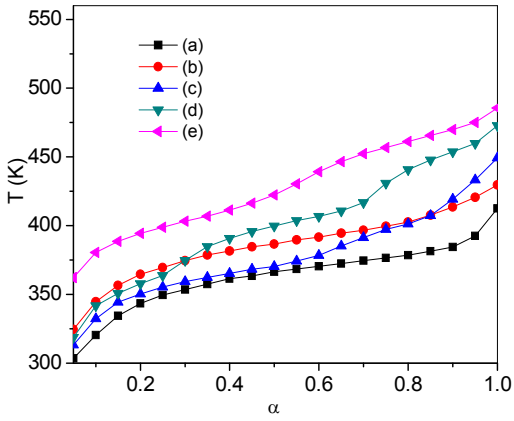

Fig. 7 The comparison of α –T curves for thermal dehydration of CC_1 (a), CC_2 (b), CC_3 (c), CC_4 (d) and CC_5 (e) at heating rate of $5Kmin^{-1}$.

Fig. 7 shows the comparison α –T curves of thermal dehydration of CC_1 (Fig. 7a), CC_2 (Fig. 7b), CC_3 (Fig. 7c), CC_4 (Fig. 7d) and CC_5 (Fig. 7e) at heating rate of $5Kmin^{-1}$. It shows that increasing the percentage of calcium oxalate, dehydration occurs at lower α value. Fig. 8 shows *Ea vs α* curve for pure, Ca(II) mixed cerium oxalate and calcium oxalate. The value of activation energy obtained by KAS and FWO method are compatible with each other. The values of Ea obtained by iterative isoconversional procedure are most apparent values of Ea which are very close to that obtained by KAS method. The values of activation energy calculated using all the methods studied show similar trend.

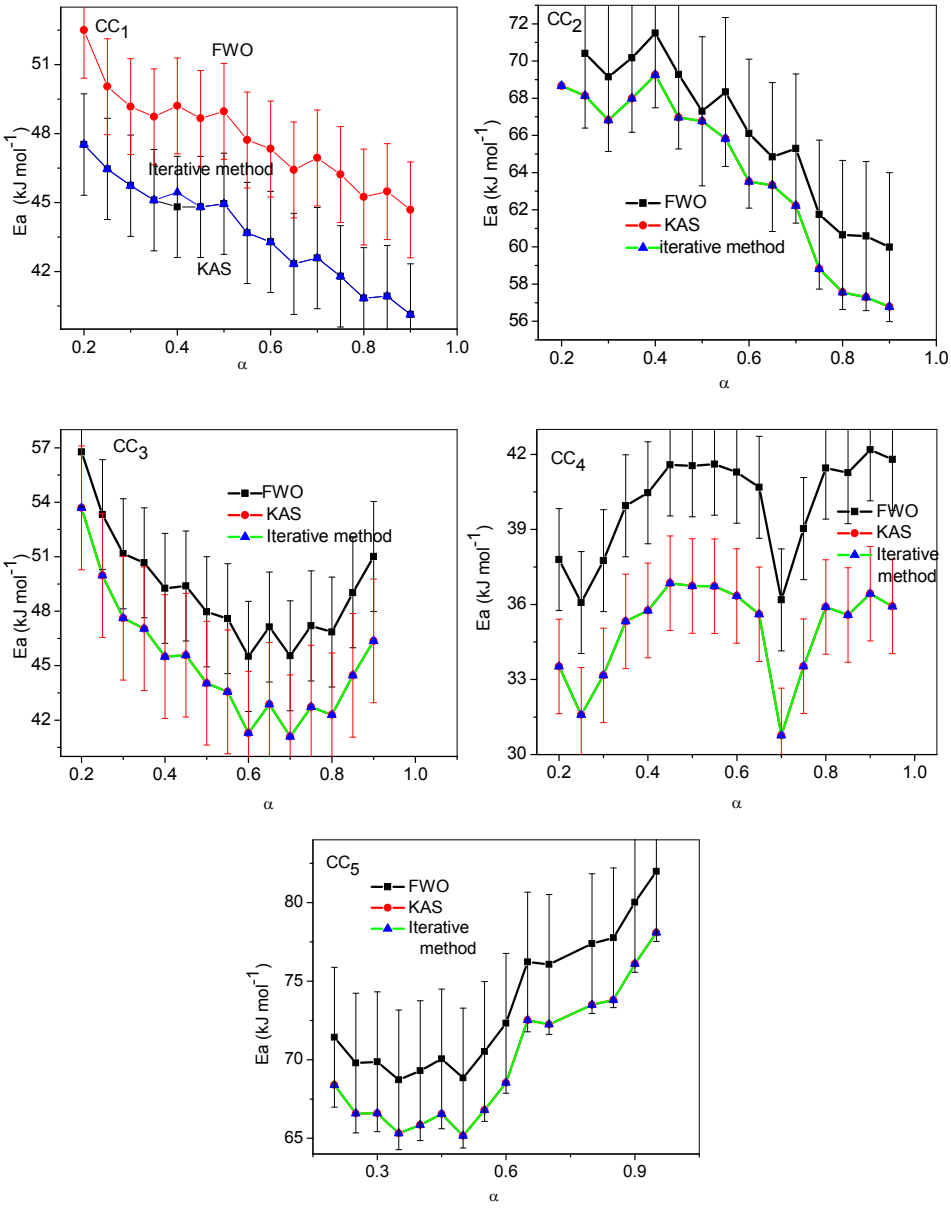

Fig. 8 *Ea* vs *α* curves for CC_1 and Ca(II) mixed cerium oxalate hydrate CC_2, CC_3, CC_4 and pure calcium oxalate dihydrate CC_5.

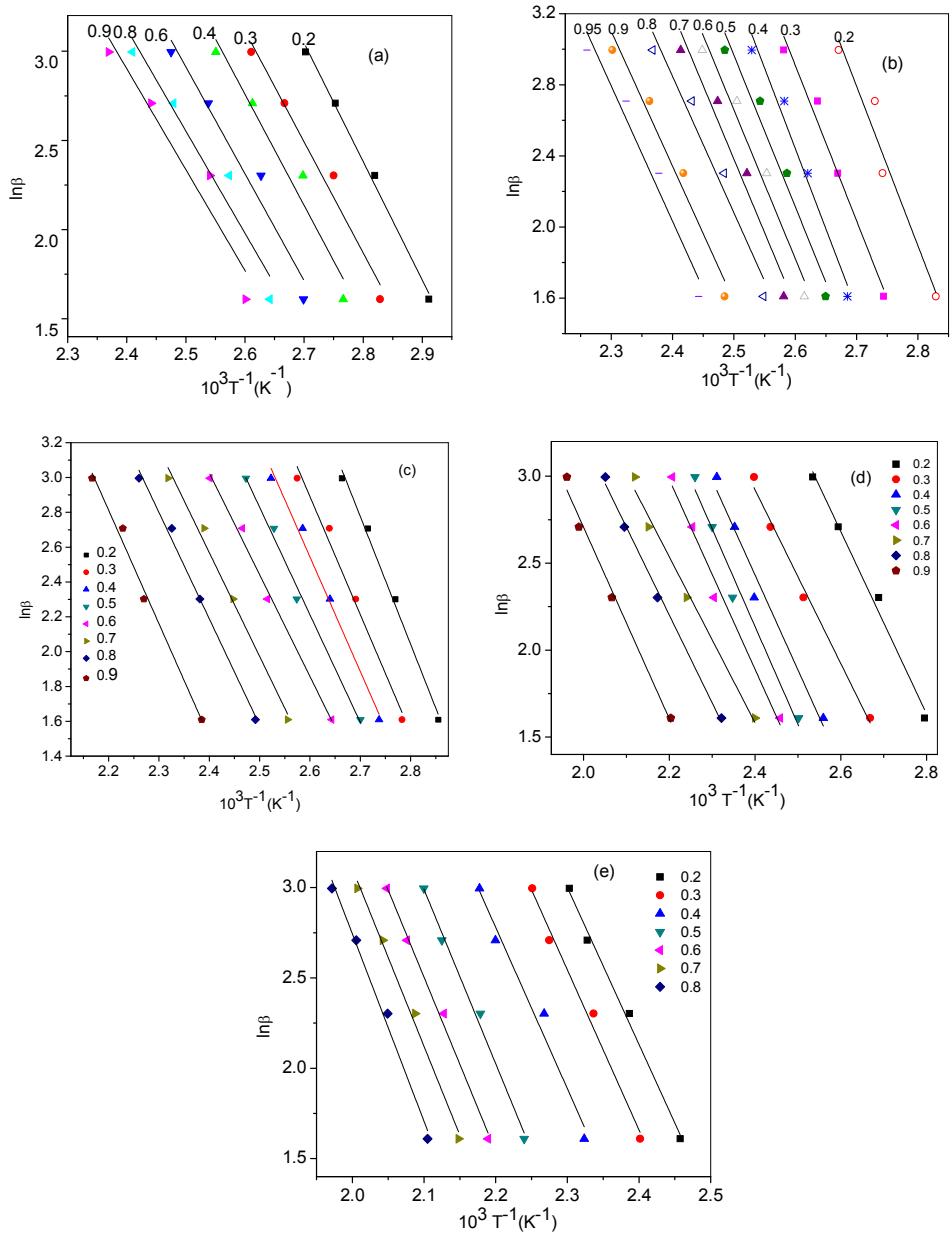

Fig. 9 FWO plots for CC_1 (a), CC_2 (b), CC_3 (c), CC_4 (d) and CC_5 (e).

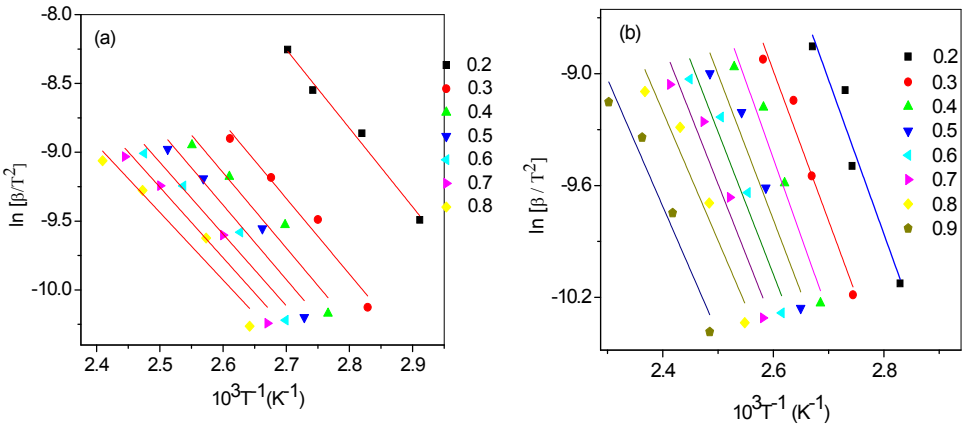

Fig. 10 KAS plots for CC_1 (a) and CC_2 (b)

The *Ea* value obtained for CC_1 decreases randomly with conversion, whereas in the case of CC_5 it increases randomly with conversion. For CC_2, *Ea* value decreases with extent of conversion and passes through a maximum value of *Ea*, 71.2 $kJmol^{-1}$ (FWO), 69.13$kJmol^{-1}$ (KAS and iterative method) at α = 0.4. For CC_3 sample, dependence of *Ea* value decreases gradually with conversion. But for CC_4, *Ea* value increases with α passing through a minimum value of *Ea* = 36.2 $kJmol^{-1}$ (FWO) and 30.5$kJmol^{-1}$ (KAS and iterative method) each at α = 0.7. Dependence of *Ea* value on extent of conversion reveals the possibility of changing mechanism during the dehydration. The plots for FWO method for each sample at specified conversion are shown in Fig. 9. The slopes of the FWO plot for CC_1 (Fig. 9a), CC_2 (Fig. 9b), CC_3 (Fig. 9c), CC_4 (Fig. 9d) and CC_5 (Fig. 9e) show much variation with α. The plots for KAS method for pure cerium oxalate decahydrate CC_1 and Ca(II) mixed cerium oxalate CC_2 are shown in

Fig. 10. For other samples CC_3, CC_4 and CC_5 similar plots were obtained. The values of *Ea* were compared.

Since thermal dehydration of incorporated water is an independent kinetic process, the following cumulative kinetic equation can be applied to the overall reaction under linear non-isothermal conditions [21-24, 37-38]

$$\frac{d\alpha}{dt} = \sum_{i=1}^{n} c_i A_i \exp\left(\frac{-E_{a,i}}{RT}\right) f_i(\alpha_i) \tag{11}$$

with $\sum_{i=1}^{n} c_i = 1$ and $\sum_{i=1}^{n} c_i \alpha_i = \alpha$

where *n* and *c* are the number of component steps and the contribution ratio of each reaction step to the overall process, respectively, and the subscript *i* denotes each component reaction step. A_i and Ea_i are the Arrhenius pre-exponential factor and the apparent activation energy, respectively, of the process *i*. The kinetics of each component process of the overall reaction can be characterized by optimizing all the kinetic parameters in Eq. 11 using nonlinear least- square analysis. Empirical kinetic model functions such as Sestak-Berggren[21, 39] SB (*m, n, p*) were employed for $f_i(\alpha_i)$ in Eq. 12 in order to accommodate any possible mechanistic feature of each reaction process[40–43].

$$f(\alpha) = \alpha^m (1-\alpha)^n [-\ln (1-\alpha)]^p \tag{12}$$

where *m*, *n* and *p* correspond to empirically obtained exponent factors.

The number of component steps for all samples are obtained through kinetic deconvolution of DTA- peaks. The initial values of the kinetic parameters were determined through a formal kinetic analysis of the kinetic data, first subjected to mathematical deconvolution using a statistical function (Weibull). After setting all of the initial values of kinetic parameters, a parameter optimization was carried out to minimize the squares of the residues (F) when fitting the calculated curve $(d\alpha/dt)_{cal}$ versus time to the experimental curve $(d\alpha/dt)_{exp}$ versus time.

$$F = \sum_{j=1}^{n} \left[\left(\frac{d\alpha}{dt} \right)_{\exp,j} - \left(\frac{d\alpha}{dt} \right)_{cal,j} \right]^2 \qquad (13)$$

where n is the number of data points

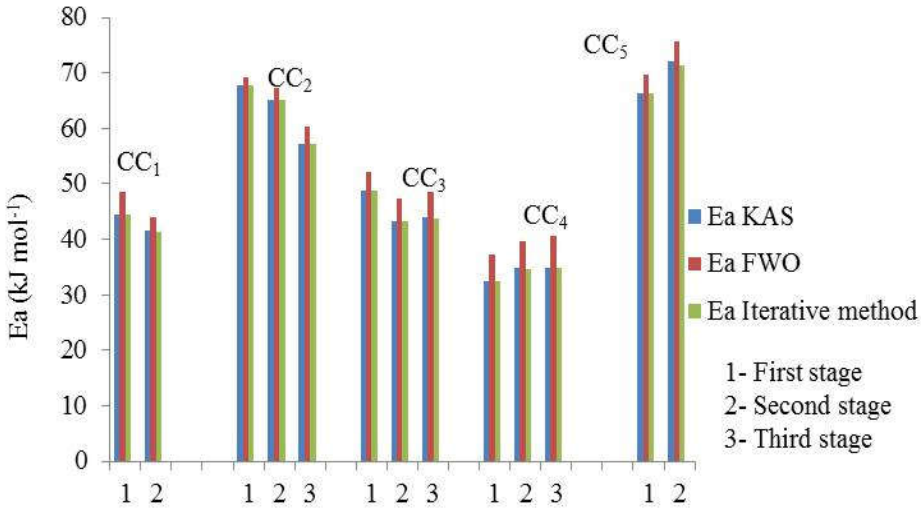

Fig. 11 Comparison of *Ea* values calculated by using KAS, FWO and iterative method for cerium oxalate, Ca(II) mixed cerium oxalate and calcium oxalate.

Fig. 11 shows comparison of *Ea* values calculated by KAS, FWO and iterative isoconversional methods by column chart. From this chart, it is revealed that estimation of Ea values by FWO method is comparatively higher than KAS and iterative method for all compositions. Due to the close agreement of the values of *Ea* calculated by KAS and iterative method, comparisons were made with *Ea* found by iterative procedure. Mixed cerium oxalates undergo thermal dehydration in three stages, while pure cerium oxalate and calcium oxalate in two stages. Hence, CC_1 and CC_5 have two stages for dehydration, whereas CC_2, CC_3 and CC_5 have three stages for the removal of water molecules. From the diagram, it ensures that increasing the mass (%) of calcium oxalate in cerium oxalate, decreases activation energy needed for proceeding thermal dehydration. Hence the value of *Ea* for mixed samples allow the order $CC_4 < CC_3 < CC_2$[43].

Fig. 12 shows kinetic deconvolution of thermal dehydration of CC_1 (Fig. 12a), CC_2 (Fig. 12b) and CC_5 (Fig. 12c) attempted based on Eq. 11 after the preliminary determination of the initial values through mathematical deconvolution and the subsequent formal kinetic analysis of each resolved reaction step. If the constituent chemical process of thermal reaction proceeds by regulating same kinetic regime, the time- or temperature- resolved thermal effect is approximated as the sum of the time derivative of each thermal effect. If component chemical reactions occur with significant time lag and in different places within the reaction system, the time or temperature resolved thermal effect of the overall reaction becomes the sum of the time derivatives of the thermal effects of component chemical processes that proceed

according to different kinetic regimes and mediates a multistep chemical reaction scheme[23]. For the sample CC_1 (Fig. 12a), CC_2 (Fig. 12b) and CC_5 (Fig. 12c), the overall mass loss process for the dehydration reaction is empirically separated in to two, three and two respectively. Even though pure oxalates of cerium and calcium proceed in complex reaction pathway for dehydration reaction, mixed samples take more complex pathways. Further, Fig. 11 confirms the enhanced thermal stability of mixed cerium oxalate sample CC_2 than CC_1.

The values of Ea_i and A_i at each degree of conversion corresponding to each resolved steps are averaged for each sample and summarized in Table 2. The values of Ea_i were calculated for each reaction step by FWO, KAS and iterative methods. The introduction of calcium oxalate made Ca^{2+} interaction, which causes to retard diffusional removal of water vapor at the surface product layer of calcium–cerium oxalate. Hence thermal stability of cerium oxalate is enhanced. Significant effect in thermal stability was observed for mixed cerium oxalate sample, CC_2 (Table 2). The average values of Ea_i needed for sample CC_1 are 45.79 ± 0.0085 $kJmol^{-1}$ (for $i = 1$) and 42.13 ± 0.0075 $kJmol^{-1}$ (for $i = 2$). Arrhenius pre-exponential factor A_i was found to be (4.80 ± 0.0096) × 10^6 (for $i = 1$) and (3.11 ± 0.009) × 10^6 (for $i = 2$). Sample CC_2 needs Ea_i of 68.00 ± 0.0011, 66.12 ± 0.0012 and 58.80 ± 0.0079 $kJmol^{-1}$ for $i = 1$, $i = 2$ and $i = 3$ respectively. The required value of A_i is (2.23 ± 0.0018) ×10^8 (for $i = 1$), (1.00 ± 0.0089) ×10^8 (for $i = 2$) and (9.46 ± 0.0026) ×10^7 (for $i = 3$). The values of Ea_i and A_i required for samples CC_3 and CC_4 are comparatively lower than sample CC_2.

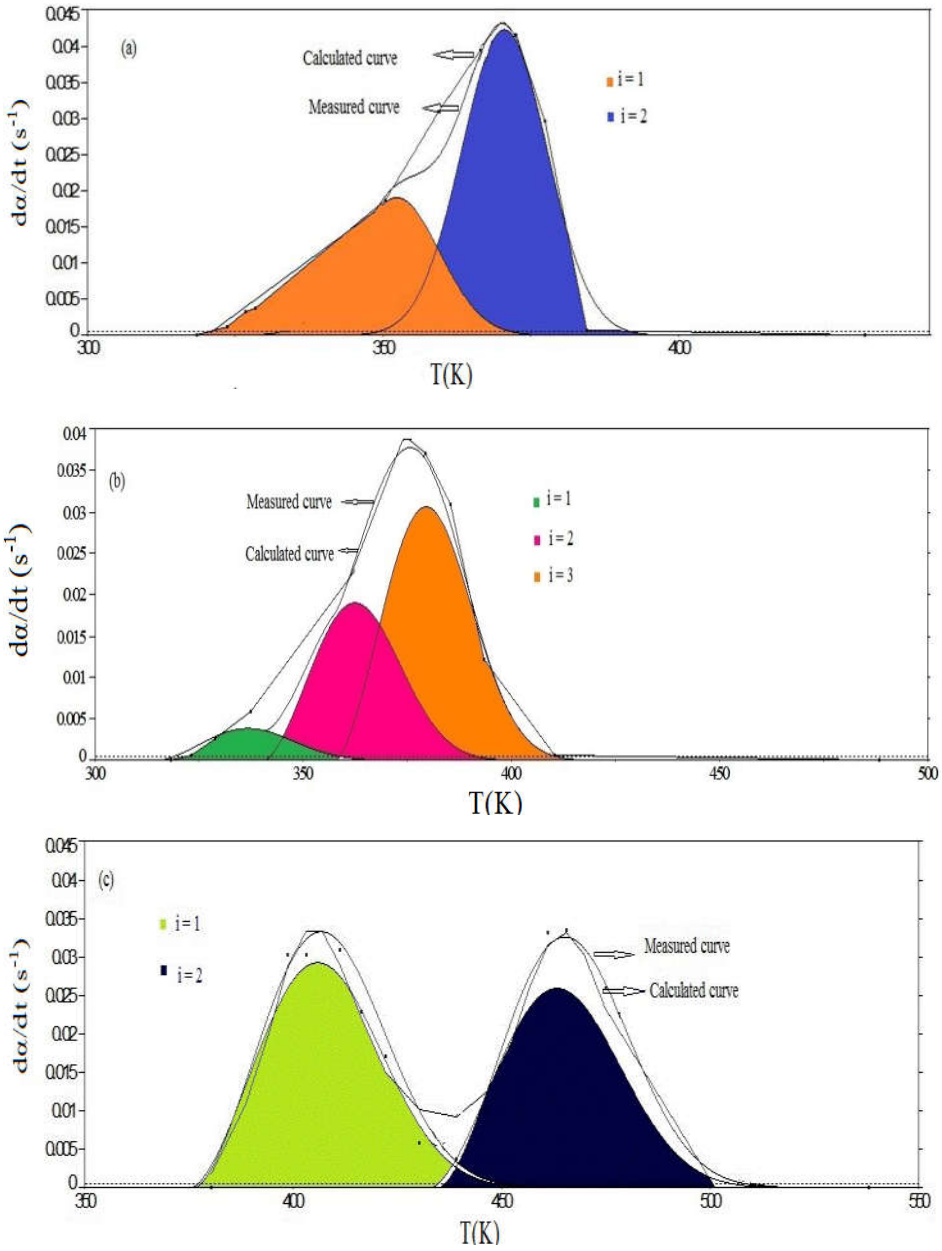

Fig. 12 The results of kinetic deconvolution analysis for the thermal decomposition of the samples CC_1 (a) CC_2 (b) and CC_5 (c) under linear non-isothermal condition at $\beta = 5$ $Kmin^{-1}$.

The amount of activation energy and pre-exponential factor needed for sample CC_5 are higher than all compositions which are studied. The value of Ea_i is 67.90 ±0.099 kJmol^{-1} (for i = 1) and 73.87 ± 0.0026 kJmol^{-1} (for i = 2). The observed value of A_i required for i = 1 is (1.01 ± 0.0034) ×10^8 and for i = 2 is (3.42 ± 0.0048) ×10^8. Therefore the values of Ea_i and A_i allow the order of $CC_4 < CC_3 < CC_1 < CC_2 < CC_5$. The reaction rate behavior of each overlapping mass-loss steps of CC_1 is best described with SB (*0*, *n*, *0*); $(1-\alpha)^n$ whereas sample CC_2 with SB (*m, n*, 0) with $m = 0.18 \pm 0.008$ and $n = 0.2 \pm 0.003$ (for i = 1) and $m = 0.06 \pm 0.009$ and $n = 1.5 \pm 0.03$ (for i = 2). The samples CC_3, CC_4, CC_5 are best described with empirical model function SB (*m, n*, *p*); $\alpha^m (1-\alpha)^n [-ln (1-\alpha)]^p$.

Table 2 Average values of kinetic parameters optimized for each reaction step of thermal dehydration of different samples

Sample	i	Ea_i (kJmol^{-1})	A_i (sec)$^{-1}$	R^2
CC_1	1	45.79 ± 0.0085	(4.80 ± 0.0096) × 10^6	0.9446
	2	42.13 ± 0.0075	(3.11 ± 0.009) × 10^6	0.9378
CC_2	1	68.00 ± 0.0011	(2.23 ± 0.0018) ×10^8	0.9887
	2	66.12 ± 0.0012	(1.00 ± 0.0089) ×10^8	0.9654
	3	58.80 ± 0.0079	(9.46 ± 0.0026) ×10^7	0.9986
CC_3	1	50.50 ± 0.014	(9.12 ± 0.0025) ×10^6	0.9663
	2	45.30 ± 0.0.009	(2.48 ± 0.0067) ×10^6	0.9876
	3	46.17 ± 0.0.0099	(2.57 ± 0.0032) ×10^6	0.9947
CC_4	1	34.85 ± 0.0.008	(3.2 ± 0.002) ×10^4	0.9896
	2	37.30 ± 0.0007	(9.54 ± 0.0087) ×10^4	0.9467
	3	37.69 ± 0.0034	(7.37± 0.0097) ×10^4	0.9369
CC_5	1	67.90 ± 0.099	(1.01 ± 0.0034)×10^8	0.9921
	2	73.87 ± 0.0026	(3.42 ± 0.0048)×10^8	0.9562

3.5. Conclusion

In the present work, thermal dehydration kinetics of cerium oxalate rods in presence of Ca(II) in varying compositions was studied. The introduction of Ca(II) impedes the diffusional removal of water vapor and has significant effect in thermal stability of the sample having a composition of 10 mass (%) of calcium oxalate. The method of kinetic deconvolution is used as a tool for characterizing the partially overlapped reaction. Performance of kinetic deconvolution was evaluated based on an accumulative equation for the independent processes in view of peak deconvolution and kinetic evaluation. Mixed cerium oxalate follows three independent process for the removal of water, whereas two independent process for pure cerium and calcium oxalates. The requisite amount of activation energy for each partially overlapped independent process is calculated using isoconversional methods such as KAS, FWO and iterative isoconversional procedure. The presence of higher amount of calcium oxalate in cerium oxalate rods decreases the amount of activation energy required for proceeding thermal dehydration. The values of Ea_i and A_i for each independent process of dehydration reaction of mixed samples allow the order $CC_4 < CC_3 < CC_2$. With increase in the mass percentage of calcium oxalate, crystalline nature of the mixture arises. Therefore, it is interesting to study about the effect of addition of CaC_2O_4 lower than 10 m/m (%) for the excellent thermal properties of hydrated cerium oxalate.

3.6. References

1. Gopalakrishnamurthy HS, Rao MS, Kutty TRN. Thermal decomposition of titanyl oxalates. II. Kinetics of decomposition of barium titanyl oxalate. *J Inorg Nucl Chem*. 1975;37:1875-1878.

2. Patra BS, Otta S, Battamisra SD. A kinetic and mechanistic study of thermal decomposition of strontium titanyl oxalate. *Thermochim Acta*. 2006;441:84-88.

3. Galway AK, Brown ME. An appreciation of the chemical approach of V. V. Boldyrev to the study of decomposition of solids. *J Therm Anal Calorim*. 2007;90:9-22.

4. Duval C. *Inorganic Thermo Gravimetric Analysis. 2nd Ed. Amsterdam: Elsevier;*; 1963.

5. Muraleedharan K, Labeeb P. Kinetics of the thermal dehydration of potassium titanium oxalate,$K_2TiO(C_2O_4)_2.2H_2O$. *J Therm Anal Calorim*. 2012;109:89–96.

6. Galina S, Gert W. Enthalpy of dissolution and thermal dehydration of calcium oxalate hydrates. *J Therm Anal Calorim*. 2015;119:2063-2068.

7. Muraleedharan K, Viswalakshmi CH, Sarada K. Synthesis, characterization and thermal dehydration and degradation kinetics of chitosan Schiff bases of o-, m- and p- nitrobenzaldehyde. *Polym Bull*. 2016:1-16.

8. Honcova P, Svoboda R, Pilny P, et al. Kinetic study of dehydration of calcium oxalate trihydrate. *J Therm Anal Calorim*. 2016;124:151–158.

9. Chambre' D, Iditoiu C, Segal E. Non-isothermal dehydration kinetics of acrylic ion exchange resins. *J Therm Anal Calorim*. 2007;88:673–679.

10. Jankovic B, Adnadevic B, Jovanovic J. Isothermal kinetics of dehydration of equilibrium swollen poly (acrylic acid) hydrogel. *J Therm Anal Calorim*. 2008;92:821–827.

11. Jakupec MA, Unfried P, Keppler BK. Pharmacological properties of cerium compounds. *Rev Physiol Biochem Pharmacol*. 2005;153:101-111.

12. George BMD, Harry WMD. The use of cerium oxalate for the relief of vomiting: an experimental study of the effects of some salts of cerium, lanthanum, praseodymium, neodymium and thorium. *Arch Intern Med*. 1909;6:517-531.

13. Zhang Y, Andersson S, Muhammed M. Nanophase catalytic oxides: I. Synthesis of doped cerium oxides as oxygen storage promoters. *Appl Catal B Environ*. 1995;6:325-337.

14. Payakgul W, Mekasuwandumrong O, Pavarajarn V, Praserthdam P. Effects of reaction medium on the synthesis of TiO_2 nanocrystals by thermal decomposition of titanium(IV)n-butoxide. *Ceram Int*. 2005;31:391-397.

15. Sungmin C, Eunseuk P, Minsu K, Jongsoo J. Photocatalytic degradation of methylene blue with TiO_2 nanoparticles prepared by a thermal decomposition process. *Powder Technol*. 2010;201:171–176.

16. Yan M, Mori T, Zou J, Drennan J. Effect of grain growth on densification and conductivity of ca-doped CeO_2 electrolyte. *J Am Ceram Soc*. 2009;92:2745-2750.

17. Ying M, Xiaodi W, Hassan AK, Bin Z, Mamoun M. Enhanced ionic conductivity in calcium doped ceria-carbonate electrolyte: a composite effect. *Int J Hydrogen Energy*. 2012;37:19401-19406.

18. Unger KK, Kreysa G, Baselt JP. *Characterization of Porous Solids. I st ed. Amsterdam: Elsevier;*; 2000.

19. Overs A, Riess I. Properties of the solid electrolyte gadolinia-doped ceria prepared by thermal decomposition of mixed cerium-gadolinium oxalate. *J Am Ceram Soc*. 1982;65:606-609.

20. Ubaldini A, Artini C, Costa GA, Carnasciali MM, Masini R. Thermal decomposition of mixed Ce and Gd oxalates and thermal properties of mixed Ce and Gd oxides. *J Therm Anal Calorim*. 2006;84:207-211.

21. Nobuyoshi K, Daisuke K, Tomoyasu K. Aragonite crystal growth and solid-state aragonite − calcite transformation: a physico − geometrical relationship via thermal dehydration of included water. *Cryst Growth Des*. 2013;13:2238-2246.

22. Kitabayashi S, Koga N. Physico-geometrical mechanism and overall kinetics othermally induced oxidative decomposition of tin(II) oxalate in air : formation process of microstructural tin(IV) oxide. *J Phys Chem C*. 2014;118:17847-17861.

23. Nakano M, Wada T, Koga N. Exothermic behavior of thermal decomposition of sodium percarbonate : kinetic deconvolution of successive endothermic and exothermic processes. *J Phys Chem A*. 2015;119:9761-9769.

24. Koga N, Goshi Y, Yamada S, Pe´rez-Maqueda LA. Kinetic approach to partially overlapped thermal decomposition processes; co-precipitated zinc carbonates. *J Therm AnalCalorim*. 2013;111:1463-1474.

25. Miguel G, Juan H, Leticia B, Joaquin N, Mario ERG. Characterization of calcium carbonate, calcium oxide and calcium hydroxide as starting point to the improvement of lime for their use in construction. *J Mater Civ Eng*. 2009;21:625-708.

26. Vimal G, Kamal PM, Biju PR, Joseph C, Unnikrishnan NV, Ittyachen MA. Structural studies and luminescence properties of CeO_2:Eu^{3+} nanophosphors synthesized by oxalate precursor method. *Appl Nanosci*. 2015;5:837-846.

27. Gabal MA, Elroby, Shabaan AK, Obaid AY. Synthesis and characterization of nano-sized ceria powder via oxalate decomposition route. *Powder Technol*. 2012;229:112-118.

28. Oman Z, Haznan A, Widayanti W. Synthesis and characterization of nanostructured CeO_2 with dyes adsorption property. *Process Appl Ceram*. 2014;8:39-46.

29. Koga N. Ozawa's kinetic method for analyzing thermoanalytical curves. *J Therm Anal Calorimrm*. 2013;113:1527-1541.

30. Kissinger HE. Reaction kinetics in differential thermal analysis. *Anal Chem*. 1957;29:1702-1706.

31. Flynn JH, Wall LA. A quick, direct method for the determination of activation energy from' thermogravimetric data. *Polym Lett*. 1966;4:323-328.

32. Ozawa T. A new method of analyzing thermo gravimetric data. *Bull Chem Soc Jpn*. 1965;38:1881-1882.

33. Zhipeng C, Qian C, Sen L, et al. Application of isoconversional calculation procedure to non-isothermal kinetic study: III. thermal decomposition of ammonium cobalt phosphate hydrate. *Thermochim Acta*. 2012;543:205-210.

34. Liqing L, Donghua C. Application of iso-temperature method of multiple rate to kinetic analysis: dehydration for calcium oxalate monohydrate. *J Therm Anal Calorim*. 2004;78:283-293.

35. Chunxiu G, Yufang S, Donghua C. Comparative method to evaluate reliable kinetic triplets of thermal decomposition reactions. *J Therm Anal Calorim*. 2004;76:203-216.

36. Pérez-Maqueda LA, Criado JM. Accuracy of Senum and Yang's approximations to the Arrhenius integral. *J Therm Anal Calorim*. 2000;60:909-915.

37. Yoshikawa M, Yamada S, Koga N. Phenomenological interpretation of the multistep thermal decomposition of silver carbonate to form silver metal. *J Phys Chem C*. 2014;118:8059-8070.

38. Yoshikawa M, Goshi Y, Yamada S, Koga N. Multistep kinetic behavior in the thermal degradation of poly (L□lactic acid): a physico-geometrical kinetic interpretation. *J Phys Chem B*. 2014;118:11397-11405.

39. Sestak J, Berggren G. Study of kinetics of the mechanism of solid state reactions at increasing temperatures. *Thermochim Acta*. 1971;3:1-12.

40. Pe´rez-Maqueda LA, Criado J M, Sa´nchez-Jime´nez PE. Combined kinetic analysis of solid-state reactions: a powerful tool for the simultaneous determination of kinetic parameters and the kinetic model without previous assumptions on the reaction mechanism. *J Phys Chem A*. 2006;110:12456-12462.

41. Málek J, Criado J M. Empirical kinetic models in thermal analysis. *Thermochim Acta*. 1992;203:25-30.

42. Šesták J. Diagnostic limits of phenomenological kinetic models introducing the accommodation function. *J Therm Anal*. 1990;36:1997-2007.

43. Nusrath K, Muraleedharan K. Effect of Ca(II) additive on the thermal dehydration kinetics of cerium oxalate rods. *J Therm Anal Calorim*. 2017;128:541-52.

NUSRATH. K “SYNTHESIS AND KINETICS OF FORMATION OF CERIA AND CERIA BASED MATERIALS via THERMAL DECOMPOSITION OF OXALATES”. THESIS. DEPARTMENT OF CHEMISTRY, UNIVERSITY OF CALICUT, 2018.

4.1. Introduction

Today, in 21st century, world has been facing severe environmental problems, that arises principally due to the evolution of exhaust gases. Chief constituents of exhaust gases are CO, NO_x and hydrocarbons. The remedial aspects for the persistence of the environment in hefty condition have been the challenging areas of many researchers. Throughout the recorded history of the oxides of rare earth elements, cerium has been the most important class of compounds, which stand as an indispensable component in catalyst promoters or supporters in the automobile mufflers and for the toxic emission control (*e.g.*, CO, hydrocarbon oxidation and NO_x reduction)[1]. Nowadays, many researchers have been going on for the better catalytic performance of ceria. Ceria achieved special optical, electrical and magnetic properties that were given by its particular electronic configuration. Vaishak Nair *et al*[2] reported that CeO_2 can be used as catalyst in the production of guaiacol and its derivatives by fast pyrolysis of alkali lignin. CeO_2 promote the formation of hydroxyl radicals *via* thermal activation, which then take part in free radical reaction to form guaiacol and its derivatives. Recently ceria materials with nano sized[3], textured[4] and one dimensional[5–8] (involving nanotubes, nanowires and nanorods) structures have been prepared by different synthetic routes. Feng Zhang *et al*[9] prepared narrowly distributed single crystalline CeO_2 nano particles using cerium nitrate and hexamethylenetetramine at room temperature. They established that larger the lattice parameter in nano crystalline ceria makes it to become a more efficient electrolyte material for fuel cell. Tok *et al*[10]

synthesized nano crystalline CeO_2 from two precursors cerium acetate and cerium hydroxide via hydrothermal route in acidic and basic P^H condition. They assayed the effect of duration of reaction on the properties of the resultant specimen CeO_2. Using the amino acid as crystal growth modifiers, mesoporous ceria with hierarchical nano architectures have been synthesized[11]. It has been observed that CeO_2 doped with Ca^{2+} have maximum availability of oxygen because it creates oxygen vacancies with an average spacing close to that of O^{2-}. Availability of oxygen vacancies tends to increase the oxygen storage capacity of the oxide. It has been observed that the oxygen storage capacity of CeO_2 can be enhanced up to about 40% with doping of Ca^{2+}. Doping of ceria with Pb^{2+} leads to the increment of redox activity of ceria[12]. Miyazako *et al*[13] prepared CeO_2 nano particle by rapid thermal decomposition by microwave heating of cerium oxalate and concluded that shape of resultant specimen depends on the precursor material shape. Masui *et al*[14] disclosed excellent redox activity and enhanced thermal stability of CeO_2-ZrO_2 solid solution, prepared from cerium-zirconyl oxalates by means of thermal decomposition in an argon flow at 1273K followed by oxidation at 673-873K in air. Kenji Higashi *et al*[15] established significant changes in thermal decomposition temperatures of solid solution oxalates of Ce(III) with rare earth elements Yb, Y, La, Nd, Sm and Gd and accounted the contribution of ionic radius of elements in thermal behavior of cerium oxalates. Depending on the ionic radius of doped oxides, the lattice parameter of the oxide also changes[15]. Because of the higher melting point of ceria (2400^{o}C), it has high temperature application such as total oxidation reaction (*e.g.*, natural gas combustion)[16].

There are wide ranges of synthetic methods for the preparation of CeO_2[17-20]. Thermally induced oxidative decomposition of Ce(III) oxalate is an important source for obtaining CeO_2 particle with different morphologies. The morphological characteristics of prepared CeO_2 vary depending on the particle size and morphology of cerium oxalate. Further, the oxalate powders have better chemical and morphological control over the final product. Particle size, morphology and surface area are the important characteristics responsible for the quality of the functionalities. Oxide solid solution or composite oxide can be prepared from the oxalate precursor at its decomposition temperature under well controlled conditions. Thermal decomposition of cerium oxalate at 600^oC for 3h yields porous spherically shaped ceria powders having size of the particle smaller than 100nm[15]. Decomposition of hydrated cerium oxalate occurs mainly in two stages; the dehydration (of 10 molecules of water around 403K) followed by the decomposition (around 633K) to ceria [21]as:

$$Ce_2(C_2O_4)_3.10H_2O \rightarrow Ce_2(C_2O_4)_3+10H_2O \quad (1)$$

$$Ce_2(C_2O_4)_3 \rightarrow 2CeO_2+2CO_2+ 4CO \quad (2)$$

The thermal decomposition processes of many of the inorganic solids are significantly controlled by physico-geometrical reaction mechanism[22–26]. In a thermally induced reaction, surface product layer is formed in the early stages of the reaction. The geometrical constraints occurring between the surface product layer and the inward advancement of the reaction interface generated at the boundary between surface product layer and internal reactant[27–31]. As the

reaction progresses, the action of surface product layer came in to act. The inhabitation effect of surface product layer on the diffusional removal of gaseous products generated at the internal reaction interface causes the formation of self-generated reaction conditions at the reaction interface. Formation of pores on the surface of solid product is closely related to the formation of a surface product layer at the early stage of the reaction and the subsequent diffusional removal of gaseous products produced by the internal reaction[25]. This occurrence of solid-gas reactions is responsible for the morphological characteristics of the product, metal or metal oxides[25]. Majority of the solid state reactions pass off *via* crack formation on the surface product layer and the splitting of the reacting particle along a specific crystallographic direction[32–34].

The elucidation of the mechanism and kinetics of thermal decomposition would contribute to the evaluation of thermal stability, life time, safe storage and fundamental information for technological applications. Font *et al*[35] discussed the correlation model with optimized kinetic parameters with respect to the pyrolysis of olive oil. They correlated dynamic and isothermal runs with same set of parameters and satisfactorily reproduced the experimental results. Researchers established the practical usefulness of the kinetic deconvolution for partially overlapping multistep thermal decomposition process of solids[25,26]. Comparisons were made with experimental deconvolution by thermo analytical techniques and mathematical deconvolution using statistical fitting function. Performance of kinetic deconvolution was evaluated based on

accumulative kinetic equation for the independent process which overlaps partially in views of peak deconvolution and kinetic evaluation [26].

In the present work, kinetic and mechanistic features of the synthesis of micro structural rods of CeO_2 *via* the oxidative thermal decomposition of cerium oxalate in air and the effect of dry mixing of 10 mass (%) calcium oxalate with cerium oxalate upon the reaction pathway and mechanism were investigated by thermo analytical techniques under linear non-isothermal condition. The physico-geometrical kinetic behavior of the reaction was illustrated through detailed kinetic analyses using the kinetic deconvolution method. The reaction was traced by thermo analytical measurements and interpreted the kinetic results on the basis of kinetic analysis of thermo analytical curves and complimented the rendition by morphological and structural observations.

4.2. Experimental

4.2.1. Materials

All the reagents were of analytical grade and used without any further purification[36]. The chemicals used for the study are cerium oxalate decahydrate (99.9%, Indian Rare Earth Products Ltd, Cochin), $CaCO_3$ (Sigma-Aldrich), 1M HCl, NH_4OH and $(NH_4)_2C_2O_4$ (Merck, India).

4.2.2. Preparation of calcium oxalate dihydrate

Calcium chloride is prepared from $CaCO_3$ and 1M HCl. The oxalate is prepared by using ammonium oxalate as precipitating agent. The precipitate is collected, washed with ethanol and water and dried in an air oven at 60^oC.

4.2.3. Preparation of mechanical mixtures of oxalates of cerium and calcium

The particle size of the oxalates of cerium and calcium were fixed in the range 95-105μm. Composition of oxalates of cerium and calcium (CC_2) was prepared by thorough mechanical mixing of cerium oxalate (90 mass (%)) and calcium oxalate (10 mass (%)) in an agate mortar. Cerium oxalate (100 mass (%)) (CC_1) was also sieved through the mesh and fixed the size in the range 95-105μm.

4.2.4. Preparation of pelletized samples

The pure (CC_1) and mixed samples (CC_2) were well-ground and the powdered samples were pressed using the hydraulic pellet press (KP, SR. No. 1718) under a pressure of $50Kgcm^{-2}$. Thermally heated samples of both CC_1 (623 and 873K) and CC_2 (623 and 953K) were also pelletized using hydraulic press under the same pressure.

4.2.5. Characterization of the sample

Characterization of the samples was done by FT-IR and XRD. The appearance and morphology of the samples were observed using an optical and scanning electron microscopy instrument.

4.2.6. Measurement of thermal behavior

TG measurements were made at four different heating rates, viz. 5, 10, 15 and 20 $Kmin^{-1}$. Duplicate runs were made under the similar conditions and found that the data overlap with each other, indicating satisfactory reproducibility. The samples heated at 873K (for CC_1) and 953K (for CC_2) in flowing atmosphere of air at a heating rate of β = 5 K $min^{-1}$and kept at a constant temperature for 20min and measured XRD pattern of each sample immediately after leaving from the furnace. The optical microscopic views of thin pellets of the samples heated at different temperatures were also observed. The optical band gap (*Eg*) of the decomposed product of each sample was calculated from UV-Visible reflectance which was measured using UV-Vis diffuse reflectance spectrum.

4.3. Results and discussions

4.3.1. Sample characterization

Fig. 1a shows the typical microscopic image of thin pellets of cerium oxalate, the surface of cerium oxalate crystals consists of rod-like crystals (Fig. 1b) having thickness in the range 1.71-2.01μm. Fig. 1c shows the microscopic image of thin pellets of cerium-calcium oxalate crystals and the SEM image (Fig. 1d) shows slight change in the rod-like crystals of cerium oxalate due to the addition of calcium oxalate. Calcium oxalate exist as separate crystals, covering the surface of cerium oxalate rods, which causes the breakdown of the rods due to the strain experienced on the surface of the rods.

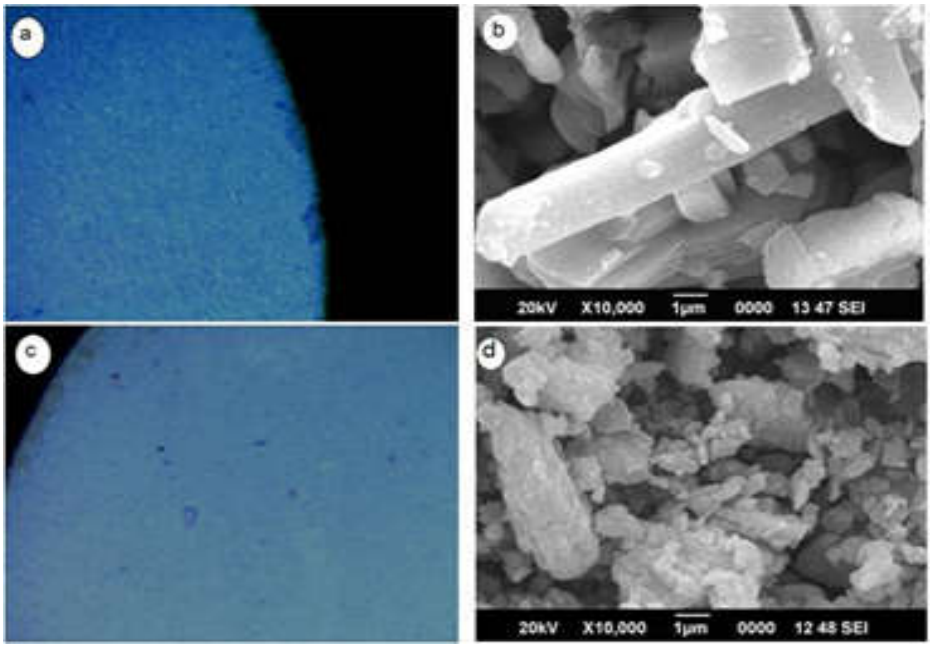

Fig. 1 Microscopic images of cerium oxalate and mixture of cerium and calcium oxalate; Optical microscopic image of cerium oxalate thin pellet (a), SEM image of anhydrous cerium oxalate heated at 623K (b), optical image of cerium-calcium oxalate thin pellet (c) and SEM image of anhydrous cerium-calcium oxalate heated at 623K (d).

FT-IR spectra and XRD patterns of the samples are shown in Fig. 2. Fig. 2a represents characteristic XRD pattern of cerium oxalate decahydrate with significant reflections at 2θ values of 20.94, 25.29, 26.12, 32.14, 32.75, 34.24, 39.58, 42.17, 44.24 and 46.18^{o}. The reflections from the sample indicate that cerium oxalate crystallizes in the monoclinic system (JCPDS. No. 20-0268). The characteristic XRD pattern of calcium oxalate dihydrate, shown in Fig. 2b, exhibit major reflections at 2θ values of 24.23, 32.51, 35.82 and 43.39^{o} (JCPDS. ASTM File No. 15-762). The powder X-ray diffraction patterns of the samples reveal good crystalline nature of calcium oxalate than cerium

oxalate. In the FT-IR spectra, the broad band observed at 3080-3433cm^{-1} corresponds to water molecules in hydrated samples which are removed only at higher temperature[37]. The very strong peak observed at 1633.9 (Fig. 2c) and 1622.45 cm^{-1} (Fig. 2d) is attributed to combined effect of asymmetric stretching and bending of water molecules[38]. The strong peak observed at 1318.39 (Fig. 2c) and 1317.01cm^{-1} (Fig. 2d) correspond to the asymmetric stretching of CO_2 molecule associated with oxalate ligand group[38,39]. The band observed at 523.8 (Fig. 2c) and 514.4 cm^{-1} (Fig. 2d) corresponds to the M-O stretching frequency[37, 40].

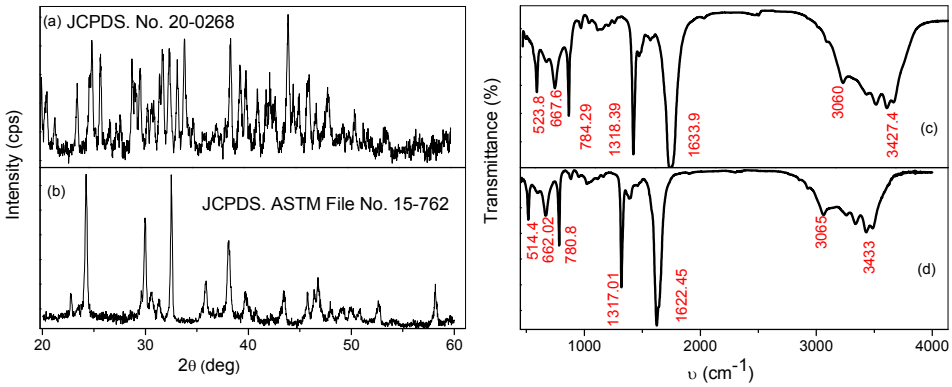

Fig. 2 The XRD patterns of cerium oxalate decahydrate (a) and calcium oxalate dihydrate (b) and the FT-IR spectra of cerium oxalate decahydrate (c) and calcium oxalate dihydrate (d).

4.3.2. Characterization of thermal decomposition behavior

Fig. 3 shows the results of TG measurements with two samples, CC_1 and CC_2, at different β values. The oxidative thermal decomposition reaction of the solids composed of multiple constituent chemical processes that occurs successively and each constituent reaction provide differently to the overall thermal effect (to be either

exothermic or endothermic)[27]. Therefore, the TG curves of the sample CC_1 shows two distinguishable mass loss processes, one at temperature below 575 K and one at temperature above 575 K. A mass loss accompanying the dehydration of water molecules is observed over the temperature region of 325-445 K, prior to the thermal decomposition of cerium oxalate in the higher temperature region of 600-760 K. The mass loss value for the overall thermal decomposition process for the sample CC_1 is 52.12%, which is in good agreement with the ideal reaction pathway for the formation of ceria from cerium oxalate decahydrate (52.48%). In Fig. 3b there exists a third mass loss step with small amplitude at 873K due to the decomposition of calcium carbonate. Hence for the sample CC_2, the overall mass loss value was increased to 55.45% due to the contribution from the thermal decomposition of calcium oxalate along with cerium oxalate. The TG curves of CC_2 sample is systematically shifted to higher temperature with increase in the value of β, whereas the TG curves of the sample S_0 show anomaly with β = 10 and 20 K min^{-1}.

The processes of multistep mass loss behavior are controlled by physico-geometrical constraints which may occur due to the changes in reaction conditions as the reaction advances [23]. Fig. 3b shows partially overlapping multistep process which would reflect in complex reaction pathway. Koga *et al*[27] stated that complex reaction proceeds in a combination of multistep behavior controlled by physico-geometrical features of solid state reactions and successive chemical reaction schemes.

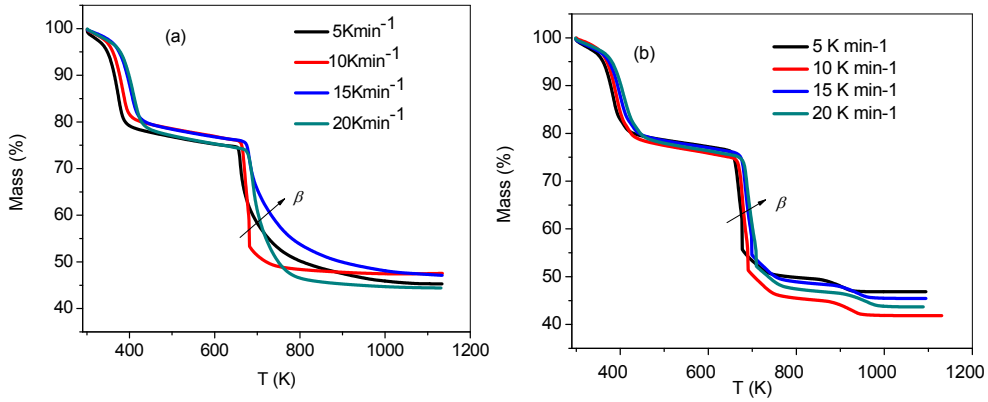

Fig. 3 The TG curves for the thermal decomposition of samples (m_0 = 10mg) in flowing air (100mLmin^{-1}) at different β values; CC_1 (a) and CC_2 (b).

Fig. 4 shows DTG curves for the thermal decomposition process of the two samples, CC_1 and CC_2. The DTG curves indicate multistep process for the thermal decomposition of cerium oxalate, CC_1 (Figs. 4a, b and c) and partially overlapped multistep reaction for cerium-calcium mixed oxalate, CC_2 (Figs. 4d, e and f). The reaction process of the sample CC_1, at both lower and higher temperature, are arrested at the very beginning when the sample is heated at a β value of 10 and 20 K min^{-1}, whereas the ratio of mass loss was found to be higher at these heating rates. Moreover at these heating rates, the curves exhibited sigmoidal shape for the lower temperature reaction.

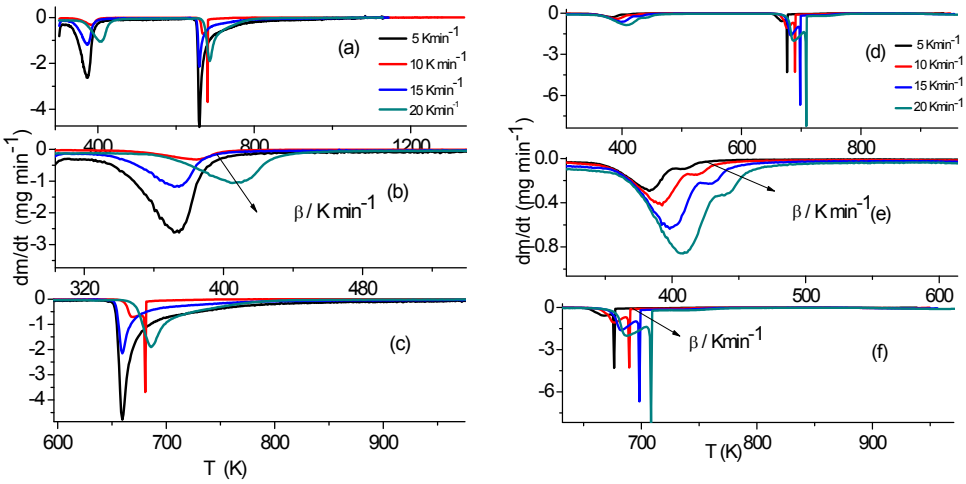

Fig. 4 The DTG curves of CC_1 and CC_2: overall thermal decomposition of CC_1 (a), first (b) and second (c) stage of CC_1, overall thermal decomposition of CC_2 (d), first (e) and second (f) stages of CC_2.

It has been reported that both the reaction time and temperature have significant influence on the crystallographic orientation of the ceria particles formed[16, 41]. Hence the β value of 10 and 20Kmin^{-1} have marked influence on thermal decomposition of cerium oxalate, which make different shape to the DTG curve compared with other heating rates. The observed changes in the shape of mass loss curve with β certainly indicate a change in the mechanistic features of the reaction. The addition of calcium oxalate to cerium oxalate cause a shift in the temperature range of the reaction process, both at lower and higher temperature, to the higher values, *i.e.*, to 340-485 and 645-790 K respectively.

For both higher and lower temperature processes of the sample CC_2, it has been observed a shift in the DTG curves to the higher

values with increasing the value of β. However, with decreasing β value, there occurs increase in mass loss ratio for both high and low temperature process for the sample CC_2. In the DTG curves of the sample CC_2 (Figs. 4d, e and f) the shoulder peaks observed is associated with the dehydration and oxidative process. This can be ascribed due to the change in the self-generated reaction condition, which is generated at the reaction interface as the reaction progresses. The sample CC_2, a mixture of cerium oxalate and calcium oxalate, upon thermal treatment under controlled condition, there occurs thermal decomposition of calcium oxalate along with cerium oxalate leading to partial overlapping of the reaction which brings changes in the self-generated reaction condition produced by cerium oxalate[23] and therefore, the shape of the DTG curves is altered.

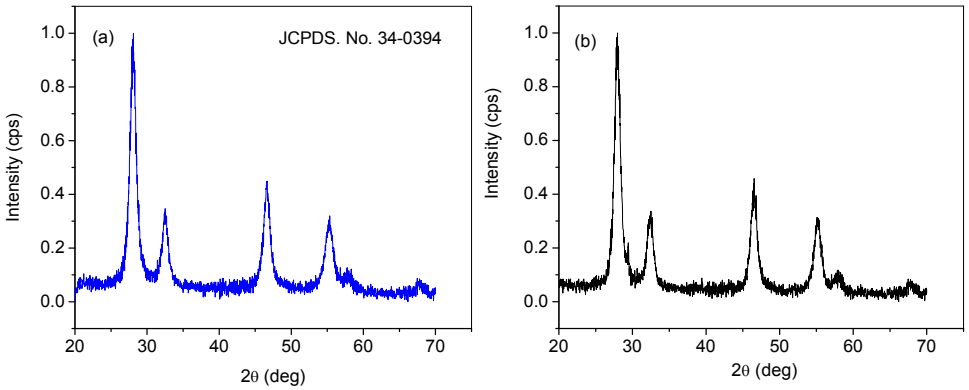

Fig. 5 The powder XRD patterns of the thermally treated samples of CC_1 and CC_2; sample CC_1 at 873 (a) and CC_2 at 953 K (b).

The changes of XRD patterns of these samples which are calcined at 873 (for CC_1) and 953K (for CC_2) were represented in Figs.

5a and b respectively. In Fig. 5b, there exists an additional peak at 2θ value 29.15^{o} and this confirms that the sample CC_2 at 953K forms mixed oxides of cerium and calcium. Masui *et al* [14] reported that oxidative process induces a lattice contraction and hence all peaks in Figs. 5a and b are shifted to higher angle compared to those in Fig. 2a. The redox reactions in pure and mixed oxalates of cerium are associated with Ce^{3+}/Ce^{4+}couple[14] and the contraction of the lattice is therefore due to the oxidation from Ce^{3+} (0.633nm) to Ce^{4+} (0.55 nm). The XRD pattern of CeO_2 confirms that ceria crystallizes in cubic fluorite structure. In cubic structure, the mobility of oxygen and desorption were strongly favored than tetragonal structure[14] and hence lower energy is required for the thermal decomposition. Since Ca^{2+} does not incorporated into the lattice of ceria frame work (Fig. 5b), the lattice strain was absent to the fluorite structure of ceria. This confirms that ceria retains its cubic structure in mixed oxides. The average crystallite size of CeO_2 calculated using the Scherrer equation from XRD pattern is 9.026nm. The cubic fluorite structure of ceria gives isolated peaks which confirm the poly crystalline nature of CeO_2 nanoparticle[36].

The FT-IR spectra of the samples treated at 873K (for CC_1) (Fig. 6a) and 953K (for CC_2) (Fig. 6b) were used for the characterization of thermal behavior. The band corresponds to 3028-30680 cm^{-1} is due to -O-H stretching of the adsorbed water molecules on the surface of the oxide. This hydroxyl group is eliminated only at higher temperature[42]. The absorption band in the region of 862.8cm^{-1} in Fig. 6a is associated with δ (Ce-O) bond[40] which undergoes blue

shift to 876.98 cm^{-1}in the sample CC_2 (Fig. 6b). This occurs due to the strengthening of δ (Ce-O) bond due to the interaction of Ca^{2+} with oxygen atom of carbonyl group during the early stages of the reaction. But the band observed at 424.73cm^{-1} represents Ce-O stretching frequency of the product formed, CeO_2 (Fig. 6a)[36,40,43] which undergo red shift to 413.19 cm^{-1} (Fig. 6b). This can be attributed to the interaction of Ca^{2+} with the unpaired electrons situated in the oxygen atom of the -O-Ce-O- bond during thermal decomposition process. The sharp band observed at 714.9cm^{-1} corresponds to the Ca-O stretching frequency[37].

For the determination of optical band gap, the samples were heated at higher temperature and for the successive interpretation of thermal behavior of the mixed cerium oxalate; the UV-Vis diffuse reflectance spectrum was measured. Fig. 7a shows the UV-Vis diffuse reflectance spectra of the samples CC_1 and CC_2 heated at 873 and 953K respectively and it shows obvious shift towards lower wavelength, *i.e.*, blue shift, due to the presence of Ca^{2+}. The presence of Ca^{2+} cause a decrease in the particle size of CeO_2 rods[44,45] *via* the breaking down of rods due to the strain experienced on the surface of the rods.

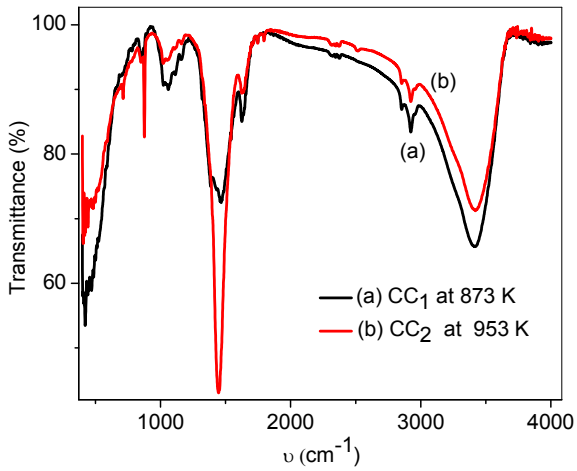

Fig. 6 The FT-IR spectra of CC_1 at 873 (a) and CC_2 at 953K (b).

An estimate of the optical band gap, *Eg*, can be determined by the Tauc-equation $(\alpha hv)^n=B(hv-Eg)$ where *hv* is the photon energy, α is the absorption coefficient, *B* is a constant relative to the material and *n* is either 2 for direct transition, or 1/2 for an indirect transition. The $(\alpha hv)^2$ versus *hv* curves (Tauc-plots) is shown in Figs. 7b and 7c, which reveals that the band gap increases from 1.546 to 2.05eV supporting the blue shift. The reported value of *Eg* corresponding to bulk CeO_2 is 1.82 eV[46]. The increase in the value of *Eg* of a material reflects the decrease of conducting properties. It has been reported that electron donors accelerate thermal mass-loss process and electron acceptors retard the thermal process[47,48]. The findings in the UV-Vis diffuse reflectance spectra and Tauc-plots of thermally treated samples at higher temperatures indicate possible contribution of Ca^{2+} to impede thermal decomposition process of cerium oxalate. Therefore, the presence of CaO along with ceria causes a decrease in the conducting properties of CeO_2. Hence it can be stated that the presence of Ca^{2+} cause to retard the thermal decomposition of cerium oxalate, whereas increases its thermal stability.

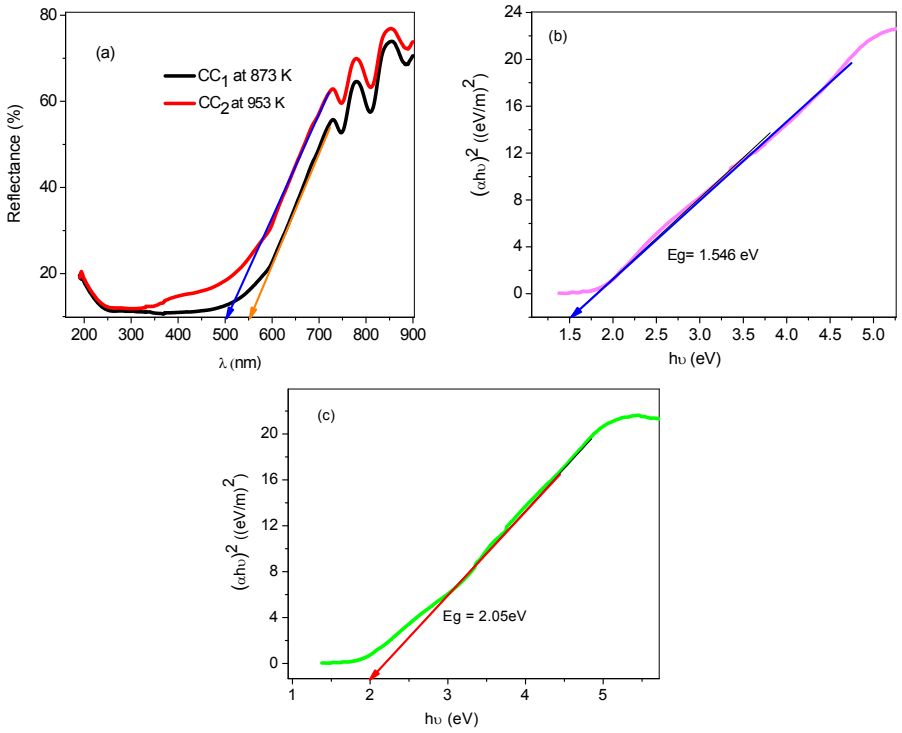

Fig. 7 The UV-Vis diffuse reflectance spectra of the samples CC_1 and CC_2 (a), Tauc-plot of the sample CC_1 heated at 873K (b) and Tauc-plot of the sample CC_2 heated at 953K(c).

4.3.3. Morphological characterization

The SEM and optical microscopic observation of each sample at different stages of decomposition reaction were performed inorder to correlate the complex reaction pathways with the physico-geometrical characteristics of the reaction. Microstructure of precursor and resultant specimen are exhibited in Figs. 8b & d. All resultant specimens acquired rod shape and formed secondary particles along with aggregated particles. Average grain size of primary and secondary particles of aggregated CeO_2 is 662.42nm and 305.94nm respectively[36]. Hence SEM image of ceria depicted that polycrystalline

CeO_2 nanoparticles are aggregated to form micro structural rods of ceria[36]. Fig. 8a shows some deformations present in the surface of the sample CC_1 which can be related to the loss of water molecules. Fig. 8b shows the surface textures of the sample $CC_{1,}$ which is dehydrated during the first stage of decomposition reaction (Fig. 4b). It shows significant boundaries between the rods, which are accompanied by the holes. This is possibly served as the diffusion channels for the removal of H_2O molecules and at this stage the cerium oxalate possess rods of smooth surfaces. Upon thermal decomposition, this smooth surface product layer of cerium oxalate gradually impedes the diffusional removal of CO_2 which is generated by the internal reaction. Therefore, this inhabitation of CO_2 release causes for the change in the self-generated reaction condition. At the end of reaction, CO_2 is diffused through the channels created by the internal pressure in the surface product layer. Fig. 8c shows the optical image of solid film of CeO_2. The surface product layer of CeO_2 is then divided into rods (Fig. 8d). These CeO_2 particles are sintered gradually and which form smooth surfaces.

Figs. 9a and b shows the optical images of thin pellet of the sample CC_2 heated at 590 and 683K respectively. These images show change in the color indicating the reaction progress. Fig. 9c shows SEM image of the sample CC_2 heated at 573K, at this temperature, the loss of water molecules are completed. This image reveals that cerium oxalate rods are covered with calcium oxalate. Hence the smoothness of rods of cerium oxalate is lost. Since the occurrence of strain on the

rods, some of the rods are broken in to small pieces. Further increase in the temperature makes the system more complex and creates the holes and cracks for the diffusive removal of gaseous products. Fig. 9d discloses that the sample CC_2 treated at 723K consists of heterogeneous reaction products, which indicate complexity of the reaction at this temperature. Both optical and SEM images show more complex pathway for the decomposition reaction of cerium oxalate in the presence of calcium oxalate.

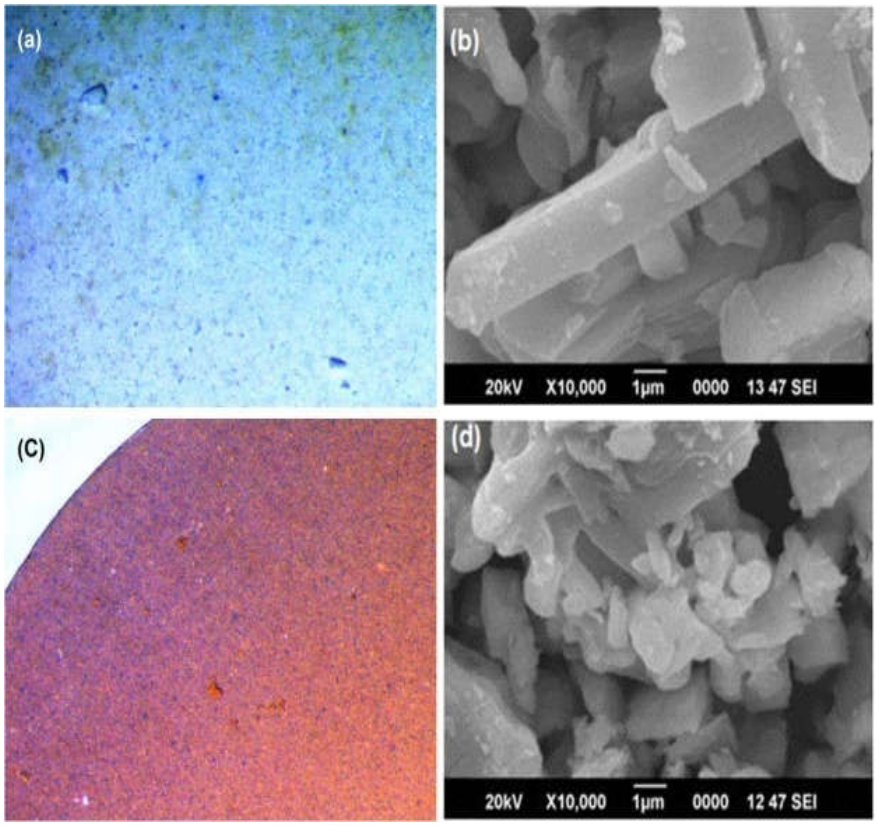

Fig. 8 The optical microscopic image of thin pellet of the sample CC_1 at 603K (a), the SEM image of the sample CC_1 at 573K (b), the optical image of thin pellet of CeO_2 (c) and the SEM image of CeO_2 (d).

Fig. 9e shows the SEM image of mixed oxides of ceria and calcium with disturbed shapes of rods. The optical image of thin pellet of mixed oxides is shown in Fig. 9f, exhibiting composite oxides.

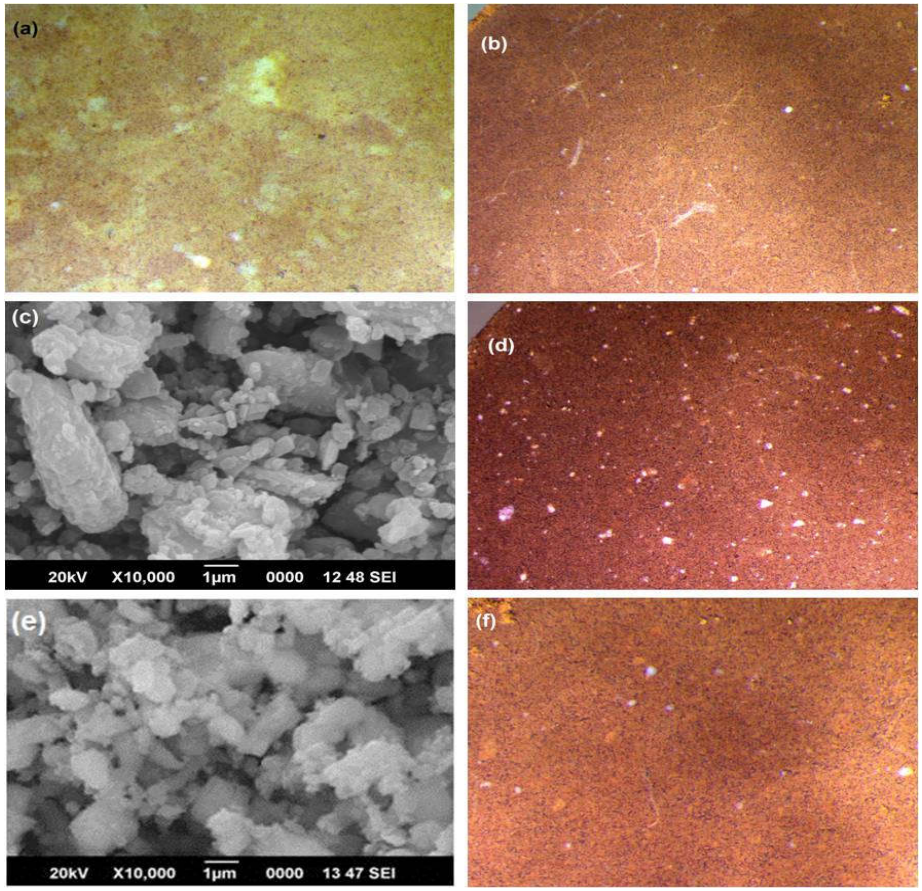

Fig. 9 The optical images of CC_2 at 590 (a) and 683K (b), SEM image of CC_2 at 573K (c), optical image of CC_2 at 723K (d), SEM image of CC_2 at 953K (e) and optical image of CC_2 at 953K (f).

4.3.4. Kinetic behaviour

Prior to conducting a detailed kinetic characterization of each mass loss step of the reaction, a formal kinetic analysis was performed

by assuming a single step reaction for the overall reaction using the fundamental kinetic equation[49].

$$\frac{d\alpha}{dt} = A\exp\left(-\frac{Ea}{RT}\right)f(\alpha) \qquad (3)$$

where t is time, T the temperature, R the ideal gas constant, A the apparent Arrhenius pre-exponential factor, Ea the apparent activation energy and $f(\alpha)$ the apparent kinetic model function used to describe the physico-geometrical reaction mechanism as a function of the fractional reaction, α. Based on Eq. 3, plots of $\ln(d\alpha/dt)$ vs T^{-1} at different α for the series of kinetic data recorded under linear non-isothermal condition, known as the Friedman plot[50-52], were examined for determining the values of Ea for different α and for evaluating variations in Ea with respect to α.

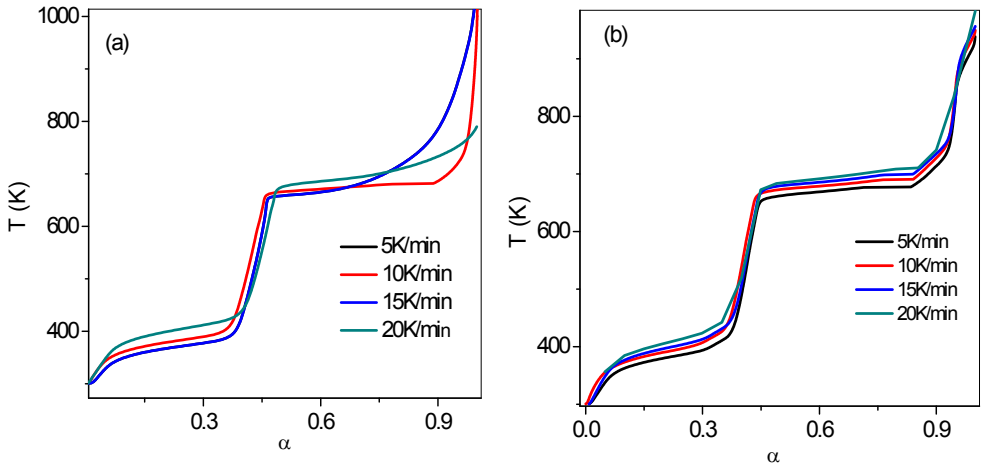

Fig. 10 The α-T curves for the sample CC_1(a) and CC_2 (b) at 5, 10, 15 & 20Kmin^{-1}.

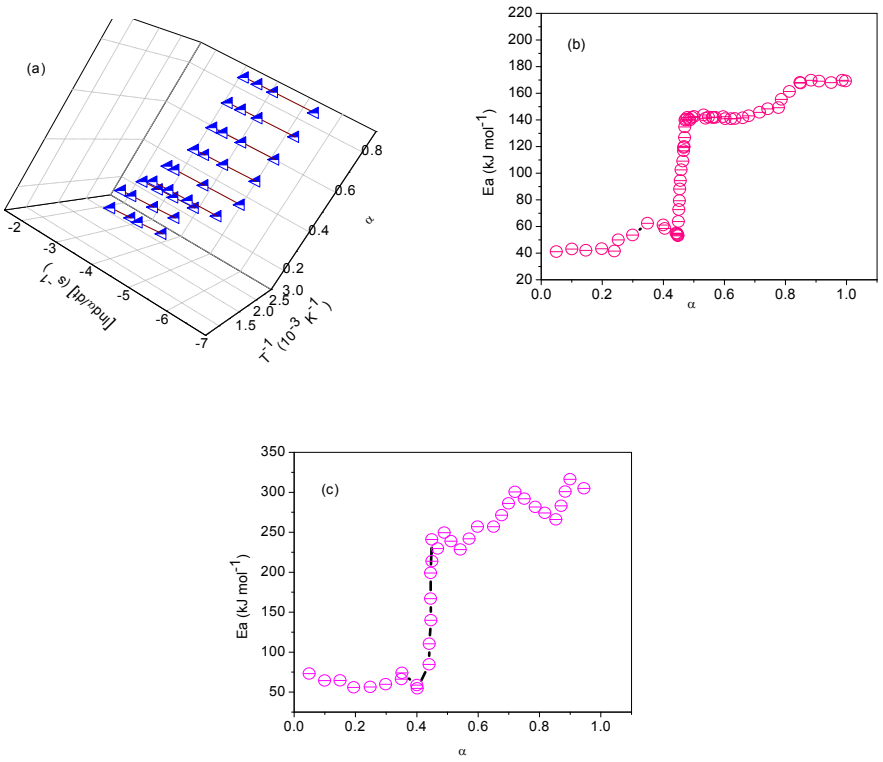

Fig. 11 The Friedman plots at different α values (from 0.1 to 0.9) for the sample CC_2 (a) and the values of *Ea* at different α for the sample CC_1 (b) and CC_2 (c).

Fig. 10 shows *α*-T curves for the pure cerium oxalate decahydrate (Fig. 10a) and Ca(II) cerium oxalate decahydrate (Fig. 10b). These curve shows multistage thermal decomposition of CC_1 and CC_2. For CC_1 there was not observed a general trend with increasing heating rate, but for sample CC_2, there was observed a genral trend; with increasing heating rate (*β*), the completion of each stage was occurred more fastly than at lower values of *β*. Fig. 11 shows the

results of the isoconversional kinetic analysis for thermal decomposition of the samples CC_1 and CC_2 using a series of kinetic data under linear non-isothermal condition. The slopes of the plots show significant variation with α (Fig. 11a). This appears in the observed α-dependent variation of *Ea* (Figs. 11b and c). The variation of *Ea* with α (Fig. 11b) is segmented majorly into two α– regions *i.e.*, $0.04 \leq \alpha \leq 0.44$ and $0.45 \leq \alpha \leq 0.99$ recalling the low temperature dehydration of incorporated water molecules (< 575K) and high temperature oxidative thermal decomposition (> 575K) reactions of sample CC_1. Similar division of α–regions is also exhibited for sample CC_2 (Fig. 11c). For both samples, *Ea* values continuously varied with α. The sample CC_1shows a minimum value of approximately 40 $kJmol^{-1}$ at $\alpha = 0.23$ and a maximum value of approximately 169. 5$kJmol^{-1}$ at $\alpha = 0.84$, whereas the sample CC_2 passes through a minimum value of approximately 54.6$kJmol^{-1}$ at $\alpha = 0.19$ and a maximum value of approximately 315.9$kJmol^{-1}$at $\alpha = 0.899$.

Since the thermal dehydration of incorporated water and the oxidative decomposition are the independent kinetic processes, the following cumulative kinetic equation can be applied to the overall reaction under linear non-isothermal conditions[22- 26, 34, 53- 57].

$$\frac{d\alpha}{dt} = \sum_{i=1}^{n} c_i A_i \exp\left(\frac{-E_{a,i}}{RT}\right) f_i\left(\alpha_i\right) \tag{4}$$

with $\sum_{i=1}^{n} c_i = 1$ and $\sum_{i=1}^{n} c_i \alpha_i = \alpha$

where n and c are the number of component steps and the contribution ratio of each reaction step to the overall process, respectively and the subscript i denotes each component reaction step. A_i and Ea_i are the Arrhenius pre-exponential factor and the apparent activation energy, respectively, of process i. The kinetics of each component process of the overall reaction can be characterized by optimizing all the kinetic parameters in Eq. 4 using nonlinear least- square analysis. Empirical kinetic model functions such as Sestak-Berggren[34,58] SB (m,n) and phase- boundary- controlled model RO (n)[59] were employed for $f_i(\alpha_i)$ in Eq. 4 in order to accommodate any possible mechanistic feature of each reaction process[60–62].

$$\text{SB}(m,n):\ f(\alpha) = \alpha^m (1-\alpha)^n \tag{5}$$

$$\text{RO}\ (n):\ f(\alpha) = n(1-\alpha)^{1-1/n} \tag{6}$$

In the present work, the initial values of the kinetic parameters were determined through a formal kinetic analysis of the kinetic data, first subjected to mathematical deconvolution using a statistical function (Weibull). The number of component steps for both samples are obtained through kinetic deconvolution of DTG-peaks. After setting all of the initial values of kinetic parameters, a parameter optimization was carried out to minimize the squares of the residues (F) when fitting the calculated curve $(d\alpha/dt)_{cal}$ versus time to the experimental curve $(d\alpha/dt)_{exp}$ versus time.

$$F = \sum_{j=1}^{n} \left[\left(\frac{d\alpha}{dt} \right)_{\exp,j} - \left(\frac{d\alpha}{dt} \right)_{cal,j} \right]^2 \quad (7)$$

where *n* is the number of data points.

Fig. 12 shows the Friedman plots for the sample $CC_{1,}$ which was used for the calculation of *Ea* for the first stage (Fig. 12a), second stage (Fig. 12b), third stage (Fig. 12c) and fourth stage (Fig. 12d). Fig. 13 shows the same plot for finding the *Ea* value of respective stage first (Fig. 13a), second (Fig. 13b), third (Fig. 13c), fourth (Fig. 13d) and overlapped stages of fifth, sixth and seventh stages of the reaction. Due to the partially overlapping of each stages with other stages, the extent of conversion α is also mingled with other stages.

Fig. 14 shows kinetic deconvolution of the oxidative thermal decomposition of the samples CC_1 and CC_2, attempted on the basis of Eq. 4 after the preliminary determination of the initial values through mathematical deconvolution and the subsequent formal kinetic analysis of each resolved reaction step. For the sample CC_1, the overall mass loss process is empirically separated in to four steps (Fig. 14a) and that of sample CC_2 into seven partially overlapping mass loss steps (Fig. 14b).

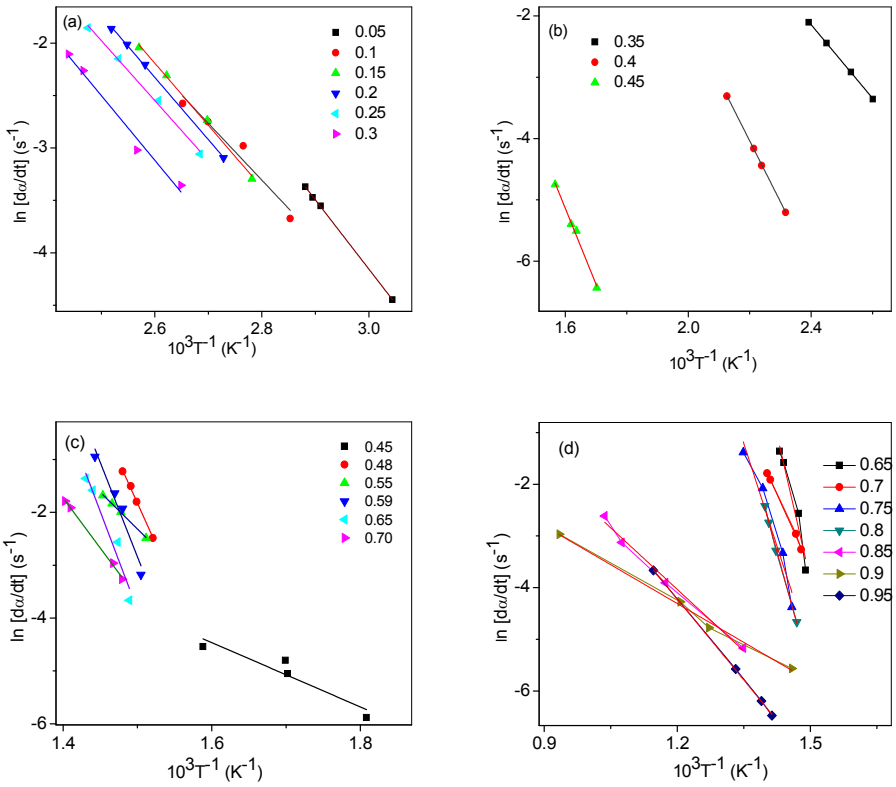

Fig. 12 The Friedman plots for first (a), second (b), third (c) and fourth stages (d) of the sample CC_1

The first low temperature reaction observed is considered as the dehydration reaction. The sample CC_1 takes two overlapping process for the removal of water molecule whereas the sample CC_2 goes on through three overlapping process since the dehydration of calcium oxalate occurs along with cerium oxalate. For the higher temperature reaction, the oxidative decomposition of CC_1 to CeO_2 is composed of two partially overlapping reaction steps due to the formation of an intermediate cerium oxy carbonate $Ce_2O_2.CO_3$[63]. The sample CC_2 goes through more complex reaction pathway during the decomposition reaction. The average values of the optimized kinetic

parameters are listed in Table 1. The values of Ea calculated for each reaction step are in good agreement with that determined from the Friedman plot.

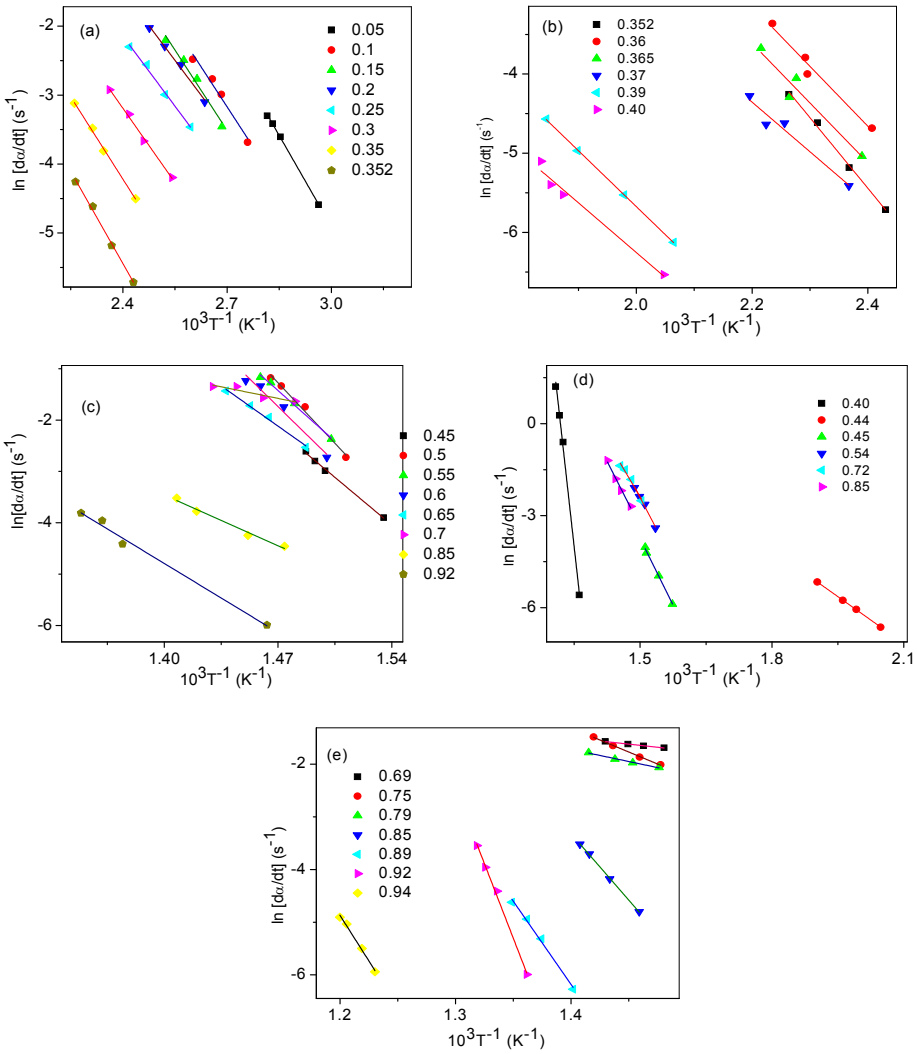

Fig. 13 The Friedman plots for the sample CC_2 for the first (a), second (b), third (c), fourth (d) and fifth, sixth and seventh (e) stages.

The oxidative decomposition given in Eqs.1and 2 can be further divided into five stages as[38]:

$$Ce_2(C_2O_4)_3.10H_2O \rightarrow Ce_2(C_2O_4)_3.3H_2O + 7H_2O^{38} \quad (8)$$

$$Ce_2(C_2O_4)_3.3H_2O \rightarrow Ce_2(C_2O_4)_3 + 3H_2O \quad (9)$$

$$Ce_2(C_2O_4)_3 \rightarrow Ce_2O_2.CO_3 + 4CO_2 + CO \quad (10)$$

$$Ce_2O_2.CO_3 \rightarrow 2CeO_2 + CO \quad (11)$$

$$CO + (1/2)\, O_2 \rightarrow CO_2 \quad (12)$$

Even though there exists complex reaction pathways for the decomposition of CC_2, the rate of decomposition reaction occurs with higher rate similar to the rate of mass loss shown in the DTG curves (Fig. 4). In Fig. 14b, the sixth and seventh step of mass loss corresponds to the decomposition reaction of calcium oxalate to CaO *via* $CaCO_3$ as the intermediate phase. The XRD curve (Fig. 5b) indicates the formation of mixture of CeO_2 and CaO as the end product of decomposition reaction, which occur during the seventh stage.

The temperature is shifted to higher temperature region due to the increase in the internal gaseous pressure and the interaction of Ca^{2+} with oxygen atom of cerium oxalate, which arrests the reaction. But at the characteristic temperature, the rate of decomposition was found to be higher due to the ease of diffusional removal of gaseous products. The reaction rate behavior of each overlapping mass-loss steps of both low temperature and high temperature reaction process of sample CC_1

has been best described with phase- boundary-controlled model (given in Eq. 6).

For the sample CC_2, each overlapping mass-loss steps of both low temperature dehydration and high temperature oxidation process have been empirically described by Sestak-Berggren SB (*m, n,* 0): $\alpha^m(1-\alpha)^n$. The empirical SB (*m, n, p*) kinetic model function can be applicable to any type of solid state reactions[60]. The change in mechanism exists due to the change in self-generated reaction condition due to the interaction of Ca^{2+} and partial overlapping with neighboring reaction interfaces. For the low temperature dehydration reaction of CC_1, the required value of *Ea* is 42 ± 0.0977 $kJmol^{-1}$ (for i = 1) and 56.5 ± 0.157 $kJmol^{-1}$ (i = 2). The higher temperature oxidative decomposition to CeO_2 passes off *via* two steps. The required value of *Ea* is 140 ± 0.96 $kJmol^{-1}$ (i = 3) and 169.2 ± 0.08 $kJmol^{-1}$ for the succeeding step (i = 4).

The sample CC_2 undergoes thermal decomposition under multistep kinetics through seven steps. The lower temperature dehydration reaction proceeds through three steps. The average value of energy needed for the respective steps are 67.42 ± 0.008 (i = 1), 68.09 ± 0.007 (i = 2) and 128.10 ± 0.0044$kJmol^{-1}$ (i = 3).

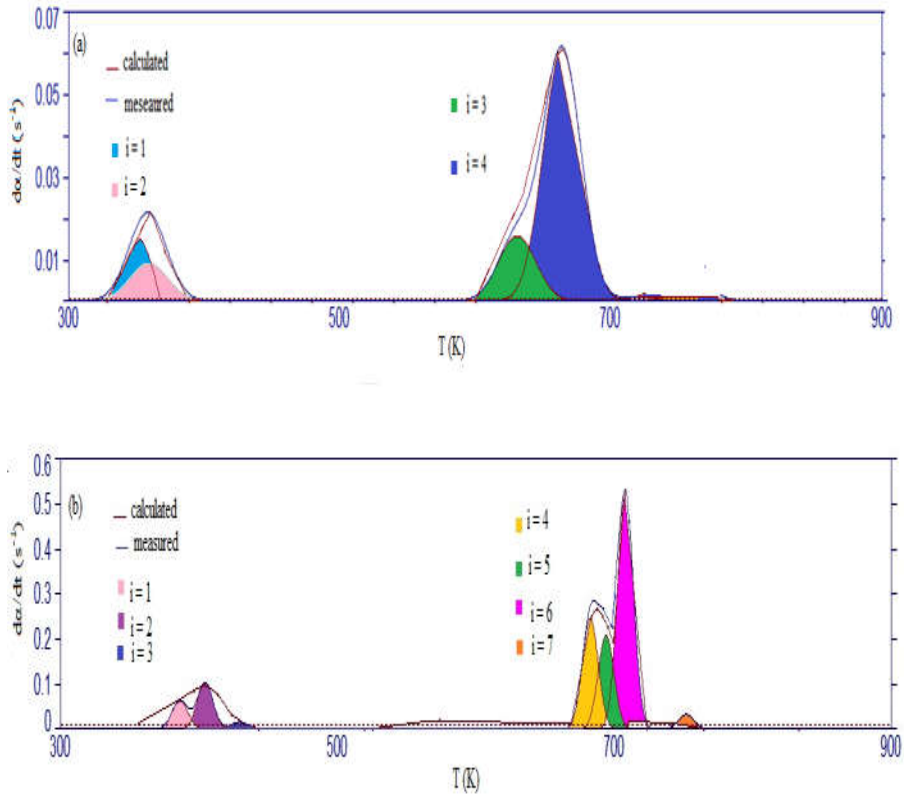

Fig. 14 The results of kinetic deconvolution analysis for the thermal decomposition of the samples CC_1 (a) and CC_2 (b) under linear non-isothermal condition at $\beta = 5$ $Kmin^{-1}$

The higher temperature reaction of the sample CC_2 comes about in four steps producing mixed oxides of cerium and calcium. The average value of energy needed for the respective steps are 239.5 (i = 4), 236.3 ± 0.02 (i = 5), 277.8 ± 0.09 (i = 6) and 290.8 ± 0.06 $kJmol^{-1}$ (i = 7). It should also be noted that difference in the values of A for the initial stages (i = 1 and 2) and final stages of CC_2 was high, indicating the higher lags of the reaction time and temperature. This difference can be attributable to the higher impedance effect on the internal

reaction due to the presence of both the surface product layer of cerium-calcium oxalate and the *in situ* Ca^{2+} interaction with lone pair of electron on the oxygen atom of cerium oxalate. When the characteristic temperature is reached, destruction of surface product layers occur and the interaction of Ca^{2+} tend to increase the rate of oxidative decomposition. The findings of present study reveal that Ca^{2+}interaction during thermal decomposition of cerium oxalate produces thermally stable excellent redox active material.

Table 1 The average values of kinetic parameters optimized for each reaction step of oxidative thermal decomposition of the samples CC_1 and CC_2.

Sample	i	Ea_i (kJmol^{-1})	A_i (sec^{-1})	R^2
CC_1	1	42.000 ± 0.097	$(6.94 \pm 0.006)\times 10^5$	0.9926
	2	56.500 ± 0.570	$(1.51 \pm 0.58)\times 10^6$	0.9925
	3	140.000 ± 0.960	$(8.63 \pm 0.15)\times 10^{12}$	0.9375
	4	169.200 ± 0.087	$(3.29 \pm 0.005)\times 10^{13}$	0.9964
CC_2	1	67.420 ± 0.008	$(2.54 \pm 0.008)\times 10^8$	0.9942
	2	68. 090 ± 0.007	$(2.78 \pm 0.0013)\times 10^8$	0.9756
	3	128. 100 ± 0.004	$(1.30 \pm 2.01)\times 10^9$	0.9467
	4	239.500 ± 0.000	$(1.77 \pm 0.003)\times 10^{16}$	0.9356
	5	236. 300 ± 0.005	$(1.62 \pm 0.05)\times 10^{16}$	0.9876
	6	277.800 ± 0.097	$(1.66 \pm 0.03)\times 10^{18}$	0.9666
	7	290. 800 ± 0.060	$(2.24 \pm 0.005)\times 10^{22}$	0.9768

4.5. Conclusion

Thermally induced oxidative decomposition of cerium oxalate decahydrate and mixed cerium oxalate with 10 mass (%) calcium oxalate in flowing air was studied. Overall kinetics of the formation of micro structural rods of CeO_2 and its mixed oxide with CaO was regulated by physico-geometrical constraints. The complexity of the reaction was found to be increased with the introduction of calcium oxalate. Even though both samples show multistep kinetic behavior, mixed cerium oxalate passes through more complex reaction pathways. The reaction stages are distinguished by the ease of diffusional removal of gaseous products formed by the internal reaction. Mixed cerium oxalate (CC_2) sample undergoes reaction with higher rate even if the temperature of the reaction shifted to higher region. Optical band gap measurement indicated higher value of *Eg* for the sample CC_2 due to the *in situ* interaction of Ca^{2+} with the lone pair of electrons on the oxygen atom of cerium oxalate. Both the surface product layer of the decomposing cerium-calcium oxalate and the interaction of the Ca^{2+} can impede the diffusional removal of gaseous products.

4.6. References

1. Bumajdad A, Eastoe J, Mathew A. Cerium oxide nano particles prepared in self-assembled systems. *Adv Colloid Interface Sci*. 2009;147–148:56–66.

2. Nair V, Vinu R. Production of guaiacols via catalytic fast pyrolysis of alkali lignin using titania, zirconia, and ceria. *J Anal Appl Pyrol*. 2016;119:31-39.

3. Yu T, Joo J, Park YI, Hyeon T. Large-scale nonhydrolytic sol-gel synthesis of uniform-sized ceria nano crystals with spherical, wire, and tadpole shapes. *Angew Chem Int Ed*. 2005;44:7411-7414.

4. Bouchara A, Mosser G, Soler-Illia GJAA, Chane-Ching JY, Sanchez C. Texturation of nano crystalline CeO_2-based materials in the presence of poly-c-benzyl-L-glutamate. *J Mater Chem*. 2004;14:2347-2354.

5. Han WQ, Wu L, Zhu Y. Formation and oxidation state of CeO_{2-x} nanotubes. *J Am Chem Soc*. 2005;127:12814-12815.

6. Tang C, Bando Y, Liu B, Golberg D. Cerium oxide nanotubes prepared from cerium hydroxide nanotubes. *Adv Mater*. 2005;24:3005-3009.

7. Tang B, Zhuo L, Ge J, Wang G, Shi Z, Niu J. A surfactant-free route to single-crystalline CeO_2 nanowires. *J Chem Commun*. 2005;28:3565-3567.

8. Vantomme A, Yuan ZY, Du G, Su BL. Surfactant-assisted large-scale preparation of crystalline CeO_2 nanorods. *Langmuir*. 2005;21:1132-1135.

9. Zhang F, Siu-Wai C, Spanier JE, et al. Cerium oxide nanoparticles: size- selective formation and structure analysis. *Appl Phys Lett*. 2002;80:127-129.

10. Tok AIY, Boey F Y C, Dong Z, Sun XL. Hydrothermal synthesis of CeO_2 nano-particles. *J Mater Process Technol*. 2007;190:217-222.

11. Zhang G, Shen Z, Liu M, et al. Synthesis and characterization of mesoporous ceria with hierarchical nano architecture controlled by amino acids. *J Phys Chem B*. 2006;110:25782-25790.

12. Zhang Y, Andersson S, Muhammed M. Nanophase catalytic oxides : I . synthesis of doped cerium oxides as oxygen storage promoters. *Appl Catal B Environ*. 1995;6:325-337.

13. Miyazaki H, Kato JI, Sakamoto N, Wakiya N, Ota T, Suzuki H. Synthesis of CeO_2 nanoparticles by rapid thermal decomposition using microwave heating. *Adv Appl Ceram*. 2010;109:123-127.

14. Masui T, Peng Y, Ken-ichi M, Gin-ya A. Reduction behavior of CeO_2-ZrO_2 solid solution prepared from cerium - zirconyl oxalate. *Chem Mater*. 1998;10:4005-4009.

15. Kenji H, Kazutoshi S, Hiroshi O, Soichiro S, Yoshihiro H. Synthesis and sintering of rare-earth- doped ceria powder by the oxalate co-precipitation method. *J Mater Res*. 1999;14:957-967.

16. Trovarelli A. *Catalysis by Ceria and Related Materials, Catalytic Science Series*. First ed., London, Imperial College Press; 2002.

17. Wei L, Lijun F, Cong Z, et al. A facile hydrothermal synthesis of 3D flowerlike CeO_2 via a cerium oxalate precursor. *J Mater Chem A*. 2013;1:6942-6948.

18. Ganguli AK, Vaidya S, Ahmad T. Synthesis of nano crystalline materials through reverse micelles: a versatile methodology for synthesis of complex metal oxides. *Bull Mater Sci*. 2008;31:415–419.

19. Ho C, Yu JC, Kwong T, Mak AC, Lai S. Morphology-controllable synthesis of mesoporous CeO_2 nano- and microstructures. *Chem Mater*. 2005;17:4514-4522.

20. Murugananthan C, Rayappan JBB, Maheshwari KU. Synthesis and characterization of cerium oxide nanoparticles by hydroxide mediated approach. *J Appl Sci*. 2012;12:1734-1737.

21. Yuksel A, Huseyin T. Structural and thermal investigations on cerium oxalate and derived oxide powders for the preparation of (Th, Ce)O_2 pellets. *J Nucl Mater*. 2001;298:316-320.

22. Takeshi W, Nobuyoshi K. Kinetics and mechanism of the thermal decomposition of sodium percarbonate : role of the surface product layer. *J Phys Chem A*. 2013;117:1880-1889.

23. Wada T, Nakano M, Koga N. Multistep kinetic behavior of the thermal decomposition of granular sodium percarbonate : hindrance effect of the outer surface layer. *J Phys Chem A*. 2015;2:9749-9760.

24. Yoshikawa M, Yamada S, Koga N. Phenomenological interpretation of the multistep thermal decomposition of silver carbonate to form silver metal. *J Phys Chem C*. 2014;118:8059-8070.

25. Kitabayashi S, Koga N. Physico-geometrical mechanism and overall kinetics of thermally induced oxidative decomposition of tin(II) oxalate in air: formation process of micro structural tin(IV)oxide. *J Phys Chem C*. 2014;118:17847−17861.

26. Koga N, Goshi Y, Yamada S, Pe´rez-Maqueda LA. Kinetic approach to partially overlapped thermal decomposition processes; co-precipitated zinc carbonates. *J Therm Anal Calorim*. 2013;111:1463-1474.

27. Nakano M, Wada T, Koga N. Exothermic behavior of thermal decomposition of sodium percarbonate : kinetic deconvolution of successive endothermic and exothermic processes. *J Phys Chem A*. 2015;119:9761-9769.

28. Tanaka H, Koga N, Galwey AK. Thermal dehydration of crystalline hydrates: microscopic studies and introductory experiments to the kinetics of solid-state reactions. *J Chem Educ*. 1995;72:251−256.

29. Galwey AK. Structure and order in thermal dehydrations of crystalline solids. *Thermochim Acta*. 2000;355:181−238.

30. Koga N, Goshi Y, Yoshikawa M, Tatsuoka T. Physico-geometrical kinetics of solid-state reactions in an undergraduate thermal analysis laboratory. *J Chem Educ*. 2014;91:239−245.

31. Pijolat M, Favergeon L, Soustelle M. From the drawbacks of the Arrhenius-f(α) rate equation towards a more general formalism and new models for the kinetic analysis of solid−gas reactions. *Thermochim Acta*. 2011;525:93−102.

32. Koga N, Kimizu T. Thermal decomposition of indium(III) hydroxide prepared by the microwave-assisted hydrothermal method. *J Am Ceram Soc*. 2008;91:4052−4058.

33. Kimura T, Koga N. Thermal dehydration of monohydrocalcite: overall kinetics and physico-geometrical mechanisms. *J Phys Chem A*. 2011;115:10491−10501.

34. Nobuyoshi K, Daisuke K, Tomoyasu K. Aragonite crystal growth and solid-state aragonite-calcite transformation: a physico-geometrical relationship via thermal dehydration of included water. *Cryst Growth Des*. 2013;13:2238-2246.

35. Font R, Rey MD. Kinetics of olive oil pyrolysis. *J Anal Appl Pyrol*. 2013;103:181-188.

36. Nusrath K, Muraleedharan K. Synthesis, characterization and thermal decomposition kinetics of cerium oxalate rods. *Devagiri J Sci*. 2016;2:118-120.

37. Miguel G, Juan H, Leticia B, Joaquin N, Mario ERG. Characterization of calcium carbonate, calcium oxide and calcium hydroxide as starting point to the improvement of lime for their use in construction. *J Mater Civ Eng*. 2009;21:625-708.

38. Vimal G, Kamal PM, Biju PR, Joseph C, Unnikrishnan NV, Ittyachen MA. Structural studies and luminescence properties of CeO_2:Eu^{3+} nanophosphors synthesized by oxalate precursor method. *Appl Nanosci*. 2015;5:837-846.

39. Gabal MA, Elroby SAK, Obaid AY. Synthesis and characterization of nano-sized ceria powder via oxalate decomposition route. *Powder Technol*. 2012;229:112-118.

40. Oman Z, Haznan A, Widayanti W. Synthesis and characterization of nanostructured CeO_2 with dyes adsorption property. *Process Appl Ceram*. 2014;8:39-46.

41. Niu F, Zhang D, Shi L, et al. Facile synthesis, characterization and low-temperature catalytic performance of Au/CeO_2 nanorods. *Mater Lett*. 2009;63:2132–2135.

42. Pavel J, Tomas HK, Martin K, Jakub E, Martin S. Thermal treatment of cerium oxide and its properties: adsorption ability versus degradation efficiency. *Adv Mater Sci Eng*. 2014;2014:1-12.

43. Kumar E, Selvarajan P, Balasubramanian K. Preparation and studies of cerium dioxide nanoparticles by microwave-assisted solution method. *Rec Res Sci Tech*. 2010;4:37–41.

44. Zhang D, Ni XM, Zheng HG, Zhang XJ, Song JM. Fabrication of rod-like CeO_2: characterization, optical and electrochemical properties. *Solid State Sci*. 2006;8:1290–1293.

45. Liao XH, Zhu JM, Zhu JJ, Xu JZ, Chen HY. Preparation of monodispersed nano crystalline CeO_2. *Chem Commun*. 2001;10:937-938.

46. Tsunekawaa S, Wang JT, Kawazoe Y, Kasuya A. Blue shifts in the ultraviolet absorption spectra of cerium oxide nano crystallites. *J Appl Phys*. 2003;94:3654-3656.

47. Schroder DK. *Semiconductor Material and Device Characterization*. Third ed., John Wiley and Sons, New York; 2006.

48. Jose John M, Muraleedharan K, Kannan MP, Ganga Devi T. Effect of semiconducting metal oxide additives on the kinetics of thermal decomposition of sodium oxalate under isothermal conditions. *Thermochim Acta*. 2012;534:71-76.

49. Koga N. Ozawa's kinetic method for analyzing thermoanalytical curves. *J Therm Anal Calorimrm*. 2013;113:1527-1541.

50. Ozawa T. Applicability of Friedman plot. *J Therm Anal*. 1986;31:547–551.

51. Koga N. Kinetic analysis of thermo analytical data by extrapolating to infinite temperature. *Thermochim Acta*. 1995;258:145−159.

52. Gotor FJ, Criado JM, Malek J, Koga N. Kinetic analysis of solid-state reactions: the universality of master plots for analyzing isothermal and non-isothermal experiments. *J Phys Chem A*. 2000;104:10777–10782.

53. Koga N, Yamada S, Kimura T. Thermal decomposition of silver carbonate: phenomenology and physico-geometrical kinetics. *J Phys Chem C*. 2013;117:326−336.

54. Sánchez-jiménez PE, Perejón A, Criado JM, Diánez MJ, Pérez-maqueda LA. Kinetic model for thermal dehydrochlorination of poly (vinyl chloride). *Polymer*. 2010;51:3998-4007.

55. Koga N, Suzuki Y, Tatsuoka T. Thermal dehydration of magnesium acetate tetra hydrate: formation and in situ crystallization of anhydrous glass. *J Phys Chem B*. 2012;116:14477−14486.

56. Yusuke N, Koga N. Phenomenological kinetics of the carbonation reaction of lithium hydroxide monohydrate : role of surface product layer and possible existence of a liquid Phase. *J Phys hem C*. 2014;118:5424-5436.

57. Yoshikawa M, Goshi Y, Yamada S, Koga N. Multistep kinetic behavior in the thermal degradation of poly (L□lactic acid): a physico-geometrical kinetic interpretation. *J Phys Chem B*. 2014;118:11397-11405.

58. Sestak J, Berggren G. Study of kinetics of the mechanism of solid state reactions at increasing temperatures. *Thermochim Acta*. 1971;3:1-12.

59. Koga N, Tanaka H. Accommodation of the actual solid-state process in the kinetic model function.1. significance of the non-integral kinetic exponents. *J Therm Anal*. 1994;41:455−469.

60. Pe´rez-Maqueda LA, Criado JM, Sa´nchez-Jime´nez PE. Combined kinetic analysis of solid-state reactions: a powerful tool for the simultaneous determination of kinetic parameters and the kinetic model without previous assumptions on the reaction mechanism. *J Phys Chem A*. 2006;110:12456-12462.

61. Málek J, Criado JM. Empirical kinetic models in thermal analysis. *Thermochim Acta*. 1992;203:25-30.

62. Šesták J. Diagnostic limits of phenomenological kinetic models introducing the accommodation function. *J Therm Anal*. 1990;36:1997-2007.

63. Subba Rao VV, Rao RVG, Biswas AB. Thermogravimetric analysis of La, Ce, Pr and Nd oxalates in air and in carbon dioxide atmosphere. *J Inorg Nucl Chem*. 1965;27:2525-2531.

NUSRATH. K “SYNTHESIS AND KINETICS OF FORMATION OF CERIA AND CERIA BASED MATERIALS via THERMAL DECOMPOSITION OF OXALATES”. THESIS. DEPARTMENT OF CHEMISTRY, UNIVERSITY OF CALICUT, 2018.

5.1. Introduction

Ceria, one of the most promising biomaterial ($\alpha = \beta = \gamma = 90^{o}$, a = b = c = 5.41120 Å, Fm-3m) has possessed multifarious properties which are diverged in catalytic, sensing, solid electrolyte, exhaust gas emission control, medicinal, etc. Most of its properties are raised due to the triggering nature of oxidation state of Ce^{3+}/Ce^{4+}. Besides its redox nature, oxygen ion vacancies, surface hydroxyl group and radical scavenging ability also contribute towards its diverse applications. Nano ceria can be prepared through variety of methods such as hydrothermal, solvothermal[1,2], sol-gel[3], micro emulsion[4], thermal decomposition[5], etc. Miyazako *et al*[6] prepared CeO_2 nano particle by rapid thermal decomposition by microwave heating of cerium oxalate and concluded that shape of resultant specimen depends on the precursor material shape. Preparation of ceria nano particle *via* solid phase thermal decomposition route has the advantage over other methods such as the use of less chemicals, less impurity (volatile chemicals vaporizes) and time saving process. Hence it is essential to know how much energy is utilized for the formation of nano particle by this solid state conversion. Here the question of kinetic parameters related with the process arises. Therefore the establishment of solid state kinetics of the concerned process is necessary.

Cerium oxalate decomposes into ceria through multistage process[7-9]. Effect of additives to the precursor salt significantly governs the rate of decomposition. Choose of additives which cause to decrease the *Ea* and increase the rate of process and its separation from the product is most considered. Ryusaburo *et al*[10] studied the effect of

transition metal oxide α-Fe_2O_3 additive on the thermal decomposition of salts of halogen oxoacids, oxalates, azide, permanganate and oxides. The effect of ferro spinel additives on kinetics and mechanism of thermal decomposition of lithium oxalate was studied[11]. John *et al*[12] explored the effect of semi conducting metal oxides CuO and TiO_2 on the thermal decomposition of sodium oxalate. Also the effect of additives CuO, MnO_2 and TiO_2 on thermal decomposition kinetics of KIO_4 to KIO_3 was investigated[13]. Up to now the effect of nano metal oxides of Fe, Co and Ni and nano ferrites of Co and Ni on the kinetic characteristics of formation of ceria nanoparticle from its oxalate precursor is not explored. Fig. 1 represents 2D structure of cerium oxalate.

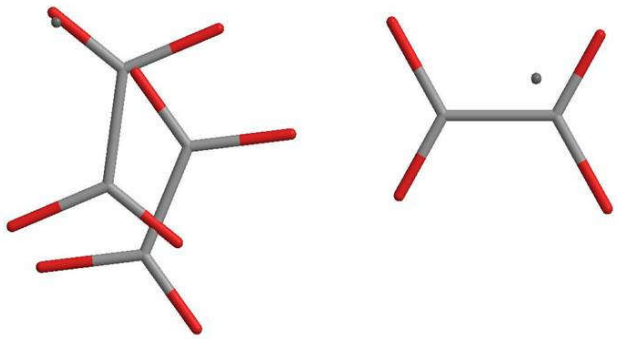

Fig. 1 2D structure of Ce(III) oxalates

Oxides of iron (both Fe_2O_3 & Fe_3O_4) can perform as the dehydrating agent for the conversion of glycerol to allyl alcohol[14]. Amorphous nanostructured metals, alloys and metal oxides play significant role as catalyst for oxidative process. The conversion of cyclohexanol to cyclohexanone can be catalyzed by amorphous Co_3O_4[15]. Yang *et al*[16] reported that first raw transition metal oxides

especially Fe, Co, Ni and binary oxides have efficient electro catalytic activity for oxygen evolution reaction (OER). Adsorbed OH^- species becomes much more stable on the surfaces of late transition metal oxides such as Fe, Co and Ni[17]. Catalytic process with the application of ferrite nanoparticle includes decomposition (in particular photo catalytic decomposition), reactions of dehydrogenation, oxidation, alkylation and C-C coupling among other process. Up to now, ferrite nano particle made up of Cu^{2+}, Co^{3+}, Ni^{2+}, Zn^{2+} and several mixed metal and core shell ferrites have application in the catalytic reaction such as for the synthesis and destruction of organic compound[18]. Oxides of iron and cobalt and ferrites of Ni and Co have strong ability to reprieve CO by oxidation. Oxidation of CO by ferrites is associated with adsorption and catalytic properties[18–23]. Use of magnetic metal oxides and ferrites has the advantage is that they can be conveniently recovered from the reaction system using strong magnetic field or magnetic separator, without loss of catalytic activity. The present work aims to synthesize nano metal oxides of Fe, Co and Ni and nano ferrites of Co and Ni *via* thermal decomposition process. Effect of these nano metal oxides and ferrites (5%) upon the kinetic characteristics of formation of nano ceria *via* thermal decomposition of cerium oxalate was established.

5.2. Experimental

5.2.1. Synthesis of metal oxides

Saturated solution of sodium oxalate (100mL) was added into a flask and stirred at room temperature. Definite amount of $FeSO_4$

$(NH_4)_2SO_4.6H_2O$, Co $(NO_3)_2.6H_2O$ and $NiCl_2.4H_2O$ were taken for the preparation of $FeC_2O_4.2H_2O$, $CoC_2O_4.2H_2O$ and $NiC_2O_4.2H_2O$ respectively and was dissolved in water and poured into aforementioned sodium oxalate solution under stirring. Appropriate quantities of $FeSO_4$ $(NH_4)_2SO_4.6H_2O$, Co $(NO_3)_2.6H_2O$ and $NiCl_2.4H_2O$ were taken for the preparation of $CoFe_2$ $(C_2O_4)_3$ (Fe: Co; 2:1) and $NiFe_2$ $(C_2O_4)_3$(Fe: Ni; 2:1). After fifteen minutes later, the precipitate is collected by filtration and washed repeatedly with distilled water and ethanol. Each precipitate of oxalate (except NiC_2O_4. $2H_2O$) was dried at 60ºC overnight. NiC_2O_4. $2H_2O$ was dried at 80ºC. Metal oxides and ferrites were prepared from corresponding metal oxalates using thermal decomposition strategy. Fe_3O_4, Co_3O_4, $CoFe_2O_4$ and $NiFe_2O_4$ were prepared by calcination of the corresponding metal oxalates at 300ºC for 3h. The heating rate was 1ºCmin^{-1}. For the preparation of NiO, the calcination temperature was 350ºC for 3h.

5.2.2. Preparation of mechanical mixture of oxalates of cerium and metal oxides

Particle size of metal oxides, ferrites and cerium oxalates were fixed in the range of 95-105μm. Cerium oxalate decahydrate (A_0), and compositions of oxalates of cerium with 2, 5 and 10m/m (%) each of different metal oxides, Fe_3O_4 (A_1), Co_3O_4 (A_2), NiO (A_3), $CoFe_2O_4$ (A_4), and $NiFe_2O_4$ (A_5) were prepared by thorough mechanical mixing in an agate mortar.

5.2.3. Characterization

FT-IR and XRD patterns of the oxides and oxalates were recorded. Average crystal size of metal oxides was calculated by using Scherrer formula. The surface morphology of the oxides and cerium oxalate were observed by scanning electron microscopy instrument. The optical band gap (*Eg*) of electro catalysts were calculated from UV–Vis reflectance which was measured using UV–Vis diffuse reflectance spectrum.

5.2.4. Measurement of thermal behavior

DSC measurements were made on TA instrument at four different heating rates, *viz.* 5, 10, 15 and 20 K min^{-1}. TG measurements were made in N_2 atmosphere at a flow rate of 50 mL min^{-1}.

5.3. Results and Discussion

XRD and FT-IR spectrum of cerium oxalate decahydrate (A_0) are shown in Figs. 2a &b respectively. The reflections from the sample in the XRD pattern indicate that cerium oxalate crystallizes in the monoclinic system (JCPDS. No. 20-0268). The broad band observed at 3080–3433cm^{-1}(Fig. 2b) associated with water molecules which are removed only at higher temperature[24]. The very strong peak observed at 1633.9 cm^{-1}(Fig. 2b) corresponds to the combined effect of asymmetric bending and stretching of water molecule[25]. The strong peak observed at 1318.4cm^{-1} represents the asymmetric stretching of CO_2 molecule associated with oxalate ligand group[25,26]. The band observed at 523.8cm^{-1}stands for M-O stretching frequency[24,26]. Fig. 3a

represents the SEM image of the cerium oxalate decahydrate. Figs. 3b & c show the images of ferrites of Co and Ni.

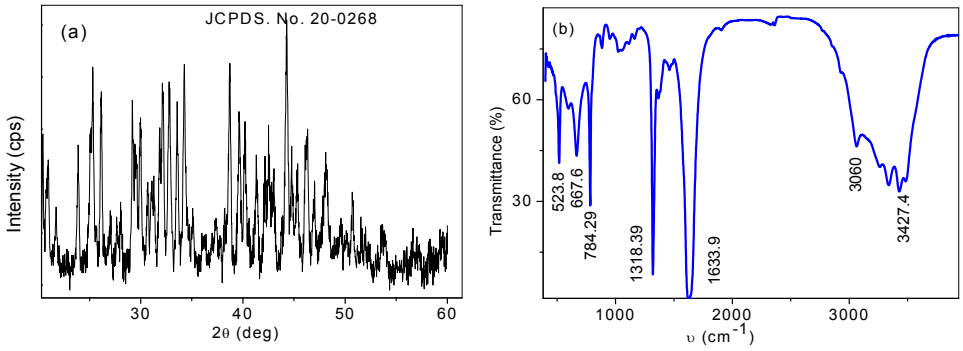

Fig. 2 XRD pattern (a) and FT-IR spectrum (b) of cerium oxalate decahydrate

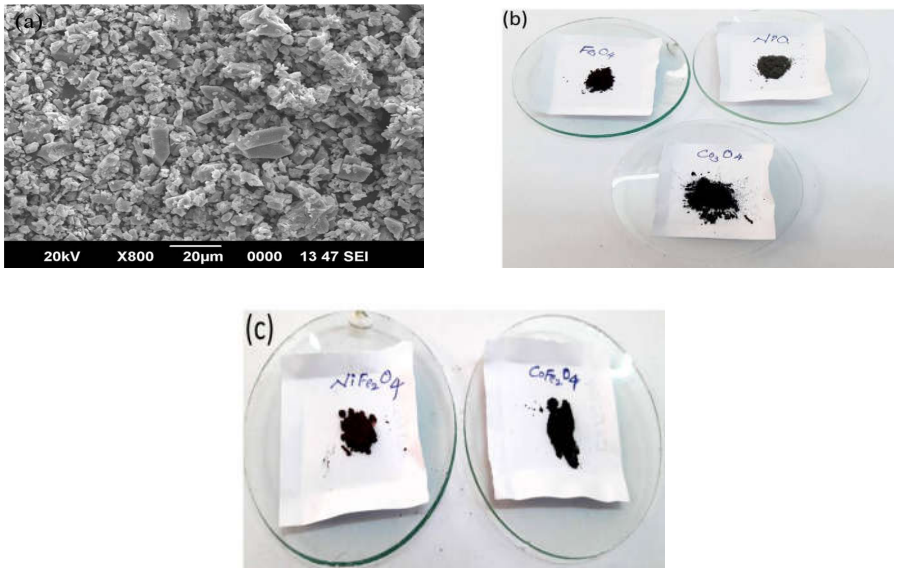

Fig. 3 SEM image of cerium oxalate decahydrate (a), photographic images of oxides of Fe, Co & Ni (b) and ferrites of Co & Ni (c).

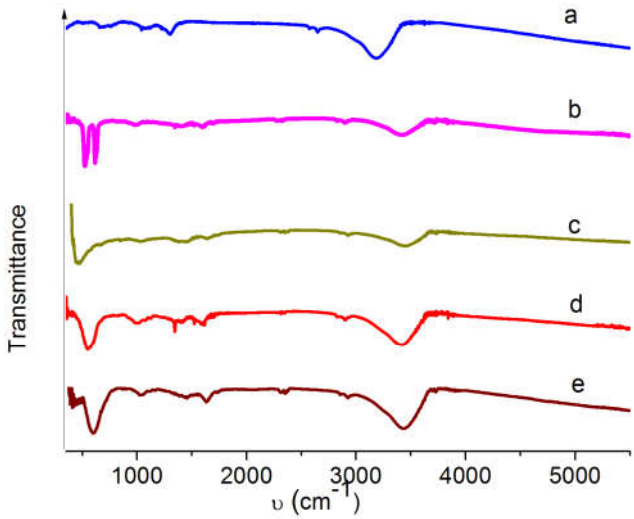

Fig. 4 The FT-IR spectra of Fe_3O_4 (a), Co_3O_4 (b), NiO (c), $CoFe_2O_4$ (d) and $NiFe_2O_4$ (e)

Fig. 4a represents FT-IR spectrum of Fe_3O_4. The band observed at 581.63cm^{-1} and 439.13 cm^{-1} correspond to Fe-O-Fe stretching frequency. Fig. 4b is attributed to FT-IR spectrum of Co_3O_4 which displays two strong bands at 572. 86 and at 666.03cm^{-1}. The first band at 572.86 cm^{-1} corresponds to OB_3 vibration in the spinel lattice, where B denotes Co^{3+} in an octahedral hole, whereas the second band at 666. 03cm^{-1} is associated with ABO_3 vibration, where A represents Co^{2+} in a tetrahedral hole. Fig. 4c exhibits FT-IR spectrum corresponding to NiO. The broad bands in 424.28- 709.01cm^{-1} indicate Ni-O stretching frequency. The broadness in absorption band arises due to the presence of nano crystals. Owing to the quantum size effect and spherical nanostructures, FTIR spectrum of NiO particles are blue shifted compared to bulk form[27]. Fig. 4d shows two bands at 433.12 and 585.12 cm^{-1} correspond to Fe-O and Co-O stretching frequency

respectively. Fig. 4e displays FT-IR spectrum of $NiFe_2O_4$. The band observed at 411.90 and 593.88cm^{-1} correspond to the intrinsic stretching frequency of M-O at tetrahedral and octahedral sites. These exposed as characteristic features of a spinel ferrite in a single phase[28].

Fig. 5 represents XRD patterns of oxides of Fe, Co and Ni (Figs. 5a, b &c respectively) and of ferrites of Co and Ni (Figs. 5d &e). All the oxides (except NiO) and ferrites show poor crystalline nature. The average crystal size was estimated by using the Scherrer equation based on the maximum intense peak of XRD pattern. It is listed in Table 1. Oxide of Fe presented is Fe_3O_4 (JCPDS No. 75-0033) due to brownish- black color of the obtained powder[29-31]. The characteristic peaks of XRD pattern of Co_3O_4 is well agreed with the reported data [JCPDS 42-1467]. The XRD pattern of nano crystalline NiO is well indexed into cubic lattice structure (JCPDS file No: 47-1049)[28]. Less intense peaks of the synthesized $CoFe_2O_4$ Nps are well suited with the JCPDS card No. 77-0426 and that of $NiFe_2O_4$ Nps with ASTM 10-325.

Table 1 Average crystallite size and optical band gap (*Eg*) values of metal oxides and ferrites

Oxides	Crystallite size (nm)	*Eg* (eV)
Fe_3O_4	2.3	1.72
Co_3O_4	1.6	1.20
NiO	8.0	1.54
$CoFe_2O_4$	1.4	1.38
$NiFe_2O_4$	15.1	1.77

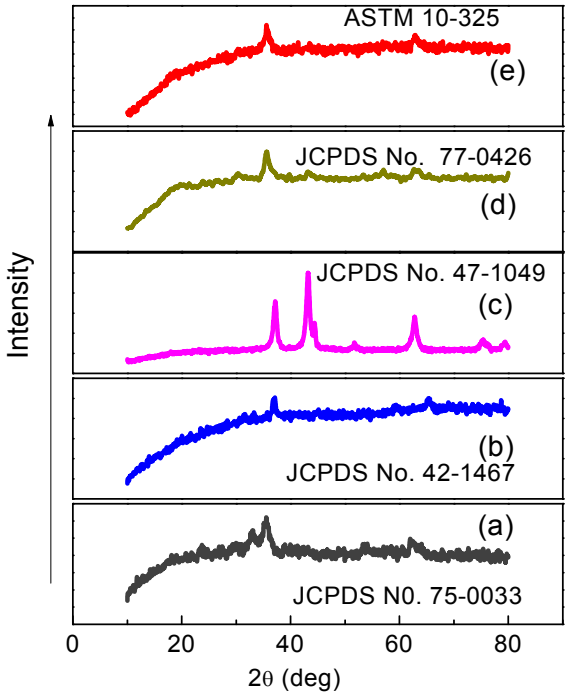

Fig. 5 The XRD patterns of Fe_3O_4 (a), Co_3O_4 (b), NiO (c), $CoFe_2O_4$ (d) and $NiFe_2O_4$ (e)

Fig. 6 represents SEM images of Fe_3O_4 (Fig. 6a), Co_3O_4 (Fig. 6b), NiO (Fig. 6c), $CoFe_2O_4$ (Fig. 6d) and $NiFe_2O_4$ (Fig. 6e). The SEM image of Fe_3O_4 shows porous flat rod like structure of Fe_3O_4 which was developed by thermal oxidation of $FeC_2O_4.2H_2O$. Some shrinkage to the rod was observed from the SEM image. Surface morphological analysis of Co_3O_4 revealed that it acquired rod like structure. Surface textures of NiO, in which the oxide nano particles are assembled to generate microspheres. SEM image of $CoFe_2O_4$ nano particle (Fig. 6d) acquired elliptical multi walled-rod morphology. Some deformations are presented on the surface of the rod related with loss of water molecule and CO upon thermal decomposition of $CoFe_2C_2O_4.2H_2O$ at 300ºC at a heating rate of $1ºCmin^{-1}$. Morphology analysis of $NiFe_2O_4$ displays the hexagonal shaped rods.

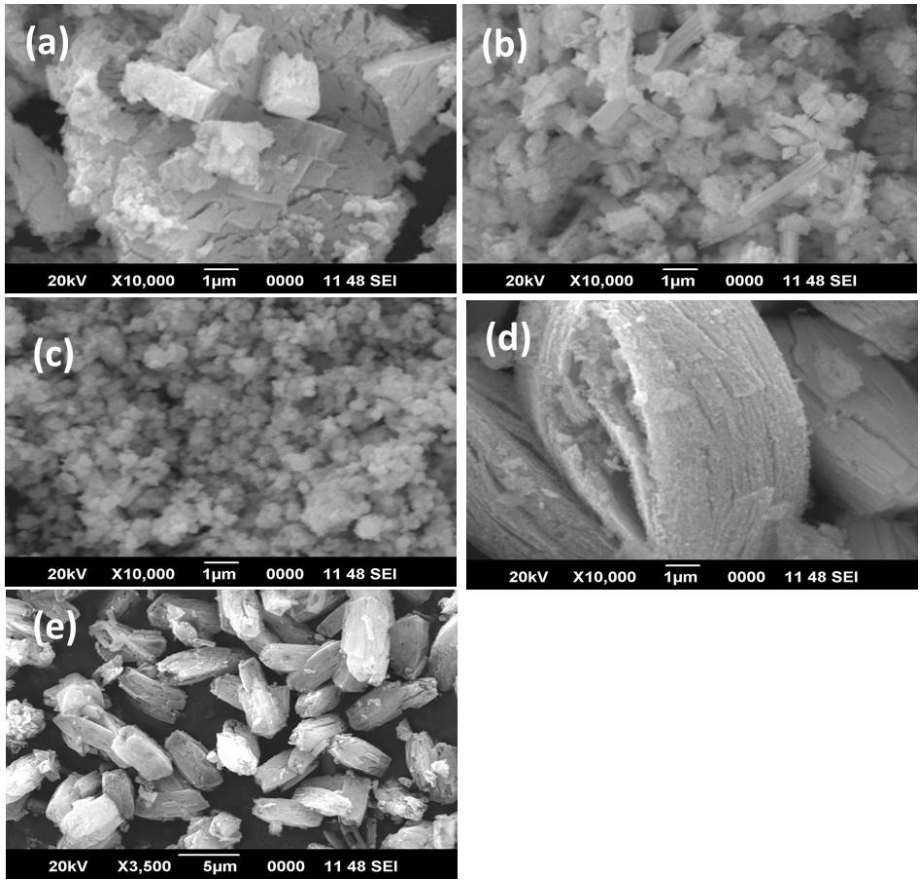

Fig. 6 SEM images of Fe_3O_4 (a), Co_3O_4 (b), NiO (c), $CoFe_2O_4$ (d) and $NiFe_2O_4$ (e)

5.3.1. Optical properties of metal oxides

An estimate of the optical band gap, *Eg* can be obtained from *Tauc* equation, $(\alpha hv)^n = B(hv\text{-}Eg)$ where *hv* is the photon energy, α is the absorption coefficient, *B* is a constant relative to the material and *n* is either 2 for direct transition, or 1/2 for an indirect transition. Fig. 7 represents the *Tauc-plots* of Fe_3O_4 (Fig. 7a), Co_3O_4 (Fig. 7b), NiO (Fig. 7c), $CoFe_2O_4$ (Fig. 7d) and $NiFe_2O_4$ (Fig. 7e). The $(\alpha hv)^2$ versus *hv* curve are plotted for Fe_3O_4, $CoFe_2O_4$, Co_3O_4 and NiO, whereas the

$(\alpha hv)^{1/2}$ versus hv curve are displayed for $NiFe_2O_4$. Lowering the optical band gap (Eg), conducting properties of the material increases. The estimated Eg values of metal oxides of Fe, Co and Ni and ferrites of Co and Ni were tabulated (Table 1).

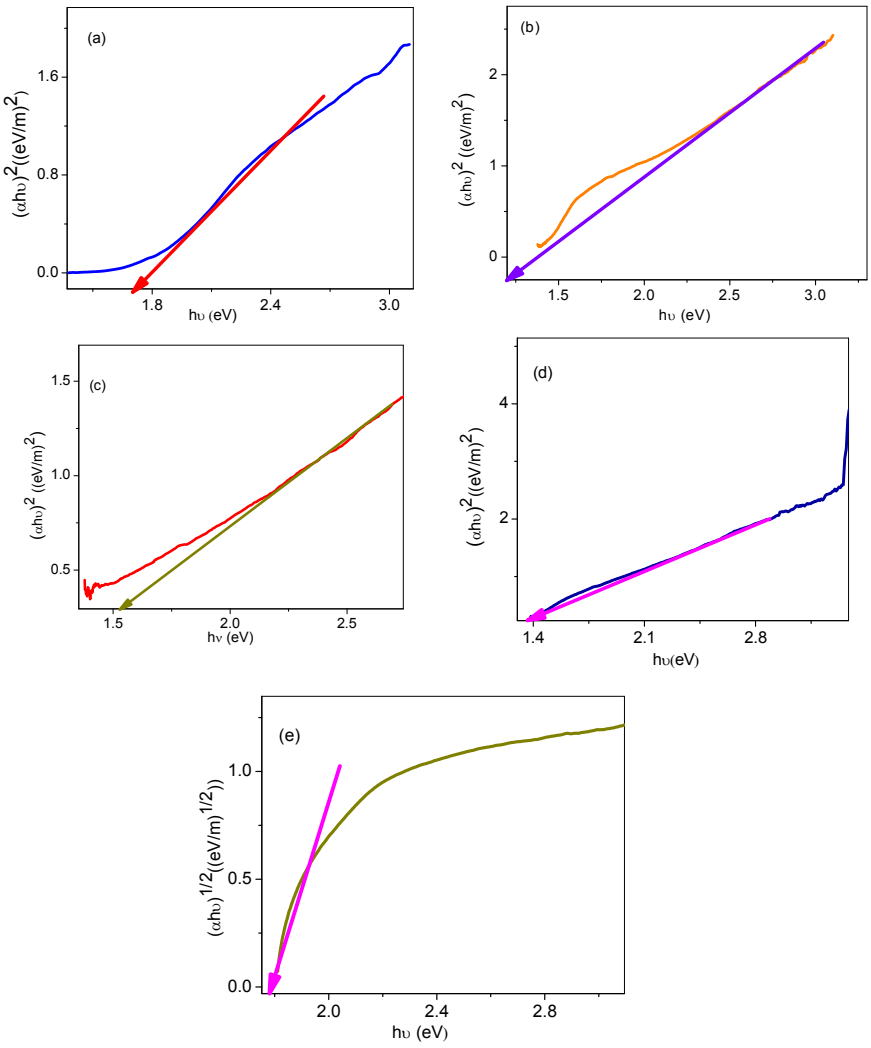

Fig. 7 *Tauc*-plots of Fe_3O_4 (a), Co_3O_4 (b), NiO (c), $CoFe_2O_4$ (d) and $NiFe_2O_4$ (e)

5.3.2. Characterization of thermal decomposition behavior

Thermal decomposition behavior of the hydrated cerium oxalate in the presence of metal oxides was studied. Fig. 8a shows the DSC curves of overall thermal decomposition behavior of cerium oxalate decahydrate (A_0) in N_2 atmosphere at different β (5, 10, 15 and 20 K min^{-1}) values. It reflects the multistage of thermal decomposition due to the occurrence of multiple constituent chemical processes that occurs successively during the linear heating program. Each constituent process contributes differently to the overall thermal effect[32–34]. Hence, the DSC curves of A_0 sample shows two independent thermal behaviors one at temperature below 550K and one at temperature above 550K. Under the linear non-isothermal condition, a multi-step heat flow process was observed from the DSC curves. A heat flow implying the dehydration of water molecule is remarked in the temperature region of 334-502 K, whereas the decomposition of sample A_0 was occurred in the higher temperature region of 600-752 K. For the lower and higher temperature reaction of A_0 sample, the DSC curves are systematically shifted to higher temperature with increasing the value of β. For the low temperature dehydration of sample A_0, the reaction is arrested at the very beginning at all β values except β = 10 K min^{-1}. Hence it can be stated that dehydration reaction is β dependent.

Even though temperature is shifted to lower value for the dehydration reaction at β = 10 than 5 K min^{-1}, the enthalpy change for the process is higher at 10 K min^{-1}.The physico-geometrical constraints have significant role in controlling the multistage thermal behavior.

This occurs due to the changes in reaction conditions as the reaction progresses[35]. Koga *et al*[32] put forwarded that the combination of multistep thermal behavior restrained by physico-geometrical features of solid state reaction and successive chemical reaction strategy. During the early stage of reaction, a smooth surface product layer is formed between the reactant and reaction interface. Upon thermal decomposition, this surface product layer come into action *i.e.*, it can impede the diffusional removal of H_2O and CO molecule. This causes to increase the internal pressure of the reactant leading to change in the reaction condition at the reaction interface.

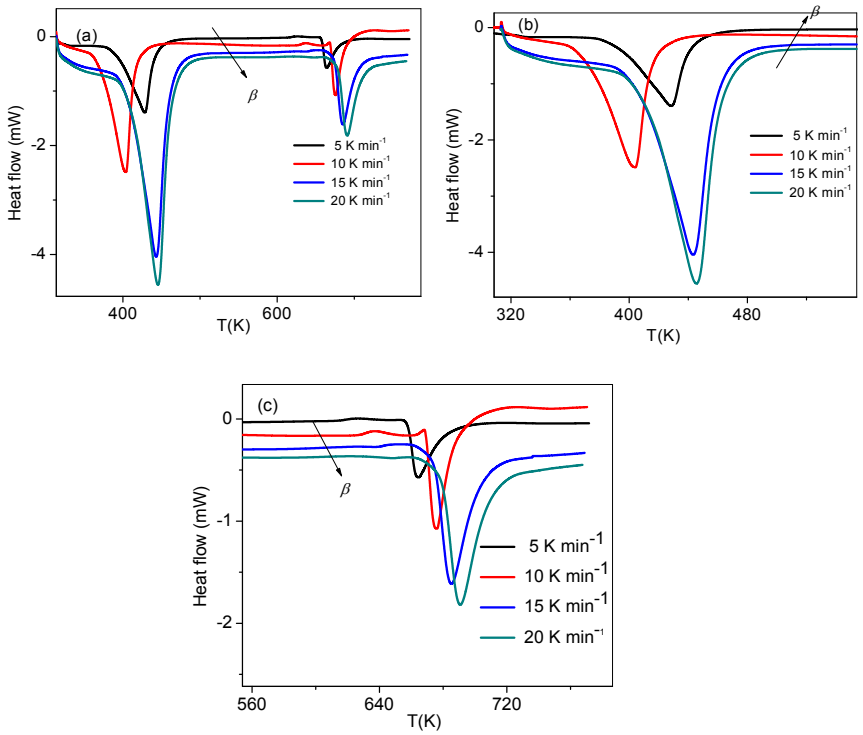

Fig. 8 The DSC curves of overall thermal decomposition of cerium oxalate decahydrate (a), dehydration reaction (b) and decomposition reaction (c).

Presence of cracks and holes on the surface of the product played as diffusion channel for the removal of gaseous products. In Fig. 8c, the DSC curves of sample A_0 is associated with a shoulder peak. This can be ascribed due to the change in self-generated reaction condition, which arises at the reaction interface as the reaction advances. As the preliminary observation of thermal decomposition of A_0 by each composition (2, 5 &10 m/m (%)), it was taken into our attention that energy required for lower temperature dehydration of Ce-Ox (A_0) with 5m/m (%) oxides is significantly lowered than 2 & 10 m/m (%). Hence, further studies regarding kinetic analysis has been carried out with samples of 5 m/m (%) oxide mixed A_0.

Figs. 9 & 10 shows the comparison of DSC curves for 2 & 10 m/m (%) oxide mixed samples (A_1, A_2, A_3, A_4 & A_5) with pure Ce-Ox A_0, for the thermal dehydration and decomposition reaction. Fig. 11 shows the comparison of the DSC curves of samples A_0, A_1, A_2, A_3, A_4 & A_5 for the overall as well as independent stages of the reaction *i.e.*, dehydration and decomposition. Both stages of the reaction need uptake of heat energy.

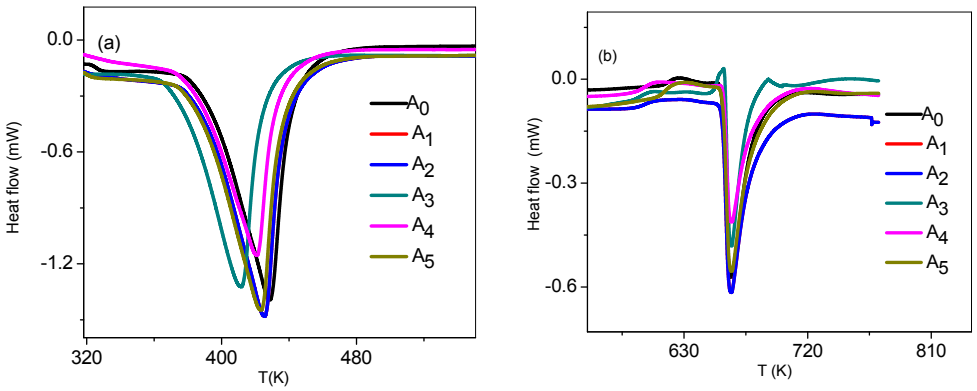

Fig. 9 The comparison of DSC curves of pure Ce-Ox, A_0, 2m/m (%) oxides mixed Ce-Ox; A_1, A_2, A_3, A_4 & A_5; dehydration (a) & decomposition (b) at 5 $Kmin^{-1}$.

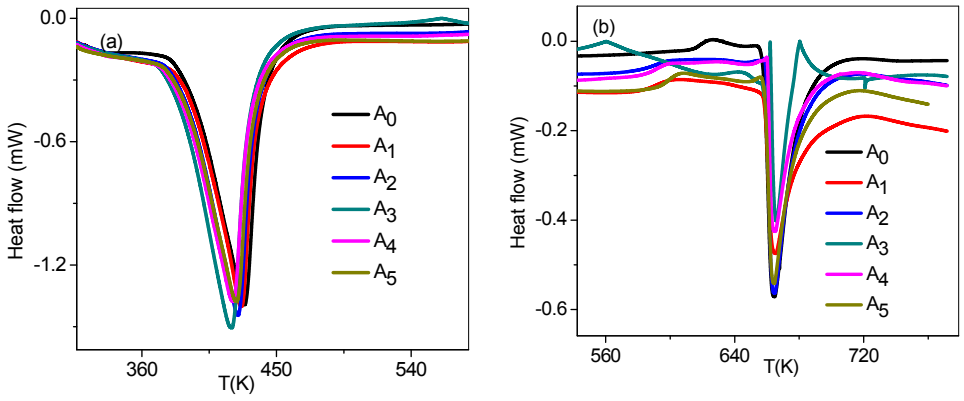

Fig. 10 The comparison of DSC curves of pure Ce-Ox, A_0, 10m/m (%) oxides mixed Ce-Ox; A_1, A_2, A_3, A_4 & A_5; dehydration (a) & decomposition (b) at 5 $Kmin^{-1}$.

Energy required for lower temperature dehydration reaction was found to be higher than higher temperature decomposition reaction. For occurring thermal reaction of the sample A_0 at a heating program of $5Kmin^{-1}$, energy required (ΔH) for the complete removal of water molecule is about $354.14kJmol^{-1}$ and for the formation of nano ceria from it at higher temperature requires energy of 82.35 kJ mol^{-1}. It was noticed that both low temperature and high temperature reactions of the samples with oxides (5m/m (%)) have remarkable shift in temperature to lower value. Among the metal oxides, Fe_3O_4 made comparatively a larger shift of temperature of dehydration to lower value.

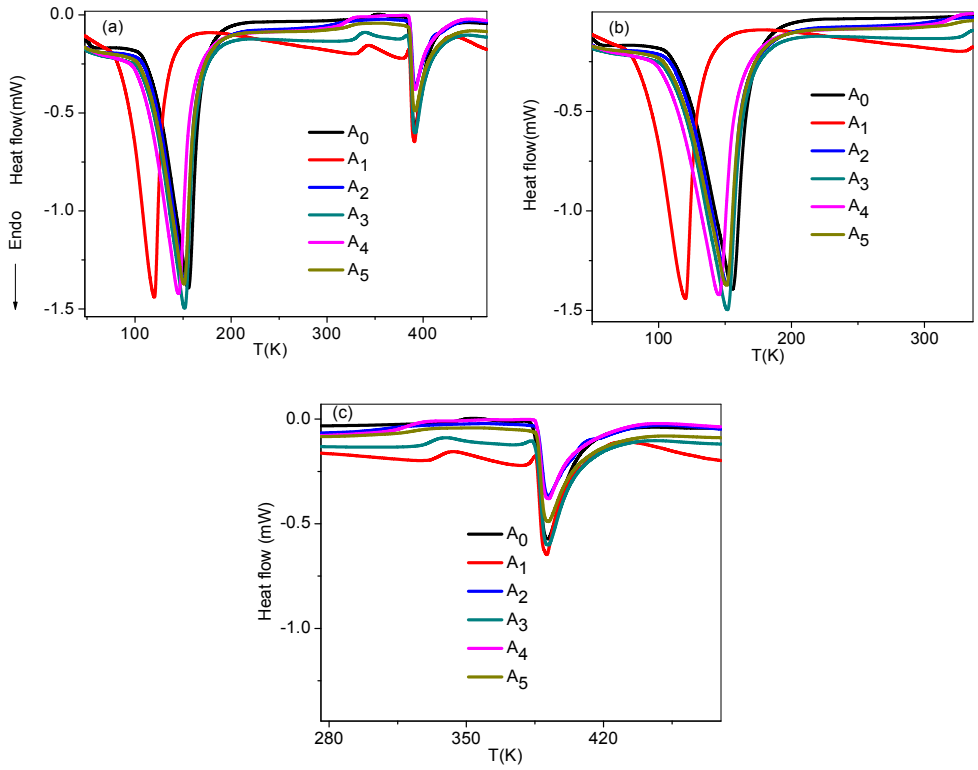

Fig. 11 Comparison of the DSC curves of 5 m/m (%) oxide mixed compositions A_0-A_5 at 5Kmin^{-1}; Curves for overall reaction (a), curves for the dehydration (b) and curves for decomposition stages (c).

The value of ΔH calculated for the dehydration from the peak area of DSC curves at a heating rate of 5Kmin^{-1} in presence of Fe_3O_4, Co_3O_4, NiO, $CoFe_2O_4$ and $NiFe_2O_4$ was respectively 295.85, 309.16, 367.94, 345.09 and 332.92kJmol^{-1}. Ascending order of ΔH values for the removal process of water from the sample A_0 is in presence of oxides and ferrites is as follows: Fe_3O_4 < Co_3O_4 < $NiFe_2O_4$ < $CoFe_2O_4$ < NiO. NiO requires extra energy 13.80 kJmol^{-1} for the dehydration than the sample A_0. The shift in temperature of the reaction was

appeared largely at lower β value (5Kmin^{-1}). There has effect of β (heating rate) on the dehydration as well as decomposition reaction of all mixed oxalates of Ce. Moreover, high temperature reaction of samples has constant peak temperature with different contribution of reaction. Existence of lower oxidation state of Ce^{3+} gives certain magnetic behavior to the generated Ce_2O_3. Hence the system became more rigid and does not increase or decrease the peak temperature of decomposition[36]. In this stage, Co_3O_4, $NiFe_2O_4$ and $CoFe_2O_4$ have lower contribution than Fe_3O_4 and NiO. Hence the system is more stabilized using Fe_3O_4 and NiO.

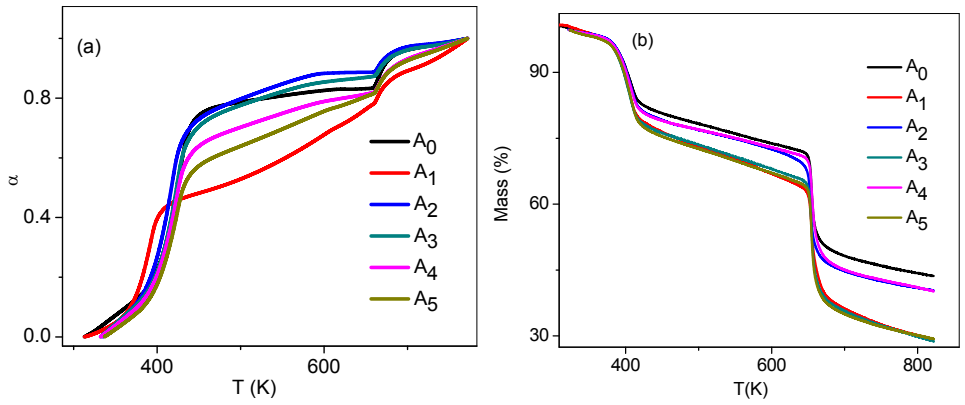

Fig. 12 Comparison of α-T curves (a) and the TG curves (b) of the overall thermal decomposition of oxide mixed (5 m/m (%)) samples (A_1-A_5) and parent sample A_0.

Progress of the overall thermal decomposition of each oxide mixed samples (A_1-A_5) as a function of temperature was compared with parent sample A_0 (Fig. 12a). It was noticed that reaction follows multistep kinetic behavior. Sample A_1 undergoes dehydration reaction at lower progress of reaction ($0.017 \leq \alpha \leq 0.424$) whereas other

samples undergo with $\alpha > 0.424$. Experimental mass loss up to the formation of oxide nano particle for each composition is depicted in Table 2. Fig. 12b shows the TG curves of all samples (A_0-A_5) from room temperature to 820K in N_2 atmosphere.

Table 2 Experimental mass loss obtained from the TG curves of each composition at $5Kmin^{-1}$

Composition	Mass loss (%)*
A_0	50.04
A_1	61.23
A_2	52.85
A_3	53.75
A_4	63.40
A_5	61.94

* Theoretical mass loss for the sample A_0 is 52.48%

5.3.3. Kinetic Analysis

Heat flow (dQ/dt) by the reaction and overall heat of reaction obtained from the experimentally resolved DSC curve after subtracting the baseline. The overall reaction rate can be expressed as

$$\frac{d\alpha}{dt} = \left(\frac{dQ}{dt}\right)\frac{1}{Q} \qquad (1)$$

Where α is the progress of the overall reaction. DSC curves for the thermal decomposition of cerium oxalate decahydrate are assumed to occur from the dehydration and decomposition to Ce_2O_3, the overall

reaction rate recorded using DSC is the sum of these two kinetic processes[32] (Fig. 13). Hence

$$\frac{d\alpha}{dt} = \sum_{i=1}^{n} c_i A_i \exp\left(\frac{-E_{a,i}}{RT}\right) f_i(\alpha_i) \qquad (2)$$

$$\text{With } \sum_{i=1}^{n} c_i = 1 \quad \text{and} \quad \sum_{i=1}^{n} c_i \alpha_i = \alpha$$

where n and c are the number of component step and contribution ratio of each reaction step to the overall process while A, Ea and $f(\alpha)$ are Arrhenius parameter, activation energy and kinetic model function in different forms respectively.

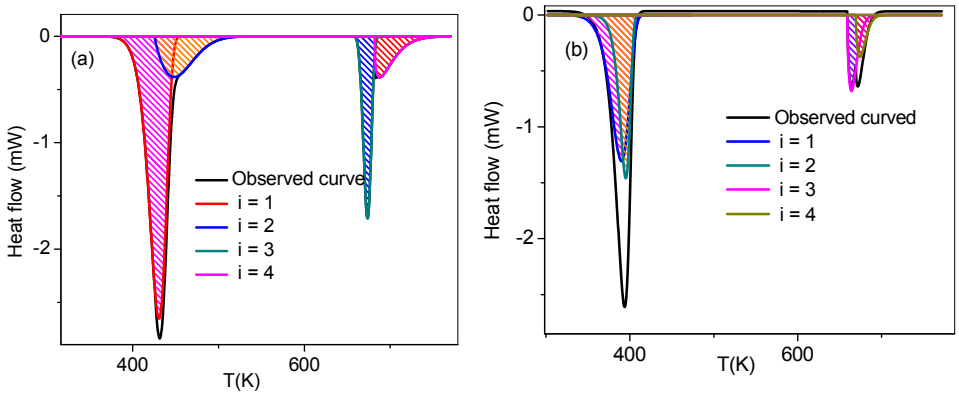

Fig. 13 The deconvoluted DSC curves of sample A_0 (a) and A_1 (b)

The contribution c_{endo} and c_{exo} can be defined as

$$c_{endo} = \frac{Q_{endo}}{Q} < 0 \text{ and } c_{exo} = \frac{Q_{exo}}{Q} > 0 \qquad (3)$$

where Q_{endo} and Q_{exo} are the heats of endothermic and exothermic process respectively. Due to the experimental inconvenience of separately tracking the component process, deconvolution of overall kinetic information into reaction component is the only possible way for interpreting the reaction scheme of the successive processes. Low temperature dehydration reaction (< 550K) of incorporated water molecule and high temperature decomposition reaction (> 550K) are kinetically independent process. Therefore the aforementioned cumulative kinetic equation (Eq. 2) can be applied to the overall reaction under linear non-isothermal condition[35,37–46] . All the kinetic parameters of each component process of overall reaction can be optimized by using non-linear least square analysis. Empirical kinetic model function such as modified Sestak Berggren SB (*m*,*n*) was employed for finding the mechanistic features, $f_i(\alpha_i)$ of each reaction process[47–49].

$$\text{SB}(m,n):\ f(\alpha) = \alpha^m (1-\alpha)^n \tag{4}$$

where *m* and *n* are kinetic exponent.

The initial values of the kinetic parameters are obtained by the kinetic deconvolution of DSC curves. Kinetic parameters for each component step are analyzed by assuming single stage kinetic analysis. Appropriate $f_i(\alpha_i)$ is obtained by merely adjusting the parameters *c, m* and *n* in Eq. 5 and such an equation fits every kinetic model proposed for solid state reactions, and also scores for the deviations of ideal kinetic model due to *for example*, particle inhomogeneity in size and shape[47].

$$\ln\left[\frac{d\alpha/dt}{(1-\alpha)^n(\alpha)^m}\right] = cA - Ea/RT \qquad (5)$$

Pearson linear correlation coefficient between left hand sides of the equation with inverse of temperature is set as an objective of optimization. The Kissinger method, which was utilized to determine the apparent activation energy for the overall reaction from the DSC curves recorded at different β.

$$\ln\left(\frac{\beta}{T_P^2}\right) = \ln\left[-\frac{f(\alpha_p)}{d\alpha}\frac{AR}{Ea}\right] - \frac{Ea}{RT_P} \qquad (6)$$

where T_p is the peak maximum temperature characteristics for the overall reaction. For the reaction of cerium oxalate decahydrate crystalline particle, the change in T_p in the DSC curves with β can be analyzed for the Kissinger plot. It is possible to apply the Kissinger plot to the reaction of A_0 and mixed samples A_1-A_5: the four subsequent endothermic peak maximum. The Kissinger plots $ln\ (\beta/T_p^2)$ versus T_p^{-1} for samples A_0 and A_1 are represented in Figs.14a & b respectively.

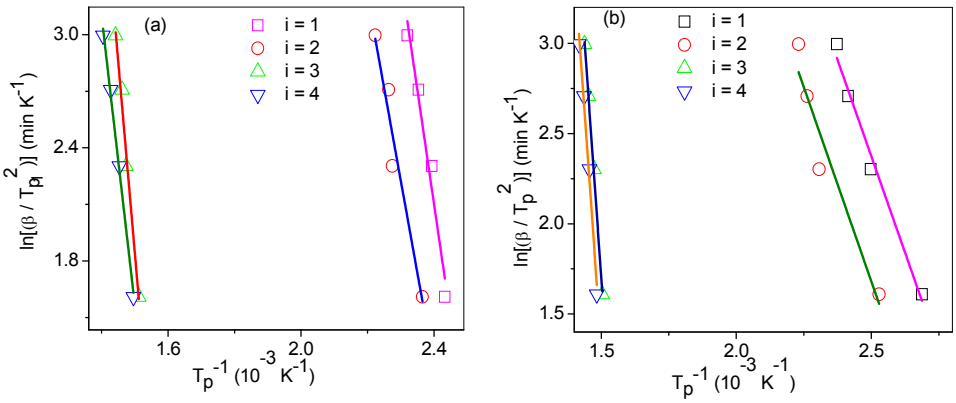

Fig. 14 Kissinger plots for each peak of samples A_0 (a) and A_1 (b).

After setting all of the initial values of kinetic parameters for each step, a parameter optimization was executed in order to minimize the squares of the residue (F) when fitting the calculated curve $(d\alpha/dt)_{cal}$ versus time to the experimental curve $(d\alpha/dt)_{exp}$ versus time.

$$F = \sum_{j=1}^{n} \left[\left(\frac{d\alpha}{dt} \right)_{\exp,j} - \left(\frac{d\alpha}{dt} \right)_{cal,j} \right]^2 \qquad (7)$$

where n is the number of data points.

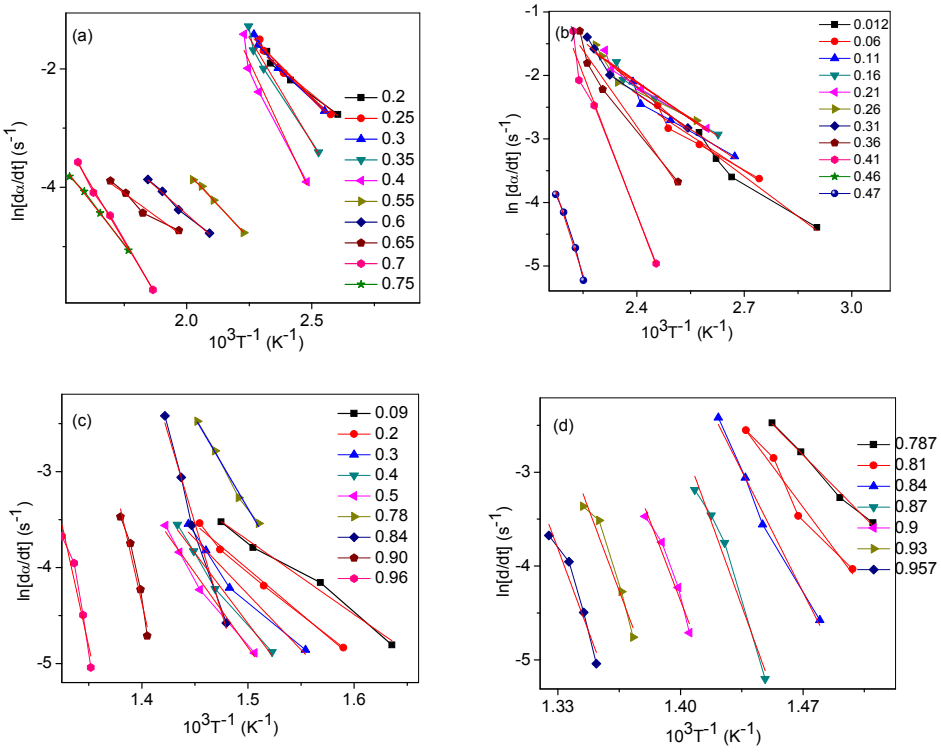

Fig. 15 The Friedman plots for each stage of decomposition of Ce-Ox in presence of iron oxide A_1; first (a), second (b), third (c) and fourth stages (d).

For finding the *Ea* values of each stage of thermal decomposition of Ce-Ox in presence of oxides, Friedman method and Kissinger methods were used. For the estimating the values of *Ea* of A_1, A_2 &A_4, Friedman method was best fitted (Figs. 15, 16&17), whereas for A_3 &A_5, Kissinger method (Fig. 18) was best suited than Friedman plots. Due to the occurrence of partially overlapped reaction, the distributed α value of each stage are merged with other stages. Fig. 15 shows the Friedman plots of each stage of A_1.

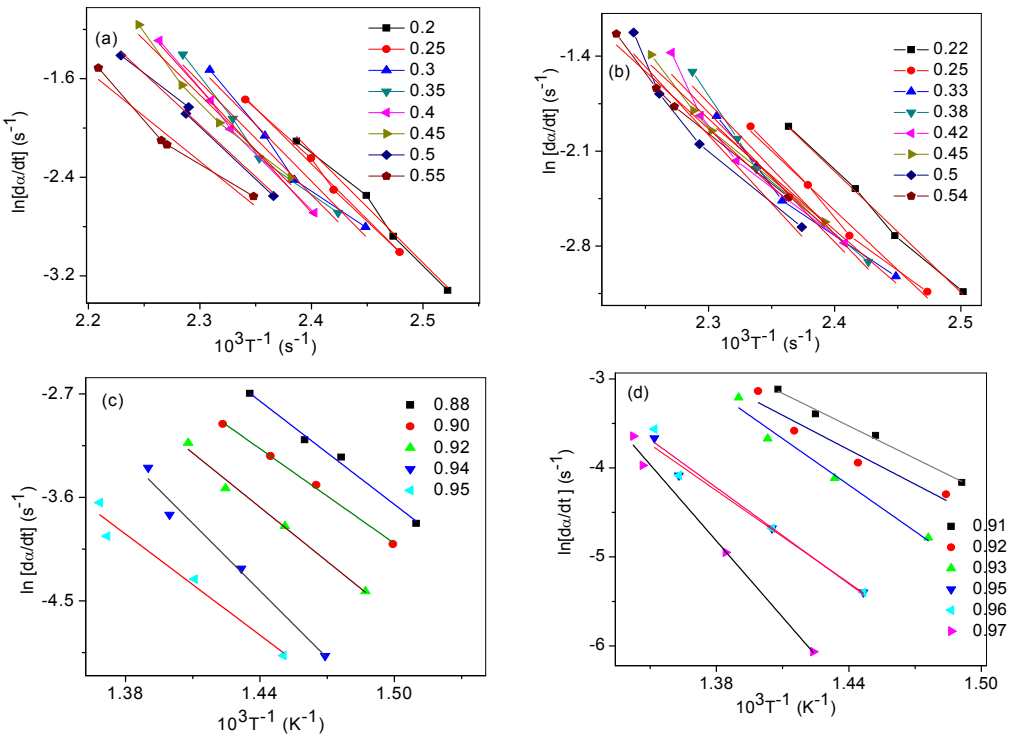

Fig. 16 The Friedman plots for each stage of decomposition of Ce-Ox in presence of Co_3O_4 A_2; first (a), second (b), third (c) and fourth stages (d).

Thermal decomposition of cerium oxalate crystalline particle is significantly influenced by the self-generated reaction condition.

Change in the internal gaseous pressure in the oxalate crystalline particle during heating play a predominant role in regulating the kinetic behavior in the early stages of the reaction. But the change in the internal gaseous pressure cannot be traced during the reaction. Hence, it is a challenge to reveal how kinetic characteristic of the reaction behave with reaction condition by tracking the heat flow process under systematically altering reaction condition. Thermal decomposition stage of cerium oxalate decahydrate in N_2 atmosphere occurs through following mechanism. Theoretical mass loss corresponding to the formation of ceria (Ce_2O_3) from cerium oxalate is 55. 06%[9]. The experimental mass loss of the decomposition of the sample A_0 from the TG curve (Fig. 12b) was found to be 50.04%. The mass loss (%) for other samples is listed in Table 2.

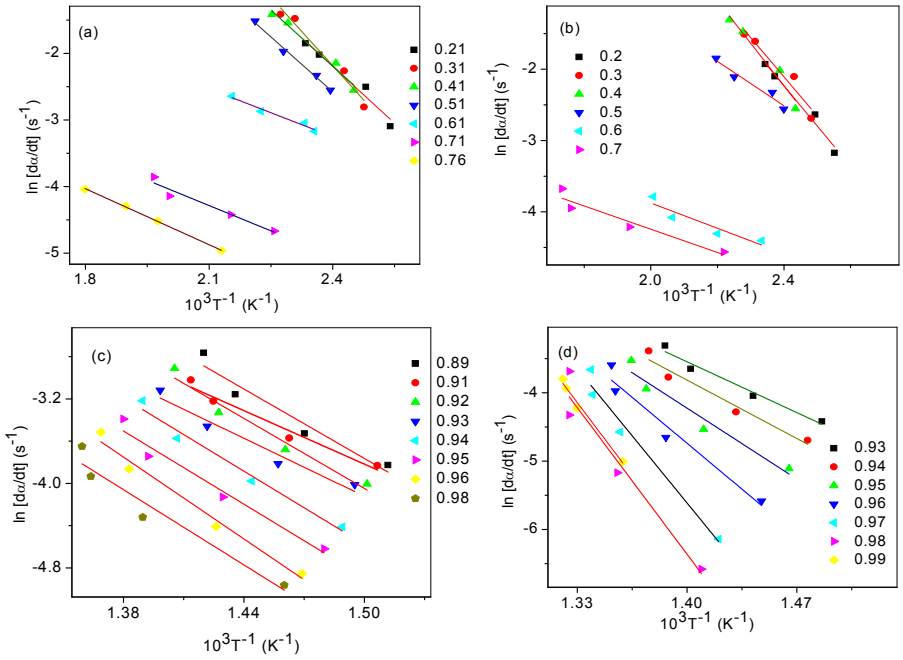

Fig. 17 The Friedman plots for each stage of decomposition of Ce-Ox in presence of $CoFe_2O_4$, A_4; first (a), second (b), third (c) and fourth stages (d).

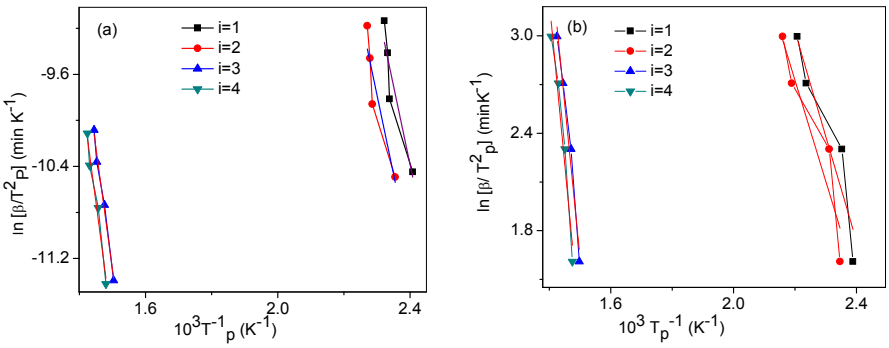

Fig. 18 Kissinger plots for each peak of samples A_3 (a) and A_5 (b).

$$Ce_2(C_2O_4)_3.10H_2O \rightarrow Ce_2(C_2O_4)_3.3H_2O + 7H_2O^{25} \quad (8)$$

$$Ce_2(C_2O_4)_3.3H_2O \rightarrow Ce_2(C_2O_4)_3 + 3H_2O \quad (9)$$

$$Ce_2(C_2O_4)_3 \rightarrow Ce_2O_2.CO_3 + 4CO_2 + CO \quad (10)$$

$$2CO \rightarrow C + CO_2 \quad (11)$$

$$Ce_2O_2.CO_3 \rightarrow Ce_2O_3 + CO_2 \quad (12)$$

For the parent and mixed sample, the overall heat absorbing process of thermal decomposition is empirically resolved into four stages as evident from Fig. 19. Fig. 19 shows kinetic deconvolution of the thermal decomposition of the samples A_0-A_5 in inert atmosphere, which was based on the Eq. 2. The first low temperature reaction of all samples is considered as dehydration reaction. Each sample goes through two overlapping stages for the dehydration reaction. Similarly, the higher temperature decomposition of each sample to Ce_2O_3 under

vacuum is composed of two partially overlapping reaction steps due to the formation of an intermediate cerium oxy carbonate $Ce_2O_2.CO_3$[47].

5.3.4. Effect of Fe_3O_4, Co_3O_4 and NiO on the removal of water of crystallization of Ce-Ox

Oxides of Fe and Co have strong affinity for the adsorption of water vapor[50–52]. These oxides act as dehydrating agent[14,15]. Heat of adsorption of water for NiO is comparatively lower than other oxides. Therefore NiO chemisorb water vapor weakly[53]. In the concerned work, Fe_3O_4 & Co_3O_4 facilitate the dehydration of Ce-Ox requiring lower *Ea* value but NiO can't facilitate the dehydration reaction. The average optimized kinetic parameters for different β values are listed in Table 3. For the entire sample, the optimized kinetic parameters for first, second, third and fourth reaction step was not much deviated from those parameters which were determined previously. The optimized *Ea* value for the dehydration of sample A_0 comes in the range of 73 to 93 kJ mol^{-1}, whereas in presence of Fe_3O_4 *Ea* value of 35 to 36 kJ mol^{-1} is needed. The *Ea* value of A_2 requires activation energy of 73-74 kJ mol^{-1}.

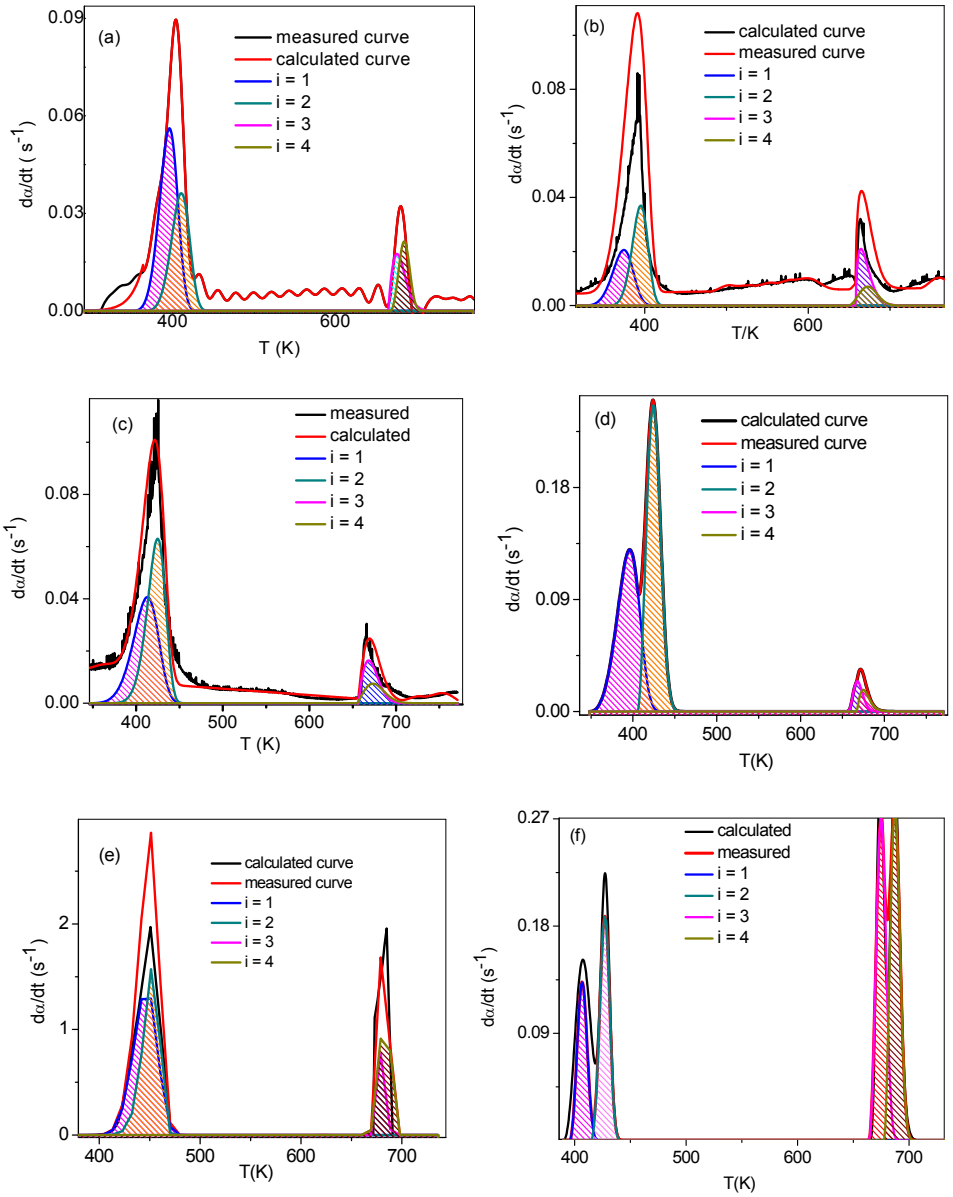

Fig. 19 The results of kinetic deconvolution analysis for the thermal decomposition of the samples A_0(a), A_1(b), A_2(c), A_3(d), A_4(e) and A_5(f) under linear non-isothermal condition at β = 5 Kmin^{-1} in N_2 atmosphere.

5.3.5. Effect of $CoFe_2O_4$ and $NiFe_2O_4$ on the removal of water of crystallization of Ce-Ox

Both $CoFe_2O_4$ and $NiFe_2O_4$ have strong affinity to adsorb water vapour[54, 55]. Therefore water vapor comes out during the dehydration of Ce-Ox, can be adsorbing by these ferrites. Hence these ferrites facilitate the process. From the Table 3, it was shown that the Ea value required by $CoFe_2O_4$ and $NiFe_2O_4$ are 43-74 and 73-74 kJ mol^{-1} respectively.

5.3.6. Effect of Fe_3O_4, Co_3O_4 and NiO on the formation of ceria nanoparticle by decomposition

Thermal decomposition of Ce-Ox to the formation of ceria releases CO. Co_3O_4 surface has strong CO oxidizing ability than Fe_3O_4 and NiO[20,23,56]. Hence any additives having capacity to oxidize these evolving CO can promote the reaction[11]. Therefore CO evolved from the Ce-Ox diffuses to the surface of Co_3O_4, CO react with oxygen on the surface of the catalyst giving CO_2[23]. Non-reducible metal supported Fe_3O_4 has strong CO oxidizing ability than Fe_3O_4 alone[20]. Also interface of NiO with other metal/metal oxide has strong ability to convert CO to CO_2[56] . The activation energy needed for the sample A_0 for the decomposition stage comes in the range of 172-175 $kJmol^{-1}$. The increasing order of *Ea* ($kJmol^{-1}$) for the samples A_2, A_3 and A_4 follows as: A_3 (163-164) < A_2 (169-175) < A_4 (187-192).

Table 3 Average values of optimized kinetic parameter for each reaction step of thermal decomposition of cerium oxalate decahydrate.

Sample	*i*	Ea_i (kJ mol^{-1})	A_i (sec^{-1})	R^2
A_0	1	93.21 ± 0.05	(2.49 ± 0.01)× 10^7	0.9985
	2	73.68 ± 0.09	(4.23 ± 0.00)× 10^4	0.9496
	3	172.20 ± 0.20	(1.50 ± 0.03) × 10^{14}	0.9205
	4	175.50 ± 0.20	(1.80 ± 0.05) × 10^{14}	0.9325
A_1	1	35.75 ± 0.05	(4.70 ± 0.05) × 10^5	0.9639
	2	36.84 ± 0.04	(2.30 ± 0.06) × 10^5	0.9484
	3	169.20 ± 0.40	(7.94 ± 0.03) × 10^{13}	0.9543
	4	175.69 ± 0.50	(2.16 ± 0.10) × 10^{14}	0.9483
A_2	1	74.270 ± 0.20	(4.62 ± 0.03) × 10^4	0.9376
	2	73.520 ± 0.12	(2.48 ± 0.04)× 10^4	0.9101
	3	163.90 ± 0.23	(8.64 ± 0.02) × 10^7	0.9838
	4	164.46 ± 0.08	(1.88 ± 0.03) × 10^8	0.9319
A_3	1	112.41 ± 0.03	(4.18 ± 0.02)× 10^9	0.9243
	2	115.00 ± 0.02	(2.63 ± 0.01)× 10^9	0.9720
	3	187.50 ± 0.01	(2.94 ± 0.02)× 10^{15}	0.9688
	4	192.60 ± 0.03	(3.54 ± 0.11)× 10^{15}	0.9765
A_4	1	78.67 ± 0.03	(3.72 ± 0.05) × 10^5	0.9980
	2	43.20 ± 0.05	(6.56 ± 0.04) × 10^4	0.9692
	3	163.20 ± 0.02	(7.80 ± 0.10) × 10^8	0.9966
	4	164.60 ± 0.01	(3.48 ± 0.04) × 10^8	0.9603
A_5	1	73.40 ± 0.30	(1.41 ± 0.01)× 10^2	0.9525
	2	74.30 ± 0.40	(5.30 ± 0.10)× 10^1	0.9479
	3	167.30 ± 0.30	(2.19 ± 0.12)× 10^{13}	0.9793
	4	165.40 ± 0.00	(4.24 ± 0.06)× 10^{13}	0.9816

5.3.7. Effect of $CoFe_2O_4$ and $NiFe_2O_4$ on the formation of ceria nanoparticle by decomposition

Ferrites of Ni and Co have strong affinity to adsorb CO and to oxidize it to CO_2[21, 22]. Hence releasing CO during the reaction diffused to surface of ferrite. *Ea* needed for the process by A_4 and A_5

respectively are 163-164 and 165-167 $kJmol^{-1}$. Fig. 20 illustrates the mechanism of thermal decomposition of cerium oxalate decahydrate in presence of ferrites. It was noticed from the Table 3 that higher difference in the values of *A* for initial (*i* = 1 and 2) and final stages (*i* = 3 and 4) of each sample was high, indicating higher lags of reaction time and temperature. *Ea* needed by the sample A_3 is higher for dehydration and decomposition due to less catalyzing effect of NiO.

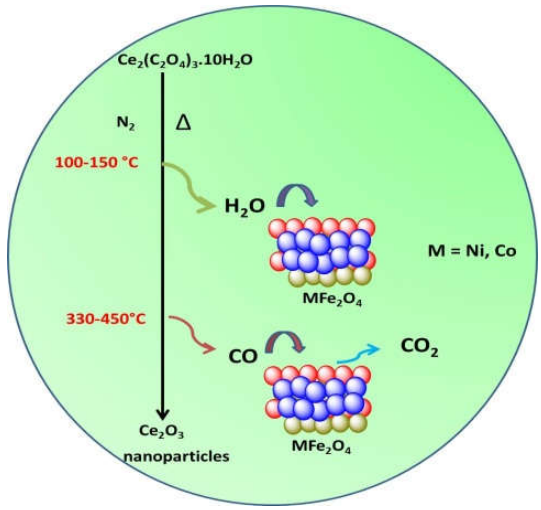

Fig. 20 Schematic representation of the mechanism of thermal decomposition of cerium oxalate decahydrate in presence of ferrites

5.4. Conclusion

Semi conducting magnetic nano metal oxides, Fe_3O_4, Co_3O_4, NiO, $CoFe_2O_4$ and $NiFe_2O_4$ were synthesized by thermal decomposition of their oxalate precursor. Characterization techniques used for the synthesized oxides were FT-IR, XRD, SEM and UV-DRS. Synthesized oxides except NiO are amorphous in nature. Effects of

nano metal oxides on thermal decomposition stages of cerium oxalate decahydrate up to the formation of ceria were studied and predicted the thermal events which were occurred during the reaction process. Using the method of kinetic deconvolution, kinetic analysis of each resolved stage was performed. It was explored that nano Fe_3O_4 facilitates the dehydration stages requiring less *Ea* value of 35-36 $kJmol^{-1}$. Nano Co_3O_4, $CoFe_2O_4$ and $NiFe_2O_4$ promoted the dehydration as well as decomposition stages of cerium oxalate decahydrate by decreasing the *Ea* value. Nano NiO has shown retarding effect on both the dehydration as well as decomposition stages.

5.5. References

1. Wright CS, Fisher C, Thompsett D, Walton RI. Hydrothermal synthesis of a cerium(IV) pyrochlore with low-temperature redox properties. *Angew Chem Int Ed*. 2006;45: 2442–2446.

2. Corradi AB, Bondioli FB, Ferrari AM, Manfredini T. Synthesis and characterization of nano sized ceria powders by microwave-hydrothermal method. *Mater Res Bull*. 2006;41:38-44.

3. Christel LR, Jeffrey WL, Erik ML, et al. Sol−gel-derived ceria nano architectures: synthesis, characterization, and electrical properties. *Chem Mater*. 2006;18:50-58.

4. Ali B, IZ M, Julian E, Lata P. Microemulsion-based synthesis of CeO_2 powders with high surface area and high-temperature stabilities. *Langmuir*. 2004;20:11223-11233.

5. Gabal MA, Elroby SAK, Obaid AY. Synthesis and characterization of nano-sized ceria powder via oxalate decomposition route. *Powder Technol*. 2012;229:112-118.

6. Miyazaki H, Kato JI, Sakamoto N, Wakiya N, Ota T, Suzuki H. Synthesis of CeO_2 nanoparticles by rapid thermal decomposition using microwave heating. *Adv Appl Ceram*. 2010;109:123-127.

7. Nusrath K, Muraleedharan K. Effect of Ca(II) on the multistep kinetic behavior of thermally induced oxidative decomposition of cerium(III) oxalate to CeO_2(IV). *J Anal Appl Pyrol*. 2016;120:379-388.

8. Nusrath K, Muraleedharan K. Effect of Ca(II) additive on the thermal dehydration kinetics of cerium oxalate rods. *J Therm Anal Calorim*. 2017;128:541-52.

9. Subba Rao VV, Rao RVG, Biswas AB. Thermogravimetric analysis of La, Ce, Pr and Nd oxalates in air and in carbon dioxide atmosphere. *J Inorg Nucl Chem*. 1965;27:2525-2531.

10. Furuichi R, Ishii T, Yamanaka Z, Shimokawabe M. Effect of α-Fe_2O_3additive on the thermal decomposition of salts of halogen oxoacids, oxalates, azide, permanganate, and oxides. *Thermochim Acta*. 1981;51:245-267.

11. Girgis MM, El-Awad AM. Kinetics and mechanism of thermal decomposition of lithium oxalate catalysed by $Cd_{1-x}Co_xFe_2O_4$(x = 0.0, 0.5 and 1.0) ferrospinel additives. *Thermochim Acta*. 1993;214:291-303.

12. Jose John M, Muraleedharan K, Kannan MP, Ganga Devi T. Effect of semiconducting metal oxide additives on the kinetics of thermal decomposition of sodium oxalate under isothermal conditions. *Thermochim Acta*. 2012;534:71-76.

13. Muraleedharan K, Kannan MP, Gangadevi T. Effect of metal oxide additives on the thermal decomposition kinetics of potassium metaperiodate. *J Therm Anal Calorim*. 2010;100:177-181.

14. Yong L, Harun T, Chun-Jiang J, et al. From glycerol to allyl alcohol: iron oxide catalyzed dehydration and consecutive hydrogen transfer. *Chem Commun*. 2010;46:1238-1240.

15. Kesavan V, Dhar D, Koltypin Y, et al. Nanostructured amorphous metals, alloys, and metal oxides as new catalysts for oxidation . *Pure ApplChem*. 2001;73:85-91.

16. Yang Y, Huilong F, Gedeng R, Changsheng X, James T. Efficient electrocatalytic oxygen evolution on amorphous nickel-cobalt binary oxide nanoporous layers. *ACS Nano*. 2014;8:9518-9523.

17. Ye-Fei L, Zhi-Pan L. Structure and water oxidation activity of 3d metal oxides. *Wires Comput Mol Sci*. 2016;6:47-64.

18. Boris IK, Rasika Dias HV, Oxana VK. Mini-review: ferrite nanoparticles in the catalysis. *Arab J Chem*. 2014. doi:10.1016/j.arabjc.2014.10.049

19. Nair TDR, Aniz CU. Effect of redox nature of impregnated ferrite catalysts on their carbon monoxide. *Res Rev J Mater Sci*. 2013;1:45-52.

20. By RM, Sh KS, Freund H-J. CO oxidation on a Pd/Fe_3O_4 (111) model catalyst. *Z Phys Chem*. 2004;218:905-914.

21. Fouad OA, Abdel Halim KS, Rashad MM. Catalytic oxidation of CO over synthesized nickel ferrite nanoparticles from fly ash. *Top Catal*. 2008;47:61-65.

22. Jasmine T, Nygil T, Frank G, et al. Synthesis of cobalt ferrite nanoparticles by constant pH co-precipitation and their high catalytic activity in CO oxidation. *New J Chem*. 2017;41:7356-7363.

23. Minjie Z, Lili C, Michal B, et al. Enhancing catalytic CO oxidation over Co_3O_4 nanowires by substituting Co^{2+} with Cu^{2+}. *ACS Catal*. 2015;5:4485-4491.

24. Miguel G, Juan H, Leticia B, Joaquin N, Mario ERG. Characterization of calcium carbonate, calcium oxide and calcium hydroxide as starting

point to the improvement of lime for their use in construction. *J Mater Civ Eng*. 2009;21:625-708.

25. Vimal G, Kamal PM, Biju PR, Joseph C, Unnikrishnan NV, Ittyachen MA. Structural studies and luminescence properties of CeO_2:Eu^{3+}nanophosphors synthesized by oxalate precursor method. *Appl Nanosci*. 2015;5:837-846.

26. Oman Z, Haznan A, Widayanti W. Synthesis and characterization of nanostructured CeO_2 with dyes adsorption property. *Process Appl Ceram*. 2014;8:39-46.

27. Nasser MH. Synthesis, characterization and optical band gap of NiO nanoparticles derived from anthranilic acid precursors via a thermal decomposition route. *Polyhedron*. 2011;30:470-476.

28. Waldron RD. Infrared spectra of ferrites. *Phys Rev*. 1955;99:1727–35.

29. Feng J, Jean Claude J, Manfred W, Alan VC, Andrew H, Peter GB. Synthesis of ordered mesoporous Fe_3O_4 and γ-Fe_2O_3 with crystalline walls using post-template reduction/oxidation. *J Am Chem Soc*. 2006;128:12905-12909.

30. Shao-Wen C, Ying-Jie Z, Ming-Yan M, Liang L, Ling Z. Hierarchically nanostructured magnetic hollow spheres of Fe_3O_4 and γ-Fe_2O_3: preparation and potential application in drug delivery. *J Phys Chem C*. 2008;112:1851-1856.

31. Guo L, Li J, Zhang L, et al. A facile route to synthesize magnetic particles within hollow mesoporous spheres and their performance as separable Hg^{2+} adsorbents. *J Mater Chem*. 2008;18:2733.

32. Nakano M, Wada T, Koga N. Exothermic behavior of thermal decomposition of sodium percarbonate : kinetic deconvolution of successive endothermic and exothermic processes. *J Phys Chem A*. 2015;119:9761-9769.

33. Tanaka H, Koga N, Galwey AK. Thermal dehydration of crystalline hydrates: microscopic studies and introductory experiments to the kinetics of solid-state reactions. *J Chem Educ*. 1995;72:251−256.

34. Galwey AK. Structure and order in thermal dehydrations of crystalline solids. *Thermochim Acta*. 2000;355:181−238.

35. Wada T, Nakano M, Koga N. Multistep kinetic behavior of the thermal decomposition of granular sodium percarbonate : hindrance effect of the outer surface layer. *J Phys Chem A*. 2015;2:9749-9760.

36. Mayfield CL, Huda MN. Free energy landscape approach to aid pure

phase synthesis of transition metal (X = Cr, Mn and Fe) doped bismuth titanate ($(Bi_2Ti_2O_7)$). *J Cryst Growth*. 2016;444:1-2.

37. Takeshi W, Nobuyoshi K. Kinetics and mechanism of the thermal decomposition of sodium percarbonate : role of the surface product layer. *J Phys Chem A*. 2013;117:1880-1889.

38. Yoshikawa M, Yamada S, Koga N. Phenomenological interpretation of the multistep thermal decomposition of silver carbonate to form silver metal. *J Phys Chem C*. 2014;118:8059-8070.

39. Kitabayashi S, Koga N. Physico-geometrical mechanism and overall kinetics of thermally induced oxidative decomposition of tin(II) oxalate in air: formation process of micro structural tin(IV) oxide. *J Phys Chem C*. 2014;118:17847−17861.

40. Koga N, Goshi Y, Yamada S, Pe´rez-Maqueda LA. Kinetic approach to partially overlapped thermal decomposition processes; co-precipitated zinc carbonates. *J Therm Anal Calorim*. 2013;111:1463-1474.

41. Nobuyoshi K, Daisuke K, Tomoyasu K. Aragonite crystal growth and solid-state aragonite − calcite transformation: a physico − geometrical relationship via thermal dehydration of included water. *Cryst Growth Des*. 2013;13:2238-2246.

42. Koga N, Yamada S, Kimura T. Thermal decomposition of silver carbonate: phenomenology and physico-geometrical kinetics. *J Phys Chem C*. 2013;117:326−336.

43. Sánchez-jiménez PE, Perejón A, Criado JM, Diánez MJ, Pérez-maqueda LA. Kinetic model for thermal dehydrochlorination of poly (vinyl chloride). *Polymer*. 2010;51:3998-4007.

44. Koga N, Suzuki Y, Tatsuoka T. Thermal dehydration of magnesium acetate tetra hydrate: formation and in situ crystallization of anhydrous glass. *J Phys Chem B*. 2012;116:14477−14486.

45. Yusuke N, Koga N. Phenomenological kinetics of the carbonation reaction of lithium hydroxide monohydrate : role of surface product layer and possible existence of a liquid Phase. *J Phys hem C*. 2014;118:5424-5436.

46. Yoshikawa M, Goshi Y, Yamada S, Koga N. Multistep kinetic behavior in the thermal degradation of poly (L□lactic acid): a physico-geometrical kinetic interpretation. *J Phys Chem B*. 2014;118:11397-11405.

47. Pe´rez-Maqueda LA, Criado JM, Sa´nchez-Jime´nez PE. Combined kinetic analysis of solid-state reactions: a powerful tool for the simultaneous determination of kinetic parameters and the kinetic model without previous assumptions on the reaction mechanism. *J Phys Chem A*. 2006;110:12456-12462.

48. Málek J, Criado JM. Empirical kinetic models in thermal analysis. *Thermochim Acta*. 1992;203:25-30.

49. Šesták J. Diagnostic limits of phenomenological kinetic models introducing the accommodation function. *J Therm Anal*. 1990;36:1997-2007.

50. Clarke NS, Hall PG. Adsorption of water vapor by iron oxides. 2. water isotherms and X-ray photoelectron spectroscopy. *Langmuir*. 1991;7:678-682.

51. Tatsuya K, Yumiko N, Takayuki M. A two-step thermochemical water splitting by iron-oxide on stabilized zirconia. *J Sol Energy Eng*. 2006;128:3-7.

52. Jia C, Annabella S. Water adsorption and oxidation at the Co_3O_4 (110) Surface. *J Phys Chem Lett*. 2012;3:2808-2814.

53. Matsuda T, Taguchi H, Nagao M. Energetic properties of nio surface examined by heat-of -adsorption measurement. *J Therm Anal*. 1992;38:1835-1845.

54. Yogendra K, Alfa S, Parasharam MS. Shape-controlled $CoFe_2O_4$ nanoparticles as an excellent material for humidity sensing. *RSC Adv*. 2017;7:55778-55785.

55. Priyank VK, Michael PS, Sidney Y, Bilge Y, Jeffrey CG. High surface reactivity and water adsorption on $NiFe_2O_4$ (111) surfaces. *J Phys Chem C*. 2013;117:5678-5683.

56. Yunan Y, Pan Z, Zuzeng Q, et al. Low temperature CO oxidation catalysed by flower-like Ni–Co–O: how physicochemical properties influence catalytic performance. *RSC Adv*. 2018;8:7110-7122.

NUSRATH. K “SYNTHESIS AND KINETICS OF FORMATION OF CERIA AND CERIA BASED MATERIALS via THERMAL DECOMPOSITION OF OXALATES”. THESIS. DEPARTMENT OF CHEMISTRY, UNIVERSITY OF CALICUT, 2018.

6.1. Introduction

Material chemists have provoked with enthusiasm to research for scaffolding ceria as potential catalyst. The creation of oxygen vacancies have predominant role for performing ceria as a promising material. For example, (1 0 0) crystal plane of nano cube ceria exhibits reactivity than (1 1 0) and (1 1 1) planes of nano sphere like ceria. Active oxygen presented on the CeO_2 surface is perturbed by different factors such as surface area, reactive facets, surface defects and elemental composition on the surface[1–4]. Hence increase in the surface concentration of active oxygen located at the CeO_2 surface is highly important to promote catalytic activity. Incorporation of isovalent cation into CeO_2 structure resulted in the formation of Ce_{1-X} M_XO_2 solid solution. Cations of first transition series such as Co^{2+}, Cu^{2+}, Ni^{2+}, and Mn^{2+} and third transition series such as Zr^{2+} enhanced the oxygen storage capacity of CeO_2. Besides, doping with lanthanides such as Y, La, Tb, Gd, Pr attributed to the formation of high concentration of defects leading to the stabilization of CeO_2. Hence prevented sintering and provided extended thermal stability[5–9]. Acceleration of oxygen exchange depends on both mobility of oxygen and number of oxygen vacancies. This took key role in the course of oxygen buffering capacity of ceria, particularly at tangible operating condition[10].

Moreno *et al*[11] discussed the role of Cu^{2+} in the ceria lattice on the oxidation of CO over CuO/CeO_2 catalyst. Both redox couple Ce^{4+}/Ce^{3+} and Cu^{2+}/Cu^{1+} is involved in the reaction. Hence ceria can provide lattice oxygen for copper, thus increasing the oxidative properties of the binary system. Moreover, the membrane – deposited

active layer of CuO-CeO_2/SG exposed higher catalytic activity for CO conversion[12]. Park *et al*[13] made a structure – reactivity correlations for the rare earth oxide promoted transition metal oxides based on emission control in the exhaust gases.

Among nano metal oxides, rare earth oxide ceria possessed excellent antioxidant and anti-inflammatory properties. This happens because of its triggering nature of Ce^{3+} and Ce^{4+} oxidation state depending on the environment[14–16]. Ying *et al*[17] reported that CeO_2 Nps are toxic to cancer cells, to inhibit invasion and to sensitize cancer cells to radiation therapy and chemotherapy. But it displays minimum toxicity to normal tissues and contributes protection from cell damage indirectly by priming cells to respond to ROS attack or directly by scavenging cellular ROS. It can protect healthy cells from radiation induced damage during radiation therapy and provides neuro protection to spinal cord neurons.

Wason *et al*[18] proposed that nano ceria act as radical scavenger of H_2O_2 in normal tissues but as a producer of H_2O_2 in cancer environment. These properties of ceria largely depend on its particle shape, size, surface chemistry, surface additives and ligand that involved in redox reaction[19–21]. Anti –invasive behavior of nanoceria was observed in human melanoma cells, whereas antitumor and anti angiogenic effects were studied *in vivo* tumor model[22]. Doping of the parent matrix with elements which can emits radiation by itself upon excitation in the UV-visible region of the spectrum[17]. Nano medicine with modified structure can kill tumor cell by increasing ROS level in tumor cells or by directing the nucleus or organ cells[23]. It was found

that CeO_2 Nps caused cytochrome C release and activated caspase-3 and caspase-9, which demonstrates that NPs induced apoptosis of tumor cells targeting the mitochondria[23]. Titanium doped CeO_2 nanoparticle possessed catalase like activity, and this enzymatic activity can reduce H_2O_2 induced apoptosis. This results in preventing macular degeneration and Alzheimer's disease[24]. Significant reduction of tumor burdens was observed with the uptake of combination of cisplatin and folic acid-CeO_2 than it alone used[18]. Wongrakpanich *et al*[25] aroused that besides the surface and core oxide composition, size of nanoparticle has key role on imparting its effect on certain diseases. Metal oxides of Si, Cu, Fe aroused the induced oxidative stress and cytotoxicity in airway epithelial cells. On the literature survey, it was taken into our mind that CuO Np of 24nm show more cytotoxic effect than 4nm CuO Np. This was attributed due to the rate of entry of Nps into the cell, which potentially influencing the amount of intracellular dissolution of Cu^{2+}.

Que *et al*[26] reported that introduction of Cu^{2+} with ceria lattice markedly changed morphology and electronic structure compared to parent ceria NCs. Along with this research, they also found that both internal and external Cu-doping affected structure and morphology (cubic to truncated octahedron). It was reported that presence of copper oxide species in the CeO_2 surface make it as significantly enhanced support in the destruction of benzene, toluene and *p*-xylene[27,28].

Even though large number of research was done based on anticancerous properties of ceria and copper Nps, there is scarcity of data regarding the cytotoxic effects made by the Cu-Ce-O solid

solution. The present work aimed to synthesize different series of Cu-Ce-O solid solutions from the oxalate precursor, estimation of kinetic characteristics of formation and the correlation of cytotoxic effects of mixed oxides towards Dalton's Lymphoma ascites cells. Analysis of kinetic characteristics of the formation of solid solution was made by isoconversional strategy under non-isothermal condition.

6.2. Experimental

6.2.1. Method of preparation

For the synthesis, chemicals used were $Ce(NO_3)_3.6H_2O$, $Cu(NO_3)_2.3H_2O$, $Na_2C_2O_4$ and surfactant cetyl trimethyl ammonium bromide (CTAB). In the distinctive synthesis of $Cu_xCe_{(1-x)}O_2$ (where x = 0.00 (s_1), 0.02 (s_2), 0.1 (s_3), 0.2 (s_4) and 0.3 (s_5), 6.91mmol Ce $(NO_3)_3.6H_2O$, 2.30mmol cetyl trimethyl ammonium bromide (CTAB) and above mentioned mol % of $Cu(NO_3)_2.3H_2O$ were taken and mixed under stirring to get an homogenous solution. Add slowly 10.36mmol of saturated sodium oxalate in order to precipitate as oxalate. Stirring was extended for further 4h. Allowed the solution to settle, collected the precipitate and washed with ethanol and water. Finally it was dried by keeping in an air oven at 353K for 24h. This procedure was followed for all doped samples. For the undoped sample, the procedure was same without using copper nitrate. The prepared oxalate samples were designated as COX (c_1), $Ce_{1-x}Cu_x$-Ox (x = 0.02) (c_2), $Ce_{1-x}Cu_x$-Ox (x = 0.1) (c_3), $Ce_{1-x}Cu_x$-Ox (x = 0.2) (c_4) and $Ce_{1-x}Cu_x$-Ox (x = 0.3) (c_5).

The chemical composition and crystal structure of both doped and un doped cerium oxalate (COX) and oxide (prepared *via* thermal decomposition) were studied by XRD. The prepared cerium oxalate precursor was calcined at 723K in muffle furnace for 5h. Similarly doped COX was also proceeded for the preparation of $Cu_xCe_{(1-x)}O_2$ (where x = 0.02, 0.1, 0.2 and 0.3). The morphology and topographical studies of the oxide samples were brought with TEM and Field emission scanning electron microscope. UV-Visible spectra of the oxide samples were taken. Photo luminescent properties are well characterized by using fluorescence spectrometer at room temperature. Energy dispersive spectra (EDS) were used for identifying elemental composition involved in each of the oxides. Electronic and crystalline properties are well characterized by using HRTEM and SAED pattern. Thermal decomposition properties of oxalate and doped oxalate were analyzed by DSC and TG analysis in N_2 (50mL) atmosphere. Raman spectra of the samples were collected using confocal Raman microscope with the excitation of 532nm laser.

6.3. Results and discussion

6.3.1. Material characterization

Fig. 1a shows the X-ray diffraction peaks corresponding to the monoclinic phase of cerium oxalate decahydrate (COX) (JCPDS No. 20-0268). Doping with Cu^{2+} made some additional peak in the XRD (Fig. 1b) pattern of COX. This reveals that addition of Cu^{2+} cause to the phase change of COX. Further thermal decomposition behavior of COX precursor and the effect of various reactant molar ratios of

Cu^{2+}:Ce^{3+} in the thermal decomposition process of COX was determined through thermogravimetry analysis measurement. Fig. 2A shows the TG curves of both COX (Fig. 2A:c_1) and COX doped with Cu^{2+} in the mol% of 2 (Fig. 2Ac_2), 10 (Fig. 2A:c_3), 20 (Fig. 2A:c_4) and 30 (Fig. 2A:c_5) in N_2 at 5 K min^{-1} between 300-873 K. It displays two major stages at the temperature range of 300-473 K (~24.42%) and 473-625K (~29.78%).

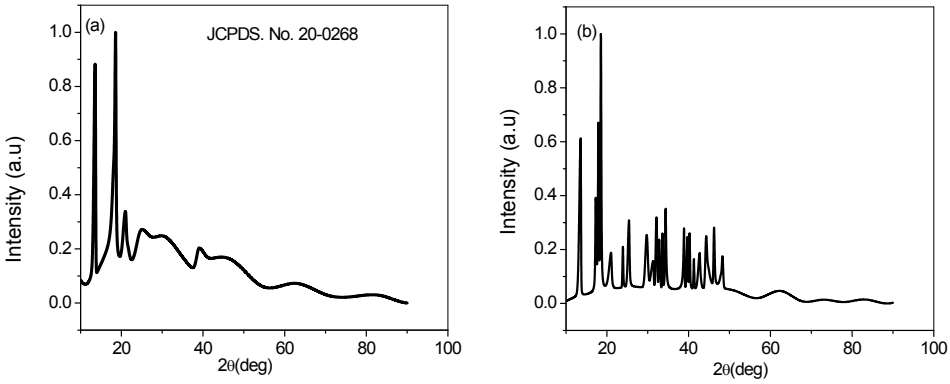

Fig. 1 The XRD pattern of COX (a) and 2 mol% Cu^{2+}-doped COX (b)

Table 1 Experimental mass loss for the thermal decomposition of the samples c_1-c_5.

Sample	Experimental mass loss (%)	
	Dehydration	Overall thermal decomposition
c_1	21.67	54.26
c_2	19.42	51.35
c_3	24.34	56.48
c_4	20.43	51.16
c_5	21.57	54.61

The first step is associated with loss of crystallized water of $Ce_2(C_2O_4)_3.nH_2O$ with the value of *n* is evaluated to be 10. The second one is due to the decomposition of oxalate which is in good agreement with the theoretical mass loss of 29.82%. It occurs with non-redox thermal decomposition of the oxalate and the formation of Ce_2O_3. Hence the TG results are compatible with XRD pattern. Specific range of mol% of dopants has significant influence on the thermal stability of Ce_2O_3. On the preliminary observation of TG curves, 2 and 20mol% copper doped sample displayed less stability and enhance to the formation of Ce_2O_3, whereas 10mol% showed higher mass loss for the dehydration as well as the formation of Ce_2O_3. Thermal stability depends on not only mass loss, but also the particle size of formed oxide and precursor oxalate, decomposing temperature, homogeneity of the sample, concentration of impurities in the lattices, etc. Table 1 shows the experimental mass loss of overall thermal dehydration and decomposition reactions of COX and Cu^{2+} doped COX. The theoretical mass loss for the overall thermal decomposition reaction of COX was found to be 52.48%. For the sample c_1 (Fig.2A:c_1), overall mass loss (%) was found to be 54.26% since the degradation of surfactant is also occurred with c_1. Fig. 2A:c_2 shows the mass loss of 19.42% for first and 51.35% for the overall decomposition stage respectively. Fig. 2A:c_3 exhibited 24.34 for first stage and 56.48% for the overall thermal decomposition. The mass loss (%) for sample c_4 and c_5 are given in Table 1.

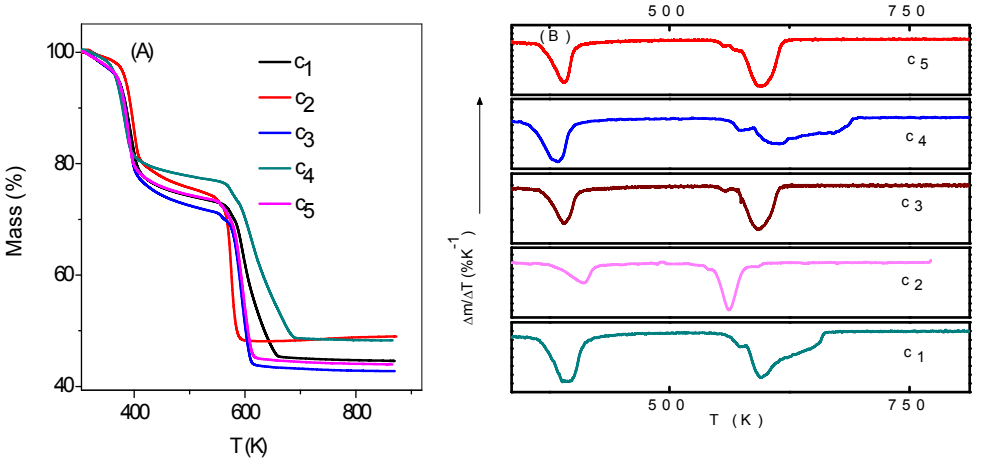

Fig. 2 TG curves (A) for COX (c_1) and Cu^{2+}-COX; 2 (c_2), 10 (c_3), 20 (c_4) and 30% (c_5) and DTG curves (B) of COX (c_1) and Cu^{2+} doped COX 2 (c_2), 10 (c_3), 20 (c_4) and 30% (c_5) at $5Kmin^{-1}$.

DTG curves (Fig. 2B) show five mass loss processes for the pure (Fig. $2Bc_1$) and doped COX (Figs. $2Bc_2$-c_5 2, 10, 20 and 30% respectively). Hence, in order to study overall endothermic thermal decomposition process, the DSC curves were deconvoluted using statistical function (Weibull) to five partially overlapping steps. In the concerned process, first two stages are the minor stages of main stage dehydration process of 10 molecules of water per molecule. In the third stage, removal process of surfactant occurs. In the fourth stage, oxy carbonate intermediate is formed and finally, the last stage is associated with the oxide Ce_2O_3 and $Ce_{2x}Cu_{(1-x)}O_{3-\delta}$.

The morphology and micro structure of the synthesized oxalate sample was characterized with Field Emission Scanning Electron microscope (FE-SEM) (Fig. 3). Energy dispersive spectra (EDS) for the doped and undoped COX were exposed in the Figs. 4a & b respectively. FE-SEM image (Fig. 3a) shows that most of the formed COX possessed disc like (flower) textures. This morphology of the

oxalate precursor was slightly destroyed with introduction of Cu^{2+} along with Ce^{3+}. This arouses the significance of Cu^{2+} dopant on the surface textural changes. The energy peak corresponding to the oxygen, cerium atoms are shown in the Fig. 4a. Additionally, the energy peak corresponding to the Cu atoms are also shown in Fig. 4b.

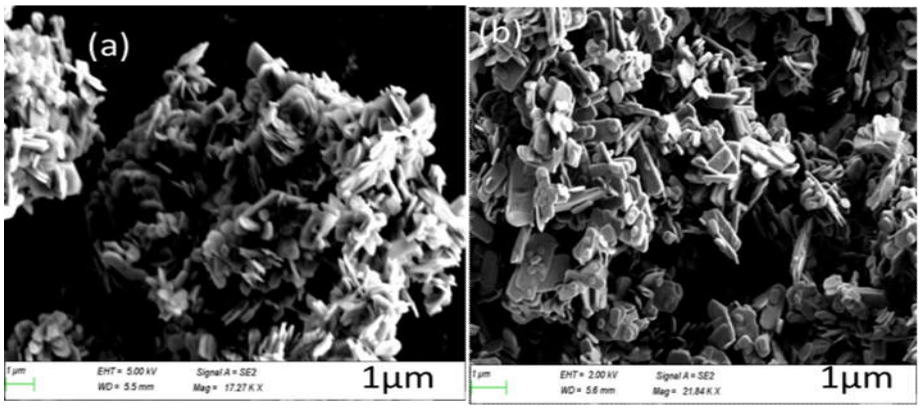

Fig. 3 FE-SEM images of COX (a) and 2 mol % Cu^{2+} - doped COX (b)

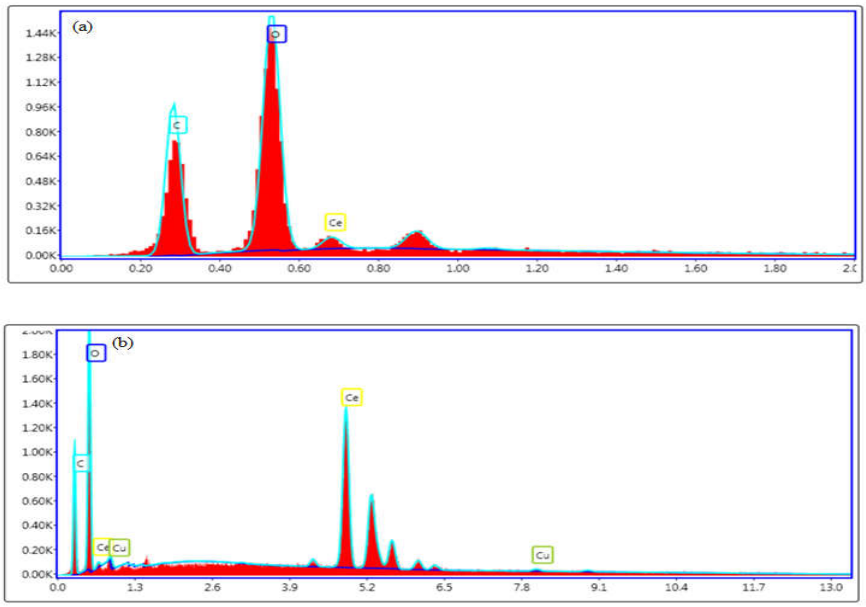

Fig. 4 The EDS of COX (a) and 2% Cu^{2+}- doped COX (b)

6.3.2. Thermal decomposition properties

COX and Cu^{2+} doped COX (2, 10, 20 and 30 mol %) were prepared through co-precipitation technique at room temperature. Thermal decomposition of COX and Cu-COX were carried out by DSC technique from room temperature to 773 K at 2, 4, 6, 8 and 10 K min^{-1}. During thermal decomposition of oxalates, self-generated reaction condition has pivotal role on the path of the reaction[29]. Change in the internal gaseous pressure and consequent alteration in the smoothness of the heat transfer process affect the kinetic behavior of the reaction[30]. Hence it is a challenge to reveal kinetic behavior of the reaction and how it can be changed with the introduction of metal ion impurities. Due to the experimental inconvenience of separately tracking the component process, deconvolution of overall kinetic information into reaction component is the only possible method for interpreting the reaction scheme of successive processes[31,32]. Hence kinetic analysis of the decomposition process was performed using the kinetic deconvolution method as per our previously published article[33]. DSC data at the prescribed heating rate were transformed to α-T data after the required calculation. DTG curve shows that cerium oxalate and doped cerium oxalate transformed to the corresponding oxide through 5 mass loss processes. So the DSC peak at each heating rate is deconvoluted using the statistical software *Peak fit* (4.12). The optimized values of *Ea* required for each stage are depicted in Table 2.

The DSC curves of pure and doped COX are shown in Fig. 5. It was noticed that 2% Cu^{2+} doped sample have significant effect on reducing the decomposition temperature *i.e*. nearly 64K than the parent

precursor. Increasing the dopant concentration, reduction in the decomposition temperature was decreased. Even if, 20% doped sample, c_4 have differential scanning calorimetric curve similar to the parent with small change in the quantity of heat absorbed. The quantity of energy absorbed take place at higher temperature for decomposition reactions; hence the value of activation energy for the same process will be higher.

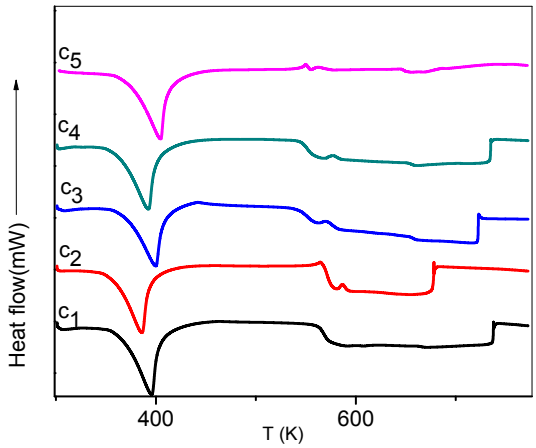

Fig. 5 The DSC curves of COX (c_1) and Cu^{2+}- doped COX 2 (c_2), 10 (c_3), 20 (c_4) and 30 (c_5) at $2Kmin^{-1}$.

The DSC curves for cerium oxalate decahydrate (Fig. 6a) and doped cerium oxalate (Figs. 6b-e) at different β values 2, 4, 6, 8, $10Kmin^{-1}$. Both doped and undoped sample display two major endothermic process, one at below 535K and other at above 535K, which are respectively corresponding to the dehydration of crystallized H_2O and decomposition of oxalate bond to form oxides of metal with the liberation of CO. When the heating rate was increased from 2 to $10Kmin^{-1}$, large amount of input energy per unit time was applied across the sample and reference cells. This would increase the overall

sensitivity of DSC instrument and shift in peak towards high temperature regions. With increasing the value of β, both lower (< 535K) and higher temperature (> 535 K) reaction of the samples systematically shifted the DSC curves to higher temperature. It was noted that the contribution of each stage was increased with the raise of values of β.

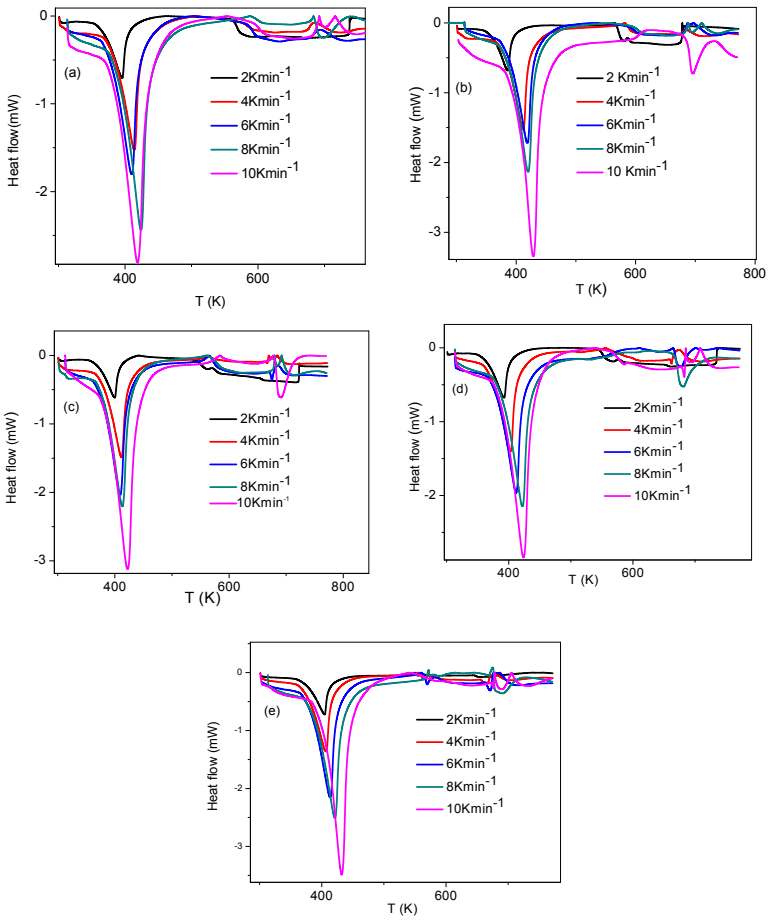

Fig. 6 The DSC curves of c_1 (a) and Cu^{2+} doped COX c_2 (b), c_3(c), c_4 (d) and c_5 (e)

6.3.3. Kinetic Analysis

The overall reaction rate can be expressed in terms of Q (overall heat flow) and dQ/dt (heat flow), which are obtained from the experimentally resolved DSC curve after subtracting the baseline.

$$\frac{d\alpha}{dt} = \left(\frac{dQ}{dt}\right)\frac{1}{Q} \tag{1}$$

Where α is the progress of the overall reaction. Thermal decomposition of cerium oxalate decahydrate is assumed to occur by the dehydration and decomposition to Ce_2O_3. Hence the overall reaction rate recorded using DSC is the sum of these two kinetic processes.

$$\frac{d\alpha}{dt} = \sum_{i=1}^{n} c_i A_i \exp\left(\frac{-E_{a,i}}{RT}\right) f_i\left(\alpha_i\right) \tag{2}$$

$$\text{With} \sum_{i=1}^{n} c_i = 1 \quad \text{and} \sum_{i=1}^{n} c_i \alpha_i = \alpha$$

where n and c are the number of component step and contribution ratio of each reaction step to the overall process, A, Ea and f (α) are Arrhenius parameter, activation energy and kinetic model functions of physic-geometrical reaction mechanism.

The contribution c_{endo} and c_{exo} can be defined as

$$c_{endo} = \frac{Q_{endo}}{Q} < 0 \quad \text{and} \quad c_{exo} = \frac{Q_{exo}}{Q} > 0$$

There are five component processes which are provided by the DTG curves. The initial values of the kinetic parameters are obtained through a formal kinetic analysis of kinetic data, first subjected to mathematical deconvolution using statistical function (Weibull). Appropriate $f_i(\alpha_i)$ is obtained by merely adjusting the parameters *c, m* and *n* in Eq. 3 and such an equation fits every kinetic model proposed for solid state reactions.

$$\ln\left[d\alpha/dt \Big/ (1-\alpha)^n (\alpha)^m \right] = cA - Ea/RT \tag{3}$$

Pearson linear correlation coefficient between left hand sides of the equation with inverse of temperature is set as an objective of optimization.

$$\ln\left(\frac{d\alpha}{dt}\right) = \ln\left[\frac{A}{f(\alpha)}\right] - \frac{Ea}{RT} \tag{4}$$

The determination of Ea values for each stage is carried out based on *Eq.* 4. Plots of ln(*dα/dt*) vs T^{-1} known as *Friedman plots*[34-36], for the series of kinetic data at different α recorded under linear non-isothermal condition were examined for determining the values of *Ea*.

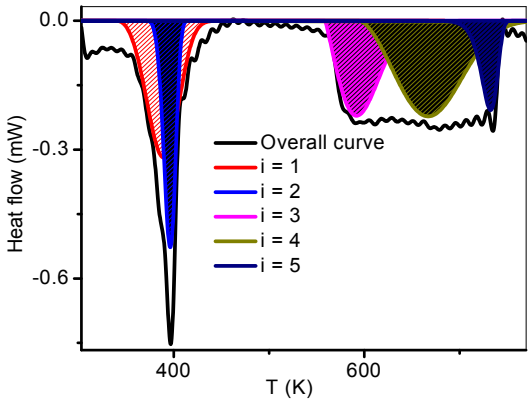

Fig. 7 Deconvoluted DSC curve of cerium oxalate decahydrate at 2Kmin^{-1}

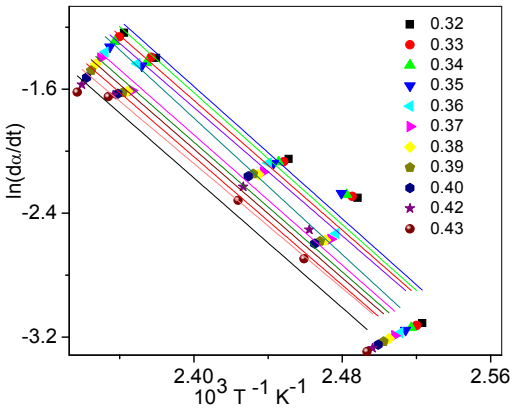

Fig. 8 Friedman plots at different α value of first stage of decomposition of cerium oxalate

After setting all of the initial values of kinetic parameters, a parameter optimization was executed using Eq. 5.

$$F = \sum_{j=1}^{n} \left[\left(\frac{d\alpha}{dt} \right)_{\exp,j} - \left(\frac{d\alpha}{dt} \right)_{cal,j} \right]^2 \qquad (5)$$

where *n* is the number of data points.

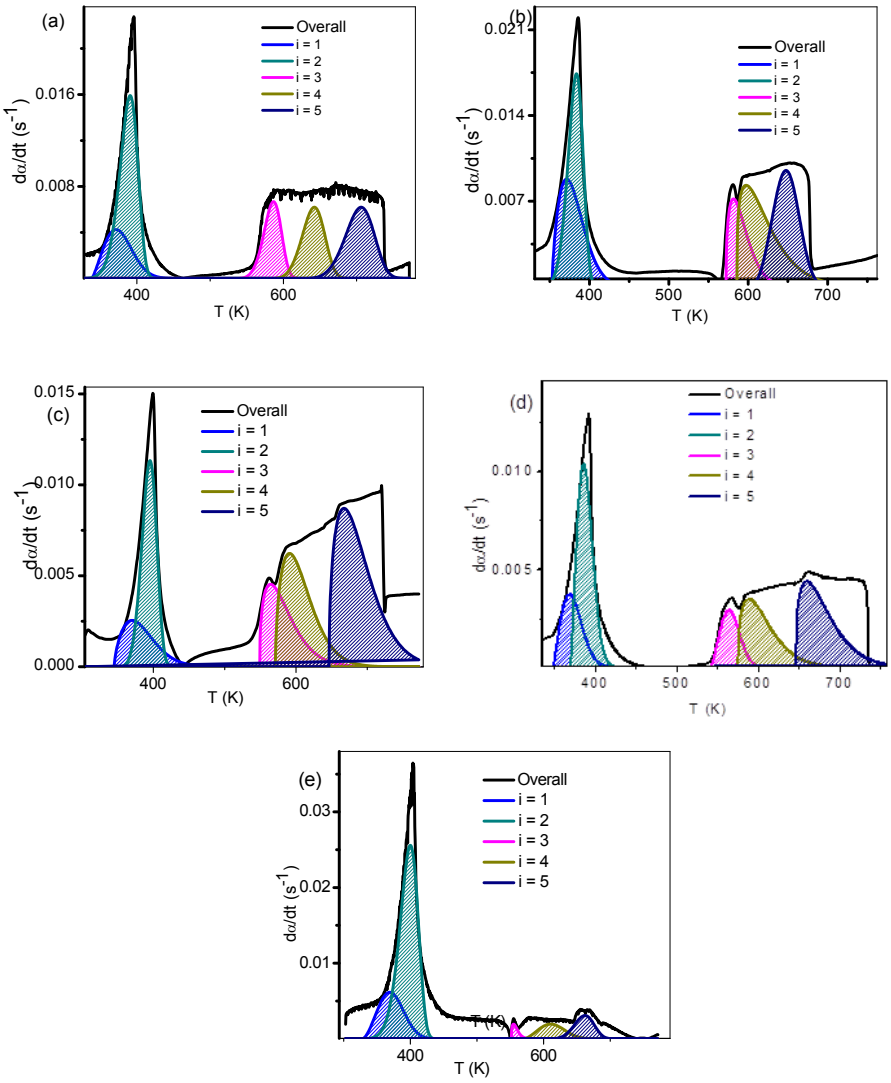

Fig. 9 The results of kinetic deconvolution of thermal decomposition of cerium oxalate and doped cerium oxalate at 2Kmin^{-1}; COX (a), 2 (b), 10 (c), 20 (d) and 30 (e) doped COX.

Fig. 7 shows the deconvoluted DSC curve of cerium oxalate. Similar deconvolution were also drawn for other samples 4, 6, 8 and 10Kmin^{-1} for establishing the initial values of kinetic parameters. Fig. 8 is the typical *Friedman plots* for the first stage of decomposition of

cerium oxalate, which was used for establishing initial values of kinetic parameter of sample c_1. Similar plots were also drawn for other samples for the same purpose. The initial values of kinetic parameters are plugged in the Eq. 2 for finding the experimental dα/dt curve. Further, the deconvolution of this curve was carried out for finding the kinetic parameters and optimizing the values. Fig. 9 shows the results of kinetic deconvolution of cerium oxalate and copper doped cerium oxalate at $2Kmin^{-1}$. The same curves were also drawn for all samples at heating rate of 4, 6, 8 and $8Kmin^{-1}$. For finding the *Ea* value of each stage of decomposition, *Friedman plot* was used. The fraction of decomposition α for each stage was distributed within α = 0 to 1. Hence Friedman plots for each stage of COX and Cu^{2+} - doped COX were used for finding the *Ea* value. Figs. 10, 11, 12, 13 &14 show the *Friedman plots* for each stage of decomposition of the samples c_1-c_5 respectively.

It was observed that pure cerium oxalate needs activation energies of 88.20, 61.66, 55.90, 164.5 and 264.63 $kJmol^{-1}$ respectively for first, second, third, fourth and fifth (Table 2). The estimated values of *Ea* for doped cerium oxalates take into our mind that the significance of the introduction of Cu^{2+} in the lattice of Ce^{3+}-oxalate. It was noted that in the thermal decomposition of 2 mole % doped cerium oxalate, substituted Cu^{2+} promote decomposition stage followed by of thermal dehydration. Whereas, increasing the concentration of dopant in the cerium oxalate, homogeneous nature of doped lattice governs the catalytic effect of Cu^{2+}. Hence, even though Cu^{2+} concentration is higher, its catalysis nature is dependent on its homogeneous covering in the oxalates[37]. Homogeneity study can be performed by calculating relative atomic concentration of each metal over the total atomic

concentration of metal ions for several points. Inhomogeneity can be determined as the ratio of standard deviation for each dopant over the average value of each dopant. Cerium oxide substituted with Cu^{2+} of molar fraction of 0.2 and 0.3 have less homogeneity in the distribution of dopants. It was almost 0.71 and 0.48 respectively for samples with 20 and 30 mol% doped cerium oxalate.

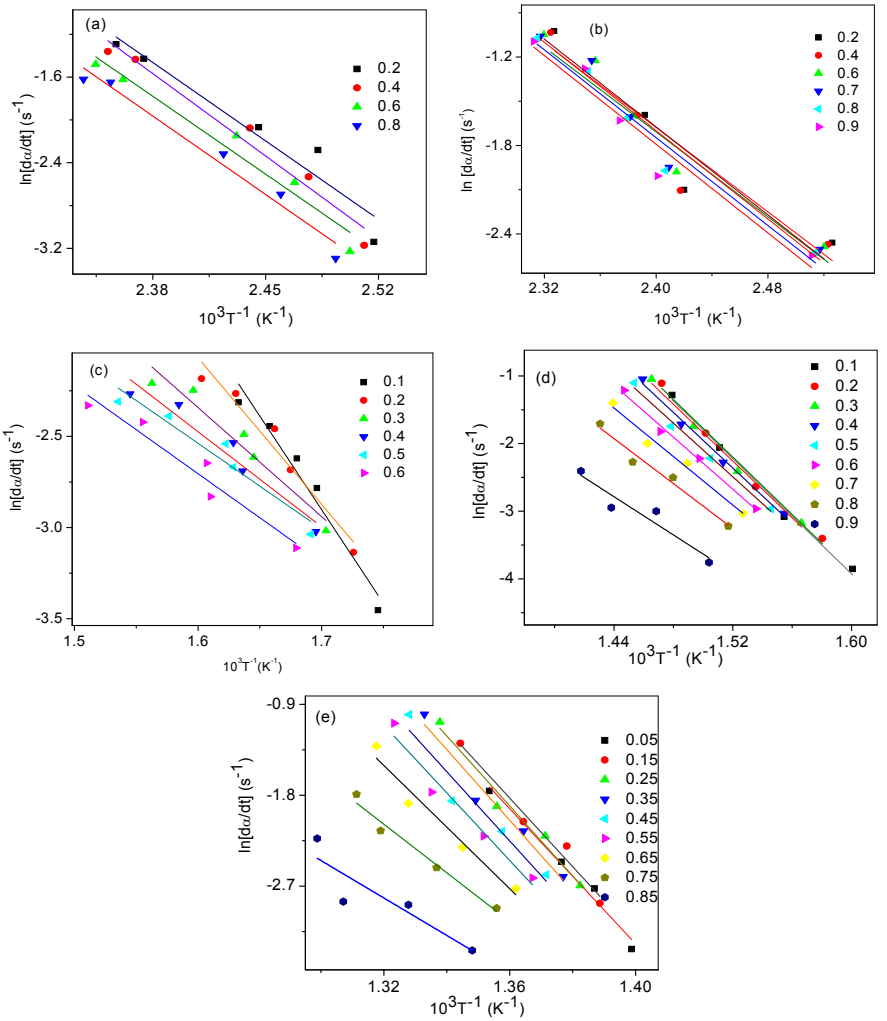

Fig. 10 The Friedman plots for the first (a), second (b), third (c), fourth (d) and fifth stages (e) of decomposition of sample c_1.

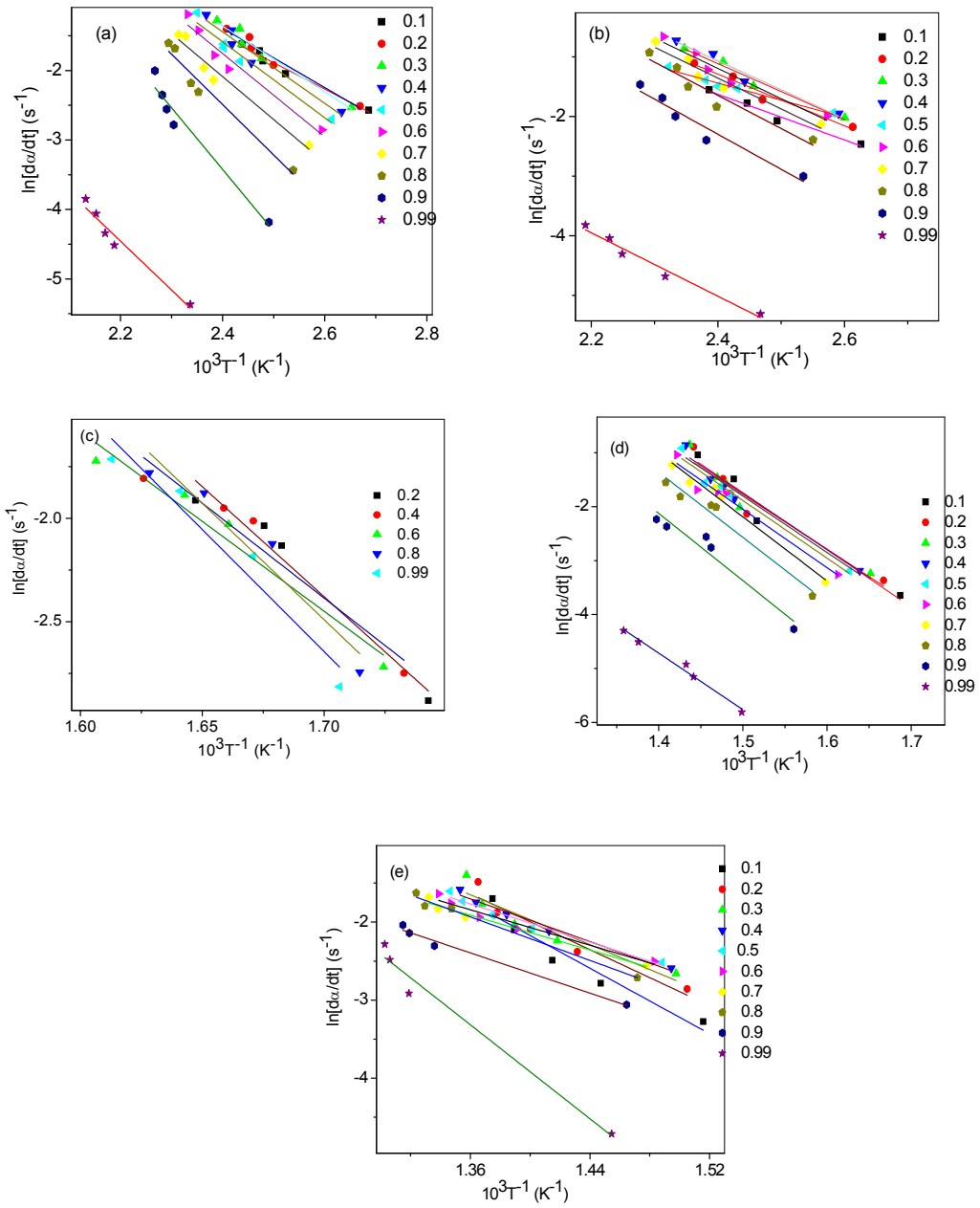

Fig. 11 The Friedman plots for the first (a), second (b), third (c), fourth (d) and fifth stages (e) of decomposition of sample c_2.

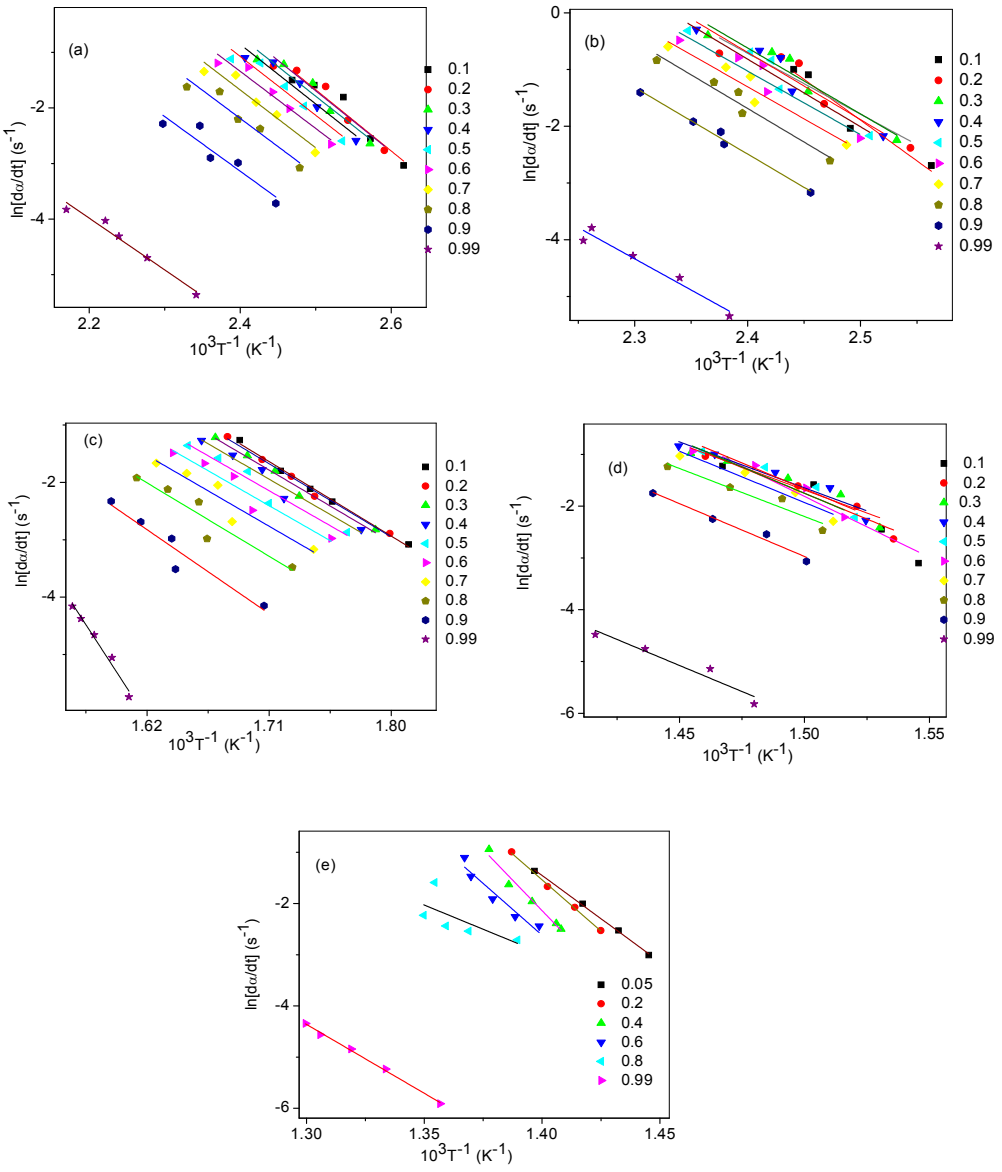

Fig. 12 The Friedman plots for the first (a), second (b), third (c), fourth (d) and fifth stages (e) of decomposition of sample c_3.

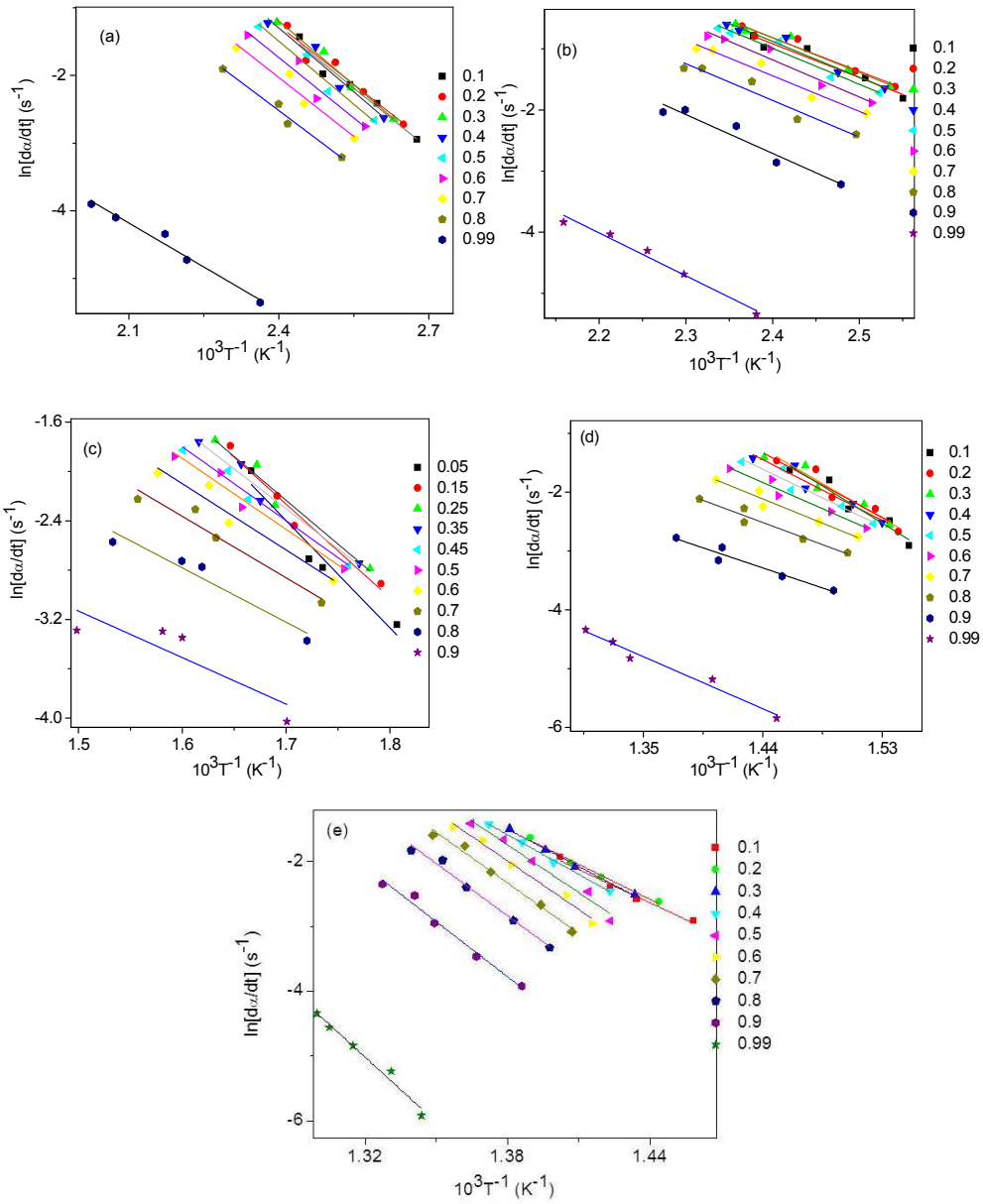

Fig. 13 The Friedman plots for the first (a), second (b), third (c), fourth (d) and fifth stages (e) of decomposition of sample c_4

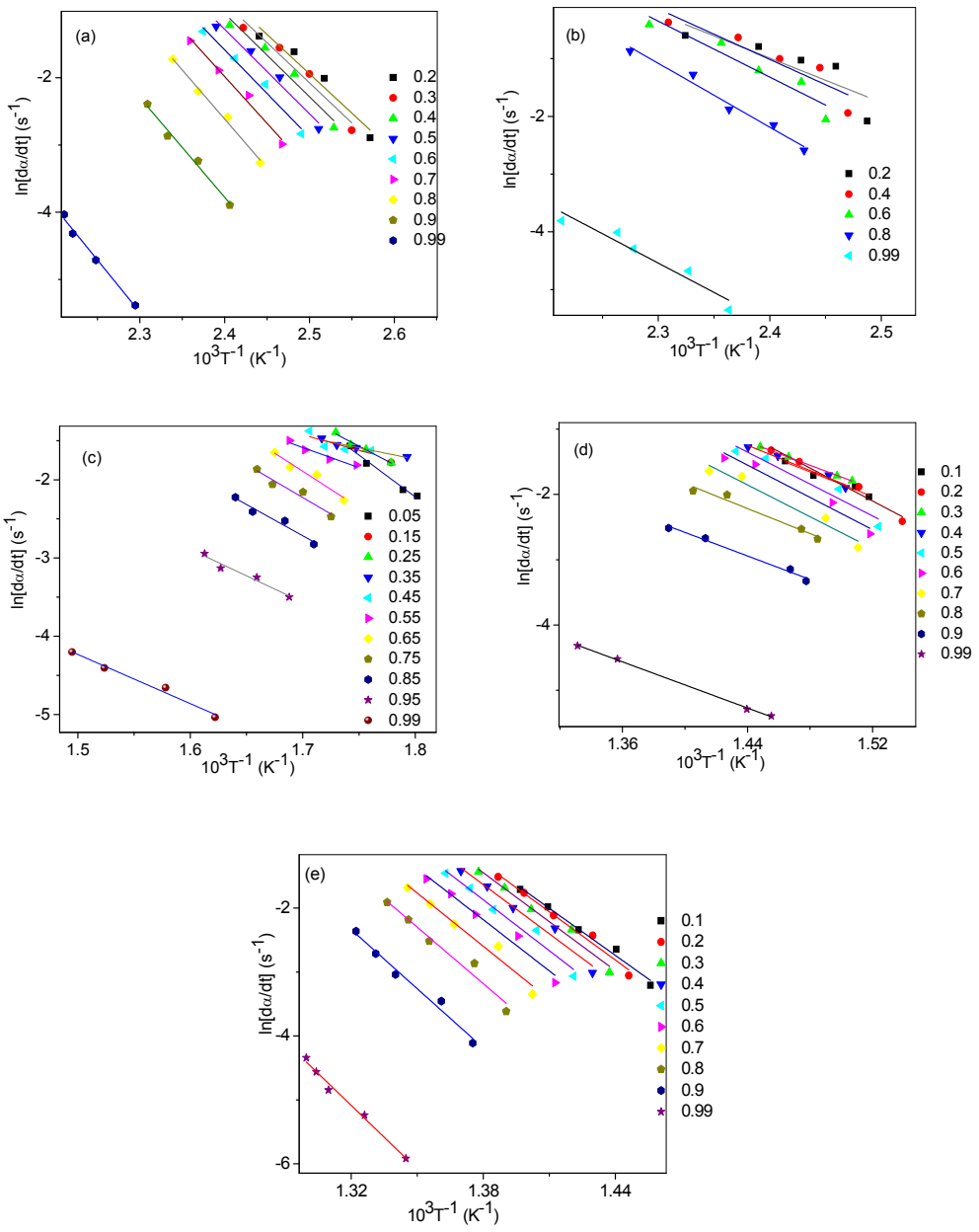

Fig. 14 The Friedman plots for the first (a), second (b), third (c), fourth (d) and fifth stages (e) of decomposition of sample c_5.

Table 2 Average values of optimized energy for each stage of decomposition of both doped and undoped cerium oxalate

Sample	Ea ($kJmol^{-1}$)				
i	1	2	3	4	5
c_1	88.20	61.66	55.90	164.50	264.63
c_2	45.50	37.88	83.44	90.06	63.33
c_3	85.67	95.90	101.86	95.20	102.72
c_4	42.88	46.90	42.56	89.28	193.89
c_5	105.01	43.98	47.98	94.97	226.78

Fig. 15 shows FE-SEM images of CeO_2 and doped cerium oxide. Fig. 15a represent s_1 (CeO_2), Fig. 15b for s_2 (2%), Fig. 15c for s_3 (10%), Fig. 15d for s_4 (20%) and Fig. 15e for s_5 (30%). Selective percentage of dopant to the ceria lattices retained disc like morphology of oxalate, which were thermally decomposed to oxide. Hence the tuning of the morphology of ceria was successively occurred by the specific reactant molar ratios (x = 0.02 and 0.1) of Ce^{3+}:Cu^{2+}. It was noted from the Table 2 that c_4 and c_5 need higher amount of activation energies for the formation of nano particle than c_2 and c_3 since they retained the morphology of bare oxalate, even at oxide formation.

Fig. 16 shows TEM, HR-TEM images and SAED pattern of ceria. TEM images show that pure ceria prepared by thermal decomposition process is mainly consists of cubic hexagonal shaped particles of size ranging between 4.6-8.8nm (Fig. 16). TEM image at a resolution of 200nm displays nano crystalline hexagon having crystallographic directions of (111), (200), (220) and (311). The inter planar distance was found to be 0.33nm as shown in Fig. 16c. This indicates the presence of branched nano hexagons with lattice fringes

similar to inter planar distance of cubic fluorite type structure of ceria. Ceria nano hexagons provided polycrystalline SAED pattern (Fig. 16d).

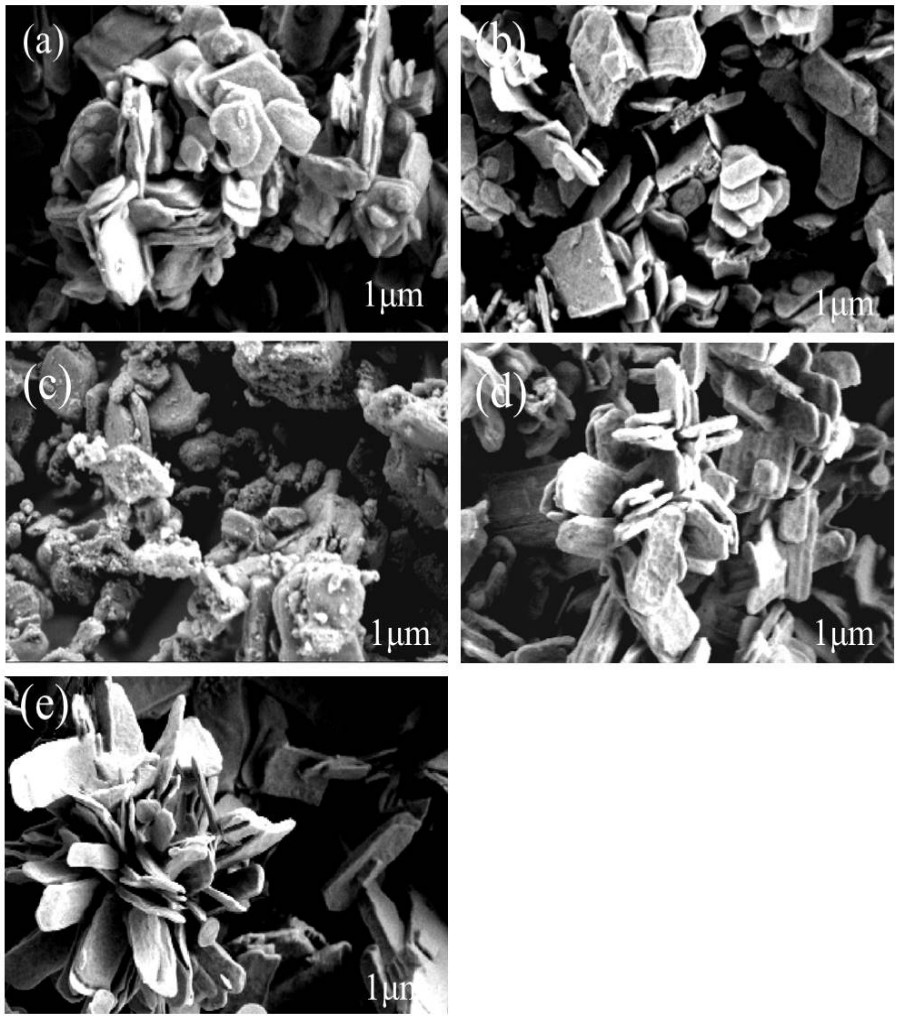

Fig. 15 FE-SEM images of s_1 (a), s_2 (b), s_3(c), s_4 (d) and s_5 (e).

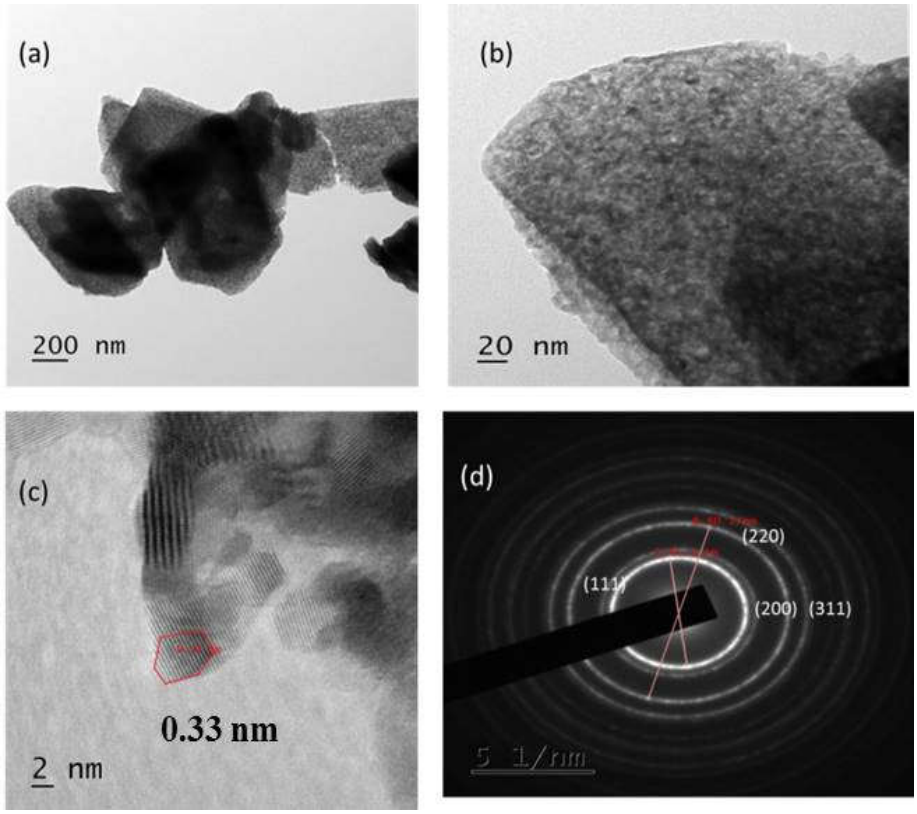

Fig. 16 TEM images of CeO_2 at 200nm (a), 20nm (b), HRTEM image (c) and SAED pattern (d) of CeO_2.

The introduction of Cu^{2+} into the CeO_2 lattice induced marked reduction of size of the particle (3.22-6.11nm) (Fig. 17). This means that Cu^{2+} dopant has predominant role in the creation of defects (oxygen vacancies) during the growth process of CeO_2. When the dopant reached into the crystal lattices, change of inters planar distance (0.28nm) was appeared (Fig. 17c). Moreover, its substitution considerably altered the morphology of hexagonal shape into truncated one. Researchers[26]investigated that both internal and external addition of Cu^{2+} caused to structural transition, along with cubic to truncated

octahedron. This indicates that lattices get relaxed with the generation of oxygen vacancies. Decrease in the size of particle and inter planar distance for the doped samples caused the lattices to get relaxed by creating new oxygen ion vacancies.

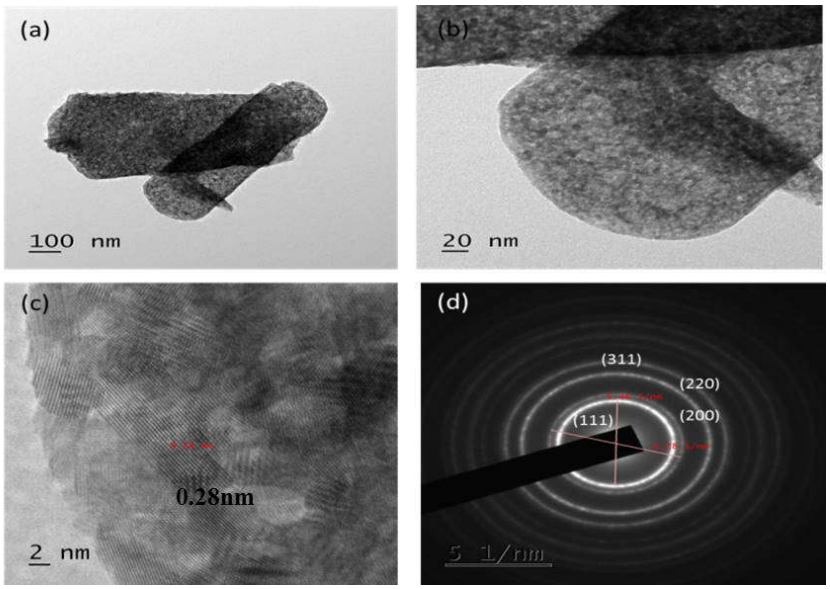

Fig. 17 TEM images at 100nm (a) & 20nm (b), HRTEM image (c) and SAED pattern (d) of s_2 (2%).

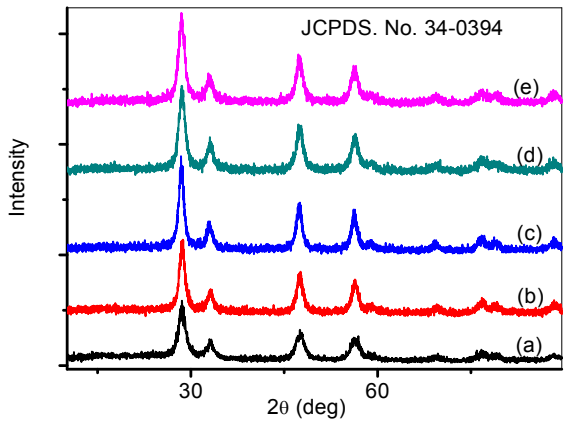

Fig. 18 The XRD patterns of s_1 (a), s_2 (b), s_3(c), s_4 (d) and s_5 (e).

Figs. 18a-e show the XRD patterns of s_1, s_2, s_3, s_4 and s_5 respectively. It was shown that Cu^{2+} is highly dispersed in the lattice of ceria because it shows no peak corresponding to CuO in the XRD pattern. But the occurrence of higher intensity and small shift in the peak of doped samples were observed. Cubic fluorite type structure of ceria (JCPDS Card No. 34-0394) was not altered with doping. It was exhibited in the XRD patterns that crystallanity was increased with increasing the dopant concentration.

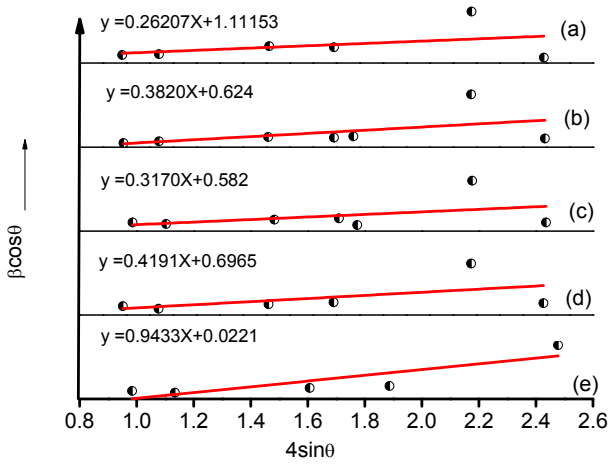

Fig. 19 Williamson-Hall plots for s_1 (a), s_2 (b), s_3(c), s_4 (d) and s_5 (e).

Figs. 19 (a-e) show the Williamsons- Hall plots, which indicate the experienced lattice strain of pure and doped ceria. Increasing the Cu^{2+}- content goes to increase the lattice strain, which may or may not depends upon particle size. The estimated lattice constant of ceria is 0.542, which was not modified with doping. This explored that strain was not happened due to particle size but occurs through the creation of oxygen vacancies. The existence of slighter peak shift towards

lower angles indicates the lattice expansion in the ceria lattices with Cu^{2+} doping (Fig. 18). Fig. 20 represents the schematic diagram for the synthetic route of nano disc (flower) like Ce-Ox and the preparation of nano discs (flower) of ceria by thermal decomposition strategy.

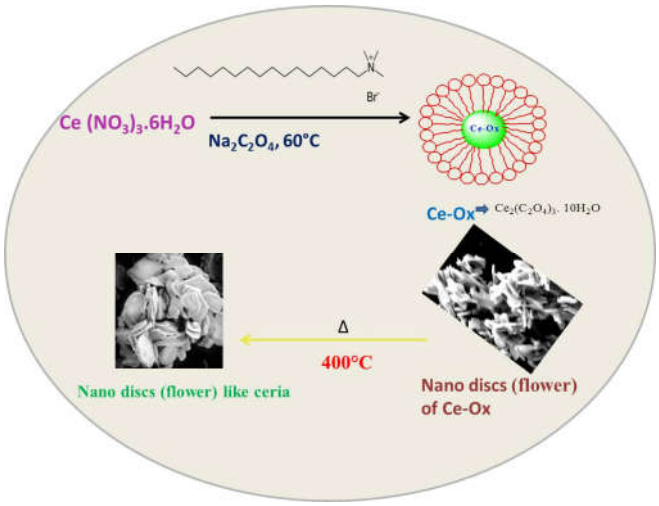

Fig. 20 Schematic illustration of the preparation of nano discs (flower) of COX and ceria.

6.3.4. Optical and luminescent properties

It is more important to study the modification of optical and luminescent properties of ceria matrix with doping of transition metals. Absorption of UV-Visible light led to excite electron in both atoms and molecules to higher energy level. The entire samples show broad strong absorption below 400nm (Fig. 21a). The broad band of absorption at 260 and 266 nm are responsible for UV C absorption which are characteristic for CT from O^{2-}(2p) to Ce^{3+} (4f) orbitals in CeO_2, while UV A absorption at 340nm are responsible for CT from

O^{2-}(2p) to Ce^{4+} (4f) orbitals[38]. In the defect lattices, CT between O^{2-} (2p) to Cu^{2+} (3d) is absent because absorption band between 220-240nm is not observed in the spectrum. It was observed that 2mol% doped ceria (Fig. $21as_2$) acquired enhanced UV absorbance compared to other doped samples (10, 20 & 30mol%, Figs. $21as_3$, s_4 & s_5 respectively) and ceria (Fig. $21as_1$). It was found that absorbance of ceria doped with 10mol% Cu^{2+} caused to lower the absorbance (Fig. $21as_3$), but redshift and broadening of the peak was observed. Further, the peak above 450nm is responsible for the d-d transition of Cu^{2+} with an octahedral environment of CuO. Since ceria perform as UV-filters, it can absorb more UV radiation from the spectrum and the intensity of the absorbance peak is related with the concentration of Ce^{3+}. Moreover, the redshift and broadening of band with the increment of dopant concentration in the UV-Visible spectra are related with surface defects of CeO_2[39]. The presence of Cu^{2+} content enhances optical absorption[40] . Fig. 21b represents the *Tauc plots* of doped and un doped ceria. It was observed that the band gap energy (*Eg*) decreases with increasing the load of copper in the ceria lattice. The band gap energy is depicted in the Table 3. It was noted that *Eg* decreases with decreasing the particle size. This indicates the significance of surface defects on the redshift of band gap energy.

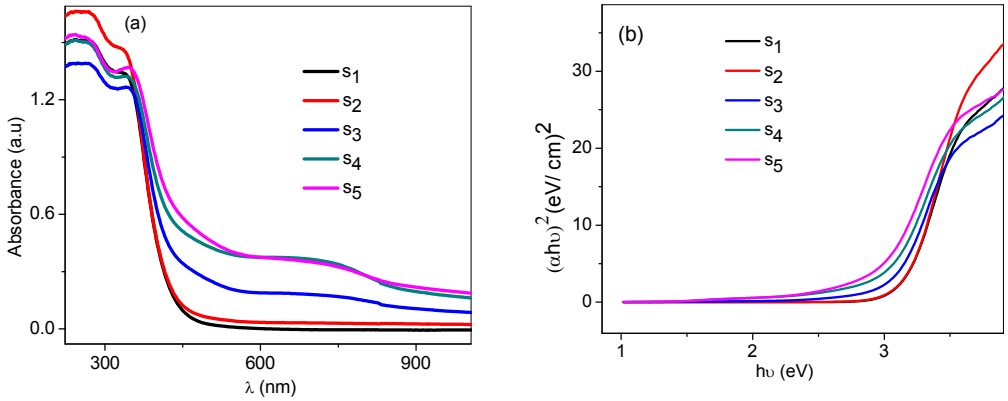

Fig. 21 UV-Visible absorbance spectra (a) and *Tauc plots* (b) of CeO_2 and Cu^{2+} doped CeO_2; Undoped CeO_2 (s_1), 2(s_2), 10 (s_3), 20 (s_4) and 30% (s_5).

Fig. 22 shows the PL spectra of CeO_2 and Cu-doped CeO_2 nanoparticles with an excited wavelength of 340nm. It was displayed that emission band intensity was reduced whereas band width was increased with increase in dopant concentration. Emission band consists of good violet bands at 419nm (2.96eV), blue emission band at 483nm (2.57eV) and green emission band at 529nm (2.35eV).

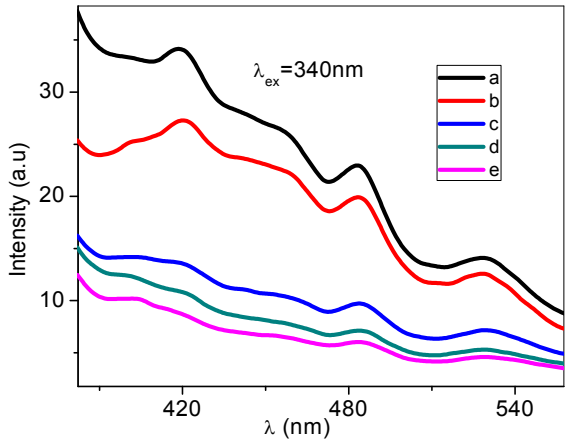

Fig. 22 Photo luminescent spectra of doped and undoped CeO_2; Undoped CeO_2 (a), 2 (b), 10 (c), 20 (d) and 30% (e).

Table 3 *Eg* value (Tauc plots) and average crystallite size (using *Scherrer* Equation)

Sample	*Eg* (eV)	Crystallite size (nm)
s_1	2.93	8.80
s_2	2.90	8.20
s_3	2.77	8.50
s_4	2.70	6.96
s_5	2.52	7.15

It was reported that PL emission in the range of 400-550nm (< 3eV) are highly associated with oxygen vacancies with trapped electrons which localized between Ce (4f) and O (2p) band in CeO_2. Increase in the molar ratio of Cu:Ce in the lattice, experiences a polaron effect which arises from strong electron-phonon interaction[41]. Broadening of the peaks with the dopant levels are associated with the enhancement in oxygen ion vacancies. These extra oxygen ion vacancies compensate the valence mismatch between the Cu^{2+} and Ce^{4+} ions[42]. Emission band intensity was decreased due to the concentration quenching phenomenon. Besides, the dissipation of energy through non-radiative transition also occurs along with the emission from 4f to 2p. Both doped and undoped ceria show stock shift characterized from the absorption and emission spectrum. Copper doping in the ceria lattice increased the stock shift. Due to higher value of stock shift 149.15nm (8.4eV), biomedical applications of doped ceria are promoted.

6.3.5. Micro Raman spectra

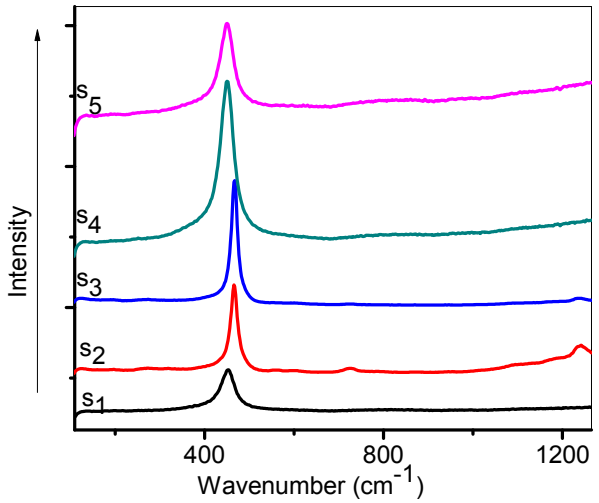

Fig. 23 Raman spectra of CeO_2 (s_1) and ceria doped with Cu^{2+} 2 (s_2), 10 (s_3), 20 (s_4) and 30% (s_5).

The incorporation of copper in the fluorite lattice of $Ce_{(1-x)}Cu_xO_2$ series are further confirmed by Raman scattering, displayed in Fig. 23. The spectrum shows the main band at 461.34cm^{-1}, which is responsible for the first order triply degenerated F_{2g} mode of vibration characteristic to the cubic structure of CeO_2[43,44] and weak bands at ca. 547.13 and near to 600 cm^{-1}. The band at ca. 547.13 cm^{-1} can assigned to oxygen vacancies introduced in to ceria in order to maintain the charge neutrality when Ce^{4+} ions are replaced by the divalent copper ions. Besides, the weak band centered approximately at 600cm^{-1} is associated with the intrinsic oxygen ion vacancies due to the presence of Ce^{3+} ions. Several factors caused for the change in Raman peak position and line width of main band. These include phonon confinement, strain, broadening associated with size distribution, defects, and variations in phonon relaxation with particle size[44]. Substitution of copper in the ceria lattice made some shift to the band.

It was noticed from Fig. 23 that substitution of copper increased the intensity of the band mentioning better crystallization of nano crystals. It was observable from the spectrum that relative intensity was increased with increasing the concentration of the dopant up to 20 mol%, while 30 mol % doped ceria shows decreased relative intensity. This pointed out that surface of doped ceria has possessed higher amount of oxygen vacancies than undoped disc (flower) like ceria. It was noticed that the peak position of main band at 461. 34cm^{-1} is shifted with lower energy shoulder and broadens asymmetrically. This can be ascribed due to the decrease of particle size with the increase of copper content in the lattice. Both shift and width of Raman line were presented due to the existence of phonon confinement and oxygen vacancies($Ce^{4+} + O^{2-} \rightarrow Cu^{2+} + VO$; VO being a doubly ionized oxygen vacancy), but the inhomogeneous strain is related with the reduced state of cerium[44-46]. Raman intensity ratio for each sample (Table 4) was calculated from the relative intensity of the peak corresponding to the peak centered near to 600 cm^{-1} and peak at 465 cm^{-1}. From the earlier reports[47], number of oxygen ion vacancies is best described with Raman intensity ratio.

Table 4 Raman intensity ratio for each sample

Sample	Raman intensity ratio (I_{600}/I_{465})
S_1	0.33
S_2	0.26
S_3	0.25
S_4	0.27
S_5	0.47

Figs. 24a-e displays the micro Raman spectra corresponding to the weak band near to 600 cm^{-1} for the samples s_1, s_2, s_3, s_4 and s_5 respectively. It was found that highest Raman intensity ratio for the sample s_5 (0.47) than others, indicating highest concentration of oxygen ion vacancies.

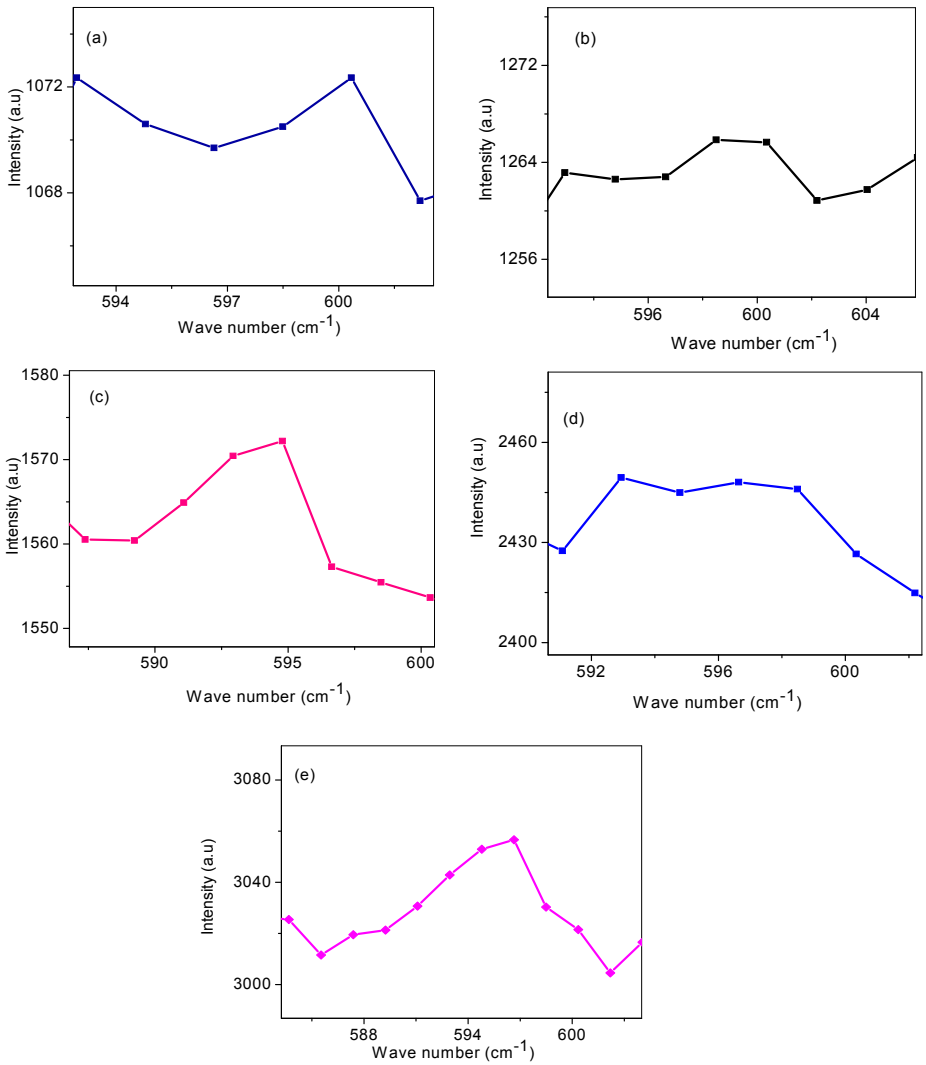

Fig. 24 Micro Raman spectra of s_1(a), s_2(b), s_3(c), s_4(d) and s_5(e) corresponding to the weak band near to 600 cm^{-1}.

6.3.6. Cytotoxic studies

The use of ceria and lattices modified ceria as anticancer drugs has much relation with its radical scavenging antioxidant capabilities, which in turn related with optical emission properties. Structural and optical properties of ceria have strong dependence with concentration of oxygen ion vacancies and Ce^{3+}. Cubic fluorite type structure of ceria permits to scavenge radicals. Further this nanoparticle is non-stoichiometric compound in which cerium atom present as Ce^{3+}/Ce^{4+}. Intrinsic oxidase behavior of ceria nanoparticle accesses them for cytotoxicity, especially when they localized into acidic cell compartment such as lysosomes. Cytotoxic behavior of nanoparticle depends on various factors such as nature, chemical composition of the nanoparticle's core, mode of preparation, size, shape, crystallanity, surface reactivity, solubility in aqueous media and degree of aggregation.

In vitro cytotoxicity for short term was studied for first time for ceria nano disc and copper modified ceria with using Dalton's Lymphoma ascite cells. Procedure of cytotoxicity assay is prescribed in *chapter 2*. It was found that percentage of cytotoxicity was increased for copper modified ceria nanoparticle and was observed enhanced for 10 mol% Cu^{2+} modified ceria. Introduction of Cu^{2+} to the ceria lattice led to enhance the intrinsic oxidase activity of ceria. Besides, creates extra oxygen ion vacancies with doping. Presence of more oxygen vacancies in the lattices make it as better radical scavengers. This results in better performance of ceria as anticancer drug. Fig. 25a represent the image of live cell (100%) and Fig. 25b shows the image of dead cell (100%).

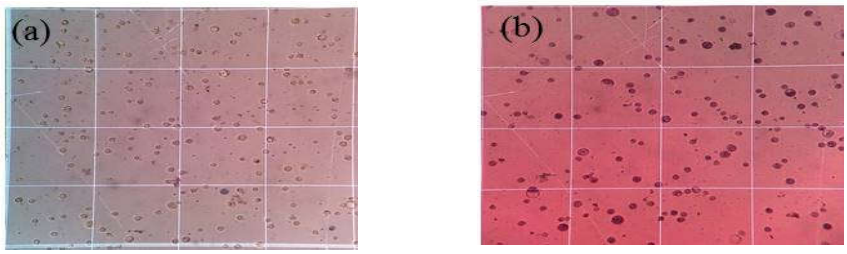

Fig. 25 The images of 100% live cell (a) and 100% dead cell (b)

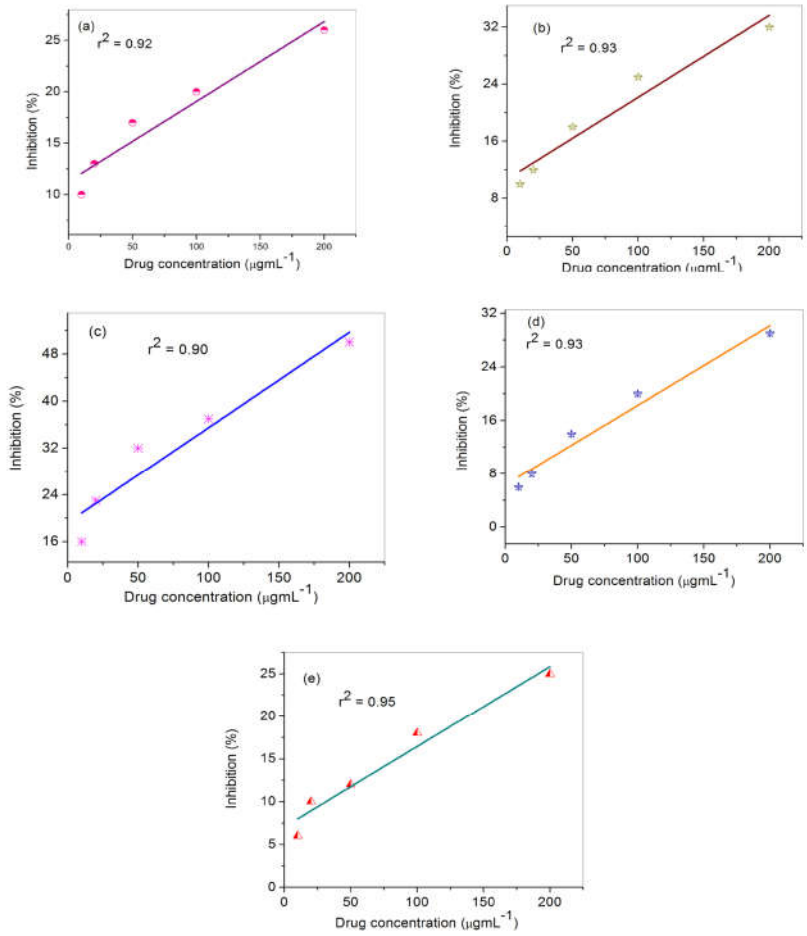

Fig. 26 Cytotoxicity of cerium oxide nanoparticle and Cu^{2+}-modified cerium oxide at different concentrations (200(a), 100 (b), 50(c), 20µ and 10µgmL^{-1} (d)); s_1(a), s_2(b), s_3(c), s_4(d) and s_5(e).

Cytotoxic assay exposed that higher toxicity was exhibited at 200μgmL^{-1} (Fig. 26) and it was lowered with decreasing the concentration of nanoparticle. Figs. 26 a-e represents respectively the percentage of inhibition of the samples s_1, s_2, s_3, s_4 and s_5. It was shown that higher toxicity by the sample s_3 (10 mol% Cu^{2+} doped). Fig. 27 represents the schematic illustration of determination of cytotoxicity of Cu^{2+} doped ceria. The value of IC_{50} was found to be 200μgmL^{-1} for the sample s_3.

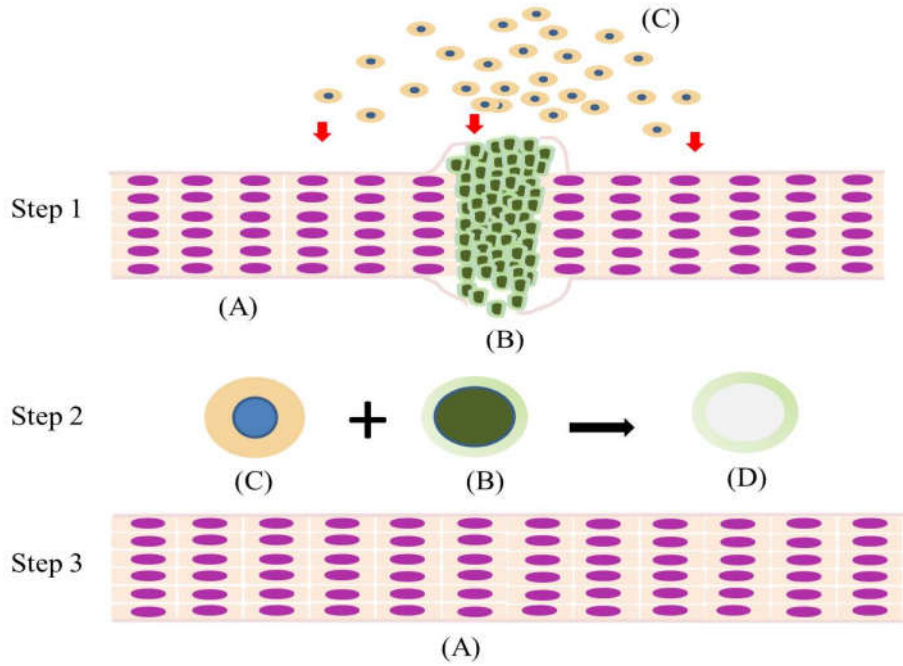

Fig. 27 Step 1 nano particles of solid solution Cu-Ce-O are given to both normal cell as well as cancer cells. Step 2: the work of Cu-Ce-O on cancer cels selectively. Step 3: normal cells remain un damaged. (A) = normal cell, (B) = cancer cell, (c) = Cu^{2+} - doped nano ceria and (D) = apoptosis of cancer cells.

6.4. Conclusion

Cerium oxalate discs (flower) were prepared through the surfactant assisted precipitation method. Nano discs (flower) of CeO_2 were formed *via* the thermal decomposition strategy of the oxalate precursors. Cu^{2+} substituted ceria (2, 10, 20 and 30 mol %) were prepared through the similar method. Kinetic analysis for the formation of corresponding oxide in N_2 atmosphere were performed and estimated the values of *Ea* taken for each step of thermal decomposition. It was displayed that energy for the entire stage was lowered with Cu^{2+} doping (2 mol %). Particle size and morphology of doped samples were altered with the addition of Cu^{2+} to the lattice of ceria. Even though band gap energy and crystallite size decreases with increasing the copper loading, dispersion of Cu^{2+} has major role on reducing the peak temperature of decomposition. Doped ceria has got flower like textures with increasing the level of copper percentage. Copper modified ceria shows enhanced photo physical properties, because of the higher optical absorption. Luminescent properties of doped ceria were enhanced by redshift and broadening of the peak, which is attributed to the creation of new extra oxygen ion vacancies. *In vitro* cytotoxicity assay with Dalton's Lymphoma ascites cancer cells revealed improved cytotoxicity for 10 mol% copper doped ceria.

6.5. References

1. Fei Y, Jingjing W, Wei L, Jinxin G, Yanzhao Y. Copper doped ceria nanospheres: surface defects promoted catalytic activity and a versatile approach. *J Mater Chem A*. 2014;2:5662-5667.

2. Carrettin S, Concepcion P, Corma A, Nieto JM, Puntes VF. Nano crystalline CeO_2 increases the activity of Au for CO oxidation by two orders of magnitude. *Angew Chem Int Ed*. 2004;43:2538-2540.

3. Mai HX, Sun LD, Zhang YW, et al. Shape-selective synthesis and oxygen storage behavior of ceria nano polyhedra, nanorods, and nanocubes. *J Phys Chem B*. 2005;109:24380-24385.

4. Nolan M, Parker SC, Watson GW. The electronic structure of oxygen vacancy defects at the low index surfaces of ceria. *Surf Sci*. 2005;595:223-232.

5. Evgeny AA, Aleksey AV. High temperature interaction of rhodium with oxygen storage component in three-way catalysts. *Top Catal*. 2016;59:1033-1038.

6. Li C, Gu X, Wang Y, et al. Synthesis and characterization of mesostructured ceria-zirconia solid solution. *J Rare Earth*. 2009;27:211-215.

7. Jun F, Xiaodong W, Lei Y, Duan W. The SMSI between supported platinum and CeO_2-ZrO_2-La_2O_3mixed oxides in oxidative atmosphere. *Catal Today*. 2007;126:303-312.

8. Dong F, Tanabe T, Suda A, Takahashi N, Sobukawa H, Shinjoh H. Investigation of the OSC performance of Pt / CeO_2. ZrO_2 . Y_2 O_3 catalysts by CO oxidation and ^{18}O / ^{16}O isotopic exchange reaction. *Chem Eng Sci*. 2008;63:5020-5027.

9. He X, Sun J, Huan Y, Hu J YD. Influence of Al_2O_3/CeZrAl composition on the catalytic behavior of Pd/Rh catalyst. *J Rare Earth*. 2010;28:59-63.

10. Ferna´ndez-Garcı´ M, Martı´nex-Arias A, Iglesias-Juez A, Belver C, Hungrı´ AB, Conesa JC SJ. Contributions of surface and bulk heterogeneities to the NO oxidation activities of ceria-zirconia catalysts with composition $Ce_{0.76}Zr_{0.24}O_2$ prepared by different methods. *Phys Chem Chem Phys*. 2010;12:13770-13779.

11. Moreno M, Bergamini L, Baronetti GT, Laborde MA, Marino FJ. Mechanism of CO oxidation over CuO / CeO_2 catalysts. *Int J Hydrog Energ*. 2010;35:5918-5924.

12. Desyatykh IV, Vedyagin AA, Kotolevich YS, Tsyrul'nikov PG. Preparation of CuO-CeO_2 catalysts deposited on glass cloth by surface self- propagating thermal synthesis. *Combust Explos Shock Waves*. 2011;47:677-682.

13. Park PW, Ledford JS. The influence of surface structure on the catalytic activity of cerium promoted copper oxide catalysts on alumina : oxidation of carbon monoxide and methane. *Catal Letters*. 1998;50:41-48.

14. Hochella MF Jr, Lower SK, Maurice PA, et al. Nano minerals, mineral nanoparticles, and earth systems. *Science*. 2008;319:1631-1635.

15. Jimmy CY, Lizhi Z, Jun L. Direct sonochemical preparation of high-surface-area nanoporous ceria and ceria-zirconia solid solutions. *J Colloid Interface Sci*. 2003;260:240-243.

16. Carl W, Soumen D, Sudipta S, et al. Catalytic properties and biomedical applications of cerium oxide nanoparticles. *Environ Sci Nano*. 2015;2:33-53.

17. Gao Y, Chen K, Ma J, Gao F. Cerium oxide nanoparticles in cancer. *Onco Targets Ther*. 2014;7:835-840.

18. Wason MS, Colon J, Das S, Seal S, Turkson J, Zhao J BC. Sensitization of pancreatic cancer cells to radiation by cerium oxide nanoparticle-induced ROS production. *Nanomedicine*. 2013;9:558-569.

19. Grulke E, Kenneth R, Matthew B, Xing H, Alastair C, Sudipta S. Nanoceria: factors affecting its pro- and anti-oxidant properties. *Environ Sci Nano*. 2014;1:429-444.

20. Kumar A, Das S, Munusamy P, et al. Behavior of nanoceria in biologically-relevant environments. *Env Sci Nano*. 2014;1:516-532.

21. Asati A, Santra S, Kaittanis C, Perez JM. Surface-charge-dependent cell localization and cytotoxicity of cerium oxide nanoparticles. *ACS Nano*. 2010;4:5321-5331.

22. Alili L, Sack M, von Montfort C, et al. Downregulation of tumor

growth and invasion by redox-active nanoparticles. *Antioxid Redox Signal*. 2013;19:765-778.

23. Wang Y, Yang F, Zhang H-X, et al. Cuprous oxide nanoparticles inhibit the growth and metastasis of melanoma by targeting mitochondria. *Cell Death Dis*. 2013;4:e783.

24. Clark A, Zhu A, Petty HR. Titanium-doped cerium oxide nanoparticles protect cells from hydrogen peroxide-induced apoptosis. *J Nanopart Res*. 2013;15:2126.

25. Wongrakpanich A Mudunkotuwa IA, Geary SM, Morris AS, et al. Size-dependent cytotoxicity of copper oxide nanoparticles in lung epithelial cells. *Environ Sci Nano*. 2016;3:365-374.

26. Nan Q, Jing Z, Ziyu W, Tiandou H, Peng L. Tuning ceria nanocrystals morphology and structure by copper doping. *Cryst Growth Des*. 2012;12:629-634.

27. Dziembaj R, Molenda M, Chmielarz L, et al. Nanostructured Cu-doped ceria obtained by reverse microemulsion method as catalysts for incineration of selected VOCs. *Catal Letters*. 2010;135:68-75.

28. Wang CH, Lin SS, Liou SB, Weng HS. The promoter effect and a rate expression of the catalytic incineration of $(CH_3)_2S_2$ over an improved CuO-MoO_3/gamma-Al_2O_3 catalyst. *Chemosphere*. 2002;49:389-394.

29. Wada T, Nakano M, Koga N. Multistep kinetic behavior of the thermal decomposition of granular sodium percarbonate : hindrance effect of the outer surface layer. *J Phys Chem A*. 2015;2:9749-9760.

30. Kitabayashi S, Koga N. Physico-geometrical mechanism and overall kinetics othermally induced oxidative decomposition of tin(II) oxalate in air : formation process of microstructural tin(IV) oxide. *J Phys Chem C*. 2014;118:17847-17861.

31. Yoshikawa M, Yamada S, Koga N. Phenomenological interpretation of the multistep thermal decomposition of silver carbonate to form silver metal. *J Phys Chem C*. 2014;118:8059-8070.

32. Koga N, Goshi Y, Yamada S, Pe´rez-Maqueda LA. Kinetic approach to partially overlapped thermal decomposition processes; co-precipitated zinc carbonates. *J Therm AnalCalorim*. 2013;111:1463-1474.

33. Nusrath K, Muraleedharan K. Effect of Ca(II) on the multistep kinetic

behavior of thermally induced oxidative decomposition of cerium(III) oxalate to CeO_2(IV). *J Anal Appl Pyrol*. 2016;120:379-388.

34. Ozawa T. Applicability of Friedman plot. *J Therm Anal*. 1986;31:547–551.

35. Koga N. Kinetic analysis of thermoanalytical data by extrapolating to infinite temperature. *Thermochim Acta*. 1995;258:145–159.

36. Gotor FJ, Criado JM, Malek J, Koga N. Kinetic analysis of solid-state reactions: the universality of master plots for analyzing isothermal and non-isothermal experiments. *J Phys Chem A*. 2000;104:10777–10782.

37. Adamopoulos O. *Ph.D Thesis*. Royal Institute of Technology, Stockholm; 2003.

38. Aškrabić S, Dohčević-Mitrović ZD, Araújo VD, Ionita G, De Lima MM, Cantarero A. F-centre luminescence in nanocrystalline CeO_2. *J Phys D Appl Phys*. 2013;46.

39. Sudarshan K, Sharma SK, Gupta R, Gupta SK, Sayed FN, Pujari PK. Role of surface defects in catalytic properties of CeO_2 nanoparticles towards oxygen reduction reaction. *Mater Chem Phys*. 2017;200:99-106.

40. Gamarra D, Munuera G, Hungria AB, et al. Structure - activity relationship in nanostructured copper-ceria-based preferential CO oxidation catalysts. *J Phys Chem C*. 2007;111:11026-11038.

41. Sun C, Li H, Zhang H, Wang Z, Chen L. Controlled synthesis of CeO_2 nanorods by a solvothermal method. *Nanotechnology*. 2005;16:1454-1463.

42. Martinez-Arias A, Sofia J, Catalu R, Conesa JC, Corberan VC. Influence of ceria dispersion on the catalytic performance of $Cu/CeO_2/Al_2O_3$ catalysts for the CO oxidation reaction. *Stud Surf Sci Catal*. 1998;116:591-600.

43. Weber WH, Hass V, McBride JR. Raman study of CeO_2: second-order scattering, lattice dynamics, and particle-size effects. *Phys ReV B Condens Matter*. 1993;48:178-185.

44. Spanier JE, Robinson RD, Zhang F, Chan S-W, Herman IP. Size-dependent properties of CeO_2 nanoparticles as studied by Raman scattering. *Phys Rev B*. 2001;64:245407-1-245407-245408.

45. Garcia MF, Arias AM, Hanson JC, Rodriguez JA. Nanostructured oxides in chemistry: characterization and properties. *Chem ReV*. 2004;104:4063-4104.

46. McBride JR, Hass KC, Poindexter BD, Weber WH. Raman and x-ray studies of $Ce_{1-x}RE_xO_{2-y}$, where RE=La, Pr, Nd, Eu, Gd, and Tb. *J Appl Phys*. 1994;76:2435-2441.

47. Carla AO, José JMÓ, Manuel FRP, Andréa MDF, Raimundo CRN, Marco AF. Ozonation of model organic compounds catalysed by nanostructured cerium oxides. *Appl Catal B Environ.* 2011;103:190-199.

NUSRATH. K “SYNTHESIS AND KINETICS OF FORMATION OF CERIA AND CERIA BASED MATERIALS via THERMAL DECOMPOSITION OF OXALATES”. THESIS. DEPARTMENT OF CHEMISTRY, UNIVERSITY OF CALICUT, 2018.

7.1. Introduction

Different morphology and dimensionality of ceria nano particle has succeeding role on creating ceria with higher performance. CeO_2 with controlled morphology exposes different crystal planes on the solid crystallites which exhibits interesting chemical and physical properties. Different morphologies of ceria are synthesized and studied, which involves nano rods, nano cube, octahedron or polyhedron, etc.[1] Morphology effect of CeO_2 depends on the executed synthetic methods. Surfaces of ceria can be activated by different factors such as surface area, elemental composition, defects and reactive facets[2–5]. Depending upon the morphology of ceria nanostructures, its catalyzing effect also varied. For example, ceria nano system such as nanowire, nano rod and nanoparticle has different redox behavior towards CO oxidation. One of the major reasons for this was due to the exposed crystal plane on the surface of ceria nanostructures[6] . Exposed crystal planes of some ceria nano structures: like nano rod and nanowire {(100) and (110)}, nano cube {(100)}, ceria nano particle and polyhedron {(111)}[1]. Nano rod like CeO_2 possessed higher activity for CO oxidation and NO reduction[7, 8] . But nanocubes show superior properties in soot combustion[9], hydrogen oxidation[10] and preferential oxidation of CO[11]. But due to the existence of large proportion of reactive planes on the surface of ceria nanowire, made it as potential redox catalyst for CO oxidation. Presence of oxygen vacancies and mobility of oxygen in the lattices are significantly altered with morphological parameters [6].

The design and synthesis of rare earth oxide ceria with chelating ligand oxalate have found rare works in the literature. Ceria nano particle from cerium oxalate can be prepared by microwave heating assisted thermal decomposition method[12]. Upon thermal decomposition of oxalate, it followed stepwise thermal decomposition strategy[13–15]. It is more important to have a fair knowledge on thermal decomposition behavior of surface modified cerium oxalate up to the formation of CeO_2/Ce_2O_3. Morphological dependency on activation energy can be derived in terms of conversion fraction α. Up to now, no exploratory work has done to deal the effect of morphological aspects of cerium oxalate on the creation of ceria with unique surface textures. Hence it has substantial interest to synthesis ceria in different design with appropriately choosing input reactant and surfactant. Besides it is equally important to understand the influence of structural features as the thermal stability or rate of decomposition of oxalate samples. It was investigated that surface modification of a polymeric material is an important tool to tune its degradation rate[16]. This happens because thermal conductivity of the surface functionalizing agents has pivotal role on reducing thermal stability of polymeric material, thereby increasing rate of its degradation process[17]. It was noted that the size of oxalate nanoparticle of calcium has noticeable effect on the kinetics of thermal decomposition process. On reducing the size of oxalates, the amount of activation energy needed for the decomposition process was decreased[18]. Bogatyreva *et al*[19] studied the effect of surface modification of the nano diamond on its thermal stability. High temperature activation followed by chemical treatment with mineral acids reduced the impurities on the top of the surface of diamond,

thereby reducing the chance of oxidation. Hence it was suggested that up to 773K, nano diamond with stands oxidation process at its surfaces.

Since the radical scavenging and antioxidant properties of ceria, it is worth to note the importance of ceria in anticancerous field. It was investigated that CeO_2 nano particles (Nps) are toxic to cancer cells and non-toxic to living cells[20]. Besides, it can inhibit invasion and sensitize cancer cells to radiation therapy and chemotherapy. This Nps are able to protect from cell damage indirectly by priming cells to respond to ROS (Reactive oxygen species) attack or directly by scavenging cellular ROS. It can save healthy cells from radiation induced damage during radiation therapy and provides neuro protection to spinal cord neurons. PEGlycated ceria nanoparticle showed enhanced radioprotection on human liver cell under γ-irradiation[21]. Shape effect of ceria on the cytotoxic properties is not well studied yet. Therefore, in the present work, different surface modified cerium oxalate (Ce-Ox) was prepared by co-precipitation and hydrothermal methods. Shape effect of cerium oxalate on thermal decomposition behavior for the formation of ceria nano structures is studied. Besides, how the anticancerous and optical properties of ceria are altered with the different surfaces of the ceria nano materials. Fig. 1 represents the comparison of synthesis of Nps with and without using stabilizers.

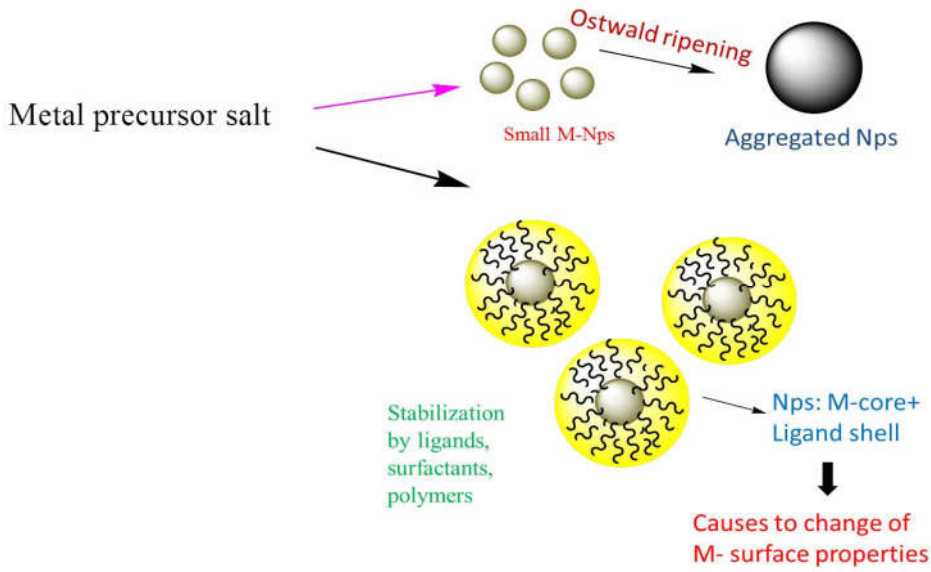

Fig. 1 Comparison of synthesis of Nps with and without using stabilizers

7.2. Experimental

7.2.1. Method of preparation

In the present work, cerium oxalate is prepared through simple precipitation and hydrothermal route. 3.07mmol cerium nitrate is dissolved in 60mL of distilled water. Add 1.02mmol CTAB and stirred the solution for 2h. The resulting supernatant solution is transferred into a sealed autoclave and kept at 120ºC for 24h. Similar procedure is also conducted with PEG as surfactant. Cerium oxalate is also synthesized through simple precipitation route using sodium oxalate as the precipitating agent and the above mentioned surfactants. The precipitate is filtered and washed with ethanol and water. The precipitate is kept at 80ºC. Fig. 2 shows the PEG assisted synthesis of ceria Nps.

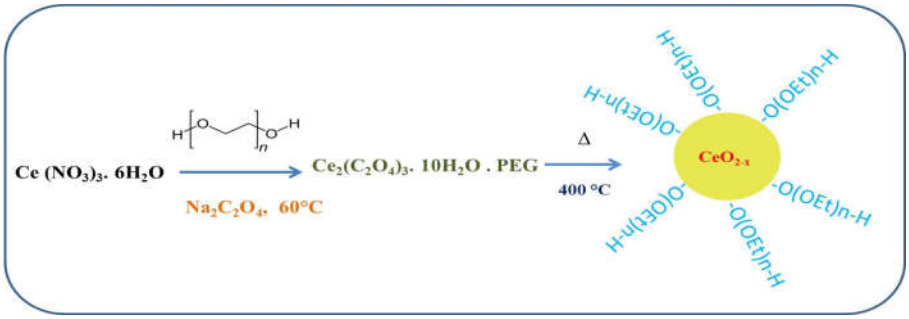

Fig. 2 PEG assisted synthesis of ceria

Designation of oxalate samples

H_1 (Ce-Ox- simple precipitation- PEG -800 as surfactant), H_2 (Ce-Ox-hydrothermal-PEG-800as surfactant), H_3 (Ce-Ox- simple precipitation- CTAB as surfactant), H_4 (Ce-Ox- hydrothermal-CTAB as surfactant).

Designation of prepared oxide samples

P_1 (synthesized branched hexagonal nanorod ceria from H_1), P_2 (synthesized multi branched nano ceria from H_2), P_3 (synthesized nano disc/flower of ceria from H_3), P_4 (synthesized 2D nano sheets of ceria from H_4).

The chemical composition and crystal structures of cerium oxide (prepared *via* thermal decomposition) were studied by XRD. (FT-IR) spectra of the samples was recorded by transmittance method. The prepared cerium oxalate precursor was calcined at 450ºC in muffle furnace for 5h. The morphology and topographical studies of the oxide samples were brought with TEM and Field emission scanning electron microscope. UV-Visible spectra of the oxide samples were taken spectrophotometer. Photo luminescent properties are well

characterized by using fluorescence spectrometer at room temperature. Electronic and crystalline properties are well characterized by using HRTEM and SAED pattern. Thermal decomposition properties of oxalates were analyzed by DSC and TG analysis in N_2 (50mL) atmosphere. Raman spectra of the samples were collected using confocal Raman microscope with the excitation of 532nm laser.

7.3. Results and discussion

7.3.1. Material characterization

Fig. 3A represents FT-IR spectra of surface modified Ce-Ox. Figs. 3Aa, b, c &d respectively show H_1, H_2, H_3 & H_4. The broad band observed at 3080–3433cm^{-1} (Fig. 3A) associated with water molecules which are removed only at higher temperature[22].

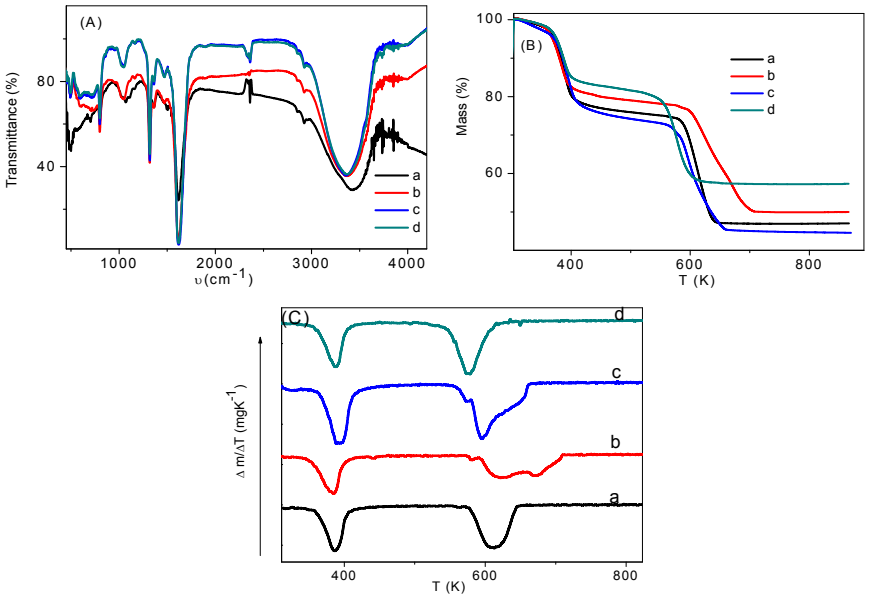

Fig. 3 FT-IR spectra (A), TG (B) and DTG curves (C) (at 5Kmin^{-1}) in N_2 atmosphere of surface modified Ce-Ox: H_1 (a), H_2 (b), H_3 (c) & H_4 (d).

Table 1 Mass loss (%) for each Ce-Ox upon thermal decomposition obtained from TG curves

Sample	Mass loss (%)
H_1	53.06
H_2	49.68
H_3	54.76
H_4	42.05

The very strong peak observed at1633.9cm^{-1}corresponds to the combined effect of asymmetric bending and stretching of water molecule[23]. The strong peak observed at 1318.4cm^{-1}represents the asymmetric stretching of CO_2 molecule associated with oxalate ligand group[23,24]. The band observed at 523.8cm^{-1}stands for M-O stretching frequency[22,24]. Thermal decomposition behavior of cerium oxalate depends on the nature of surface modifier, its chemical bond with surface of the oxalate sample, mechanism and kinetics of thermal reaction. From the TG curves (Fig. 3B), it is understood that the method of preparation of the sample (history) also depends on the rate of mass loss process during thermal decomposition. It can be realized from the kinetics of decomposition that, significant variation with distinct surface textures of cerium oxalate upon the rate of formation of ceria. The mass loss (%) corresponding to each surface modified Ce-Ox by the thermal decomposition process are displayed in Table 1. It was found that mass loss (%) for the sample H_4 (42.05%) is lower than others indicating lower thermal stability of array of nano hexagonal Ce-Ox. Highest mass loss was found for nano disc Ce-Ox (H_3), 54.76% and nano flower petals Ce-Ox (H_1), 53.06% prepared by co-

precipitation method. Ce-Ox synthesized through hydrothermal methods (H_2 & H_4) has lower percentage of mass loss. Theoretical mass loss for the formation of ceria from cerium oxalate was found to be 52.48%. The higher experimental mass loss was occurred with the degradation of surfactant along with Ce-Ox. Fig. 3C shows the DTG curves of all surface modified Ce-Ox, H_1 (Fig. 3C: a), H_2 (Fig. 3C: b), H_3 (Fig. 3C: c) and H_4 (Fig. 3C: d). DTG curves passes through with non-homogeneous behavior at several regions of the temperature, implying partially overlapped multistep process. Sample H_4 and H_1 occur at much lower temperature for the formation ceria nano particle than other samples, whereas sample H_2 take place at higher temperature for the production of nano particle.

Fig. 4A represents FE-SEM images of Ce-Ox nano materials (sample H_1, H_2, H_3 & H_4). Fig. 4Aa shows the Ce-Ox nano flower petals (H_1). Fig. 4Ab exposes like nano plates of Ce-Ox (H_2). Fig. 4Ac displays like nano discs/flower of Ce-Ox (H_3). Array of nano hexagons of Ce-Ox (H_4) is represented in Fig. 4Ad. Fig. 4B displays the DSC curves of nano materials of Ce-Ox at $2Kmin^{-1}$. DSC curve shows two main stages up to the temperature 800K, the first stage corresponding to the loss of crystallized water of Ce-Ox and second for the decomposition of oxalates forming ceria nano structures.

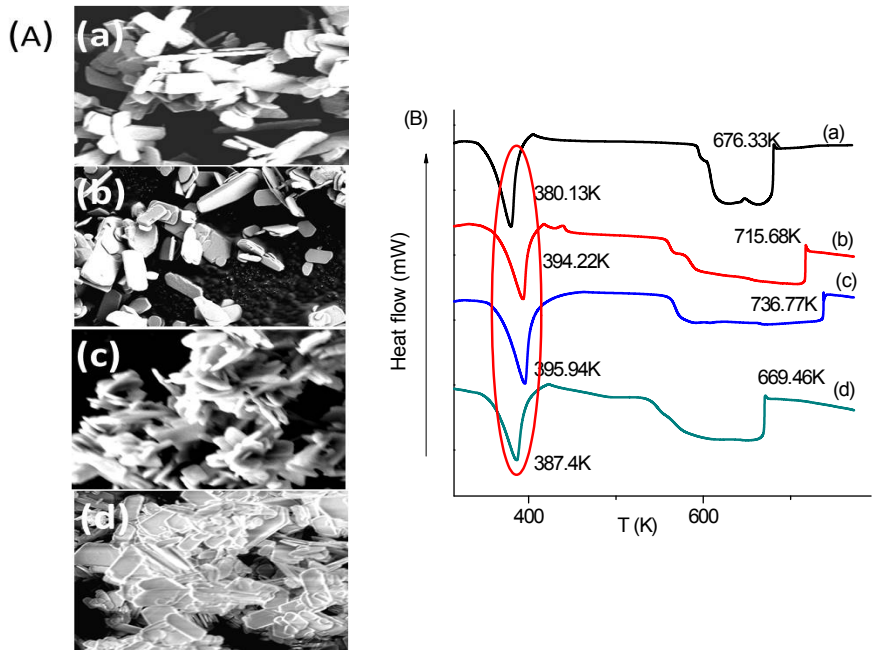

Fig. 4 FE-SEM images (A) and DSC curves (B) of oxalate samples at 2Kmin^{-1}; H_1 (a), H_2 (b), H_3 (c) & H_4 (d)

It is displayed that changing the surface morphology of Ce-Ox, changes in the decomposition as well as dehydration temperature was occurred (Fig. 4B). This happens due to the difference in the diffusion controlled reaction mechanisms of solid state decomposition of each nanomaterial of Ce-Ox. Ce-Ox nano flower petals (H_1) (Fig. 4A:a) undergo dehydration at lower temperature (380.13K) than others (Fig. 4B:a). The samples H_2, H_3 & H_4 losses water at 394.22K, 395.94K and 387.4K (Figs. 4B:b, c & d). On moving to the decomposition part at 2Kmin^{-1}, H_4 has lower decomposition temperature 669.46K (Fig. 4B:d) than H_1, H_2 & H_3. Hence it is informed that the significant influence of morphology of Ce-Ox on the thermal decomposition behavior of Ce-Ox up to the formation of ceria nano particle.

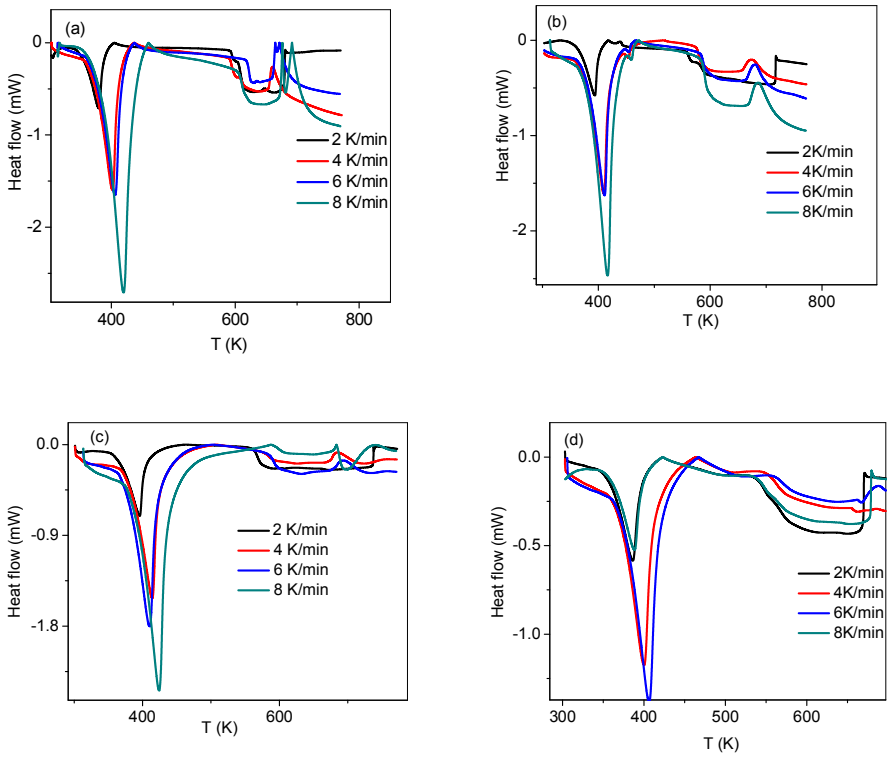

Fig. 5 The DSC curves of Ce-Ox at 2, 4, 6 and 8Kmin^{-1} in N_2 atmosphere.

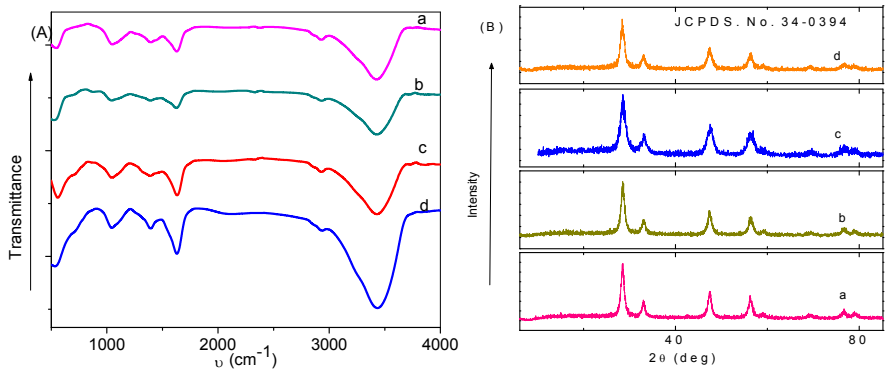

Fig. 6 FT-IR spectra (A) and XRD patterns (B) of ceria: P_1 (a), P_2 (b), P_3(c) & P_4 (d)

Fig. 5 represents the DSC curves at 2, 4, 6 and 8Kmin^{-1} for the samples H_1 (Fig. 5a), H_2 (Fig. 5b) H_3 (Fig. 5c) and H_4 (Fig. 5d). It was observed that increasing temperature, the absorbed heat energy was decreased than lowest temperature reaction. Besides, increasing heating rate, marked increasing in the absorbed heat energy with respect to β, but this shift was found to be only at lower reaction and rather disappeared at higher temperature reaction. It was noticed that the peak width of sample H_4 is higher at all heating rates than other samples.

Figs. 6A &B show the FT-IR spectra and XRD patterns of different surface modified ceria; where a, b, c and d represent respectively branched hexagonal nano rod (P_1), multi branched (P_2), nano disc/flower (P_3) and array of nano hexagons (P_4). The IR band at 3000-4000cm^{-1} corresponds to water molecule associated with oxides. The band at 520-550cm^{-1} corresponds to M-O bond. Fig. 6B represents the diffraction peaks corresponding to cubic fluorite type structure of ceria (JCPDS Card No. 34-0394). Among the different morphologies of ceria, intensities of diffraction peaks are comparable.

Fig. 7 shows the FE-SEM images of formed ceria nano materials. Nano ceria P_1 (Fig. 7a) have surface morphology of hexagonal rod with branching in one direction. But P_2 shows nano rod morphology with branches in many directions. These branches to the surfaces were occurred due to the influence of surfactant PEG. Ceria nano material, P_3 (Fig. 7c) and P_4 (Fig. 7d) display like nano discs/flower and array of *2D* nano sheets respectively. From the surface morphological analysis of ceria, it can be seen that thermal

decomposition of Ce-Ox nano materials significantly altered its shape. Both the synthetic route and surfactants used affect the morphology of Ce-Ox, which has influence on the creation varieties of ceria nanostructures.

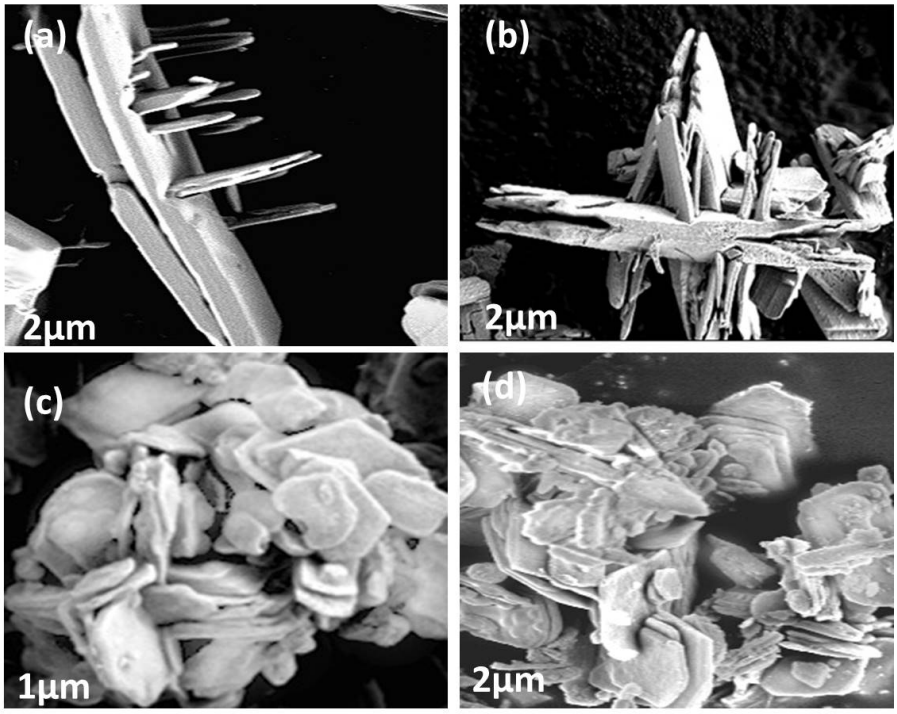

Fig. 7 FE-SEM images of ceria nano structures prepared from Ce-Ox; P_1 (a), P_2 (b), P_3 (c) and P_4 (d).

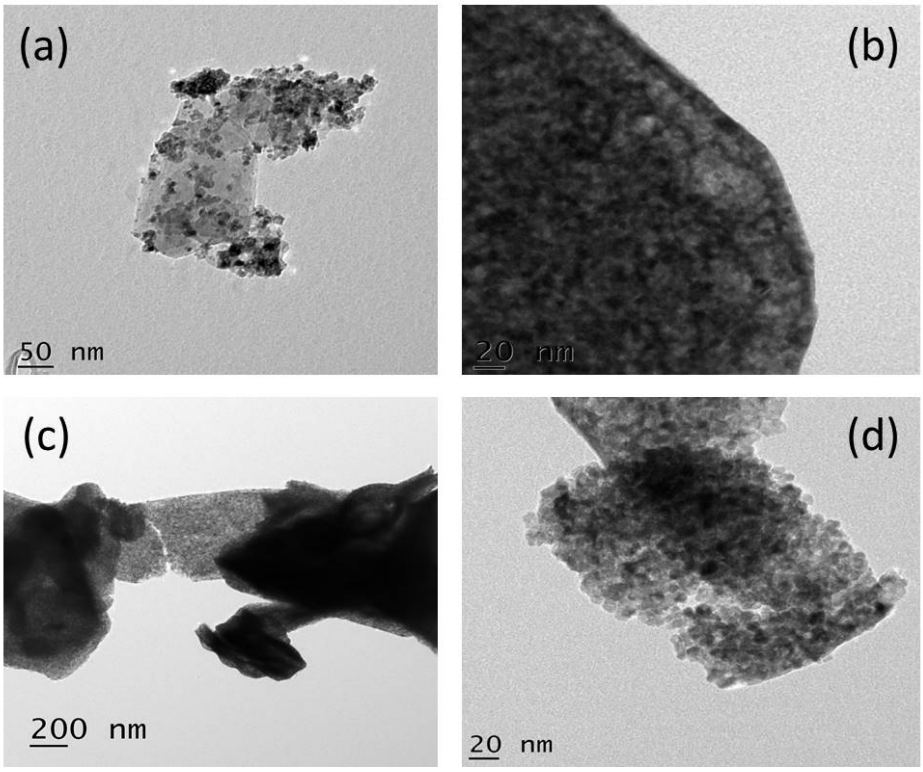

Fig. 8 TEM images of ceria nano structures; P_1 (a), P_2 (b), P_3 (c) and P_4 (d).

Fig. 8 shows the TEM images of ceria nano materials. Thermal decomposition of Ce-Ox nano flower petals P_1 yields nano hexagonal particles having size 2.11-3.98nm (Fig. 8a). The inter planar distance was found to be 0.3nm (Fig. 9a). This indicates the presence of branched nano hexagons with lattice fringes similar to inter planar distance of cubic fluorite type structure of ceria. Thermal reactions of branched Ce-Ox (H_2) resulted in the formation of aggregates of nanoparticle with size in the range of 3.8-8.39nm (Fig. 8b). The distance between two successive planes of this branched ceria was found to be 0.32nm (Fig. 9b).

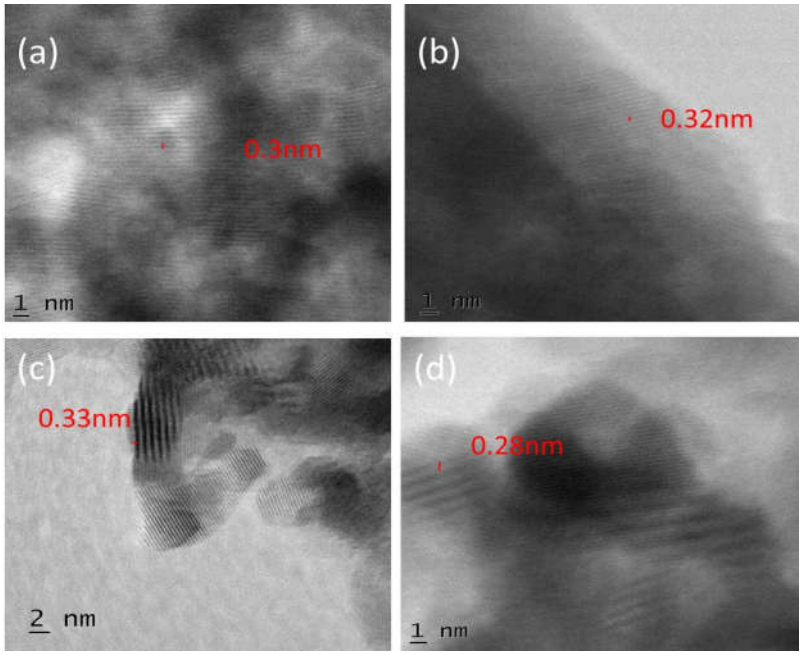

Fig. 9 HRTEM images of P_1 (a), P_2 (b), P_3 (c) and P_4 (d).

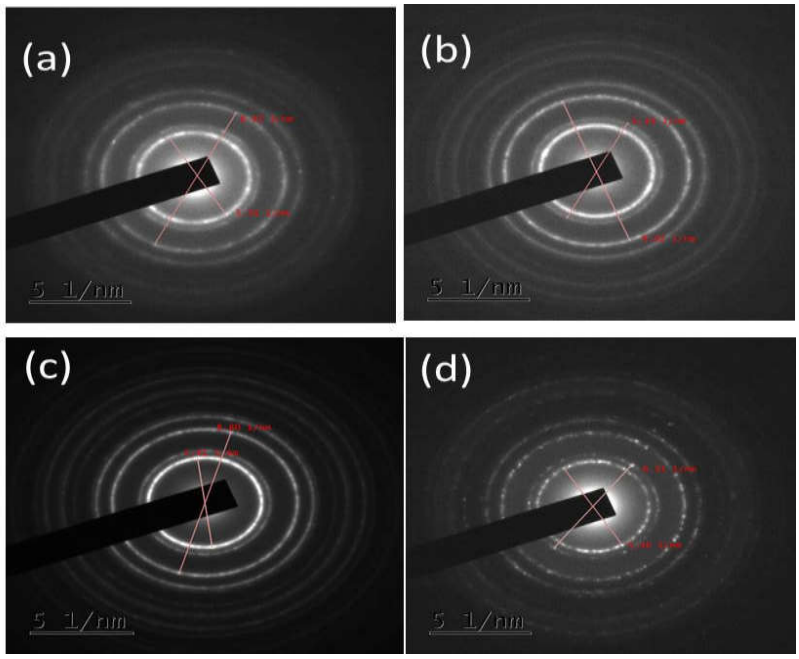

Fig. 10 SAED patterns of ceria: P_1 (a), P_2 (b), P_3 (c) and P_4 (d).

The nano disc/flower like Ce-Ox (H_3) upon thermal decomposition yields nano discs/flower of ceria (P_3). These nano discs/flower are composed of ceria nanoparticles of size 4.6-8.8nm (Fig. 8c). The inter planar distance was observed to be 0.33nm (Fig. 9c). Array of nano hexagonal Ce-Ox (H_4) altered its surface textures upon thermal decomposition to yield *2D* nano sheets (P_4) (Fig. 7d), these sheets are composed of ceria nano spheres having size in the range of 2.92-9.32nm (Fig. 8d). The inter planar distance of P_4 was observed to be 0.28nm (Fig. 9d), indicating the cubic fluorite type structure. The calculated values of lattice constant for each ceria nano structures are listed in Table 2.

It was observed that lattice constant of each ceria nano structure is altered. Changes occurred for each ceria lattice constant and inter planar distance is ascribed to the existence of difference in the experiencing lattice strain which arises due to the difference in particle size and oxygen ion vacancies. Decreasing of particle size and inter planar distance for the samples causes the lattices to be relaxed by creating new oxygen ion vacancies. Sample P_1 acquired lower particle size distribution compared to others. Hence, this sample reduces its lattice strain by creating more number of oxygen ion vacancies by converting more Ce^{4+} to Ce^{3+}.

Table 2 The values of lattice constant, particle size and inter planar distance of ceria nanostructures

Sample	Lattice constant (nm)	Particle size (nm)	Inter planar distance (nm)
P_1	0.52	2.11 - 3.98	0.30
P_2	0.55	3.80 - 8.39	0.32
P_3	0.57	4.60 - 8.80	0.33
P_4	0.49	2.92 -9.32	0.28

Fig. 10 shows SAED patterns of each synthesized ceria nano structures. P_1, P_2 & P_3 show highly crystalline ceria nano particle. But P4, array of nano sheets composed of nano sphere like particles exhibited semi crystalline nature as evident from the SAED pattern (Fig. 10d).

7.3.2. Photo physical properties

7.3.2.1. UV-absorbance

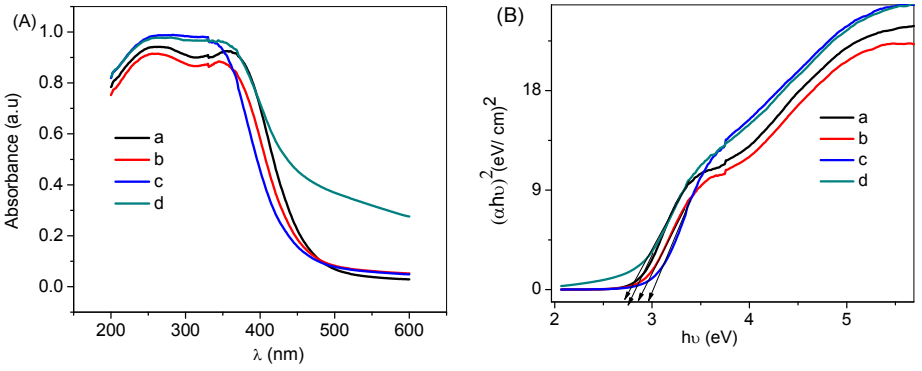

Fig. 11 UV-Visible absorbance spectra of ceria nanostructures (A); P_1 (a), P_2 (b), P_3 (c) and P_4 (d) & *Tauc* plots (B); P_1 (a), P_2 (b), P_3 (c) and P_4 (d).

Fig. 11A represents UV-Visible absorbance spectra of the entire ceria nano structures which show broad strong absorption below 400nm. The absorbance spectrum shows two absorption maxima. The peaks about 256nm correspond to charge transfer from O^{2-}(2p) to Ce^{3+} (4f) orbitals in CeO_2, while UV A absorption at 340nm are responsible for CT from O^{2-}(2p) to Ce^{4+} (4f) orbitals[25]. Fig. 11A: a, corresponds to ceria hexagonal nano rods (P_1) while Figs. 11A: b, c &d respectively represent ceria with multi branches (P_2), nano discs/flower (P_3) and nano sheets (P_4). On comparing the UV-absorbance, nano discs/flower (P_3) show highest UV- absorbance. Fig. 11B displays *Tauc* plots for each ceria nanostructure. Figs. 11B: a, b, c &d respectively represent *Tauc* plots for P_1, P_2, P_3 & P_4. Lower *Eg* value was observed for *2D* nano sheets (Fig. 11B: d). It is followed that *Eg* value in the order of $P_4 < P_1 < P_2 < P_3$. *Eg* values calculated from the *Tauc plots* is listed in the Table 3. This confirms that UV-absorbance and optical band gap significantly altered with respect to morphology of ceria.

Table 3 The values of optical band gap *Eg* calculated from *Tauc plots*

Sample	*Eg* (eV)
P_1	2.77
P_2	2.87
P_3	2.97
P_4	2.73

7.3.2.2. Luminescent properties

Fig. 12 shows the significance of photo luminescent (PL) spectra of ceria nano structures at an excitation wavelength of 340nm.

It was observed that depending upon the surface morphology of ceria, distinct level of intensity of emission band was occurred. Hence surface morphology of nanostructures plays significant influence in the emission band intensity. Fig. 12a represents PL of ceria with branches in one direction (P_1). Figs. 12b, c &d represent PL of ceria P_2, P_3 &P_4. Emission band consists of good violet bands at 419nm (2.96eV), blue emission band at 483nm (2.57eV) and green emission band at 529nm (2.35eV). It was reported that PL emission in the range of 400-550nm (< 3eV) are highly associated with oxygen vacancies with trapped electrons which localized between Ce (4f) and O (2p) band in CeO_2. Highest luminescent intensity was observed for P_3.

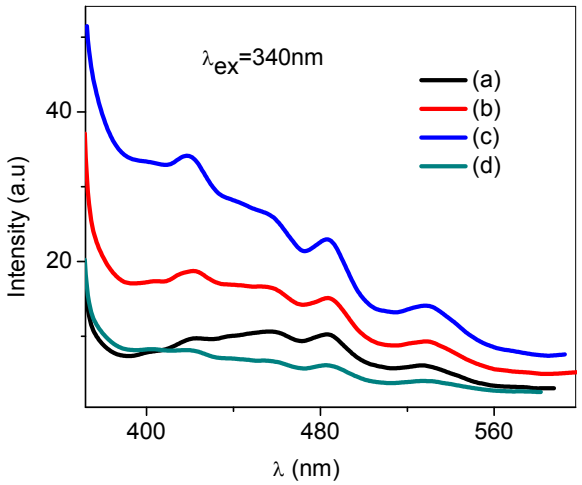

Fig. 12 PL spectra of ceria nano structures; P_1 (a), P_2 (b), P_3 (c) and P_4 (d).

7.3.3. Thermal properties

7.3.3.1. Estimation of Ea values for the decomposition process of Ce-Ox up to the formation of nano structures

During thermal decomposition process, self–generated reaction condition has predominant role on controlling the reaction path ways[26]. Change in the internal gaseous pressure can alter the smoothness of heat transfer process, which affects kinetics of the reaction. Cerium oxalate decomposes to ceria through multistage decomposition stages. Due to the experimental inconvenience of separately tracking the each component process; the deconvolution of overall kinetic information into reaction component is the only possible method for interpreting multistage reaction scheme[27,28]. Each kinetically resolved stage is studied by formal kinetic analysis. Fig. 13 shows the deconvoluted DSC curve of the sample H_4 at $2Kmin^{-1}$.

Ea for each independent process was measured by using *Friedman plots*. The determination of *Ea* values for each stage was based on *Eq.* 1. Plots of ln ($d\alpha/dt$) vs T^{-1} known as *Friedman plots*[29–31], for the series of kinetic data at different α recorded under linear non-isothermal condition were examined for determining the values of *Ea*. From the slope of the plot, the values of *Ea* can be evaluated. *A* can be calculated from the intercept, after incorporating the best reaction model $f(\alpha)$ using modified Sestak-Berggren model(SB (m, n)[32,33].

$$\frac{d\alpha}{dt} = A\exp\left(-\frac{Ea}{RT}\right) f(\alpha) \qquad (1)$$

$$f(\alpha) = \alpha^{m}(1-\alpha)^{n} \qquad (2)$$

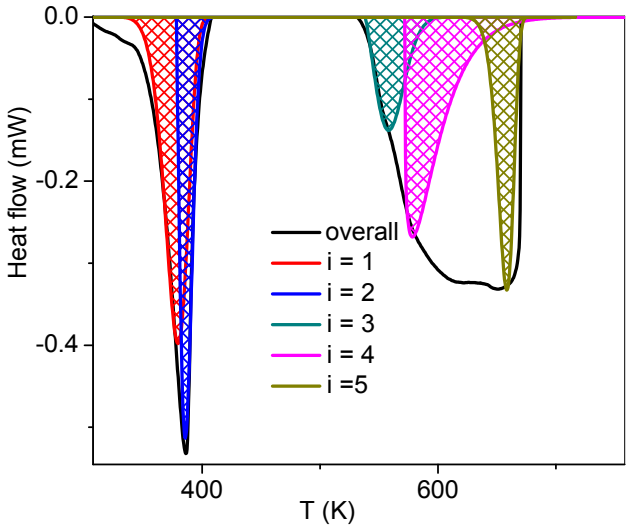

Fig. 13 The deconvoluted DSC curve of sample H_4 at 2Kmin^{-1}.

Fig. 14 shows the Friedman plots for first (Fig. 14a), second (Fig. 14b), third (Fig. 14c), fourth (Fig. 14d) and fifth (Fig. 14e) stages of thermal decomposition of array of nano hexagonal Ce-Ox (H_4), which were used for finding the initial values of *Ea* and *A* of the sample H_4. Similarly, initial values of *Ea* and *A* values of other oxalate samples were also calculated by the Friedman plot. The contribution of each stage was calculated from the area or quantity of heat absorbed in the DSC curve. The method of kinetic deconvolution procedure (*as described in previous chapters*) was executed for finding the optimized values of *Ea*.

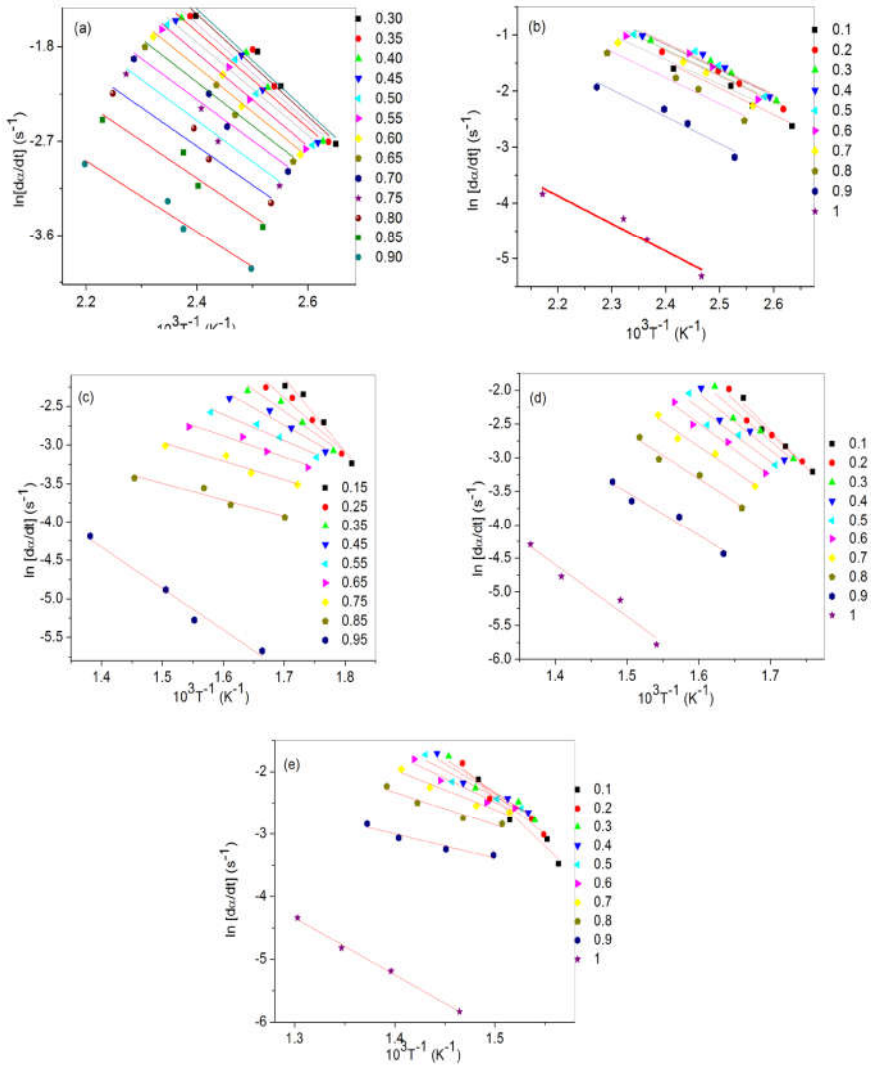

Fig. 14 *Friedman plots* at different α value of first (a), second (b), third (c), fourth (d) and fifth stages (e) of thermal decomposition of array of nano hexagonal Ce-Ox (H_4).

Table 4 Average values of *Ea* optimized for each stage of thermal decomposition of Ce-Ox; H_1, H_2, H_3 and H_4.

Sample	*Ea* (kJmol^{-1})				
	1	2	3	4	5
H_1	47.15	48.13	130.37	146.24	68. 40
H_2	42.98	79.59	123.26	134.07	245.03
H_3	89.04	62.47	53.96	162.77	266.26
H_4	36.67	37.67	43.76	69.75	75. 53

The comparison of *Ea* value for the formation of each nano structure is listed in Table 4. Significance of surface characteristics of each Ce-Ox upon the thermal reaction condition can be depicted from finding the *Ea* value throughout each stage. From the Table 4, it is known that array of nano hexagonal Ce-Ox (H_4) takes easiest reaction path for removing crystallized water and for forming *2D* nano sheets as the end product. Comparatively higher amount of activation energy was needed by Ce-Ox nano disc/flower (H_3) to form as nano discs/flower as the reaction product. This means that H_3 proceeds through the diffusion controlled reaction mechanism which tends to higher thermal prevention for the decomposition. Change in *Ea* value was observed throughout the reaction at different extent for samples H_1 &H_2. This informs that synthetic route and substrate surface characteristics control the thermal reaction programs for forming ceria nanostructures.

The plots used for finding optimized *Ea* values are represented in Figs. 15, 16, 17 and 18 for first, second, third, fourth and fifth stages of decomposition of each Ce-Ox.

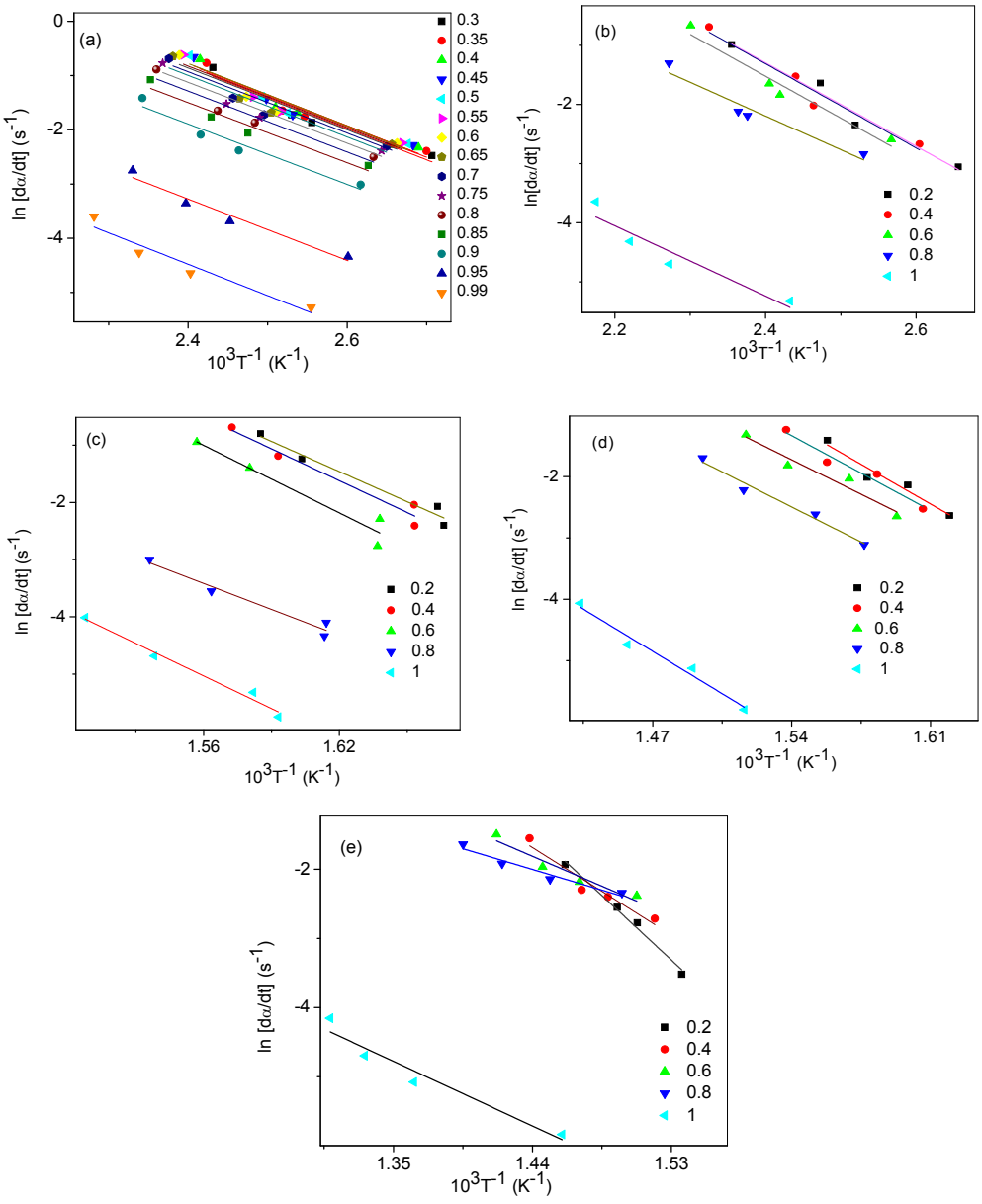

Fig. 15 The *Friedman plots* at different α value of first (a), second (b), third (c), fourth (d) and fifth (e) stages of thermal decomposition of the sample H_1.

The plots at specified α values were drawn only for most linearly fitted data. For some plots, slope at specified α values are coinciding to each other. Fig. 19 depicts how thermal event occurs in the initial stages of the sample H_4 (Figs. 19a & b), reminding that *Ea* value decreases with reaction (for first) and *Ea* value almost constant towards the end of the stage (for second). Change in *Ea* value occurs due to the happening of change in reaction pathway as the reaction progresses. Fig. 19 also shows the dependence of *Ea* with respect to *α* for third (c), fourth (d) and fifth (e) stages respectively.

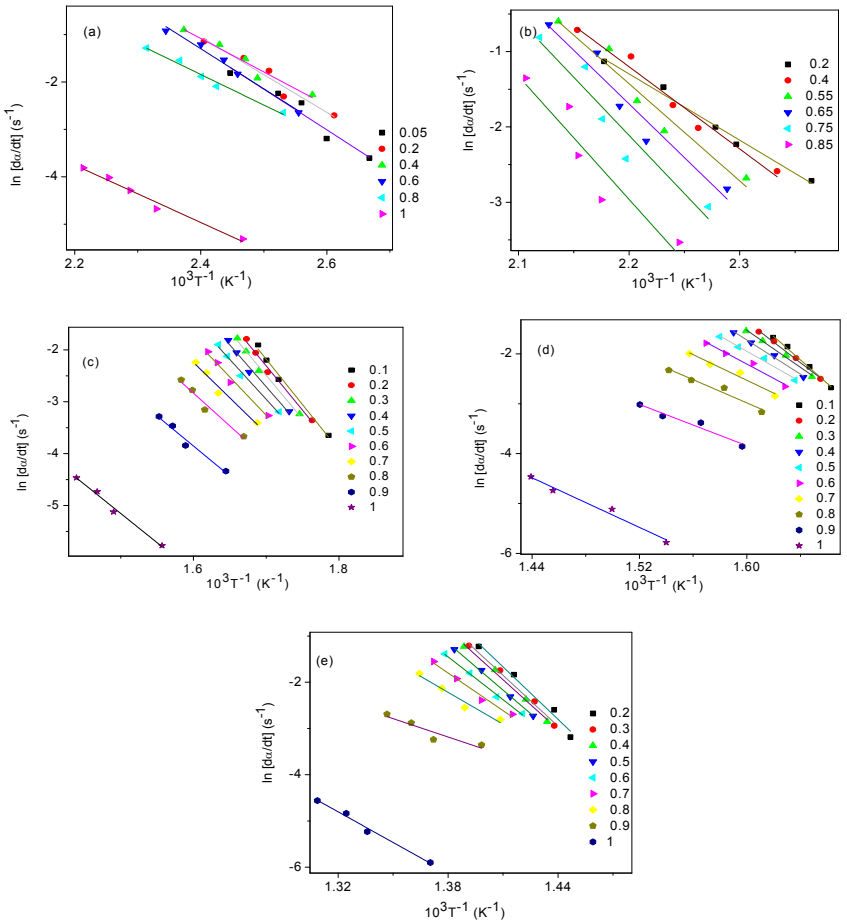

Fig. 16 The *Friedman plots* at different α value of first (a), second (b), third (c), fourth (d) and fifth (e) stages of thermal decomposition of the sample H_2.

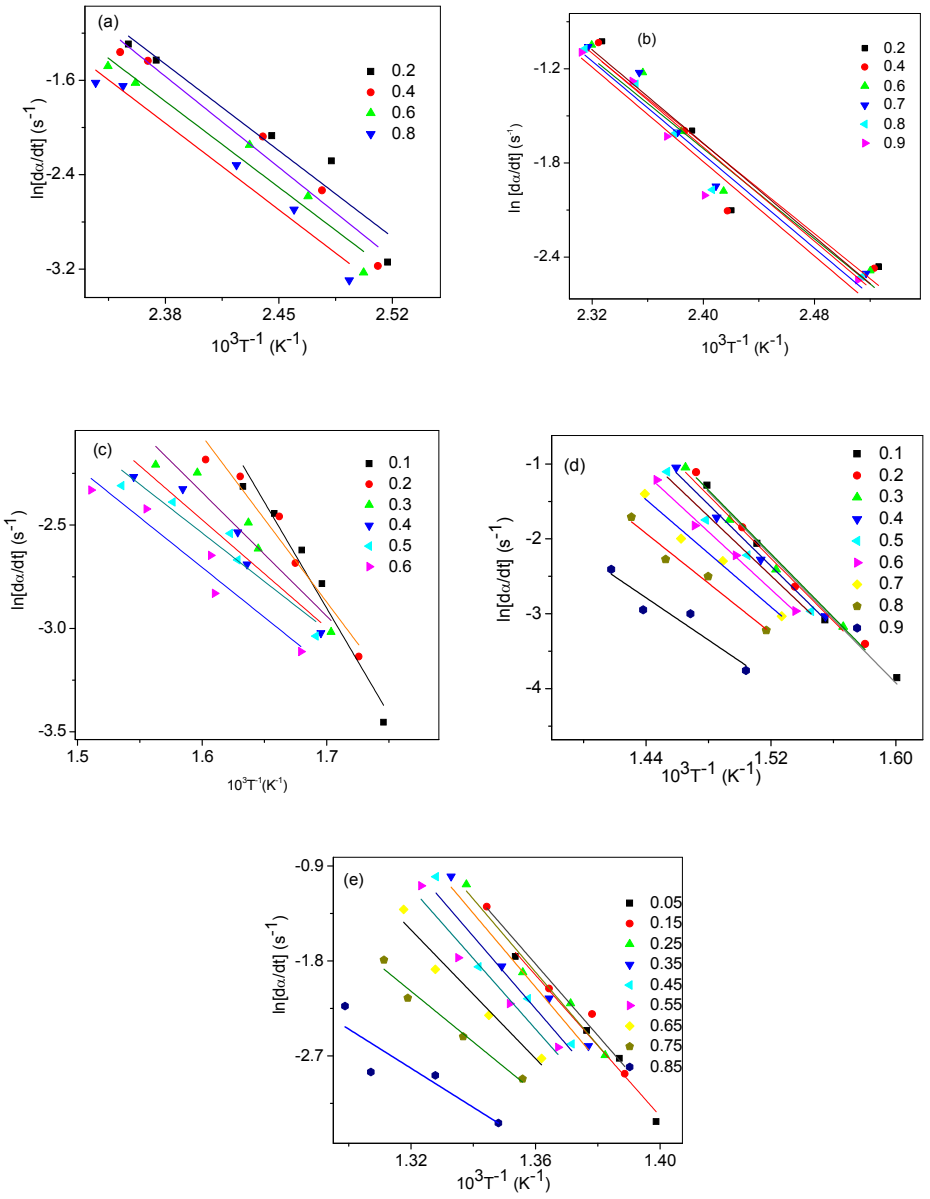

Fig. 17 The *Friedman plots* at different α value of first (a), second (b), third (c), fourth (d) and fifth (e) stages of thermal decomposition of the sample H_3

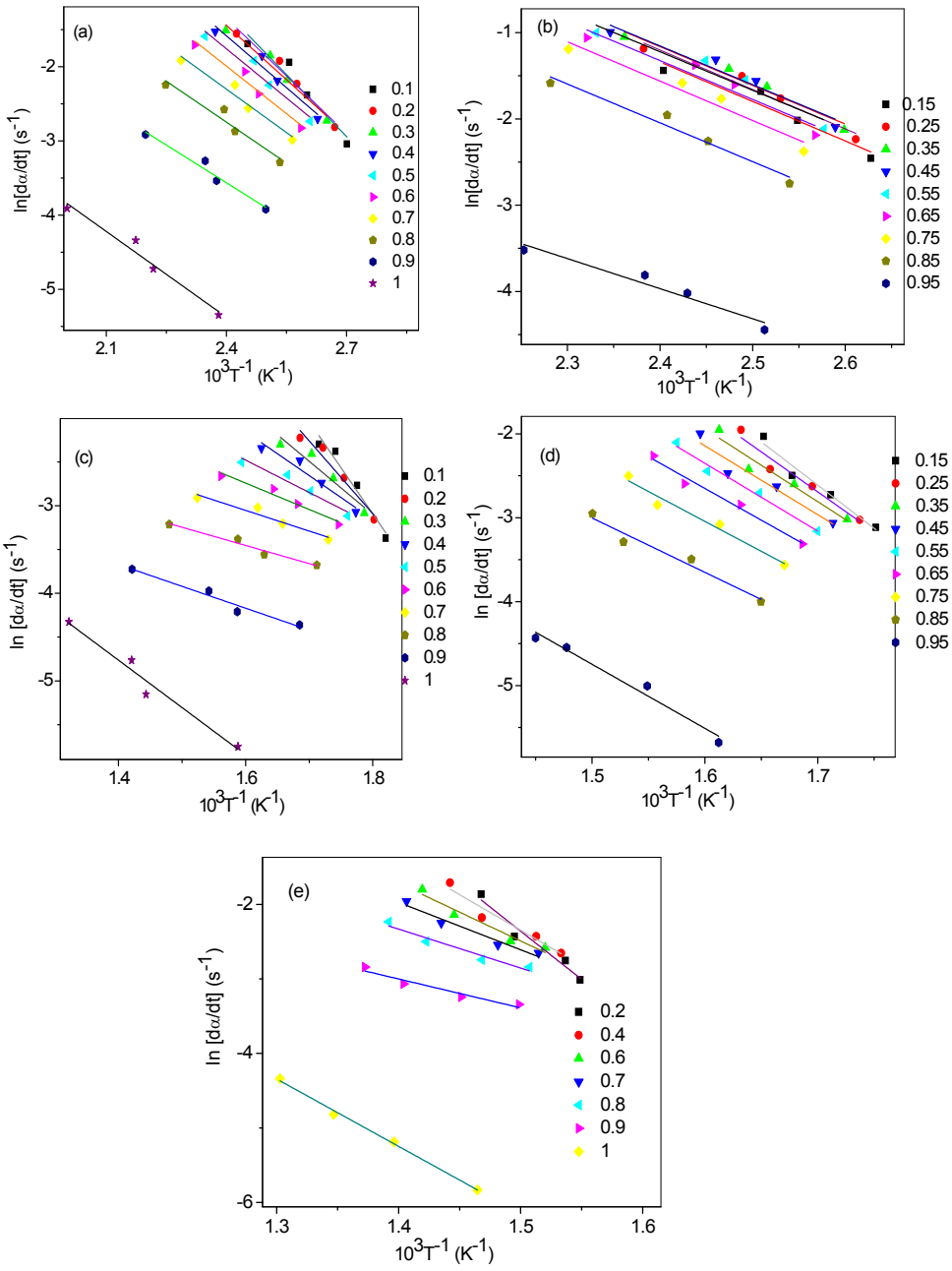

Fig. 18 The *Friedman plots* at different α value of first (a), second (b), third (c), fourth (d) and fifth (e) stages of thermal decomposition of the sample H_4.

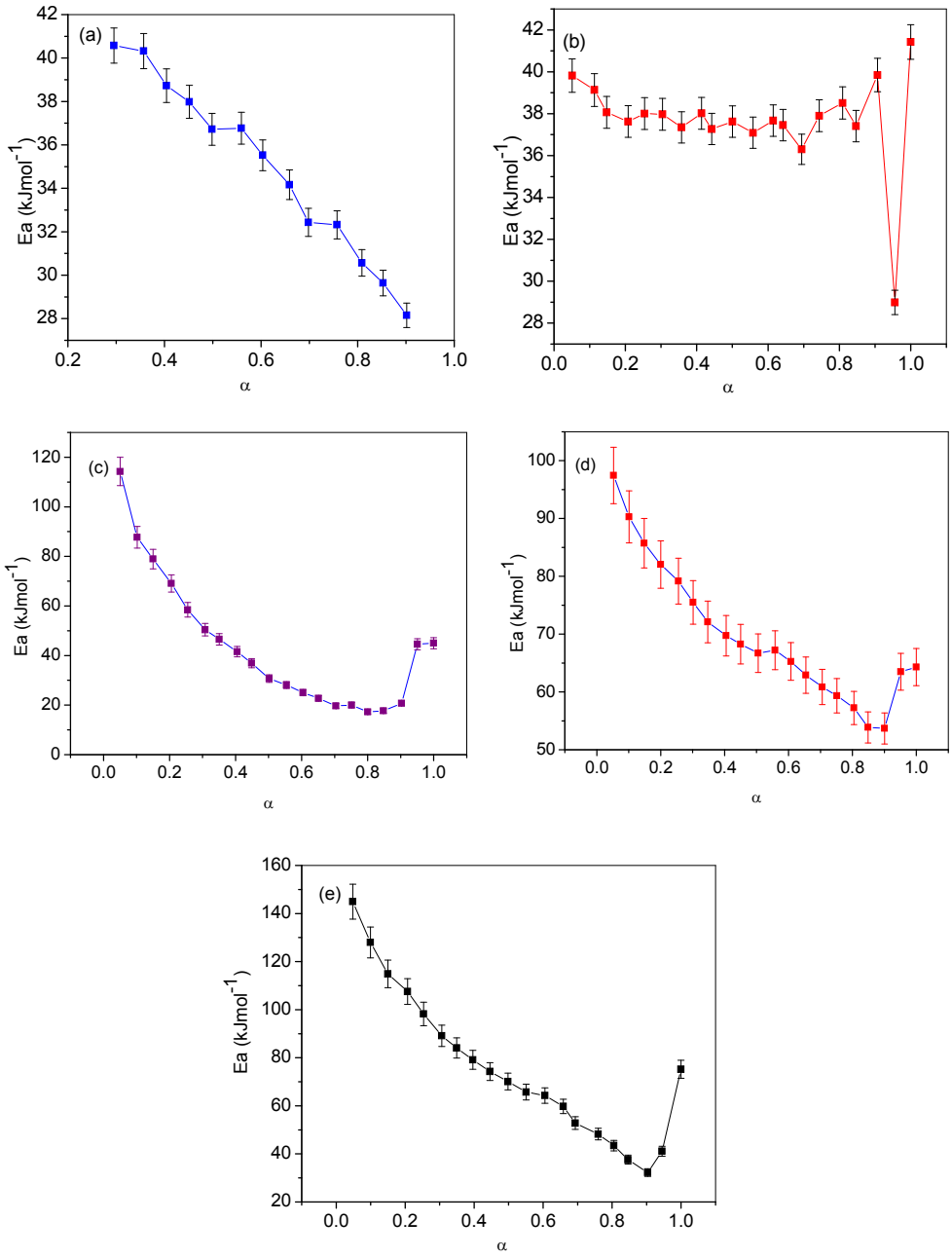

Fig. 19 Dependence of *Ea vs α* for first (a) second (b), third (c), fourth (d) and fifth (e) stages for the sample H_4

7.3.4. Micro Raman spectra

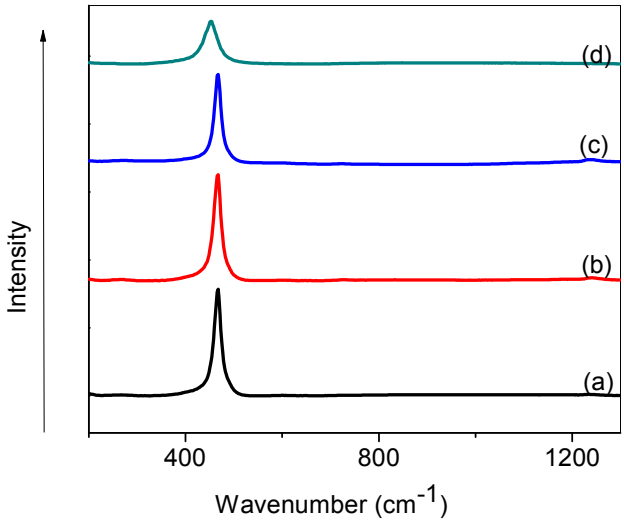

Fig. 20 Micro Raman spectra of CeO_2 nano structures; P_1 (a), P_2 (b), P_3(c) and P_4 (d)

The influence of surface morphology of ceria nanostructures are further confirmed by Raman scattering (Fig. 20). The spectrum shows the main band at 465.34cm^{-1}, which is responsible for the first order triply degenerated F_{2g} mode of vibration characteristic to the cubic structure of CeO_2[34,35]. The weak band near to 600cm^{-1} is associated with the intrinsic oxygen ion vacancies due to the presence of Ce^{3+} ions. Several factors caused for the change in Raman peak position and line width of main band. These include phonon confinement, strain, broadening associated with size distribution, defects, and variations in phonon relaxation with particle size[35]. It was

observable from the spectrum that comparatively higher intensity for the sample P_1 (Fig. 20a), P_2 (Fig. 20b) and P_3 (Fig. 20c). But lower intensity for the band was appeared for P_4. The increased intensity of the band is associated with increased oxygen ion vacancies. For the sample P_4, widening of the characteristic peak was observed than others. Therefore this sample experiences lattice strain by the creation of more oxygen ion vacancies. Presence of more oxygen ion vacancies in the lattice of ceria, make it as better radical scavenger. Raman intensity ratio was calculated from the relative intensity of weak band near to 600cm^{-1} and intense peak at 465.34cm^{-1}. Figs. 21a-d displays the micro Raman spectra corresponding to the weak band near to 600 cm^{-1} for the samples P_1, P_2, P_3 and P_4 samples respectively.

Table 5 Raman intensity ratio for each ceria nanostructures

Sample	Raman intensity ratio (I_{600}/I_{465})
P_1	0.005
P_2	0.005
P_3	0.173
P_4	0.008

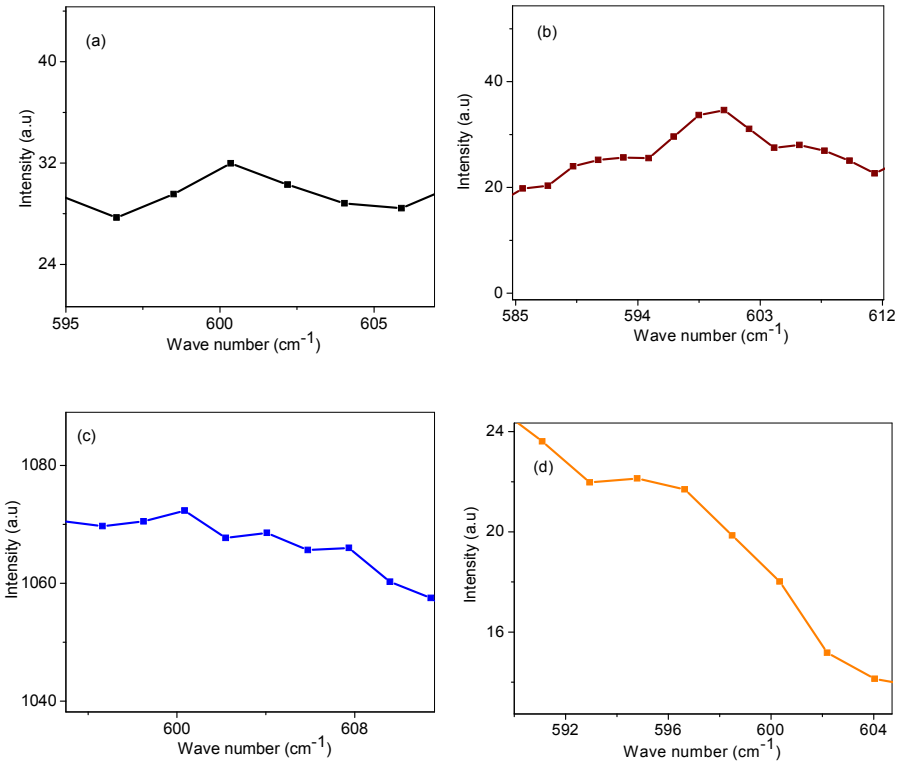

Fig. 21 Micro Raman spectra of P_1 (a), P_2 (b), P_3(c) and P_4 (d) corresponding to the weak band at near to 600 cm^{-1}.

From the Table 5, highest Raman intensity ratio was found for sample P_3. From the earlier reports[36], number of oxygen ion vacancies is best described with Raman intensity ratio. Hence, concentrations of oxygen ion vacancies are found to be large for the sample P_3.

7.3.5. Cytotoxicity studies

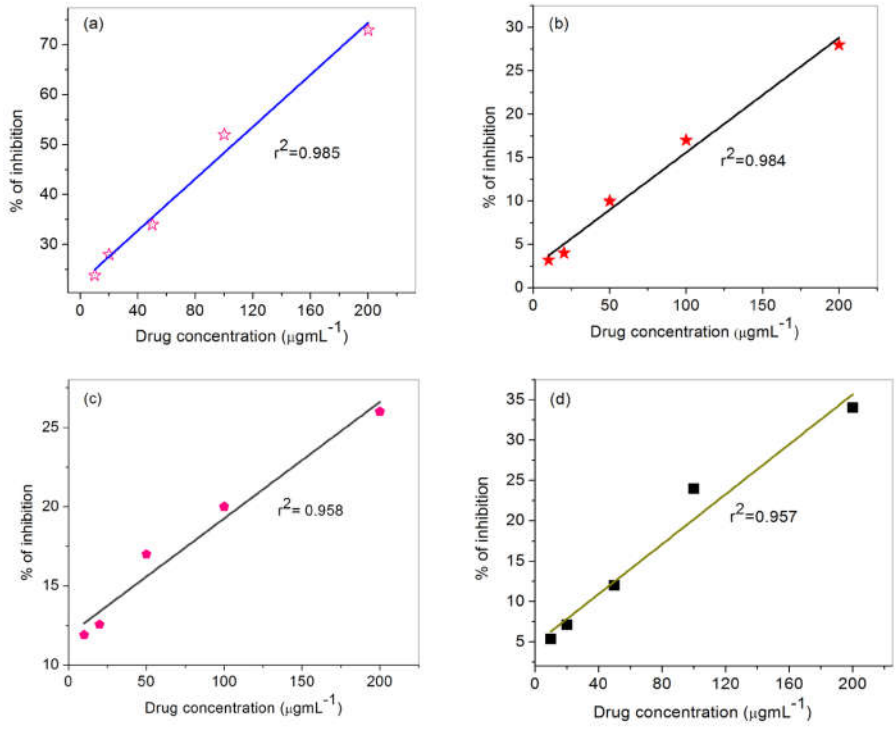

Fig. 22 Results of *in vitro* cytotoxic studies for different ceria nanostructures: P_1 (a), P_2 (b), P_3(c) & P_4 (d)

Fig. 22 shows the results of *in vitro* cytotoxicity for different surface modified ceria, using Dalton's Lymphoma ascite cells. Procedure for assay is described *in chapter 2*. This assay exposed highest percentage of inhibition for cancerous cell by the sample P_1, branched hexagonal ceria nanorods (Fig. 22a) than other ceria nano materials considered. The value of IC_{50} was observed at drug concentration of 105.3μgmL^{-1} for sample P_1. 73% of inhibition of cancer cells by P_1 was occurred at concentration of 200μgmL^{-1}. Multi branched (P_2, Fig. 22b), nano disc/flower (P_3, Fig. 22c) & nano sheet

(P_4, Fig. 22d) like ceria performed comparatively lesser cytotoxicity towards cancer cells than nano hexagonal branched rods of ceria (P_1). Hence the significance of surface morphologies of ceria nanomaterial has great influence in performing it as anticancerous drug. Ceria with surface modified by PEG, P_1 displayed as better anticancer drug.

7.4. Conclusion

Nano *flower petals*, *nano plates*, *nano disc/flower* and *array of nano hexagonal* Ce-Ox were synthesized *via* simple precipitation and hydrothermal methods. Executing thermal decomposition strategy for the oxalate precursors; surface modified ceria nanostructures like *branched hexagonal nano rod*, *multi branched*, *nano discs/flower* and *nano sheets* were synthesized and characterized. Surface modification of Ce-Ox has pivotal role on the thermal decomposition strategy, particle size and shape, formation of oxygen ion vacancies, optical and anticancerous properties. It was explored that for the formation of *nano sheet* like ceria, *Ea* values are lowered. But nano discs/flower of Ce-Ox has higher thermal prevention for the decomposition process to produce nano discs/flower of ceria. Enhanced luminescent and UV-absorbing properties were observed for *nano disc/flower* like ceria. But enhanced inhibition (73%) towards Dalton's Lymphoma ascite cells was performed by ceria (P_1), surface modified with PEG (*branched hexagonal nanorod*).

7.5. References

1. Ren Z, Peng F, Li J, Liang X, Chen B. Morphology-dependent properties of Cu/CeO_2 catalysts for the water-gas shift reaction. *Catalysts*. 2017;7:48.

2. Fei Y, Jingjing W, Wei L, Jinxin G, Yanzhao Y. Copper doped ceria nanospheres: surface defects promoted catalytic activity and a versatile approach. *J Mater Chem A*. 2014;2:5662-5667.

3. Carrettin S, Concepcion P, Corma A, Nieto JM, Puntes VF. Nano crystalline CeO_2 increases the activity of Au for CO oxidation by two orders of magnitude. *Angew Chem Int Ed*. 2004;43:2538-2540.

4. Mai HX, Sun LD, Zhang YW, et al. Shape-selective synthesis and oxygen storage behavior of ceria nano polyhedra, nanorods, and nanocubes. *J Phys Chem B*. 2005;109:24380-24385.

5. Nolan M, Parker SC, Watson GW. The electronic structure of oxygen vacancy defects at the low index surfaces of ceria. *Surf Sci*. 2005;595:223-232.

6. Du X, Zhang D, Shi L, Gao R, Zhang J. Morphology dependence of catalytic properties of Ni/CeO_2 nanostructures for carbon dioxide reforming of methane. *J Phys Chem C*. 2012;116:10009-10016.

7. Huang XS, Sun H, Wang LC, Liu YM, Fan KN, Cao Y. Morphology effects of nano scale ceria on the activity of Au/CeO_2 catalysts for low-temperature CO oxidation. *Appl Catal B*. 2009;90:224–232.

8. Zhang ML, Li J, Li HJ, Li Y, Shen WJ. Morphology-dependent redox and catalytic properties of CeO_2 nanostructures: nanowires, nanorods and nanoparticles. *Catal Today*. 2009;148:179–183.

9. Aneggi E, Wiater D, De Leitenburg C, Llorca J, Trovarelli A. Shape-dependent activity of ceria in soot combustion. *ACS Catal*. 2013;4:172–181.

10. Désaunay T, Bonura G, Chiodo V, et al. Surface-dependent oxidation of H2 on CeO_2 surfaces. *J Catal*. 2013;297:193-201.

11. Gamarra D, López Cámara A, Monte M, et al. Preferential oxidation of CO in excess H_2 over CuO/CeO_2 catalysts: Characterization and performance as a function of the exposed face present in the CeO_2 support. *Catal Today*. 2014;229:104-113.

12. Miyazaki H, Kato JI, Sakamoto N, Wakiya N, Ota T, Suzuki H. Synthesis of CeO_2 nanoparticles by rapid thermal decomposition using microwave heating. *Adv Appl Ceram*. 2010;109:123-127.

13. Nusrath K, Muraleedharan K. Effect of Ca(II) on the multistep kinetic behavior of thermally induced oxidative decomposition of cerium(III) oxalate to CeO_2(IV). *J Anal Appl Pyrol*. 2016;120:379-388.

14. Nusrath K, Muraleedharan K. Effect of Ca(II) additive on the thermal dehydration kinetics of cerium oxalate rods. *J Therm Anal Calorim*. 2017;128:541-52.

15. Subba Rao VV, Rao RVG, Biswas AB. Thermogravimetric analysis of La, Ce, Pr and Nd oxalates in air and in carbon dioxide atmosphere. *J Inorg Nucl Chem*. 1965;27:2525-2531.

16. Höglund A, Hakkarainen M, Edlund U, Albertsson AC. Surface modification changes the degradation process and degradation product pattern of polylactide. *Langmuir*. 2010;26:378-383.

17. Moraczewski K. Effect of surface layer modification method on thermal stability of electroless metallized polylactide. *Polimery*. 2017;62:750-756.

18. Fu Q, Cui Z, Xuea Y. Size dependence of the thermal decomposition kinetics of nano- CaC_2O_4: A theoretical and experimental study. *Eur Phys J Plus*. 2015;130:1-14.

19. Bogatyreva GP, Marinich MA, Zabuga VY, Tsapyuk GG, Panova AN, Bazalii GA. The effect of surface modification on thermal stability of nano diamonds. *J Superhard Mater*. 2008;30:305–310.

20. Gao Y, Chen K, Ma J, Gao F. Cerium oxide nanoparticles in cancer. *Onco Targets Ther*. 2014;7:835-840.

21. Li H, Yan ZY, Liu C, et al. PEGylated ceria nanoparticles used for radioprotection on human liver cells under γ-ray irradiation. *Free Radic Biol Med*. 2015;87:26-35.

22. Miguel G, Juan H, Leticia B, Joaquin N, Mario ERG. Characterization of calcium carbonate, calcium oxide and calcium hydroxide as starting point to the improvement of lime for their use in construction. *J Mater Civ Eng*. 2009;21:625-708.

23. Vimal G, Kamal PM, Biju PR, Joseph C, Unnikrishnan NV, Ittyachen MA. Structural studies and luminescence properties of CeO_2:Eu^{3+}

nanophosphors synthesized by oxalate precursor method. *Appl Nanosci*. 2015;5:837-846.

24. Oman Z, Haznan A, Widayanti W. Synthesis and characterization of nanostructured CeO_2 with dyes adsorption property. *Process Appl Ceram*. 2014;8:39-46.

25. Aškrabić S, Dohčević-Mitrović ZD, Araújo VD, Ionita G, De Lima MM, Cantarero A. F-centre luminescence in nanocrystalline CeO_2. *J Phys D Appl Phys*. 2013;46.

26. Wada T, Nakano M, Koga N. Multistep kinetic behavior of the thermal decomposition of granular sodium percarbonate : hindrance effect of the outer surface layer. *J Phys Chem A*. 2015;2:9749-9760.

27. Yoshikawa M, Yamada S, Koga N. Phenomenological interpretation of the multistep thermal decomposition of silver carbonate to form silver metal. *J Phys Chem C*. 2014;118:8059-8070.

28. Koga N, Goshi Y, Yamada S, Pe´rez-Maqueda LA. Kinetic approach to partially overlapped thermal decomposition processes; co-precipitated zinc carbonates. *J Therm AnalCalorim*. 2013;111:1463-1474.

29. Ozawa T. Applicability of Friedman plot. *J Therm Anal*. 1986;31:547–551.

30. Koga N. Kinetic analysis of thermo analytical data by extrapolating to infinite temperature. *Thermochim Acta*. 1995;258:145−159.

31. Gotor FJ, Criado JM, Malek J, Koga N. Kinetic analysis of solid-state reactions: the universality of master plots for analyzing isothermal and non-isothermal experiments. *J Phys Chem A*. 2000;104:10777–10782.

32. Nobuyoshi K, Daisuke K, Tomoyasu K. Aragonite crystal growth and solid-state aragonite − calcite transformation: a physico − geometrical relationship via thermal dehydration of included water. *Cryst Growth Des*. 2013;13:2238-2246.

33. Sestak J, Berggren G. Study of kinetics of the mechanism of solid state reactions at increasing temperatures. *Thermochim Acta*. 1971;3:1-12.

34. Weber WH, Hass V, McBride JR. Raman study of CeO_2: second-order scattering, lattice dynamics, and particle-size effects. *Phys ReV B Condens Matter*. 1993;48:178-185.

35. Spanier JE, Robinson RD, Zhang F, Chan S-W, Herman IP. Size-dependent properties of CeO_2 nanoparticles as studied by Raman scattering. *Phys Rev B*. 2001;64:245407-1-245407-245408.

36. Carla AO, José JMÓ, Manuel FRP, Andréa MDF, Raimundo CRN, Marco AF. Ozonation of model organic compounds catalysed by nanostructured cerium oxides. *Appl Catal B Environ.* 2011;103:190-199.

NUSRATH. K “SYNTHESIS AND KINETICS OF FORMATION OF CERIA AND CERIA BASED MATERIALS via THERMAL DECOMPOSITION OF OXALATES”. THESIS. DEPARTMENT OF CHEMISTRY, UNIVERSITY OF CALICUT, 2018.

8.1. Introduction

Ceria, one of the most important rare earth metal oxides exhibit unique chemical and physical properties. As a result of its high thermal and mechanical stability, excellent oxygen storage capacity and enhanced redox properties[1], it can find wide variety of applications in catalysis[2], oxygen sensors[3], UV-filters[4], solid oxide fuel cell[5], medicinal fields[6], etc. It can perform as better promoters in Three Way Catalysts (TWC) [1]. Modification of properties of ceria was enabled by isomorphous substitution of Ce by other metals (such as Cu, Ni, La, Gd, Eu, Pt, Au, Ru, etc.) to form solid solutions. This solid solution can withstand the change in the cubic fluorite type structure of ceria up to the higher concentration of dopants in the range of 1-50%. Recently DFT investigations have given valuable qualitative and quantitative descriptions about the structure of ceria and its solid solutions. Using this approach many of the properties of the material can be explored by solving the Schrödinger equation for the electrons of the atom, molecule, and assemblies of atoms in solids or liquids. The combination of molecular dynamics and electronic structure methods called *ab initio* molecular dynamics which can predict approximate solutions for the problems of many electron systems. The plane wave based *ab initio* DFT package of VASP[7] is now used for making solutions to the problems of many body problems. The calculations are based on Kohn-Sham equations[8] using exchange correlation functional GGA[9] or LDA[10]. In this approach, the employment of pseudo potentials are carried out by using relatively small set of plane waves. DFT method can simplify the problems of large experimental work

regarding which concentration of dopant can be effective for the best description of properties of ceria[1]. Carlos *et al*[1] carried out both experimental and DFT studies regarding the addition of Ni and Cu to the ceria lattice and calculated the formation energies for a range of concentration of dopant. The effect of group IV (a & b) elements (C, Si, Ge, Sn, Pb, Ti, Zr, Hf) as dopants to the ceria lattice within the frame work of DFT+U was carried out. This study revealed the change in formation energies of the solid solution $Ce_{1-x}Z_xO_2$ where $0 \leq x \leq 0.2$ with respect to the concentrations of dopants[11]. Effect of rare earth dopants (La, Pr, Nd, Pm, Sm, Eu and Gd) on the bulk properties of ceria was investigated within the frame work of DFT+U and found that earlier rare earth elements are more suitable for promoting oxygen storage capacity and migration of oxygen ion vacancies[12]. Adsorption of Cu, Ag and Au on the CeO_2 surface (110) is quantum mechanically predicted using the plane wave DFT code of VASP. While adsorption, Cu and Au are oxidized to Cu^{2+} and Au^{2+} [13]. *ab initio* DFT calculations of the structural, electronic, and thermodynamic properties of cerium ortho vanadate, $CeVO_4$, were performed utilizing the LDA, GGA-PBE, LDA+*U*, and GGA-PBE+*U* functional. The LDA+*U*, GGA-PBE+*U*, LDA, and GGA-PBE methods show deviations of equilibrium volumes of about −2.4%, +3.6%, −7.4%, and −0.8% respectively from the experimental results[14]. Jalborg *et al*[15] studied the electronic structure of super cells (2×2×2) $CeO_{2-\delta}$ within the frame work of DFT+GGA. The equilibrium properties of bulk ceria such as lattice constants, bulk moduli and magnetic moments of super cells were well characterized with exchange correlational GGA. At present a lot of computational studies are reported regarding the electronic structure and bulk

properties of ceria, studies on quantum mechanical predictions on the electronic structure of bulk ceria with single lattice containing 12 atoms and the substitution of one of its Ce by divalent Cu were carried out using plane wave based approach using DFT package of VASP *5.4.1*.

In the present chapter, *ab initio* plane wave DFT package of VASP is used for the investigations of electronic structure of ceria (1×1×1) unit cell and to find out solution for how the electronic properties are varied with respect to Cu in the lattice. Based on this structural examination, band structure, total density of states (TDOS), projected density of the states (PDOS) and charge density distribution of rare earth oxide ceria were established. The results were compared by utilizing both GGA and LDA exchange correlation functional.

8.2. Computational methods

DFT calculations were performed using Vienna ab initio simulation package (VASP 5.4.1)[16, 7] choosing plane wave basis set with an energy cut off 180eV for accounting the valence electrons. In order to study the effect of core electron on the valence electron density, projected augmented wave approach (PAW) was employed. The interaction between the ions and valence electrons are accounted by the standard frozen-core potentials which are utilized in the PAW method. The exchange correlational functional was introduced by generalized gradient approximation (GGA) and local density approximation (LDA) of Perdew and Wang (PW91). In order to study the convergence calculation of bulk ceria (1×1×1) unit cell, we have

computed volume and total energy of the bulk CeO_2 using plane wave cut off energies in the range of 170-450eV. The Brillouin-zone convergence calculations were performed using Monkhorst-Pack grids of (7×7×7), (8×8×8), (9×9×9), (10×10×10), (11×11×11), (12×12×12), (13×13×13), (14×14×14), (15×15×15), (16×16×16), (17×17×17) and (18×18×18). It was found that calculations are well converged for a *k*-point grid of (11×11×11) and energy cut off 180eV. Lattice convergence calculations show the lattice constant of 5.4Å for the cubic fluorite type structure of ceria. After the convergence calculations, electronic structure of bulk ceria (1×1×1) single lattice was investigated by calculating the band structure, total density of states and projected density of states and charge density distribution of the material. Further in this chapter, the effect of Cu-doping on the total energy, lattice constant, Brillouin zone and plane wave cut off energy were measured as same above for the bulk ceria. The volume of the defect unit cell was computed from the converged lattice parameter. The influence of dopant on the band structure, density of states and charge density of the state were also evaluated. DFT+*U* (GGA) methodology with varying values of *U* in the range of 3-5 eV was performed for the evaluation of the contribution of localized strongly correlated Ce 4f states.

8.3. Results and discussion

8.3.1. Convergence of lattice parameter, k-point grid, and energy cut off

The converged plane wave cut off energy, k-point grid and lattice constants were investigated. From the bulk convergence calculation, the total energy and equilibrium volume were calculated. Fig. 1 represents convergence of plane wave cut off (Fig. 1a), k-point grid (Fig. 1b) and lattice parameter (Fig. 1c) of bulk ceria. For this calculation, DFT based on GGA introduced by PW91 were used. Fig. 1a shows that the energy cut off for the bulk ceria unit cell (1×1×1) is 180eV. Brillouin zone grid is converged for (11×11×11) (Fig. 1b) and lattice parameter convergence of 5.4 Å (Fig.1c).

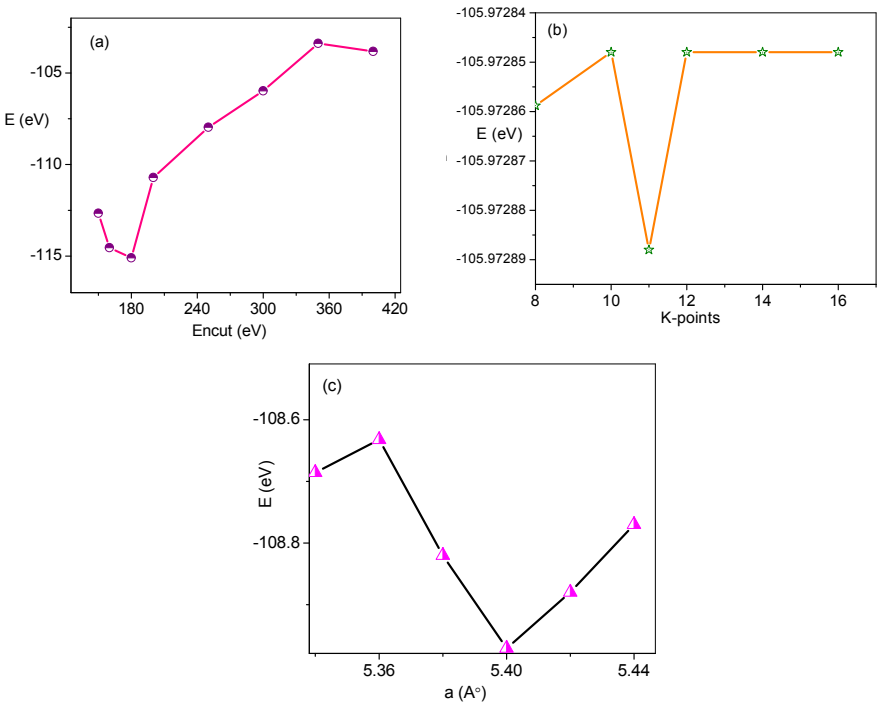

Fig. 1 Plots of convergence of Encut (a), k-point (b) and lattice parameter of bulk ceria (c) (calculated based on DFT+GGA).

The total ground state energy for the bulk ceria was found to be -112.94eV and the volume computed from the lattice parameter was 157.46Å^3. The DFT calculation based on LDA introduced by PAW approach is also performed in order to make comparison with DFT+GGA.

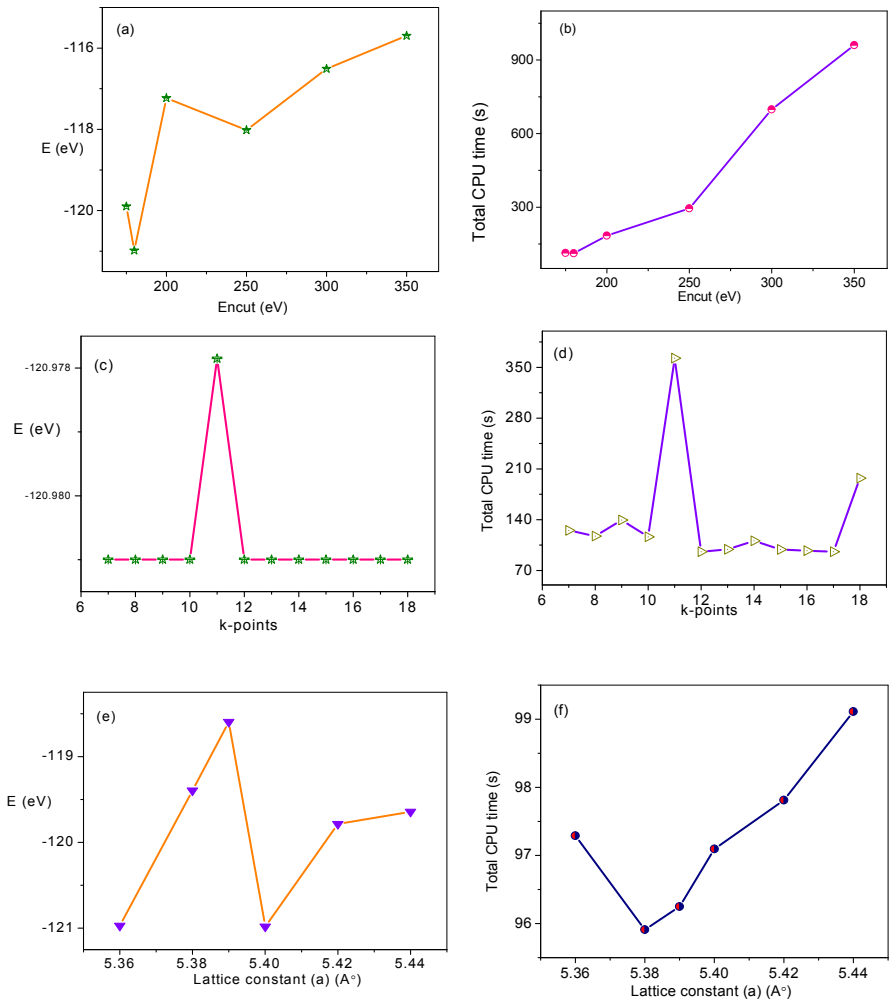

Fig. 2 The plots of convergence of Encut (a), Encut *vs* Total CPU time (b), k-point (c), k-point *vs* Total CPU time(d) and lattice parameter of bulk ceria(e) and lattice parameter *vs* Total CPU time(f) (calculated based on DFT+LDA).

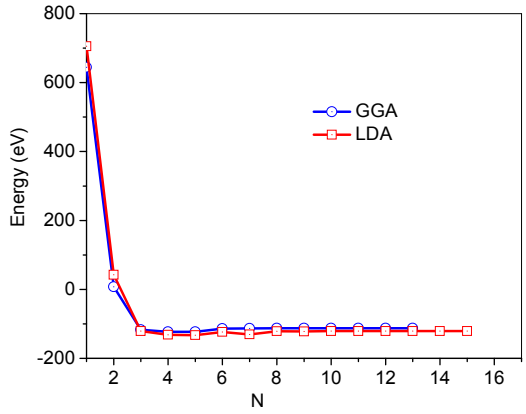

Fig. 3 The comparison of total energy convergence plots made by DFT+GGA and DFT+LDA of bulk ceria

Fig. 2 shows the plots of convergence of energy cut off, k-point grid and lattice parameter and total CPU time needed for each convergence. The results show that these values are concomitant with those evaluated by GGA method. LDA chooses delocalized electron interaction while GGA account localized electron interaction. Literature reports that for studying bulk properties of materials, DFT with GGA is more profound than LDA. Fig. 2a corresponds to the convergence graph of plane wave cut off energy in the range of 175-350eV and total CPU time needed for the plane wave energy convergence (Fig. 2b). It was displayed that converged plane wave cut off energy is 180eV, which requires comparatively lesser CPU time than others. Fig. 2c represents the convergence of k-point grid and Fig. 2d exhibits that k-point grid of (12×12×12) requires lower time and energy for its convergence. Fig. 2e displays the convergence plot of lattice parameter and was found that the calculations were converged at lattice constant, *a*, at 5.4Å. Fig. 2f exhibits the time need for the lattice constant convergence and was observed that the factors, time and energy are the key component in determining the converged values of a bulk crystalline material. Fig. 3 represents the plots of total energy

convergence carried out by GGA and LDA exchange correlation functional. The converged total energy by LDA methods takes more iteration steps for the optimization and the value was found to be -120. 834eV.

Fig. 4 represents the DFT+GGA calculation for the convergence of lattice parameter, k-point grid and plane wave cut off energy for the copper doped ceria. The presence of displacement of Ce with Cu has not made changes to the k-point grid (11×11×11) and lattice parameter (5.38 Å). But the energy utilized for the plane wave basis set remains unchanged. The presence of Cu^{2+} increases the total ground state energy of the bulk material to -95.82eV. Hence, the volume computed from the lattice parameter was found to be 155.72$Å^3$. The decrease of volume occurs because of the prevailing lattice strain due to the introduction of copper.

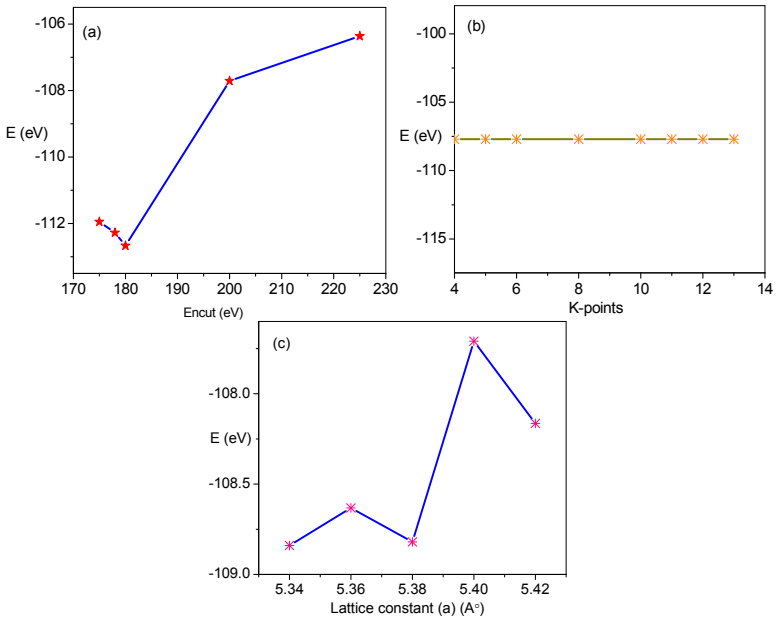

Fig. 4 The plots of convergence of Encut, k-point and lattice parameter of Cu^{2+}-doped ceria (calculated based on DFT+GGA).

The same convergence calculations are repeated with exchange correlation functional LDA introduced by projected augmented wave approach. Fig. 5 shows the results of convergence calculation of copped doped ceria made by LDA method. The calculated converged values of copper doped ceria was found to be 210eV (Fig. 4a) for the Encut value of plane waves with Monkhorst pack grid of 20×20×20 (Fig. 4c). Figs. 4b&d respectively displays the total CPU time *vs* Encut and k-point grid. The introduction of copper to the ceria lattice markedly enhances the value of plane wave cut off and k-point grid. But the presence of copper made some lattice strain causing a decrease in lattice parameter. This has aroused the total ground state energy of the bulk ceria to -106.46eV.

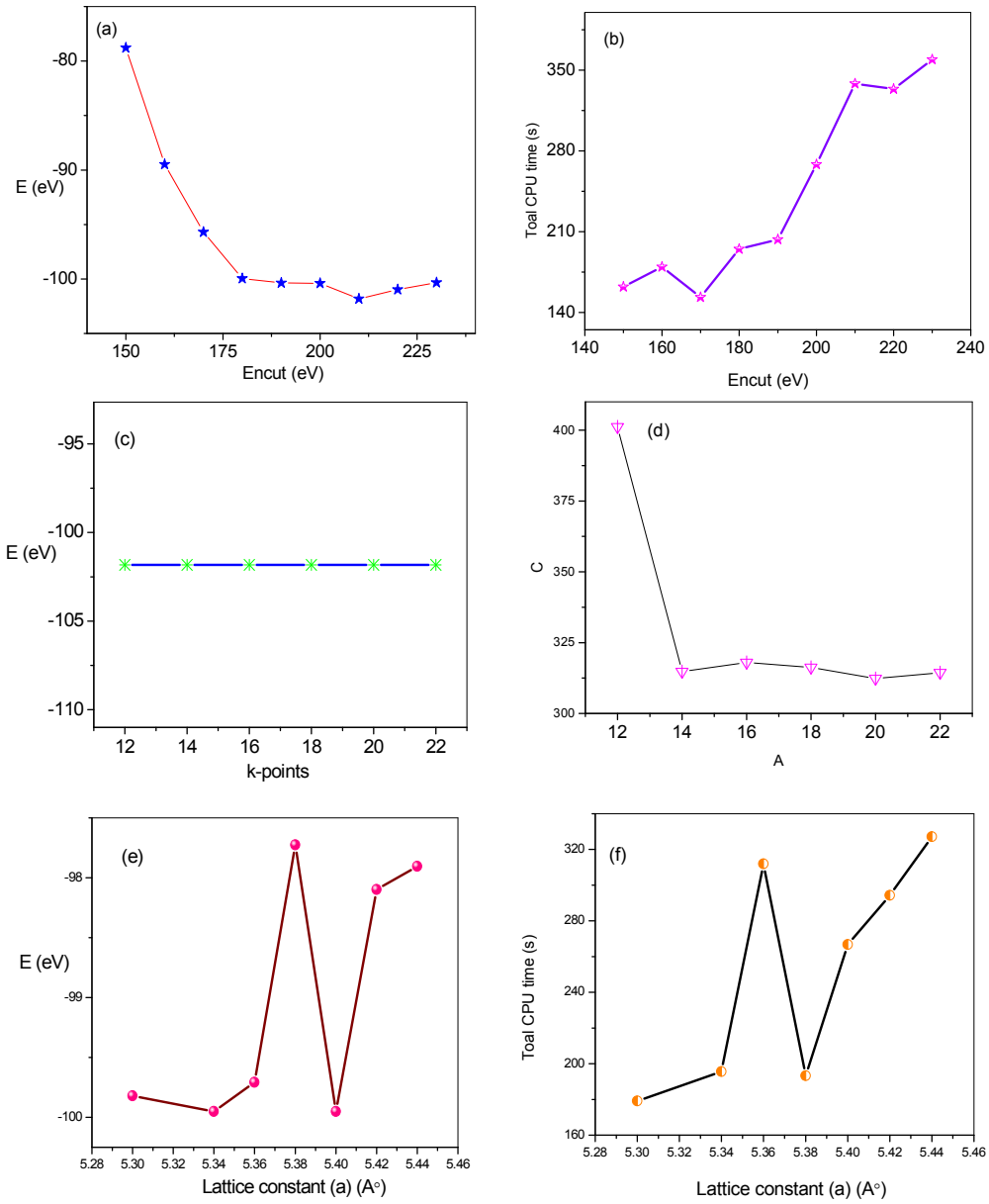

Fig. 5 The plots of convergence of Encut (a), Encut *vs* Total CPU time(b), k-point (c), k-point *vs* Total CPU time(d), lattice parameter of copper doped ceria (e) and lattice parameter *vs* Total CPU time (f) (based on DFT+LDA).

From the comparison of total energy convergence plots of doped ceria (Fig. 6), it has been found that LDA method takes more optimization steps than GGA method and hence lowers the convergence value of total ground state energy (E_0).

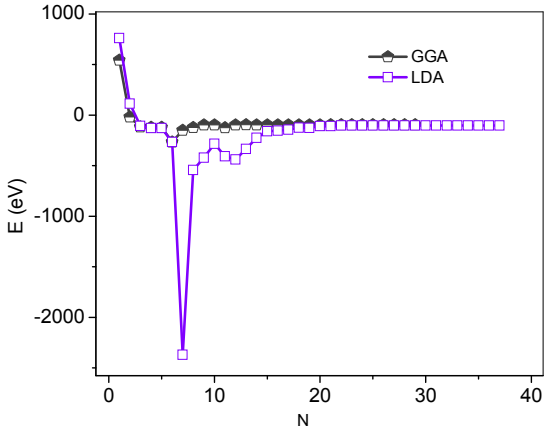

Fig. 6 The comparison of total energy convergence plots made by DFT+GGA and DFT+LDA of Cu^{2+} doped ceria

8.3.2. Band structure and density of states

CeO_2 has cubic fluorite type structure with four Ce atoms and 8 oxygen atoms per unit cell. Band structure of bulk ceria and Cu^{2+} doped ceria were calculated by the non-self-consistent field energy calculation by DFT with exchange energy correlational brought out by GGA and LDA. Fig. 7 exhibits the band structure of CeO_2 described by DFT+GGA method. The low lying bands are not included in the plot. Fig. 8 represents the band structures of low lying Ce (5s) &Ce (5p), highest occupied valance band orbitals of Ce (5d) and lowest conduction bands of Ce (4f) orbitals. The low lying 5s orbitals of Ce are overlapped to form bands in the energy range of -32.05 - -32.65eV

(Fig. 8a). Fig. 8b represents bands of 5p orbitals of Ce in the energy range of -11- -20eV (which are below the valence bands). The 5d atomic orbitals of Ce are overlapped to form valence band in the region of -0.5- -0.45eV (Fig. 8c). The narrow conduction band is formed from the overlapping of 4f atomic orbitals of cerium atom; these are above the Fermi level in the range of 2.1-2.5 eV (Fig. 8d).

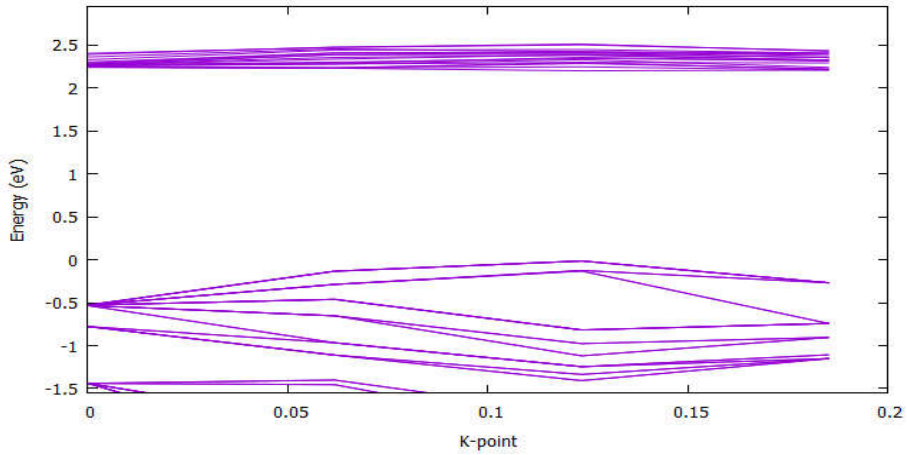

Fig. 7 The band structure of CeO_2 calculated from DFT+GGA method

Fig. 9a consists of bands constructed from the 2s atomic orbitals of oxygen atom of CeO_2. These bands are occupied just below the valence bands in the region of -11- -20eV. Besides, the Figs. 8b & 9a exposed that there exist interaction between 5p (Ce) and 2s orbitals of oxygen atom. Fig. 9b corresponds to the band structure of 2p atomic orbitals of oxygen atom in the region of -1.5 - -4.5eV. The valence band between -0.5 - 4.5eV are composed of O (2p) and small mixture of Ce 5d atomic orbitals. The nature of Ce active site is not well described yet since the 4f electrons are laying far above the Fermi level.

The width of the band increases as the electronic overlap increases. The interatomic orbitals or core orbitals (valence f or d orbitals) will tend to form narrow bands with high effective masses. The band structure of ceria (Fig. 7) shows non- zero Fermi energy. A Fermi level is the highest occupied electronic state, and now in the considered work, it is placed just below the zero energy. The range of forbidden energy between the energy bands are known as band gaps. The lower energy bands are formed from the core orbitals and form narrow bands and for most cases, they are treated as a set of localized atomic orbitals. This occurs due to the strong interaction of nuclei with these orbitals that prevent the overlapping of orbitals of neighboring nuclei. For small molecules, the greater overlap leads to greater energy difference between valence band and conduction band. Similarly, in continuous solids, the greater overlap causes to greater spread of energies called band width of the resulting band[17].

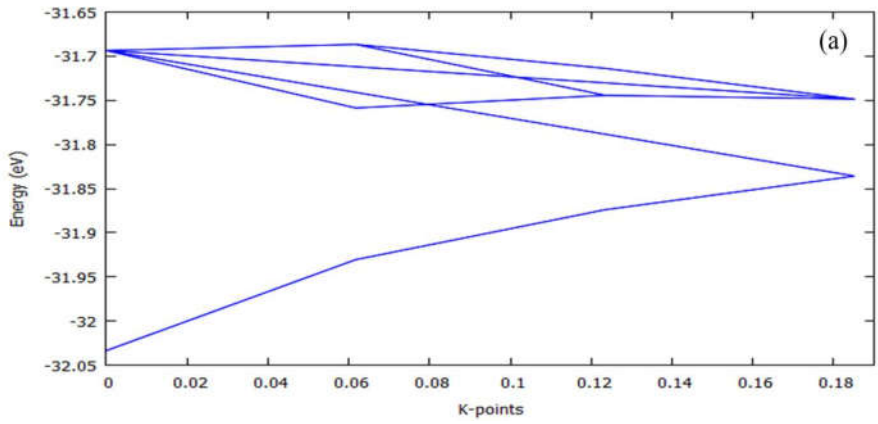

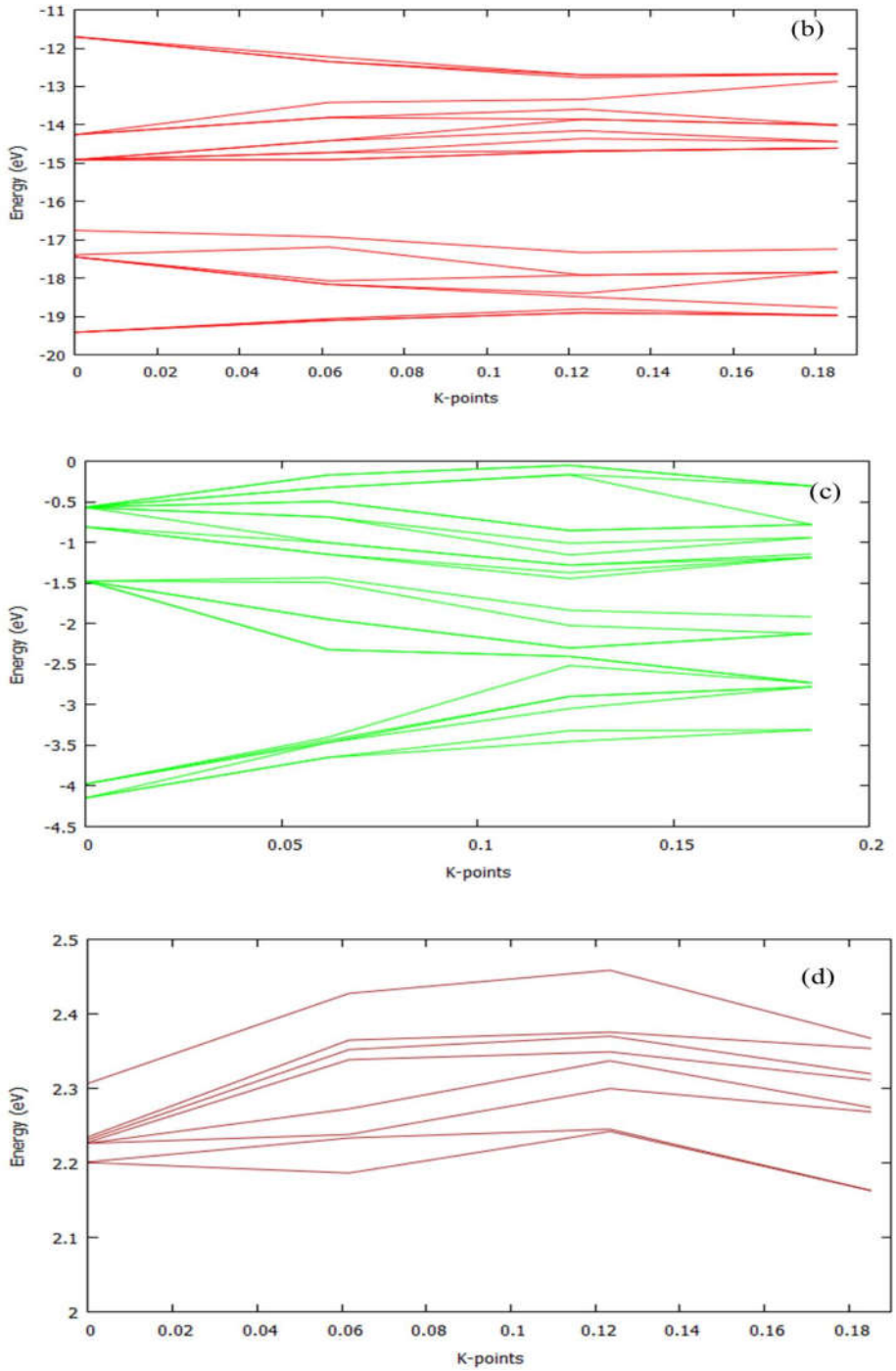

Fig. 8 The band structures of 5s (a), 5p (b), 5d (c) and 4f (d) orbitals of cerium atom

The qualitative description of an electronic conduction can be predicted for materials with band gaps. If the band gap value is lower than the 3eV, the material is semiconductor and if the band gap value is wider, it is said to be insulator. The direct band gap between highest occupied valence band and lowest region of conduction band indicates a band gap of 2.09eV. This value is comparable to the experimentally and theoretically observed band gap, 1.82eV, of bulk CeO_2 crystals[18]. Hence the bulk CeO_2 is a semiconductor material. For the metals, the forbidden region is also occupied with energy bands.

One important quantity which can be used to define electronic state of a material is the electronic density of the material. Electronic density of state ρ (E) dE = number of electronic states with energies in interval E, E+dE. Plane wave DFT calculation expresses the electronic density in function of the form *exp (ik.r)*. Electron associated with plane wave has the energy $E = hK^2/2m$. The electronic density is determined by integrating the resulting electron density in k-space.

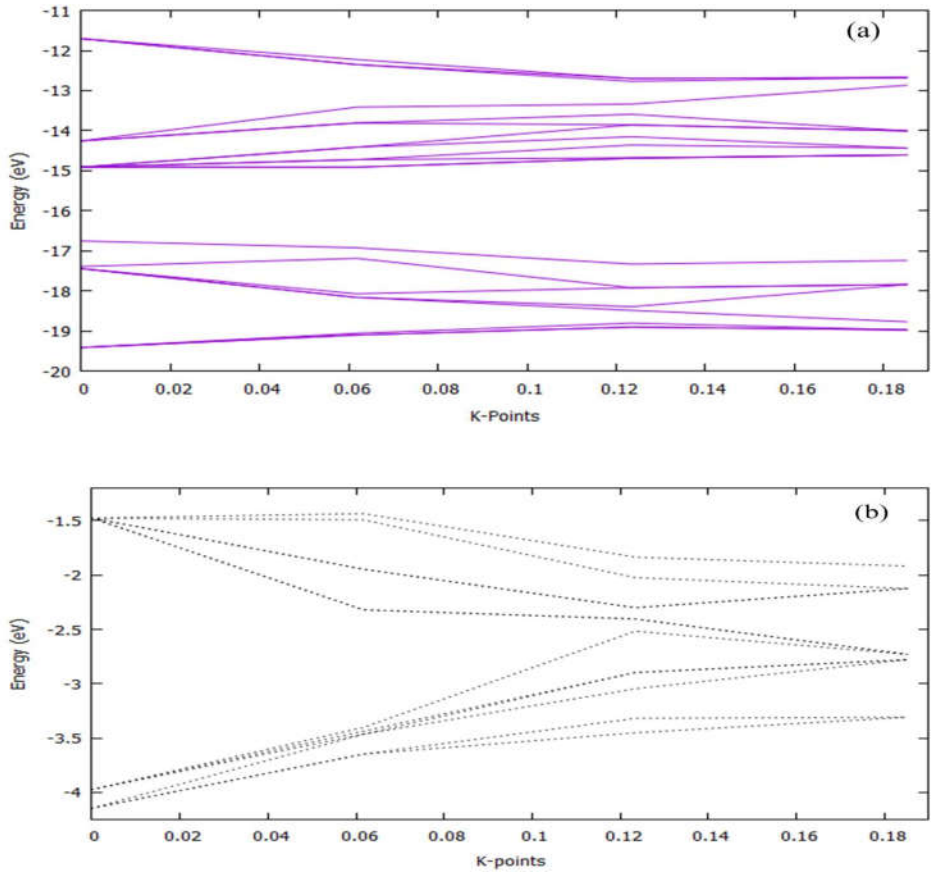

Fig. 9 The band structure of 2s (a) and 2p (b) atomic orbitals of oxygen atom

Fig. 10a shows the total density of states (TDOS) plot calculated by non-spin polarized method. As shown in Fig. 10, density of states (DOS) can be separated into two regions, valence band and conduction band. Valence band is the collection of all occupied electronic states while in conduction band; all the states are not occupied. From the density plot, the band gap is the region where valence band and conduction band have no density of states. The slope of the plot varies discontinuously in a number of places (hence indicates the presence of van Hove singularities). Fig. 10b represents

the electron density calculated by the spin polarized DFT method. But the marked difference in electron density calculated by with and without spin polarization was absent. This considered that no change in the total ground state energy of the bulk material. Calculation performing with considering spin of electron tends to lower the energy of the bulk material substantially[7]. Moreover, the density of states of spin up and spin down were cancelled to each other giving non-magnetic ceria unit cell. TDOS calculated without spin of electron shows the non-zero Fermi energy, while TDOS performed with considering spin of electron indicates zero Fermi energy.

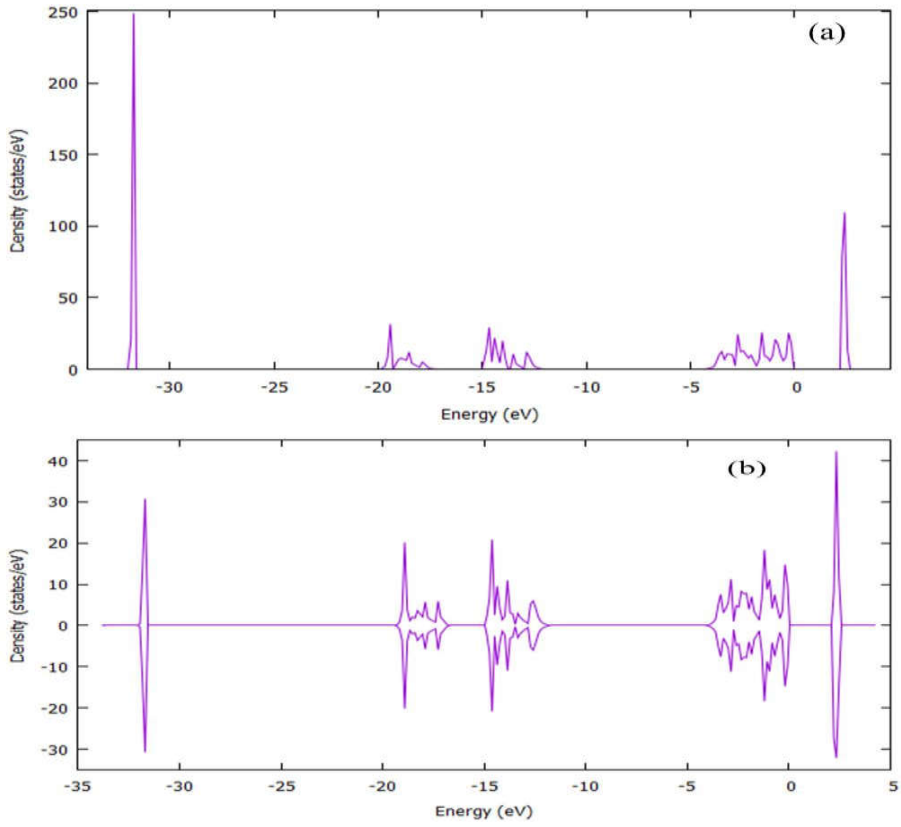

Fig. 10 The total electron density of the material (TDOS): calculated by non-spin polarization (a) and spin polarization (b) of CeO_2.

In order to study the electronic structure of material, it is often important to study which state is important in the vicinity of atom. One standard method is to do is the calculation of projected density of states (PDOS). It is defined as the number of electronic states at a specified energy weighted by the fraction of the total electron density for these states that appears in a specified volume around the nuclei. For performing PDOS computation, need effective radii of atom. PDOS predicts the contribution of each band. Fig. 11 shows the PDOS for 5s (Fig. 11a), 5p (Fig. 11b), 5d (Fig. 11c) and 4f (Fig. 11d) atomic orbitals of Ce.

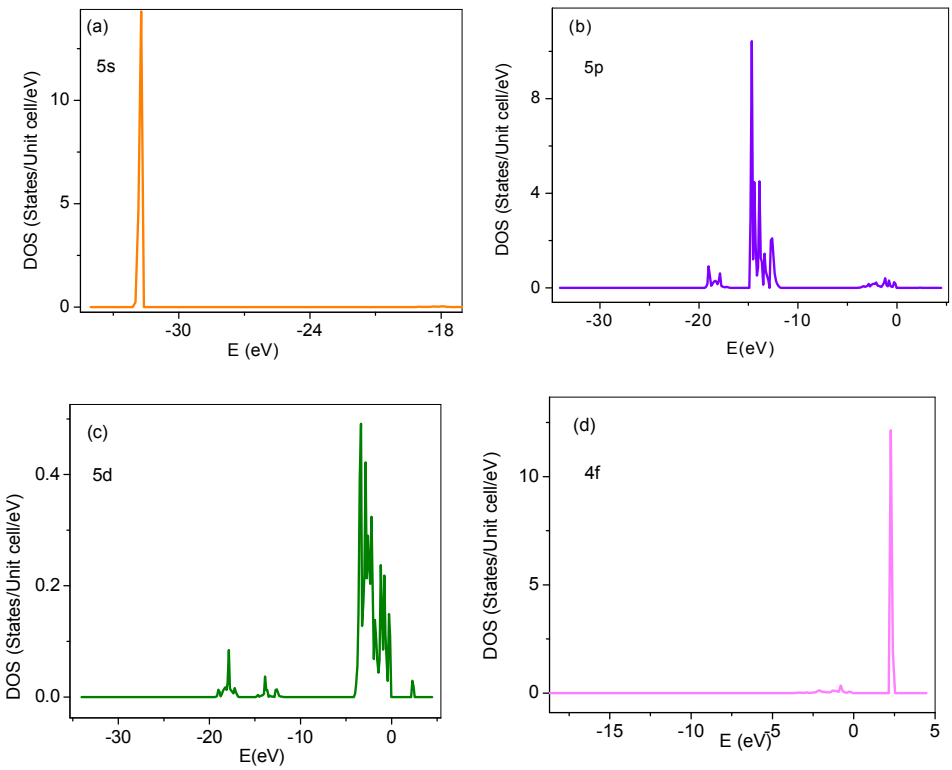

Fig. 11 The PDOS of the 5s (a), 5p (b), 5d (c) and 4f (d) of Ce.

The PDOS of 5s (Fig. 11a) and 5p (Fig. 11b) shows the low lying core electron density. The electron densities of these orbitals are also higher compared to other PDOS. Towards the valence band regions, the contributions of 5d electrons are predominant (Fig. 11c). A small contribution of 5d electrons are also found in the above Fermi energy level. The electron density of 4f orbitals is far above from the Fermi level (Fig. 11d). Fig. 12 shows the PDOS plots of 2s and 2p orbitals of oxygen atom in ceria. 2s bands are overlapped with 5p atomic orbitals of Ce in the region of -10 - -20eV, whereas 2p bands are overlapped with 5d bands of Ce in the valence band region. Fig. 13 shows the PDOS plots of 5s (Fig. 13a), 5p (Fig. 13b), 5d (Fig. 13c) and 4f (Fig. 13d) atomic orbitals of the copper doped ceria.

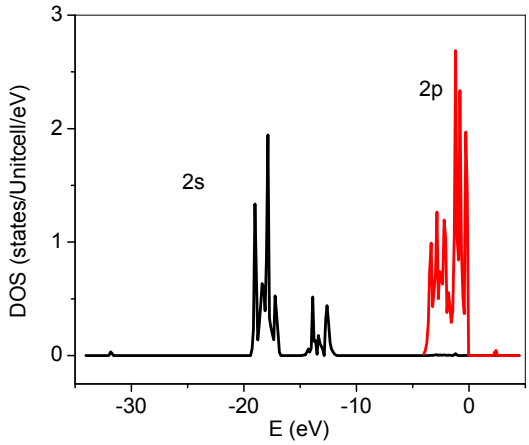

Fig. 12 The PDOS plots of the 2s and 2p orbitals of oxygen.

.

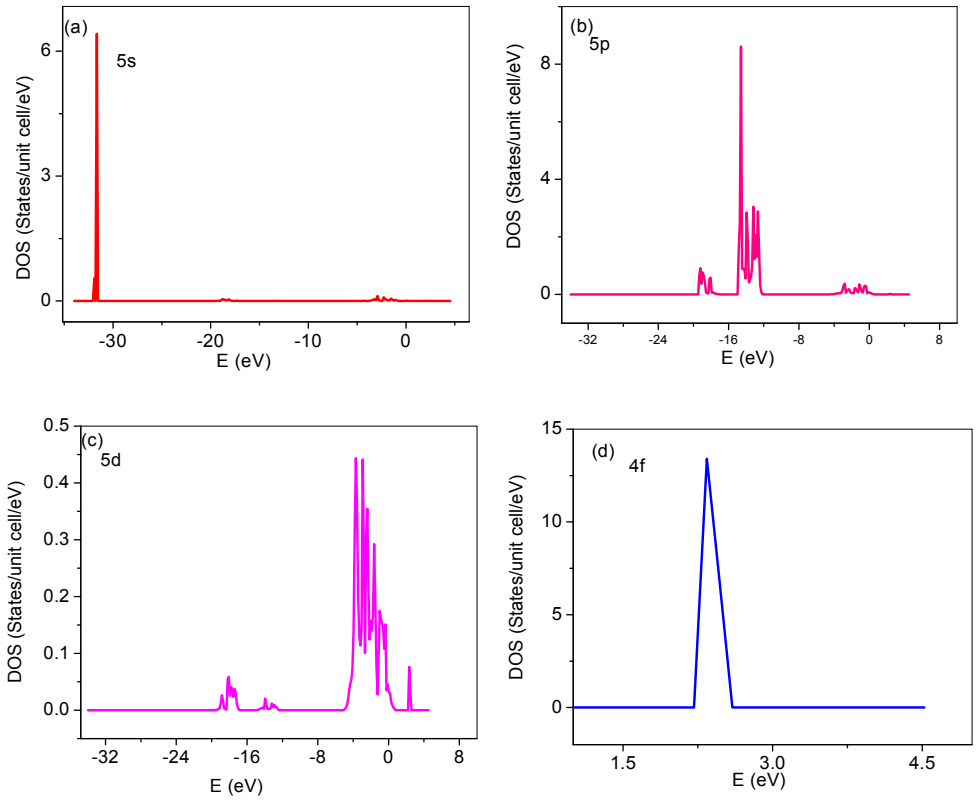

Fig. 13 The PDOS plots of the 5s (a), 5p (b), 5d (c) and 4f (d) atomic orbitals of copper doped ceria.

Density of states of localized atomic orbital 5s (Fig. 13a) was reduced in copper doped ceria, so that the peak became sharper. DOS of 5p atomic orbital remain unchanged in the Cu-Ce-O while significant change in the 5d orbital is seen (Fig. 13c). A similar broadening is observed for 4f orbital (Fig. 13d). These changes were occurred due to the overlapping of 3d and 2p atomic orbitals of copper. The 2s atomic orbital of oxygen atom is retained its DOS, but 2p atomic orbitals (Fig. 14) experiences overlapping which led to increase in the Fermi energy of the doped ceria than the undoped ceria. Fig. 15

indicates that valence shell atomic orbitals (3d, 3p & 4s) and 2p atomic orbitals take part in the overlapping with valence shell orbital 5d of Ce. Hence the 5d peaks of doped ceria get broadened and increase the Fermi energy level of ceria. Besides, rather smaller overlapping of 4f orbital with 5d, 2p, 3p and 4s orbitals, the narrow peak of conduction band is get broadened. This led to reduction of the forbidden region. Hence the electron transport and conductance properties of copper doped ceria shows enhanced performance than the pure ceria. Fig. 16 displays the calculated TDOS plot of Cu-Ce-O calculated by non-spin polarized DFT with exchange correlation functional GGA.

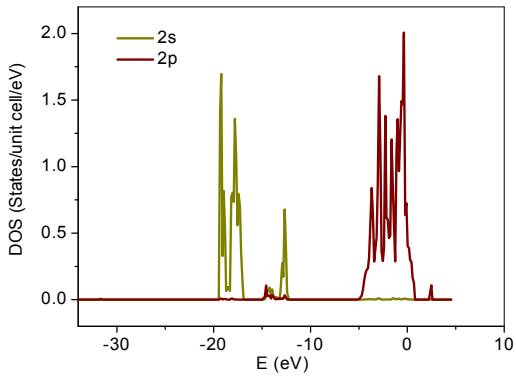

Fig. 14 The PDOS plots of 2s and 2p atomic orbitals of Ce

Upon doping the density of the mixed oxide was decreased markedly as seen from Figs. 10a &b and Figs. 16a&b. Moreover, the ground state energy calculated by considering both spin of electron in the copper doped ceria shows lowering of the ground state energy by small fraction. Also, the DOS of spin up and down are unequal, imparting some un paired character in the single unit cell of ceria due to the overlapping of the orbitals of Cu^{2+}. The electronic state

concentrated in wider range of energies and higher electron density of un-occupied or partially occupied electronic states above the Fermi energy level specifies that Cu-Ce-O has gained enhanced chemical reactivity[7].

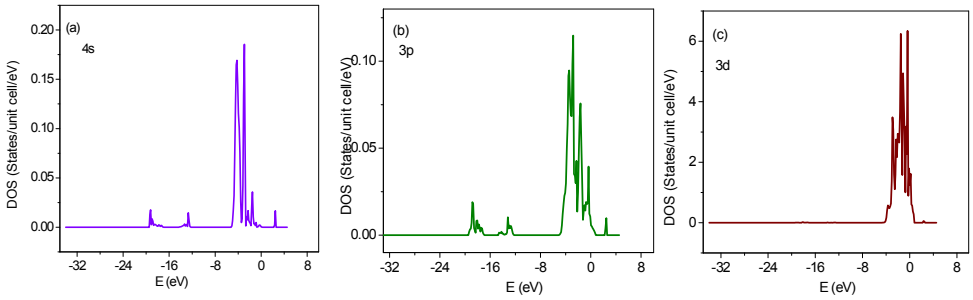

Fig. 15 The PDOS plots of 4s (a), 3p (b) and 3d (c) atomic orbitals of Cu^{2+} in ceria.

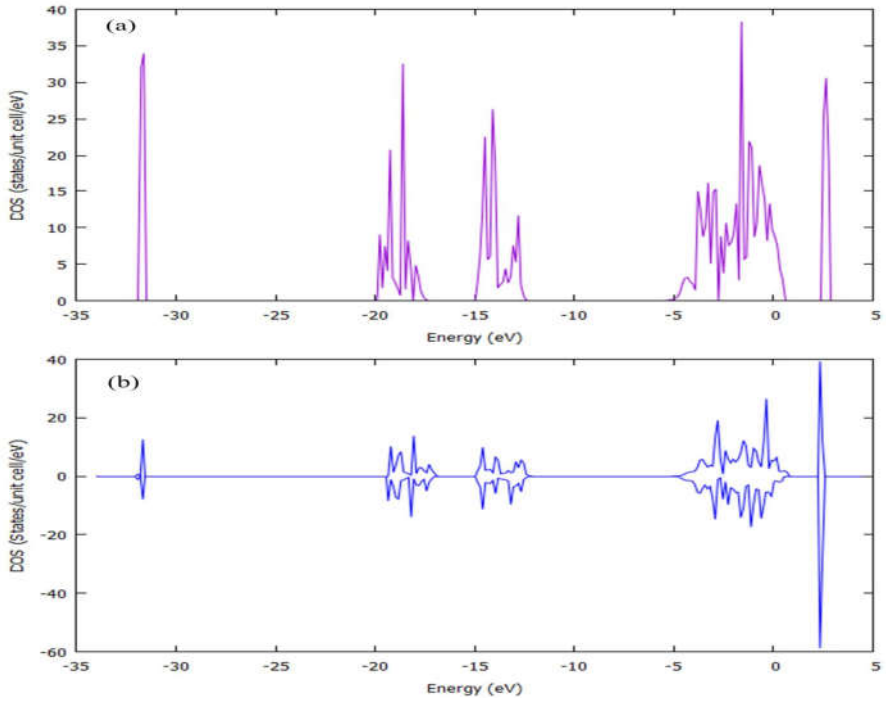

Fig. 16 TDOS plot of Cu-Ce-O non-spin polarized (a) and spin polarized (b)

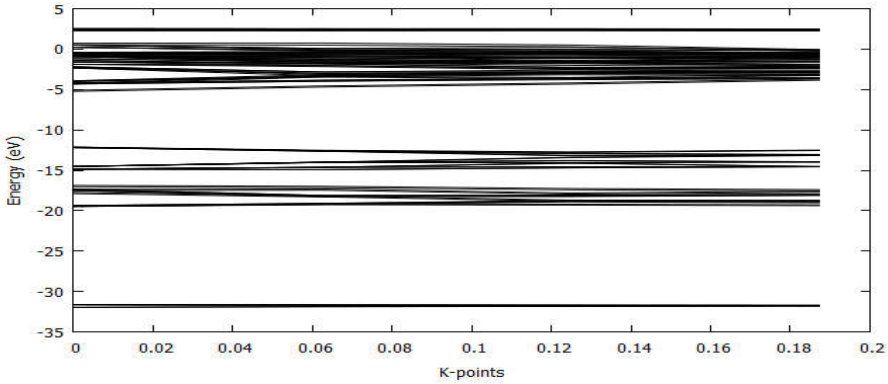

Fig. 17 The total band structure of copper doped ceria

Fig. 17 exposes the total band structure of copper doped ceria unit cell. As indicated in figure, the valence bands are moved nearest to the conduction band. Hence energy of highest occupied energy levels increases, causing a decrease of band gap to 1.54eV. Presence of metal impurities in the ceria lattice can enhance the electron hole recombination rate since it enhances the electronic states within the band gap. This can generate increment in conducting properties of the ceria. Fig. 18 displays the significant changes in the band structures of Cu-Ce-O for the atomic orbitals of 5s, 5p, 5d, and 4f. Fig. 19 reminds the effect of copper doping on the individual bands of 2s and 2p atomic orbitals of oxygen atom of Cu-Ce-O. The band width of 2s (Fig. 19a) and 2p (Fig. 19b) orbital band were increased. The 2p bands were moved towards the forbidden region of ceria whereas the 2s bands to low lying energy region.

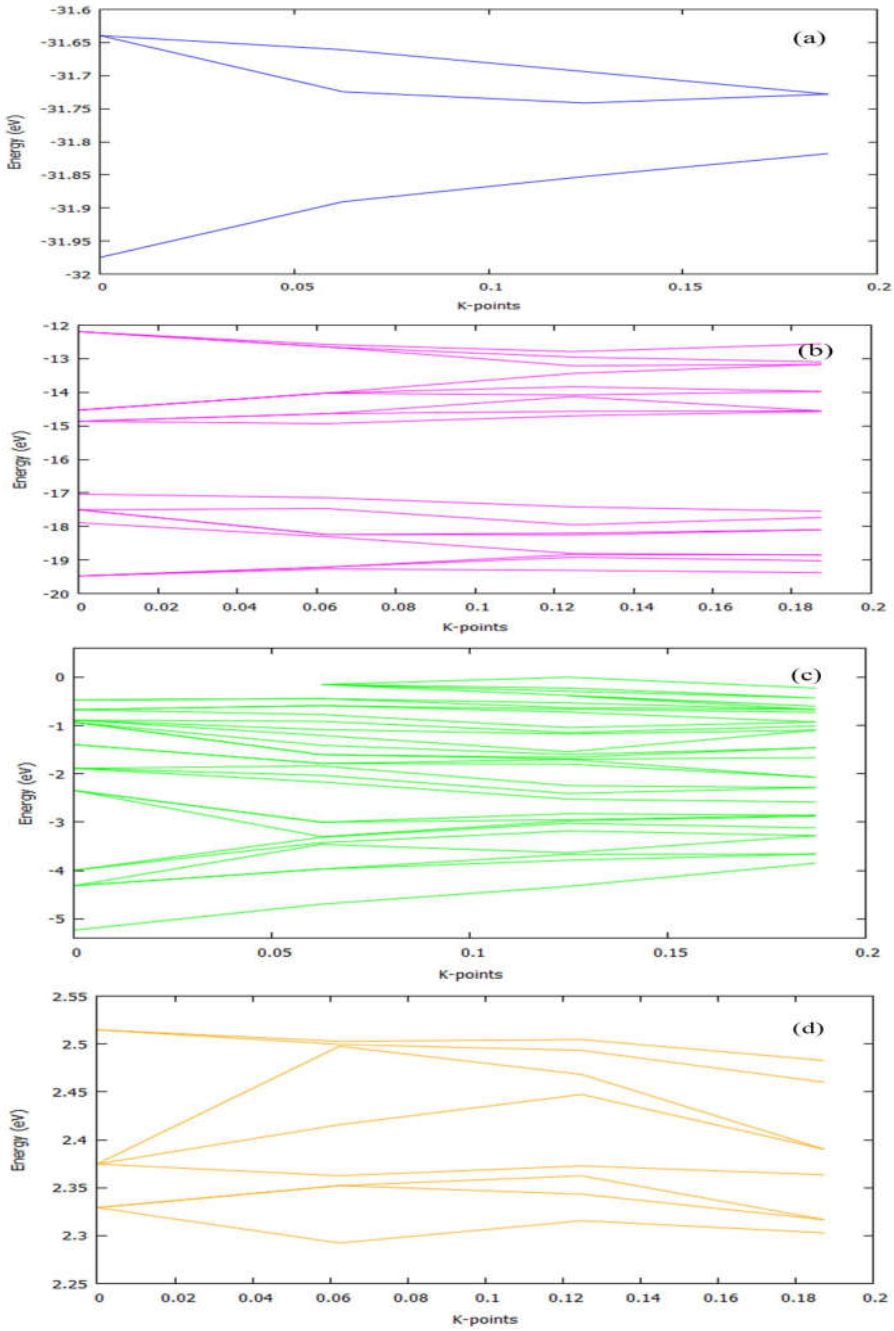

Fig. 18 The band structures of 5s (a), 5p (b), 5d(c) and 4f (d) atomic orbitals of Ce of doped ceria

The 4s orbital bands of copper lie in the region of energies of -3 to -5.25eV just below the valence band (Fig. 20a). The 3p orbital bands are spread out in the range of -0.9 to -4.5eV (Fig. 20b). The more electron dense 3d orbital bands are lying in the energy range of 0.75 - 4.25eV (Fig. 20c).

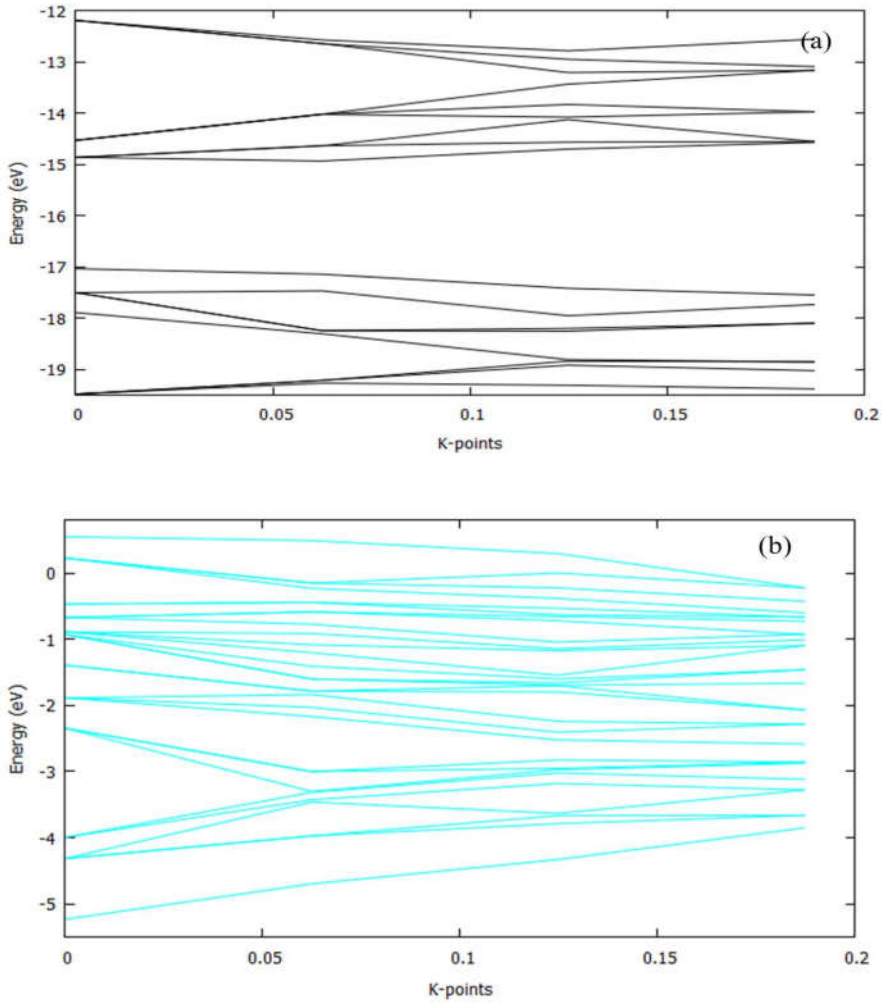

Fig. 19 The band structures of 2s (a) and 2p (b) atomic orbitals of oxygen

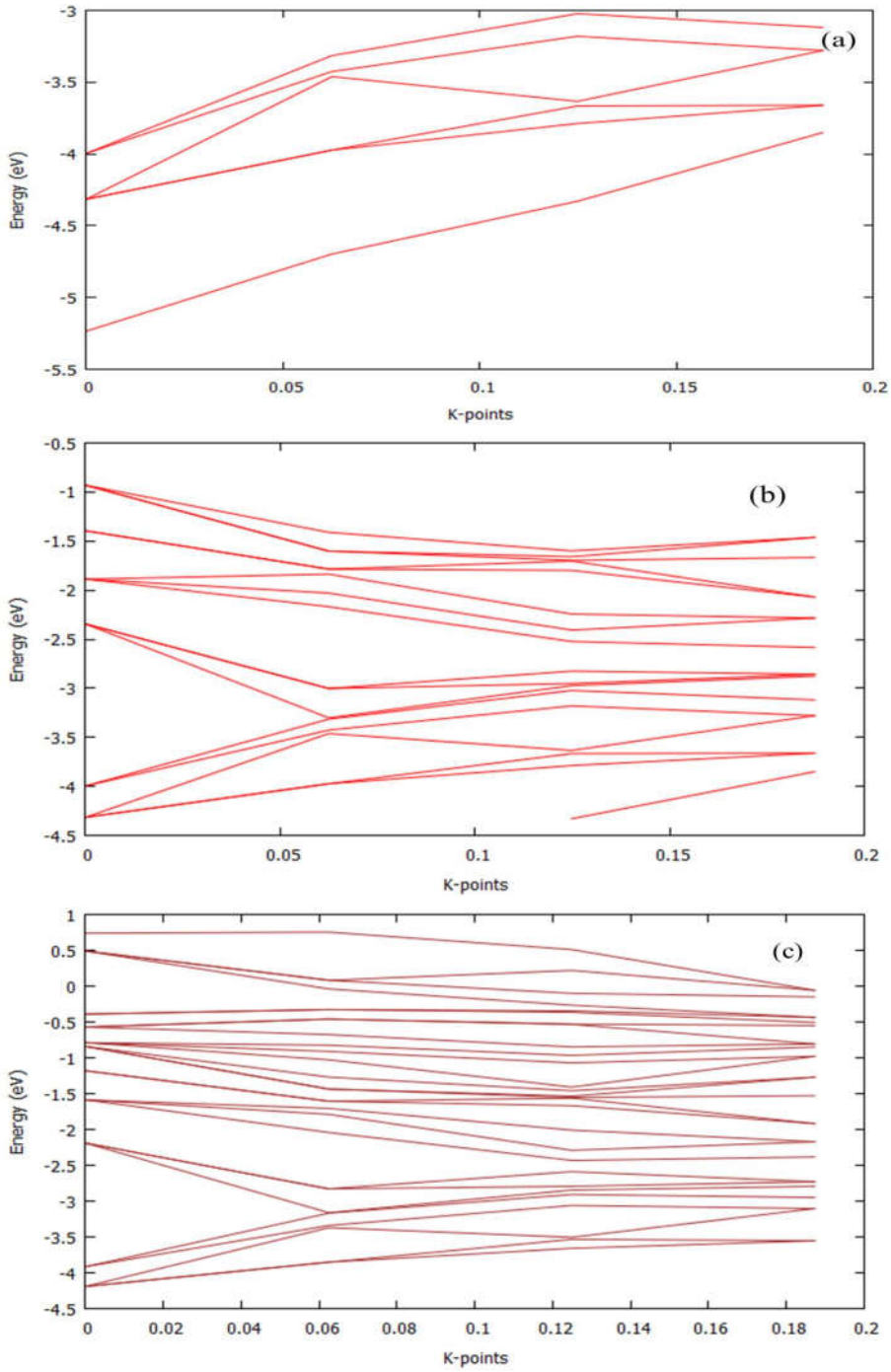

Fig. 20 The band structures of 4s (a), 3p (b) and 3d (c) atomic orbitals of Cu

The broadness of the band near Fermi energy level increased due to the presence of electronic contributions from the Cu 3d, 4s and 3p (Fig. 20) atomic orbitals with 5d orbitals of Ce. The core electron orbital 5s of Ce decreases its band width upon doping whereas; the band width of 4f orbital enhances which makes the oxide more chemically reactive.

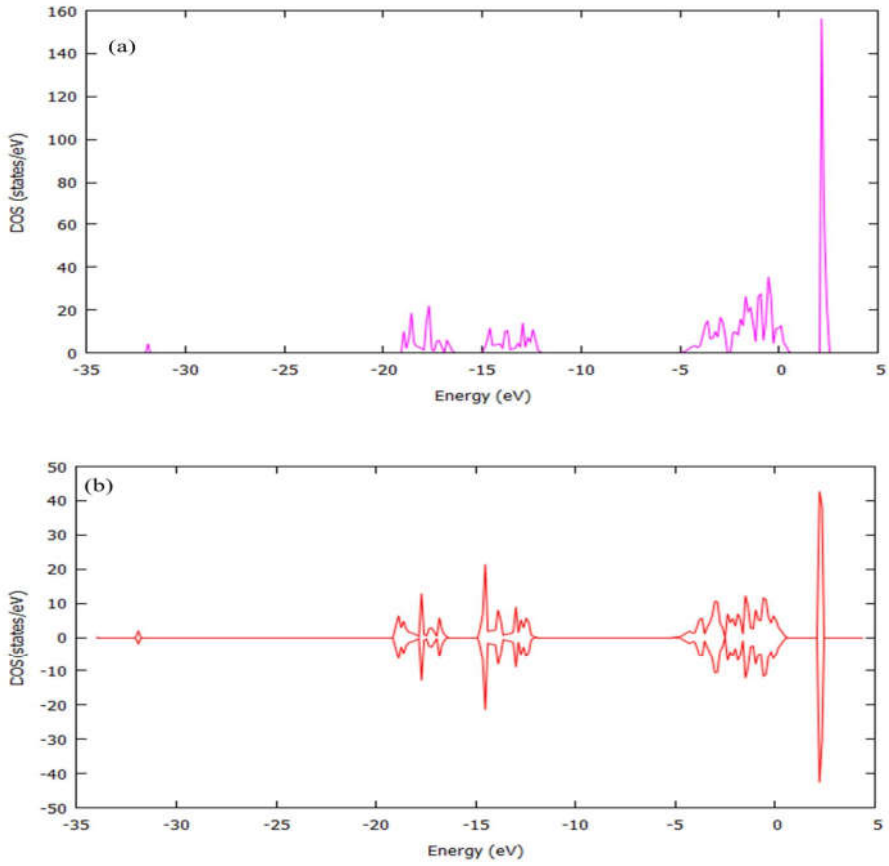

Fig. 21 The DOS plot of copper doped ceria: non-spin polarized (a) and spin-polarized (b) (DFT+LDA method)

Density of states (Fig. 21) and band structure (Fig. 22) calculated by the DFT+LDA shows much difference compared to that

depicted by using GGA correlation functional. Fig. 21a expresses the DOS of non-polarized spin, while spin polarized DOS is expressed in Fig. 21b. LDA is best suitable for giving correction to the contribution to delocalized electrons, while GGA contribute gradient in density and more suitable for localized electron contribution. From the figures one can ensure that GGA correlation functional predict more accurately the DOS and band structure to an extent. For the purpose of studying bulk properties of a material, GGA provides more accurate predictions than LDA method.

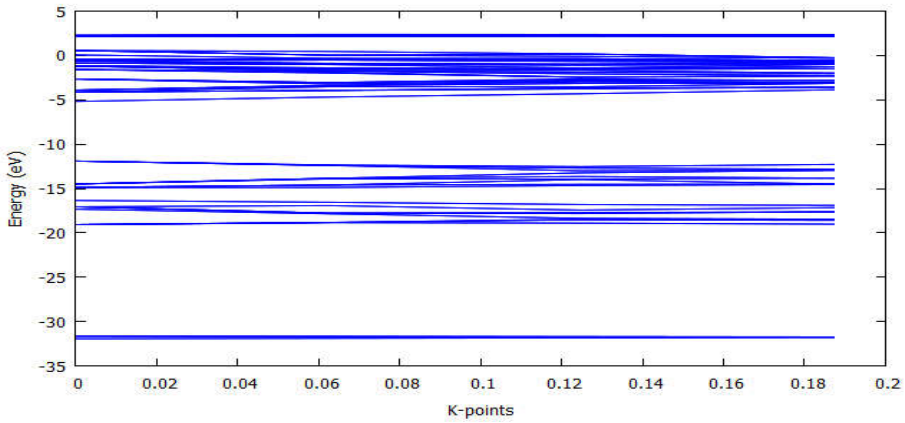

Fig. 22 The band structure of copper doped ceria calculated by DFT+LDA

The calculated band gap between O-2p valence band and 4f conduction band is found to be 1.7eV, which is higher than that predicted by DFT+GGA method.

8.3.3. Charge density distribution

Figs. 23 & 24 explains the charge density distribution of ceria and copper doped ceria along (011) and (001) planes. There exists

significant change in the distribution of electron density along different crystalline planes. This indicates the absence of uniformity of charge density along different crystallographic directions. The charge density distribution of the doped ceria shows the marked influence of copper in the ceria lattice. It increases the charge densities of the bulk ceria, besides, the overlapping of Cu-3d with O-2p and Ce-5d atomic orbitals. In the charge density distribution plots, red region indicates more electron density, while that of blue for more electropositive region.

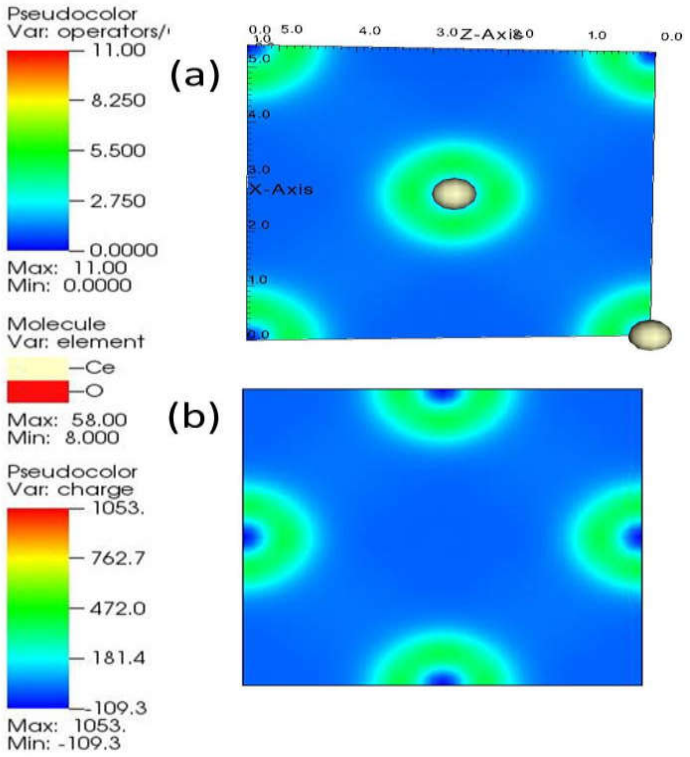

Fig. 23 The charge density distribution of bulk (1×1×1) ceria along (011) (a) and (001) (b) planes

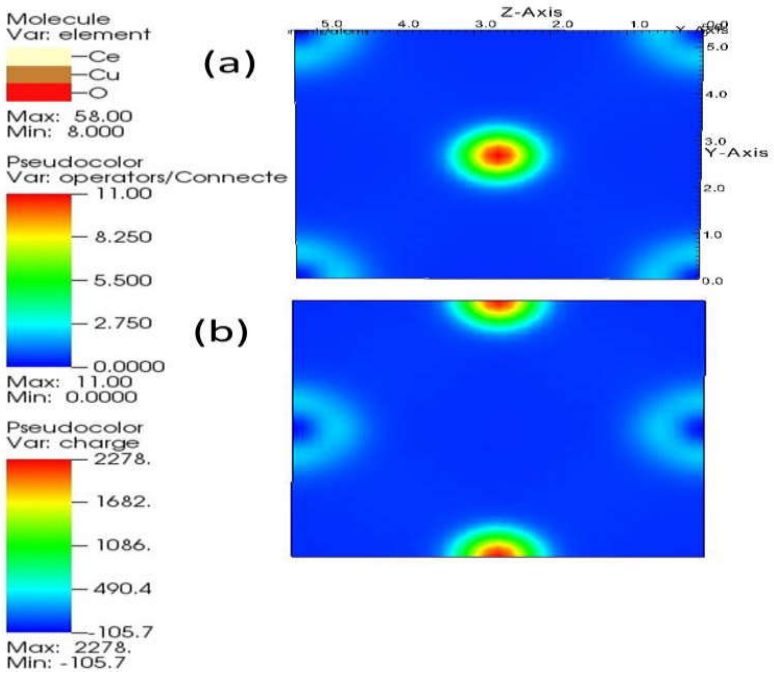

Fig. 24 The charge density distribution of Cu-Ce-O (1×1×1) along (011) (a) and (001) (b) planes.

The existence of higher charge density in the defect ceria clarifies the possibility of bond formation of Cu with Ce and O atoms in the lattice. Hence the bulk energy was increased to -95.82eV. Therefore, the presence of copper in the ceria lattice can empower the performance of ceria to become an eventual material.

DFT method predicts the structure by considering the electron delocalization of the overall Ce atoms in the simulation cell. In order to demonstrate the most accurate ground state properties of ceria and defect ceria, the strongly correlated Ce *4f* states in ceria were performed with DFT+*U* methodology. Coulomb parameter *U* (Hubbard correction) varying in the range of 3-5eV is deployed in the GGA scheme. It was arrived at a conclusion that simulation does not

change the total ground state energy, band structure, and DOS. This happens because the corrections with *U* effectively work with many-body system rather than single lattice structures. However, for single lattices, it was observed that variation of *U* made change in the total CPU time needed for the simulation. In the concerned work, simulation with U = 3.2 eV required lesser time than other *U* values.

8.4. Conclusion

The convergence of lattice parameter, k-point grid, and plane wave energy cut off for ceria and copper doped ceria was performed by DFT+GGA and DFT+LDA. DFT+GGA method is more accurate to predict the electronic structures which are comparable with both theoretical and experimental studies. The total ground state energy of the single cubic unit cell of ceria is -112.94eV (DFT+GGA) and -120.834eV (DFT+LDA) methods. The computed volume from the lattice parameter is 157.46$Å^3$. For the copper doped ceria, the total ground state energy is increased to -95.82eV (DFT+GGA) and -106.46eV (DFT+LDA). The volume of the cell was reduced to 155.72$Å^3$. The calculated direct band gap between highest occupied energy band (O2p band) and lowest unoccupied (4f band) was found to be 2.02eV. The presence of Cu^{2+} in the crystal lattice of ceria caused to decrease the band gap to 1.54eV (GGA scheme). Simulation with DFT+*U* (GGA) did not provide any change in the ground state properties of ceria and defect ceria single lattices. The charge density distribution plots along (011) and (001) planes confirmed the absence of uniformity of charge distribution along different crystallographic directions. The introduction of Cu^{2+} increases the electronic charge density of the ceria lattice.

8.5. References

1. Eugenio FD, Carlos AC, Robinson LM, Mariana MVMS, Ricardo BA, Martin S. Combined DFT and experimental study of the dispersion and interaction of copper species in Ni-CeO_2 nanosized solid solutions. *RSC Adv*. 2016;6:5057-5067.

2. Hua G, Zhang L, Fei G, Fang M. Enhanced catalytic activity induced by defects in mesoporous ceria nanotubes. *J Mater Chem*. 2012;22:6851.

3. Izu N, Itoh T, Nishibori M, Matsubara I, Shin W. Effects of noble metal addition on responsof ceria thick film CO sensors. *Sensors Actuators B Chem*. 2012;171-172:350-353.

4. Rui-Juan Q, Ying-Jie Z, Guo-Feng C, Yue-Hong H. Sonochemical synthesis of single-crystalline $CeOHCO_3$ rods and their thermal conversion to CeO_2 rods. *Nanotechnology*. 2005;16:2502-2506.

5. Balaguer M, Vert VB, Navarrete L, Serra JM. SOFC composite cathodes based on LSM and co-doped cerias ($Ce_{0.8}Gd_{0.1}X_{0.1}O_{2-\delta}$, X = Gd, Cr, Mg, Bi, Ce). *J Power Sources*. 2013;223:214-220.

6. Marzi L, Joaquin De L, Ramos D, et al. Cytotoxicity and genotoxicity of ceria nanoparticles on different cell lines in vitro. *Int J Mol Sci*. 2013;14:3065-3077.

7. Kresse G, Furthmüller J. Efficiency of ab initio total energy calculations for metals and semiconductors using a plane-wave basis set. *Comput Mater Sci*. 1996;6:15-50.

8. Kohn W, Sham LJ. Self-consistent equations including exchange and correlation effects. *Phys Rev*. 1965;140:1133-1138.

9. Xiang W, Shan Q, Ziyu W. Generalized gradient approximation calculations of the pressure-induced phase transition of $_{YAlO3}$ perovskite. *J Phys Condens Matter*. 2006;18:3907-3916.

10. Karin E, Oliver T, Holger O, Marco H, Reinhart A. Auxiliary basis sets to approximate Coulomb potentials. *Chem Phys Lett*. 1995;240:283-289.

11. Vanpoucke DEP, Cottenier S, Van Speybroeck V, Van Driessche I, Bultinck P. Tetravalent doping of CeO_2: The impact of valence electron character on group IV dopant influence. *J*

Am Ceram Soc. 2014;97:258-266.

12. Alaydrus M, Sakaue M, Kasai H. A DFT+U study on the contribution of 4f electrons to oxygen vacancy formation and migration in Ln-doped CeO_2. *Phys Chem Chem Phys*. 2016;18:12938-12946.

13. Lixia C, Yuanhao T, Zhang H, et al. First-principles investigation of transition metal atom M (M = Cu, Ag, Au) adsorption on CeO_2 (110). *Phys Chem Chem Phys*. 2012;14:1923-1933.

14. Juarez LFDS, Verónica Ganduglia-pirovano M, Joachim S. Formation of the cerium orthovanadate $CeVO_4$: DFT+U study. *Phys Rev B*. 2007;76:125117-1-125117-10.

15. Jarlborg T, Barbiellini B, Lane C, et al. Electronic structure and excitations in oxygen deficient $CeO_{2-\delta}$ from DFT calculations of calculations. 2014;89:165101-1-165101-165107.

16. Kresse G, Hafner J. Ab initio molecular-dynamics simulation of the liquid-metal–amorphous-semiconductor transition in germanium. *Phys Rev B*. 1994;49:14251-14269.

17. Lesley ES, Elaine AM. *Solid State Chemistry: An Introduction*. 3 rd. Taylor & Francis Group, LLC; 2005.

18. Tsunekawa S, Wang JT, Kawazoe Y, Kasuya A. Blueshifts in the ultraviolet absorption spectra of cerium oxide nanocrystallites. *J Appl Phys*. 2003;94:3654-3656.

NUSRATH. K “SYNTHESIS AND KINETICS OF FORMATION OF CERIA AND CERIA BASED MATERIALS via THERMAL DECOMPOSITION OF OXALATES”. THESIS. DEPARTMENT OF CHEMISTRY, UNIVERSITY OF CALICUT, 2018.

- Elucidation of kinetics of thermal decomposition of cerium oxalate decahydrate (utilizing thermo analytical techniques, TG/DTA/DSC in an atmosphere of nitrogen/air) up to the formation of ceria micro/nano structures.

- Established significant influence of various mass % of CaC_2O_4, semiconducting nano metal oxides (5 mass %) of Fe, Co and Ni, ferrites of Co and Ni, various molar concentrations of Cu^{2+} dopant and effect of surface morphology and synthetic route of oxalate precursors on the kinetics and thermal decomposition behaviors.

- Kinetics of the thermal dehydration of solid state reaction between cerium oxalate micro rods and calcium oxalate was studied using non-isothermal TG/DTA technique.

- The introduction of calcium oxalate in varying compositions significantly impeded the diffusional removal of incorporated water molecules due to the blocking action of surface product layer and the interaction of Ca(II).

- Significant effect in thermal stability was observed for compositions containing lower mass % of calcium oxalate (10 mass %). The average values of Ea_i for each independent process of thermal dehydration of mixed oxalates are in the order $CC_4 < CC_3 < CC_2$.

- Kinetic and mechanistic features of the synthesis of micro structural rods of CeO_2 *via* the oxidative thermal decomposition

of cerium oxalate in air and the effect of dry mixing of 10 mass (%) calcium oxalate with cerium oxalate upon the reaction pathway and mechanism were investigated.

- The *in situ* Ca^{2+}interaction and the consequent increase in the internal gaseous pressure varied the temperature range of the reaction to higher values and hence higher value of *Ea* was needed for the mixed sample. Mixed cerium oxalate (CC_2) undergoes reaction with increased rate even if the temperature of the reaction shifted to higher region.

- Nano iron oxide promotes the dehydration stages by lowering the *Ea* value to 35-36 $kJmol^{-1}$. Nano Co_3O_4, $CoFe_2O_4$ and $NiFe_2O_4$ promote both the dehydration as well as decomposition stages, by decreasing the *Ea* value. But nano NiO shows retarding effect on both dehydration as well as decomposition stages.

- Cerium oxalate discs/flower was synthesized through the surfactant assisted precipitation method. Following the stepwise thermal decomposition strategy of the oxalate precursor, ceria nano discs/flower were synthesized and characterized.

- Significant influence of various reactant molar ratios of Cu^{2+}:Ce^{4+} have pivotal role on the creation of new oxygen vacancies, decomposition strategy, particle size and shape.

- Homogeneous distribution of Cu^{2+} on the oxalate precursor have significant role on the catalyzing activity for the destruction of oxalate bond to oxide. Doped ceria with Cu^{2+} (x = 0.02) promoted breaking of oxalate bonds in nitrogen atmosphere.

- Raman intensity ratio and hence the concentration of oxygen ion vacancies were highest for the ceria lattice containing higher concentration of copper (x = 0.3).

- *In vitro* cytotoxicity study reveals doped ceria (x = 0.1) exposed enhanced anticancerous properties towards Dalton's Lymphoma ascites cells.

- Effects of synthetic route (simple precipitation and hydrothermal) and surface characteristics of the oxalate precursor (nano *flower petals*, *plates*, *discs/flower* and *array of nano hexagonal* Ce-Ox) on the kinetics of thermal decomposition process were investigated

- Upon thermal decomposition, ceria nano structures with *branched hexagonal nanorod*, *multi branched*, *nano discs/flower* and *2D nano sheets* were synthesized. The values of *Ea* were found to be lowest for the production of *2D* ceria *nano sheets*.

- Highest luminescent and UV-absorbing properties were observed for ceria *nano discs/flower*.

- ❖ Raman intensity ratio and hence the concentration of oxygen ion vacancies were highest for the *nano disc/flower* like ceria.

- ❖ *In vitro* cytotoxicity assay reveals that medicinal properties of ceria are largely dependent on the surface characteristics of ceria nano structures. The sample P_1 exhibits enhanced inhibition (73%) towards Dalton's Lymphoma ascite cells.

- ❖ Computation of electronic structure (DOS and band structure) of bulk ceria (1×1×1) and copper doped ceria were performed by plane wave based DFT method using *Vasp 5.4.1* version.

- ❖ The comparisons of electronic structure were made by introducing different exchange correlational, GGA and LDA.

- ❖ Presence copper in the ceria single unit cell enhanced the ground state energy, decreases the value of band gap and increases the charge density along (001) and (011) crystallographic direction.

Future Outlook

- Concerning the medicinal field, it is more profound to pass through the modification of anticancerous properties of ceria by doping with various reactants molar ratios of rare earth elements.

- *In vitro* and *in vivo* cytotoxicity and genotoxicity studies with ceria nano particle having various surface modifications.

- As the extension of the computational investigations, simulation of surface reactions of ceria nano clusters for removing the pollutants such as CO, NO_x and organic molecules such as benzene, toluene, etc. can be performed and hence to go through catalytic design based on DFT.

- First principle calculation based on DFT for the elastic and thermo electric properties, oxygen vacancy formation and migration in ceria nano clusters can be brought out.

- DFT studies relating the reactivity of size dependent cerium oxide nano clusters for the redox and photo dissociation reactions.